Designing an Elastomeric Binder for Large-Volume-Change Electrodes for Lithium-Ion Batteries

by

Zonghai Chen

Submitted in partial fulfillment of the requirements
for the degree of Doctor of Philosophy

at

Dalhousie University
Halifax, Nova Scotia
Feburuary 2004

Your file Votre référence
ISBN: 0-612-89799-0
Our file Notre référence
ISBN: 0-612-89799-0

DALHOUSIE UNIVERSITY

DEPARTMENT OF CHEMISTRY

The undersigned hereby certify that they have read and recommend to the Faculty of Graduate Studies for acceptance a thesis entitled "Designing an Elastomeric Binder for Large-Volume-Change Electrodes for Lithium-Ion Batteries" by Zonghai Chen in partial fulfillment of the requirements for the degree of Doctor of Philosophy.

Dated: February 20, 2004

External Examiner:

Research Supervisor:

Examining Committee:

Departmental Representative:

DALHOUSIE UNIVERSITY

DATE: Febuary 20, 2004

AUTHOR: Zonghai Chen

TITLE: Designing an Elastomeric Binder for Large-Volume-Change Electrodes for Lithium-Ion Batteroes

DEPARTMENT OR SCHOOL: Chemistry

DEGREE: Ph.D CONVOCATION: May YEAR: 2004

Permission is herewith granted to Dalhousie University to circulate and to have copied for non-commercial purposes, at its discretion, the above title upon the request of individuals or institutions.

Signature of Author

Table of Contents

List of Figures.....x

List of Tables.....xxiv

Abstract.....xxv

List of Abbreviations and Symbols.....xxvi

Acknowledgements.....xxx

Chapter 1 Introduction to lithium-ion batteries.....1

1.1 Importance of lithium-ion battery development.....1

1.2 Electrochemistry of lithium-ion batteries.....2

1.3 Advanced negative electrode materials for lithium-ion batteries.....6

1.4 Tether model and proposal.....10

1.5 Scope of this thesis.....16

Chapter 2 Introduction to polymer mechanics.....18

2.1 Mechanical properties of polymer samples.....18

2.2 Random walk model for elastomers.....20

2.3 Mechanical models.....22

2.4 Chemical modification of polymers and their solids-filled composites.....23

2.4.1 Crosslinking agents.....23

2.4.2 Coupling agent.....25

2.4.3 Plasticizer.....28

Chapter 3 Experimental details.....30

3.1 Polymers investigated in this thesis.....30

3.2 Preparation of polymer and polymer/SS films for mechanical and electrical measurements.....31

3.3 Preparation of samples for the peel test.....32

3.4 Preparation of electrodes.....33

3.4.1 MCMB electrode using PVDF.....33

3.4.2 a-$Si_{0.64}Sn_{0.36}$/Ag electrode using PVDF.....33

3.4.3 a-$Si_{0.64}Sn_{0.36}$/Ag electrodes using elastomers.....33

3.4.4 Combinatorial electrode film using PVDF.....34

3.4.5 Combinatorial electrode film using PVDF-TFE-P.....36

3.5 Mechanical and electrical characterization.....37

3.5.1 Investigation of dry binder films.....39

3.5.2 Investigation of swelled binder films.....42

3.5.3 Peel test.....45

3.6 Soaking Test.....46

3.7 In-situ Resistance technique.....46

3.8 Coin cell construction and testing.....52

3.9 In-situ thickness measurement.....54

3.10 Other physical characterizations.....55

3.11 Specifications of negative electrode materials used.....56

Chapter 4 PVDF-HFP-based elastomeric binder system.....59

4.1 Introduction.....59

4.2 Mechanical and electrical characterization of FC2178 and FC2178/SS samples.....60

4.2.1 Mechanical models.....60

4.2.1.1 The linear model.....60

4.2.1.2 The non-linear model.....61

4.2.2 Poor mechanical properties of PVDF compared to FC2178.....63

4.2.3 Effect of carbon black on the properties of FC2178.....64

4.2.4 Crosslinking of FC2178 with TETA.....65

4.2.5 Introducing the non-linear element in the mechanical model.....70

4.2.6 Effect of TETA on the properties of FC2178 films containing 25 pph SS.....75

4.3 Mechanical and electrical characterization of swelled FC2178 and FC2178/SS films.....79

4.3.1 Swelling of TETA-crosslinked FC2178 in EC/DEC (1:2, v/v).....79

4.3.2 Mechanical properties of swelled FC2178 samples.....80

4.3.3 Mechanical and electrical properties of swelled FC2178/SS samples..81

4.4 Importance of the coupling agent.....85

4.5 Electrochemical characterization of a-$Si_{0.64}Sn_{0.36}$/Ag electrodes.....90

4.6 Summary.....94

Chapter 5 Effect of the Molecular Weight of PVDF-HFP.....96

5.1 Introduction.....96

5.2 Comparison of dry binder films.....96

5.3 Comparison of swelled binder films.....102

5.4 Electrochemical characterization.....106

5.5 Summary.....108

Chapter 6 PVDF-TFE-P-based Elastomeric Binder System.....110

6.1 Introduction.....110

6.2 Mechanical and electrical study of PVDF-TFE-P and PVDF-TFE-P/SS films.....111

6.2.1 Effect of chemical additives.....111

6.2.2 Mechanical properties of crosslinked PVDF-TFE-P films.....115

6.2.3 Mechanical and electrical properties of crosslinked PVDF-TFE-P/carbon black composites.....122

6.3 Mechanical and electrical study of swelled PVDF-TFE-P and PVDF-TFE-P/SS samples.....126

6.3.1 Swelling of crosslinked PVDF-TFE-P and carbon-filled PVDF-TFE-P composites.....126

6.3.2 Mechanical properties of bisphenol-crosslinked PVDF-TFE-P swelled in EC/DEC.....128

6.3.3 Mechanical properties of TETA-crosslinked PVDF-TFE-P swelled in EC/DEC.....130

6.3.4 Mechanical and electrical properties of bisphenol-crosslinked PVDF-TFE-P/SS swelled in EC/DEC.....133

6.3.5 Mechanical and electrical properties of TETA-crosslinked PVDF-TFE-P/SS swelled in EC/DEC.....134

6.4 Effect of the coupling agent.....136

6.4.1 Coupling between PVDF-TFE-P and SS.....136

6.4.2 Coupling between PVDF-TFE-P and the silicon surface.....141

6.5 Effect of heating.....144

6.5.1 Effect of heating on TETA-crosslinked PVDF-TFE-P films.....144

6.5.2 Effect of heating on TETA-crosslinked PVDF-TFE-P/SS films.....148

6.6 Electrochemical characterization.....151

6.6.1 Effect of SS loading.....151

6.6.2 Superiority of the elastomeric binder.....156

6.6.3 Effect of the electrode thickness and the electrolyte.....159

6.7 Mechanical degradation of binder.....162

6.7.1 In-situ resistance of MCMB electrodes.....163

6.7.2 In-situ resistance of an a-$Si_{0.64}Sn_{0.36}$/Ag electrode incorporating PVDF binder.....165

6.7.3 In-situ resistance of an a-$Si_{0.64}Sn_{0.36}$/Ag electrode incorporating PVDF-TFE-P binder.....171

6.8 Summary.....178

Chapter 7 Combinatorial and In-situ Experiments.....180

7.1 Introduction.....180

7.2 Characterization of the thickness gradient.....180

7.3 Effect of the active material loading of electrodes.....185

7.4 Effect of the lower cutoff potential.....189

7.5 Effect of the compression of electrodes.....192

7.6 Effect of the electrolyte type.....194

7.7 Summary of the combinatorial experiment.....195

7.8 Observation of different cell behaviors with in-situ experiments.....199

7.8.1 In-situ resistance.....199

7.8.2 In-situ thickness experiment.....202

7.9 Summary.....206

Chapter 8 Conclusions and future work.....208

8.1 Conclusions.....208

8.2 Future work.....209

8.2.1 Basic science of materials.....209

8.2.2 Battery technology.....211

8.2.3 Methodology.....212

References.....213

List of Figures

Figure 1.1 Comparison of different battery technologies in terms volumetric and gravimetric energy density.....3

Figure 1.2 Schematic illustration of a lithium-ion cell during discharge.....3

Figure 1.3 Voltage vs. specific capacity for negative electrode and positive electrode materials presently used or under serious consideration for the next generation of rechargeable lithium and lithium-ion batteries.....4

Figure 1.4 Cell potential vs. specific capacity of an MCMB electrode showing the definition of reversible capacity and irreversible capacity.....6

Figure 1.5 Change in length, width, height, volume, and electrode potential of an a-Si tower vs. AFM scan number.....9

Figure 1.6 Change in average area, height, volume, and electrode potential of an a-$Si_{0.64}Sn_{0.36}$ tower vs. AFM scan number.....10

Figure 1.7 Schematic of the tether model showing the impact of particle shuffling.....13

Figure 1.8 Schematic of the chemical route proposed to improve the mechanical properties of the solid-filled elastomeric composite (the elastomeric binder).....15

Figure 2.1 Force displacement curves showing the dependence of the spring constant on springs in series or parallel.....19

Figure 2.2 F/A vs. X/L_0 showing that the Young's modulus is independent of the size of the sample (spring).....20

Figure 2.3 Schematic of (a) the Kelvin or Voigt model, (b) the Maxwell model, and (c) the four-element model (the linear model).....23

Figure 2.4 Schematic of a crosslinked polymer network.....24

Figure 2.5 Types of network defects present in a crosslinked polymer system: (a) loose loop; and (b) loose end.....25

Figure 2.6 Some examples of commonly used silanes.....26

Figure 2.7 Schematic illustration of ordering arrangement of monomers.....28

Figure 3.1 Schematic of a sample for the peel test.....32

Figure 3.2 Schematic of the production of the electrode with the combinatorial thickness gradient.....35

Figure 3.3 The array of PVDF-based electrodes prepared.....35

Figure 3.4 The array of PVDF-TFE-P-based electrodes prepared.....36

Figure 3.5 (a) View of the dual-unit stress-stress tester, (b) side view of the actuator, and (c) top view of the sample holder for dry samples.....38

Figure 3.6 Schematic of a stress-strain tester.....38

Figure 3.7 A snapshot of the software interface for stress-strain testers and in-situ resistance testing units.....39

Figure 3.8 (a) stress vs. strain, and (b) nominal resistivity vs. strain of a TETA-crosslinked PVDF-HFP/SS composite film showing the definitions of breaking strain, breaking stress, and Young's modulus (E).....41

Figure 3.9 (a) stress vs. strain, and (b) nominal resistivity vs. strain of a TETA-crosslinked PVDF-HFP/SS composite film under cyclic deformation showing the definitions of the maximum stress (σ_{max}), and the rebound after stretching.....41

Figure 3.10 (a) stress vs. time, and (b) nominal resistivity vs. time of a PVDF-HFP/SS composite film during a relaxation test.....42

Figure 3.11 Schematic of the specially designed grips to study the mechanical and electrical properties of binder films swelled in the liquid solvent.....43

Figure 3.12 Typical resistance change of a TETA-crosslinked PVDF-HFP/SS film swelled in EC/DEC (1:2, v/v).....44

Figure 3.13 (a) stress vs. strain, and (b) nominal resistivity vs. strain of a TETA-crosslinked PVDF-HFP/SS composite film swelled in EC/DEC (1:2, v/v).....44

Figure 3.14 Typical data for a peel test to measure the adhesion strength between the binder film and the silicon wafer.....45

Figure 3.15 Schematic of the negative electrode on the negative electrode plate used for the in-situ resistance measurement.....47

Figure 3.16 Exploded view of the in-situ resistance cell.....48

Figure 3.17 A photograph of the dual-unit in-situ resistance testing system.....50

Figure 3.18 A typical voltage response of an a-$Si_{0.64}Sn_{0.36}$/Ag electrode to the pulse current sequence.....51

Figure 3.19 Current flow carried by the ionic path during resistance measurement.....51

Figure 3.20 The equivalent circuit used to fit the experimental data of a-$Si_{0.64}Sn_{0.36}$/Ag electrodes.....52

Figure 3.21 An exploded view of a coin type test cell.....53

Figure 3.22 An exploded view of the in-situ thickness cell.....55

Figure 3.23 Schematic of the in-situ thickness measuring system.....55

Figure 3.24 (a) SEM image of a-$Si_{0.64}Sn_{0.36}$ (low magnification), (b) SEM image of a-$Si_{0.64}Sn_{0.36}$ (high magnification), (c) SEM image of a-$Si_{0.64}Sn_{0.36}$/Ag (low magnification), and (d) SEM image of a-$Si_{0.64}Sn_{0.36}$/Ag (high magnification).....57

Figure 3.25 XRD patterns of a-$Si_{0.64}Sn_{0.36}$ and a-$Si_{0.64}Sn_{0.36}$/Ag.....58

Figure 4.1 Schematic of the linear model used to describe the mechanical properties of polymer films.....61

Figure 4.2 Schematic of the non-linear model used to describe the mechanical properties of polymer/carbon black films.....62

Figure 4.3 The stress-strain curve of the non-linear element proposed.....63

Figure 4.4(a) Stress vs. strain and (b) nominal resistivity vs. strain showing the elongation till break behavior of PVDF/SS and FC2178/SS films.....64

Figure 4.5 (a) Stress vs. strain and (b) nominal resistivity vs. strain showing the effect of the SS content on the breaking behavior of FC2178/SS films.....65

Figure 4.6 Stress vs. strain curves of TETA-crosslinked FC2178 films.....67

Figure 4.7 The effect of crosslinking on the parameters of the linear model for FC2178 films.....69

Figure 4.8 The effect of TETA on the mechanical properties of FC2178 films.....70

Figure 4.9 An attempt to describe the stress-strain curve of an FC2178 film incorporating 25 pph SS and 6.0 pph TETA using the linear model.....71

Figure 4.10 Features that cannot be explained by the linear model.....73

Figure 4.11 Testing the non-linear model's description of carbon-filled crosslinked FC2178.....75

Figure 4.12 Stress vs. strain curves showing the effect of TETA on the mechanical properties of FC2178 films with 25 pph SS.....77

Figure 4.13 Nominal resistivity vs. strain curves showing the effect of TETA on the electrical properties of FC2178 films with 25 pph SS.....78

Figure 4.14 Swelling ratio vs. TETA content of TETA-crosslinked FC2178.....80

Figure 4.15 Stress vs. strain of TETA-crosslinked FC2178 films swelled in EC/DEC (1:2, v/v).....81

Figure 4.16 Nominal resistivity of TETA-crosslinked FC2178/SS films as a function of swelling time.....83

Figure 4.17 (a) Stress-strain and (b) Nominal resistivity-strain curves of TETA-crosslinked FC2178/SS swelled in EC/DEC (1:2 by volume).....84

Figure 4.18 (a) Stress vs. strain and (b) nominal resistivity vs. strain of FC2178/SS composites using APTES as the coupling agent.....86

Figure 4.19 (a) Stress vs. strain and (b) nominal resistivity vs. strain of FC2178 composite incorporating 25 pph SS and 5.0 pph APTES.....87

Figure 4.20 (a) Stress vs. strain and (b) nominal resistivity vs. strain of FC2178 composite incorporating 25 pph SS, 5.0 pph APTES, and 5.0 pph TETA...89

Figure 4.21 (a) Cyclic tress vs. strain and (b) nominal resistivity vs. strain of the FC2178 composite incorporating 25 pph SS, 5.0 pph APTES, and 5.0 pph TETA.....89

Figure 4.22 (a) Stress vs. strain and (b) nominal resistivity vs. strain of swelled FC2178 composite incorporating 25 pph SS, 5.0 pph APTES, and 5.0 pph TETA.....90

Figure 4.23 Capacity vs. cycle number of a-$Si_{0.64}Sn_{0.36}$/Ag electrodes incorporating 2.0 pph TETA and different amounts of APTES.....91

Figure 4.24 Capacity vs. cycle number of thermally treated a-$Si_{0.64}Sn_{0.36}$/Ag electrodes incorporating 2.0 pph TETA and different amounts of APTES.....92

Figure 4.25 Capacity vs. cycle number of a-$Si_{0.64}Sn_{0.36}$/Ag electrodes incorporating 4 pph APTES different amounts of TETA.....93

Figure 4.26 Capacity retention of a-$Si_{0.64}Sn_{0.36}$/Ag electrodes incorporating PVDF and PVDF-HFP-based elastomeric binder showing the effect of the binder.....94

Figure 5.1 Stress vs. strain curves of TETA-crosslinked PVDF-HFP films of different molecular weights.....97

Figure 5.2 Stress-strain curves of (a) FC2211, (b) FC2230, (c) FC2261Q, and (d) FC2178 crosslinked with 4 pph TETA.....98

Figure 5.3 (a) Stress vs. strain, and (b) nominal resistivity vs. strain of TETA-crosslinked PVDF-HFP/SS films containing 4.0 pph TETA and 25 pph SS.....99

Figure 5.4 Stress vs. strain and nominal resistivity vs. strain curves of TETA-crosslinked PVDF-HFP/SS films under cyclic deformation.....101

Figure 5.5 (a) Stress-strain and (b) nominal resistivity-strain curves of FC2211/SS film cyclically deformed to 100% strain.....101

Figure 5.6 Swelling ratios of TETA-crosslinked PVDF-HFP samples.....102

Figure 5.7 Stress-strain curves of swelled PVDF-HFP films.....104

Figure 5.8 (a) Stress vs. strain, and (b) nominal resistivity vs. strain of swelled PVDF-HFP/SS films containing 4.0 pph TETA and 25 pph SS.....105

Figure 5.9 Voltage curves of a-$Si_{0.64}Sn_{0.36}$/Ag electrodes using different polymers.....107

Figure 5.10 Specific capacity vs. cycle number of a-$Si_{0.64}Sn_{0.36}$/Ag electrodes using PVDF-HFP-based binders.....108

Figure 6.1 Stress-strain curves of cured PVDF-TFE-P (110°C for 24 hours) showing the effect of the additives MgO and CaO.....112

Figure 6.2 Stress-strain curves of TETA-crosslinked PVDF-TFE-P showing the effect of DABCO and CaO.....114

Figure 6.3 Stress-strain curves of cured PVDF-TFE-P (curing conditions listed in the inset) with strains up to 250%.....116

Figure 6.4 Stress-strain curves of TETA-crosslinked PVDF-TFE-P with strains up to 250%.....117

Figure 6.5 Fitting stress-strain curves of TETA-crosslinked PVDF-TFE-P.....118

Figure 6.6 Cyclic stress-strain curves of bisphenol-crosslinked PVDF-TFE-P films at 110°C.....119

Figure 6.7 Cyclic stress-strain curves of TETA-crosslinked PVDF-TFE-P films with different TETA contents.....120

Figure 6.8 Comparison of the best-fit parameters of the linear model to the data in Figures 6.6 and 6.7.....122

Figure 6.9 (a) Stress-strain and (b) nominal resistivity-strain curves of the bisphenol-crosslinked (110°C, 24 hours) SS-filled PVDF-TFE-P composites (25 pph SS).....124

Figure 6.10 (a) Stress-strain and (b) nominal resistivity-strain curves of the TETA-crosslinked SS-filled PVDF-TFE-P composites (25 pph SS).....125

Figure 6.11 Cyclic stress-strain curves of the TETA-crosslinked SS-filled PVDF-TFE-P composites.....125

Figure 6.12 Cyclic nominal resistivity-strain curves of TETA-crosslinked SS-filled PVDF-TFE-P composites.....126

Figure 6.13 The swelling ratios of crosslinked PVDF-TFE-P in EC/DEC(1:2, v/v).....127

Figure 6.14 Stress-strain curves of bisphenol-crosslinked PVDF-TFE-P heated at 110°C.....129

Figure 6.15 Cyclic stress-strain curves of bisphenol-crosslinked PVDF-TFE-P heated at 110°C.....130

Figure 6.16 Stress-strain curves of TETA-crosslinked PVDF-TFE-P.....131

Figure 6.17 Cyclic stress-strain curves of TETA-crosslinked PVDF-TFE-P.....132

Figure 6.18 (a) Stress-strain and (b) Nominal resistivity-strain curves of bisphenol-crosslinked PVDF-TFE-P/SS immersed in EC/DEC (1:2, v/v).....133

Figure 6.19 (a) Stress-strain and (b) Nominal resistivity-strain curves of TETA-crosslinked PVDF-TFE-P/SS immersed in EC/DEC (1:2, v/v).....135

Figure 6.20 Stress versus strain and nominal resistivity versus strain during cyclic deformation of TETA-crosslinked PVDF-TFE-P/SS composites immersed in EC/DEC (1:2, v/v).....135

Figure 6.21 (a) Stress vs. strain, and (b) nominal resistivity vs. strain of PVDF-TFE-P/SS composites showing the effect of APTES.....137

Figure 6.22 (a) Stress vs. strain, and (b) nominal resistivity vs. strain of PVDF-TFE-P/SS composites showing the effect of APTES.....138

Figure 6.23 (a) The stress and (b) the nominal resistivity at 10% strain of PVDF-TFE-P/SS composites showing the impact of added APTES.....138

Figure 6.24 (a) Cyclic stress-strain and (b) nominal resistivity-strain curves of a PVDF-TFE-P/SS composite containing 25 pph SS and 5.1 pph APTES.....139

Figure 6.25 (a) Stress-strain and (b) nominal resistivity-strain curves of a PVDF-TFE-P/SS composite containing 25 pph SS, 5.0 pph TETA, and 3.6 pph APTES.....140

Figure 6.26 (a) Cyclic stress-strain and (b) nominal resistivity-strain curves of a PVDF-TFE-P/SS composite containing 25 pph SS, 5.0 pph TETA, and 3.6 pph APTES.....141

Figure 6.27 Peel tests of binder films without TETA on silicon wafers showing the significant impact of APTES.....142

Figure 6.28 Peel tests of binder films with TETA on silicon wafers showing the counter effect of TETA on the adhesion strength.....143

Figure 6.29 Stress vs. strain of TETA-crosslinked PVDF-TFE-P films after heating in an argon flow at 110°C for 24 hours.....145

Figure 6.30 Cyclic stress-strain curves of heated PVDF-TFE-P films with different amounts of TETA.....146

Figure 6.31 Stress vs. strain curves of heated and TETA-crosslinked PVDF-TFE-P films after swelling in EC/DEC (1:2, v/v).....147

Figure 6.32 Cyclic stress-strain curves of heated and TETA-crosslinked PVDF-TFE-P films after swelling in EC/DEC (1:2, v/v).....147

Figure 6.33 (a) Stress vs. strain, and (b) nominal resistivity vs. strain of heated PVDF-TFE-P/SS composites incorporating 25 pph SS and different amounts of TETA and APTES.....149

Figure 6.34 (a) Stress vs. strain, and (b) nominal resistivity vs. strain of heated and TETA-crosslinked PVDF-TFE-P/SS films after swelling in EC/DEC (1:2, v/v).....151

Figure 6.35 Voltage profile of Li/a-$Si_{0.64}Sn_{0.36}$ cells incorporating different amounts of SS.....153

Figure 6.36 Voltage profile of Li/a-$Si_{0.64}Sn_{0.36}$/Ag cells incorporating different amounts of SS.....154

Figure 6.37 Capacity retention of a-$Si_{0.64}Sn_{0.36}$ electrodes showing the impact of the SS content.....155

Figure 6.38 Capacity retention of a-$Si_{0.64}Sn_{0.36}$/Ag electrodes showing the impact of the SS content.....155

Figure 6.39 Specific capacity vs. cycle number for electrodes A-E (Table 6.5) showing the effect of the binder system on the cycling performance of a-$Si_{0.64}Sn_{0.36}$/Ag composite electrodes.....158

Figure 6.40 Specific capacity vs. cycle number for thin electrodes showing the effect of the electrolyte.....161

Figure 6.41 Voltage versus specific capacity of a Li/(a-$Si_{0.64}Sn_{0.36}$/Ag) cell using the LiBETI-based electrolyte.....161

Figure 6.42 Schematic of the tether model showing the motivation for the in-situ resistance experiment.....163

Figure 6.43 A typical voltage response of the MCMB electrode to the pulse current sequenc.....164

Figure 6.44 (a) The resistance of the MCMB electrode and (b) the cell potential vs. the cumulative capacity of the MCMB electrode.....165

Figure 6.45 A typical voltage response of an a-$Si_{0.64}Sn_{0.36}$/Ag electrode to the pulse current sequence.....166

Figure 6.46 (a) Cell potential, (b) electrical resistance, (c) expanded view of the electrical resistance at the start of the experiment, (d) ionic resistance and (e) capacitance of the a-$Si_{0.64}Sn_{0.36}$/Ag electrode incorporating PVDF binder and 20 pph Super-S carbon black.....168

Figure 6.47 Voltage response of the a-$Si_{0.64}Sn_{0.36}$/Ag electrode incorporating PVDF binder to the pulse current sequence at 0.2 V for the (a) 1st and (b) 2nd cycle.....170

Figure 6.48 Voltage response of the a-$Si_{0.64}Sn_{0.36}$/Ag electrode incorporating PVDF to the pulse current sequence at (a) 1.0 V, (b) 0.6 V during discharge, (c) 0.2 V, and (d) 0.6 V during charge.....171

Figure 6.49(a) cell potential, (b) electrical resistance, (c) ionic resistance and (d) capacitance of the a-$Si_{0.64}Sn_{0.36}$/Ag electrode incorporating a PVDF-TFE-P-based elastomeric binder.....172

Figure 6.50 Electrical resistance of the a-$Si_{0.64}Sn_{0.36}$/Ag electrode incorporating the PVDF-TFE-P-based elastomeric binder vs. cycle number at different cell potentials.....174

Figure 6.51 Electrical resistance of the a-$Si_{0.64}Sn_{0.36}$/Ag electrode using PVDF as the binder vs. cycle number at different cell potentials.....175

Figure 6.52 Ionic resistance change of the a-$Si_{0.64}Sn_{0.36}$/Ag electrode incorporating the PVDF-TFE-P-based elastomeric binder vs. cycle number at different cell potentials.....176

Figure 6.53 Voltage response of the a-$Si_{0.64}Sn_{0.36}$/Ag electrode incorporating the PVDF-TFE-P-based elastomeric binder to a pulse current sequence input at 0.2 V of the (a) 1st, (b) 2nd, (c) 5th, and (d) 10th cycle.....177

Figure 6.54 Voltage response of the a-$Si_{0.64}Sn_{0.36}$/Ag electrode incorporating the PVDF-TFE-P-based elastomeric binder to the pulse current sequence at (a) 1.0V, (b) 0.6V during discharge, (c) 0.2V, and (d) 0.6V during charge for the 10th cycle.....178

Figure 7.1 (a) The mass of active material per electrode and (b) the thickness of PVDF-TFE-P-based electrodes as functions of electrode position.....182

Figure 7.2 (a) The mass of active material per electrode and (b) the thickness of PVDF-based electrodes as functions of electrode position.....183

Figure 7.3 Voltage versus specific capacity of Li/(a-$Si_{0.64}Sn_{0.36}$/Ag) cells using the proposed PVDF-TFE-P-based elastomeric binder.....186

Figure 7.4 The specific capacity vs. cycle number showing the effect of electrode loading (thickness) on the capacity retention of a-$Si_{0.64}Sn_{0.36}$/Ag electrodes using the proposed PVDF-TFE-P-based elastomeric binder.....187

Figure 7.5 The specific capacity vs. cycle number showing the effect of electrode loading (thickness) on the capacity retention of a-$Si_{0.64}Sn_{0.36}$/Ag electrodes using the PVDF-based binder.....189

Figure 7.6 The specific capacity vs. cycle number showing the effect of the lower cutoff potential on the capacity retention of a-$Si_{0.64}Sn_{0.36}$/Ag electrodes using the proposed PVDF-TFE-P-based elastomeric binder.....191

Figure 7.7 Specific capacities vs. cycle number of a-$Si_{0.64}Sn_{0.36}$/Ag electrodes showing the impact of the binder and the lower cutoff potential.....193

Figure 7.8 Specific capacity vs. cycle number of a-$Si_{0.64}Sn_{0.36}$/Ag electrodes using PVDF-TFE-P-based elastomeric binder showing the effect of compression.....194

Figure 7.9 The specific capacity vs. cycle number of a-$Si_{0.64}Sn_{0.36}$/Ag electrodes using the proposed PVDF-TFE-P-based elastomeric binder showing the effect of the electrolyte type.....197

Figure 7.10 The charge-discharge cycle number at which 80% of the maximum cell capacity was reached vs. the loading of active material showing (a) the effect of lower cutoff potential, (b) the effect of compression, and (c) the effect of the electrolyte salt.....198

Figure 7.11 Specific capacity of the in-situ resistance cell showing the effect of the lower cutoff potential.....200

Figure 7.12 The resistance variation vs. cycle number of the electrode film during discharge.....202

Figure 7.13 Specific capacity of the in-situ thickness cell showing the effect of the lower cutoff potential.....203

Figure 7.14 (a) cell potential, (b) LVDT potential, and (c) thickness variation of the negative electrode of the in-situ thickness cell during cycling (cycles 1-3).204

Figure 7.15 (a) cell potential, (b) LVDT potential, and (c) thickness variation of the negative electrode of the in-situ thickness cell during cycling.....205

List of Tables

Table 2.1 Nine classes of silane coupling agents.....27

Table 3.1 Specification of the polymers used.....30

Table 4.1 Best-fit parameters of the linear model to crosslinked FC2178 films.....68

Table 4.2 Best-fit parameters of the non-linear model to experiments (Figure 4.9 and 4.11).....72

Table 4.3 Best-fit parameters of the non-linear model to crosslinked FC2178 films containing SS.....79

Table 5.1 A comparison of PVDF-HFP samples crosslinked with 4 pph TETA.....99

Table 6.1 Best-fit parameters of the linear model to the data shown in Figures 6.1 and 6.2.....113

Table 6.2 Best-fit parameters of equations 6-5 and 6-6 to the data in Figure 6.5 for the highly crosslinked PVDF-TFE-P films.....118

Table 6.3 Best-fit parameters of the linear model to the stress-strain curves of bisphenol-crosslinked PVDF-TFE-P films (Figure 6.6).....120

Table 6.4 Best-fit parameters of the linear model to the stress-strain curves of TETA-crosslinked PVDF-TFE-P (Figure 6.7).....121

Table 6.5 Preparation recipes of electrodes A-E to study the effect of the binder system.....157

Table 7.1 Experimental details of the PVDF-TFE-P-based electrodes used in the cycling tests.....184

Table 7.2 Experimental details of the PVDF-based electrodes used in the cycling tests.....184

Abstract

It is of commercial importance to develop high capacity negative and positive electrode materials for lithium-ion batteries to meet the energy requirements of portable electronic devices. Excellent capacity retention has been achieved for thin sputtered films of amorphous Si, Ge and Si-Sn alloys even when cycled to 2000 mAh/g and above, which suggests that amorphous alloys are capable of extended cycling. However, PVDF-based composite electrodes incorporating a-$Si_{0.64}Sn_{0.36}$/Ag powder (10 wt% silver coating) (~10μm) still suffer from severe capacity fading because of the huge volumetric changes of a-$Si_{0.64}Sn_{0.36}$/Ag during charge/discharge cycling. It is the objective of this thesis to understand the problem scientifically and to propose practical solutions to solve this problem.

Mechanical studies of binders for lithium battery electrodes have never been reported in the literature. The mechanical properties of commonly used binders, such as poly(vinylidene fluoride) (PVDF), haven't been challenged because commercially used active materials, such as $LiCoO_2$ and graphite, have small volumetric changes (<10%) during charge/discharge cycling. However, the recently proposed metallic alloys have huge volumetric changes (up to 250%) during cycling. In this case, the mechanical properties of the binder become critical.

A tether model is proposed to qualitatively understand the capacity fading of high-volume-change electrodes, and to predict the properties of a good binder system. A crosslinking/coupling route was used to modify the binder system according to the requirements of the tether model. A poly(vinylidene fluoride-tetrafluoroethylene-propylene)-based elastomeric binder system was designed to successfully improve the capacity retention of a-$Si_{0.64}Sn_{0.36}$/Ag composite electrodes.

In this thesis, it has also proven nontrivial to maximize the capacity retention of large-volume-change electrodes even when a fixed elastomeric binder system was used. The parameters that affect the capacity retention of large-volume-change electrodes at least include the mass loading of the active material, the lower cutoff voltage, the compression pressure on the electrodes, and the salt in the electrolyte.

List of Abbreviations and Symbols

ε	Strain
σ	True Stress
λ	Elongation
ρ	Resistivity
ρ_n	Nominal Resistivity
μ_-	Chemical Potential of Lithium Atoms in the Negative Electrode
μ_+	Chemical Potential of Lithium Atoms in the Positive Electrode
e	Electron Charge
f	Nominal Stress
hrs	Hours
k	Spring Constant
k_B	Boltzmann's Constant
l_{rms}	Root Mean Square Length
p(r)	Distribution Function
pph	Part Per Hundred Ratio
r	Distance
v/v	Volume Fraction
wt%	Percentage by Weight
x	Length Change of a Spring
A	Cross-sectional Area
A_0	Original Cross-sectional Area
AFM	Atomic Force Microscopy
AP	Adhesion Promoter

APTES	3-aminopropyltriethoxysilane
C	Capacitance
C_p	Heat Capacity
CPTES	3-chloropropyltriethoxysilane
DABCO	1,4-diazabicyclo[2.2.2]octane
DEC	Diethyl Carbonate
DSC	Differential Scanning Calorimetry
E	Young's Modulus
EC	Ethylene Carbonate
EV	Electric Vehicle
F	Force
G	Adhesion Energy
GOPTES	3-glycidoxypropyltriethoxysilane
HEV	Hybrid Electric Vehicle
HFP	Hexafluoropropylene
ICPTES	3-isocyanatopropyltriethoxysilane
IRC	Irreversible Capacity
IT	Information Technology
K_1, K_2, K_3	Spring Constants in Mechanical Models
K_{d1}, K_{d2}	Dashpot Viscosities in Mechanical Models
K_{s1}, K_{s2}	Constants for the Nonlinear Element
L	Length
L_0	Original Length
LiBETI	$LiN(SO_2CF_2CF_3)_2$
LVDT	Linear Voltage Displacement Transducer

MCMB	Mesocarbon Microbeads
MEK	Methyl Ethyl Ketone
MOPTES	3-methacryloxypropyltriethoxysilane
MPTES	3-mercaptopropyltriethoxysilane
MW	Molecular Weight
NMP	N-methyl Pyrrollidinone
P	Propylene
PAni	Polyaniline
PE	Polyethylene
PP	Polypropylene
PSI	Pounds Per Square Inch
PVC	Poly(vinyl chloride)
PVDF	Poly(vinylidene fluoride)
PVDF-HFP	Poly(vinylidene fluoride-hexafluoropropylene)
PVDF-TFE-P	Poly(vinylidene fluoride-tetrafluoroethylene-propylene)
R	Electrical Resistance
R_i	Ionic Resistance
SBR	Styrene Butadiene Rubber
SEI	Solid Electrolyte Interphase
SEM	Scanning Electron Microscopy
SS	Super-S Carbon Black
T	Temperature
T_g	Glass Transition Temperature
TCPTES	3-cyanatopropyltriethoxysilane
TESPT	Bis-[3-(triethyloxysilane)propyl]-tetrasulfide

TETA	Triethylenetetramine
TFE	Tetrafluoroethylene
V	Cell Potential
VDF	Vinylidene Fluoride
VTES	Vinyltriethoxysilane
XRD	X-ray Diffraction

Acknowledgements

I would like to first thank my supervisor, Jeff Dahn, for his constant encouragement, support, and discussion throughout my stay at Dalhousie. I really appreciate the great challenge he offered. It is his great patience that allowed me to start from zero. Special thanks go to his endless "crazy" ideas that brighten my career and made me excited all along.

Thanks are also due to all the members in the Dahn Lab. I appreciate all the valuable help, discussions, and suggestions on my research project. I also need to thank them for teaching me about all aspects of lithium-ion batteries and science. I am happy and proud to be a member of such nice and wonderful team. I would like to thank Simon Trussler in the machine shop for the numerous projects he has done for me.

I would also like to thank the members of my committee, Prof. Neil Burford, Prof. Mary Anne White, and Prof. Philip D. Pacey, for their support and guidance.

Finally, big thanks go to my family. It's their continuous love and support that brightens my life.

Chapter 1 Introduction to lithium-ion batteries

1.1 Importance of lithium-ion battery development

Environmental pollution and the looming energy crisis have been attracting more and more worldwide attention. Much of the criticism has been directed to the consumption of fossil fuels and the greenhouse gases emitted by automobiles. Automobiles consume almost 1/3 of all fossil fuels produced. The main component of the exhaust gas emitted by automobiles is carbon dioxide (CO_2), which is a greenhouse gas and contributes to global warning [1, 2]. Moreover, the exhaust gas also contains some toxic gases, such as carbon monoxide (CO) from the incomplete combustion of the fossil fuels.

Fossil fuels are a non-renewable natural resource, and we need to find alternatives before we finally use up all that is available. In the meanwhile, we should reduce the fossil fuel consumption by automobiles. The recently introduced hybrid electric vehicle (HEV), which combines a small internal combustion engine and a rechargeable battery, has been a big step forward. Furthermore, the electric vehicles (EV) under development could completely eliminate greenhouse gas emission and the air pollution from vehicles. Both the HEV and EV need high-energy-density batteries to minimize the size and weight of the battery and the vehicle.

Advanced battery technology is also required by modern information technology (IT) as well. Portable electronics with onboard computers, displays and memory have proliferated. As these become more complex, the power requirements increase. Thus, there is a need for batteries with high energy density, so that this power requirement can

be met, without increasing the size of the batteries packed in the devices. In order to do this, one must develop high capacity negative and positive electrode materials to increase the capacity density of the batteries.

1.2 Electrochemistry of lithium-ion batteries

Figure 1.1 shows a comparison of different battery technologies in terms of volumetric and gravimetric energy density. Lithium-ion batteries have the largest energy density of all rechargeable batteries and therefore have become the most popular choice for portable electronic devices.

Figure 1.2 schematically illustrates a lithium-ion cell during discharge. Typically, a lithium-ion cell consists of a negative electrode (usually graphite-based material) and a lithium transition metal oxide positive electrode (usually $LiCoO_2$), a polypropylene microporous separator (not shown in Figure 1.2), and an organic electrolyte with a dissolved lithium salt (typically $LiPF_6$). During discharge, lithium atoms are extracted from the negative electrode material and pairs of electrons and lithium ions (Li^+) are formed.

$$Li_xC_6 \rightarrow xLi^+ + xe^- + C_6 \qquad (1\text{-}1)$$

Then, the Li^+ transports through the electrolyte to the positive electrode while the electron (e^-) travels through the external circuit. Finally, the e^- and Li^+ combine at the positive electrode and the lithium atom formed inserts into the positive electrode material.

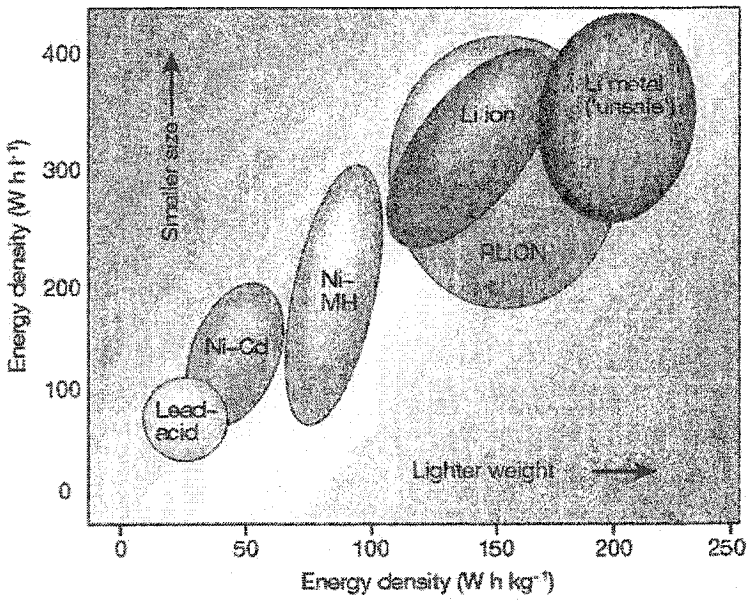

Figure 1.1 Comparison of different battery technologies in terms volumetric and gravimetric energy density

(Extracted from reference [3])

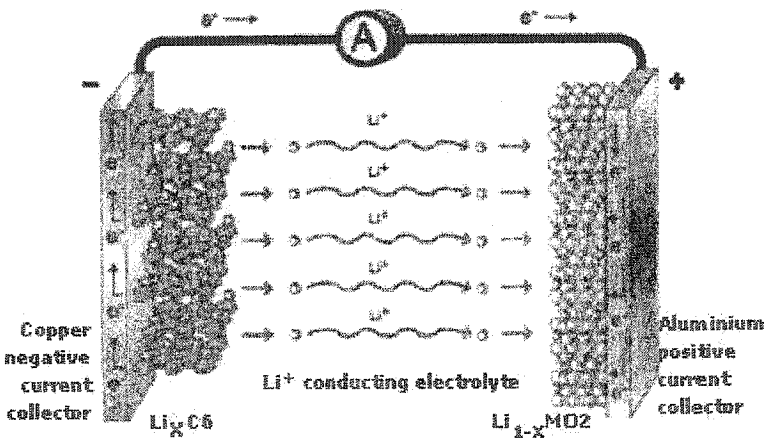

Figure 1.2 Schematic illustration of a lithium-ion cell during discharge

(www.agmbat.co.uk/liiontechnology.html)

$$xLi^+ + xe^- + MO_2 \rightarrow Li_xMO_2 \qquad (1\text{-}2)$$

During charge, the reverse process takes place.

The voltage of the electrochemical cell depends on the difference in the chemical potential of the lithium atoms in both electrode materials (negative electrode and positive electrode).

$$V=(\mu_- - \mu_+)/e \qquad (1\text{-}3)$$

where μ_- and μ_+ are the chemical potential of lithium atoms in the negative electrode and positive electrode materials respectively and e is the magnitude of the electron charge (1.6×10^{-19}C). The potential range and specific capacity of different active materials for lithium and lithium-ion batteries are shown in Figure 1.3. Generally, the negative electrode materials have lower potential vs. Li/Li^+, while the positive electrode materials have higher potential.

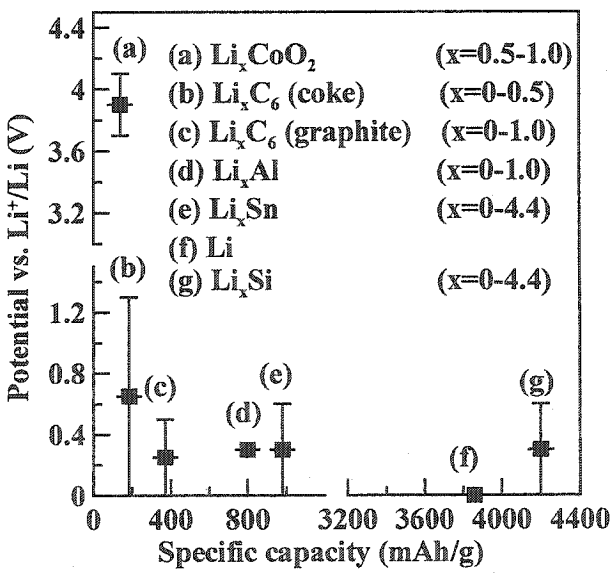

Figure 1.3 Voltage vs. specific capacity for negative electrode and positive electrode materials presently used or under serious consideration for the next generation of rechargeable lithium and lithium-ion batteries

Normally, an electrode for an electrochemical cell consists of active material particles, carbon black as a conductive filler, and a polymer as the binder. This type of electrode is called a composite electrode. The carbon black filled polymer composite is required to maintain the physical integrity of the electrode and provide an electronic pathway between the active material particles and the current collector.

Figure 1.4 shows the potential vs. specific capacity of a Li/MCMB (graphitized mesocarbon microbeads, a negative electrode material for a lithium-ion cell) electrochemical cell to schematically indicate the reversible capacity and the irreversible capacity of the electrode. The reversible capacity corresponds to the valence electrons associated with those lithium atoms that can reversibly react with the MCMB electrode. The irreversible capacity (IRC) corresponds to the valence electrons associated with those lithium atoms that are trapped in the electrode after the first insertion and removal cycle. During the first discharge, lithium ions are removed from the negative electrode (lithium metal) and inserted into the positive graphite electrode (MCMB). The lithium atoms hosted in the graphite particles can diffuse to the surface of the graphite particles and react with the electrolyte surrounding the graphite particles. The products of the reaction will then cover the surface of the particles. This layer of "special material", which prevents the electrolyte from further reaction with lithium atoms, is called a solid electrolyte interphase (SEI) [4, 5]. Normally, irreversible capacity mainly results from lithium loss during the formation of the SEI since the formation of the SEI is irreversible. Irreversible capacity loss has been shown to vary linearly with the surface area of the active material [4]. Therefore, active materials with small specific surface area are highly desired to minimize the irreversible capacity.

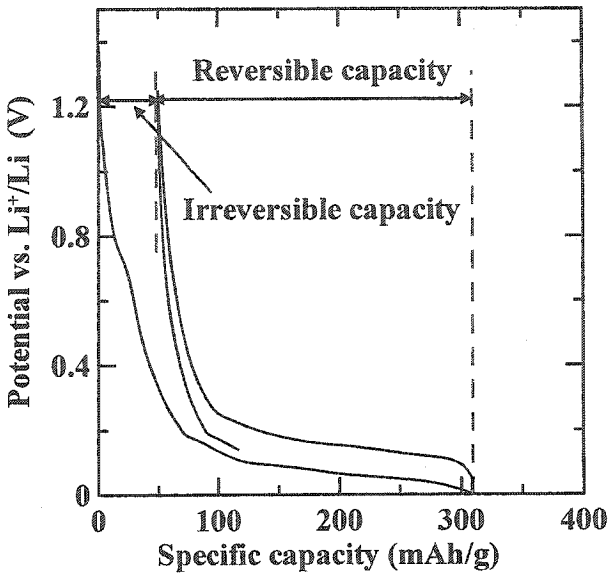

Figure 1.4 Cell potential vs. specific capacity of an MCMB electrode showing the definition of reversible capacity and irreversible capacity.

1.3 Advanced negative electrode materials for lithium-ion batteries

Today, graphite-based negative electrode materials, such as mesocarbon microbeads (MCMB), are widely used as the negative electrode materials for lithium-ion batteries. However, the theoretical capacity of graphite is only 372 mAh/g (see Figure 1.3). The intercalation of lithium into MCMB can be expressed as equation 1-1.

$$C_6 + Li \rightleftharpoons LiC_6 \qquad (1\text{-}1)$$

In order to meet the increasing energy requirement of both information technology and HEVs/EVs, one must develop high capacity negative and positive electrode materials to increase the capacity density of batteries.

Recently, metallic alloys, such as $Si_{1-x}Sn_x$, have been proposed as the high capacity negative electrode materials for lithium-ion batteries and have been attracting lots of scientific and industrial interest [6-29]. The reaction of $Si_{1-x}Sn_x$ with lithium is

$$Si_{1-x}Sn_x + 4.4Li \rightleftharpoons Li_{4.4}Si_{1-x}Sn_x. \quad (1\text{-}2)$$

However, the reversible capacity of metallic alloy based composite electrodes decreases quickly with charge/discharge cycling number. This phenomenon is called "capacity fading", which is believed to be caused by the huge volumetric changes of such active materials during charge/discharge cycling. The commercialization of such metallic negative electrode materials has been severely hindered by their rapid capacity fading.

Substantial research has been done to address the capacity fading of metallic negative electrode materials. The crystal structures of Li-M alloy phases, i.e. LiSn and Li_2Sn_5, have different lattice constants and different volumes per metalloid atom.[30]. When different Li-M alloy phases coexist in the same particle during charge/discharge cycling, inhomogeneous strain generally occurs. This results in the cracking of the particles, loss of electrical contact and the capacity fading. Some solutions proposed include using fine powdered materials (sub-micron size) [14, 27, 28, 31] and active/inactive composite materials [18, 32-36] to suppress the cracking of active material particles during charge/discharge cycling. However, fine-powdered materials have large specific surface area, which leads to high irreversible capacity, and low packing efficiency in electrodes, which limits the amount of active material that can be loaded per unit volume of the electrode. On the other hand, active/inactive composite materials can have large particle size and high packing efficiency. However, only part of the composite material is "active". If we can get rid of the inactive phase while eliminating the

inhomogeneous expansion of active material particles, more practical specific capacity can be exploited.

Recently, amorphous metallic alloys, such as a-Si [37] or a-SiSn [12], were proposed to solve the cracking problem of the active material. Excellent capacity retention has been achieved for thin sputtered films of amorphous Si [6], Ge [7] and SiSn [8] alloys even when cycled to 2000 mAh/g and above which suggests that amorphous alloys are capable of extensive cycling. When Li is added to amorphous alloys, the bulk intermetallic phases of the Li-metal phases (Li-M) are not formed [12]. Thus, the ratio of Li to metal can vary continuously and inhomogeneous strain, which results from the different lattice constant of coexisting Li-M phases, can be eliminated.

These ideas were greatly supported by in-situ atomic force microscopy (AFM) experiments on amorphous Si and $Si_{0.64}Sn_{0.36}$ metallic particles [10]. The samples were prepared by magnetron sputtering. Active material "towers" were deposited on a polished stainless steel disc through a fine mesh (7.6×7.6 μm openings) with a periodicity of 12.6 μm. The typical height of the towers was 0.3-0.5 μm. The morphology and size change of the active material towers during charge/discharge cycling was monitored with an in-situ AFM. Figure 1.5 and 1.6 show the analysis of the AFM images collected during experiments on a-Si and a-$Si_{0.64}Sn_{0.36}$ electrodes, respectively. Both a-Si and a-$Si_{0.64}Sn_{0.36}$ towers can reversibly expand/contract upon the insertion/removal of the lithium atoms without cracking. In both cases, a volumetric expansion of about 250% was observed when the electrodes were fully discharged.

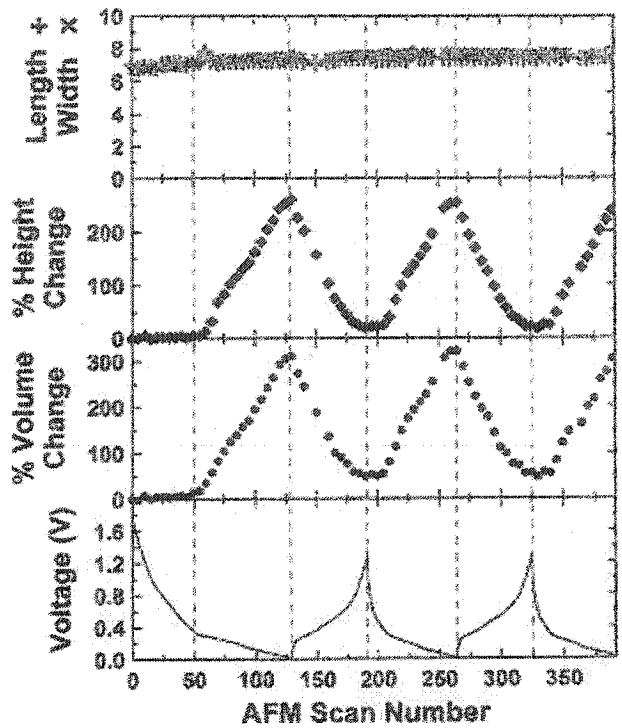

Figure 1.5 Change in length, width, height, volume, and electrode potential of an a-Si tower vs. AFM scan number

(Extracted from reference [10])

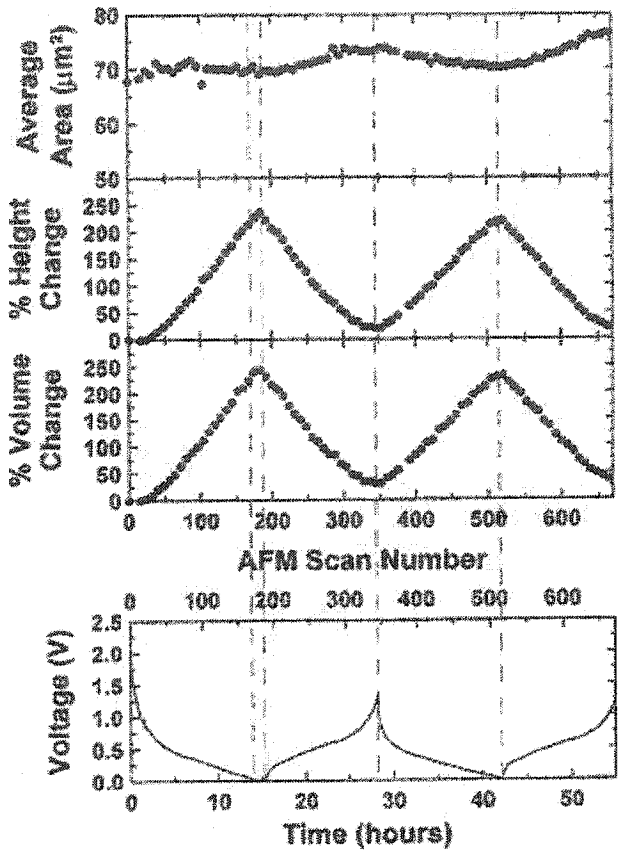

Figure 1.6 Change in average area, height, volume, and electrode potential of an a-$Si_{0.64}Sn_{0.36}$ tower vs. AFM scan number

(Extracted from reference [10])

1.4 Tether model and proposal

Although in-situ AFM results confirmed that the particle-cracking problem can be solved by using amorphous materials, the huge volumetric changes of the active material during charge/discharge cycling are not suppressed at all. We also have found that capacity fading is still problematic for conventional composite a-$Si_{0.64}Sn_{0.36}$/Ag electrodes containing particles of silver-coated amorphous $Si_{0.64}Sn_{0.36}$ active material (10-20 μm), carbon black and a conventional polymeric binder like poly(vinylidene fluoride)

(PVDF). Therefore, we believe that the loss of the capacity for amorphous materials is not caused by the cracking of the negative electrode material particles, but is dominated by the mechanical degradation of the binder, which holds the negative electrode material particles to the current collector. It is our view that the critical importance of the binder system has been widely underestimated or ignored until recently.

The first report about the importance of the binder choice, which made a significant difference to the cycling of composite electrodes of metallic alloys, came from Besenhard's group [13]. However, in most literature work on composite electrodes of high-volume-change alloys, a poor polymer binder, such as PVDF [16, 17, 19-26, 28, 29], was used to evaluate the charge-discharge cycling performance of the alloys. There is no reason for us to believe that such poor binders can tolerate the large volumetric changes (~250%) of negative electrode particles. Therefore, it is very dangerous to evaluate high-volume-change electrodes using such a binder system. It is the scope of this thesis to understand the critical importance of the binder system to the cycling performance of amorphous metallic negative electrode materials and to find practical solutions to improve their capacity retention.

Figure 1.7 schematically shows the tether model we proposed to understand the capacity fading of amorphous metallic negative composite electrodes. Figure 1.7a schematically shows the initial state of an electrode. The tethers between the active particles and the current collector are polymeric binder strands containing carbon black to maintain the physical integrity of the electrode and to provide an electronic pathway between particles and the current collector. For small-volume-change materials, such as MCMB, the electrode contains sufficient porosity to accommodate the ca. 10% expansion

and contraction of individual particles without substantial interparticle collision and motion.

The situation for large-volume-change materials, such as a-Si and a-$Si_{0.64}Sn_{0.36}$, however, is quite different. When the particles undergo large expansions, they will eventually touch one another (Figure 1.7b). If further expansion occurs, a "shuffling" of the particles, involving substantial interparticle motion, is necessary to accommodate the expansion. Figure 1.7c shows the electrode after such a "shuffling" has occurred. As particles move in the z-direction, some of the binder strands or tethers will become highly stretched, and many of them may break if the strain exceeds the breaking strain or if the force on the tether is larger than the adhesion strength between the tether and the particles. The broken tethers will increase the electrical resistance of the electrode and some electrically isolated active particles may be formed as depicted in Figure 1.7c. Electrically isolated particles cannot be charged or discharged again and contribute to capacity loss of the electrode. Resistance growth of the electrode can also contribute to the capacity loss of the electrode.

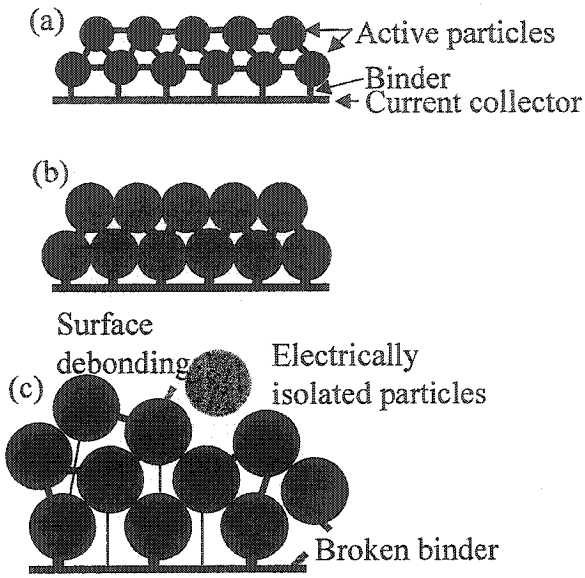

Figure 1.7 Schematic of the tether model showing the impact of particle shuffling

Using Figure 1.7 as a guide, it is clear that a "good" binder should be one that satisfies the following criteria.

(1) It should be a highly extensible elastomer that can tolerate the huge volumetric change of the active material particles.

(2) It should be electrically and ionically conductive (for Li^+ ions). To ensure electrical conductivity, a certain amount of carbon black must be added to the polymer. At the same time, the binder/solids blend should also satisfy rule (1). To ensure lithium ion conductivity, the binder/solids blend should uptake a certain amount of liquid electrolyte.

(3) It must maintain acceptable mechanical properties in the liquid electrolyte. When a polymer is immersed in the organic solvent, it may absorb the solvent and swell. In some cases, the polymer will completely dissolve in the solvent. The swelling of the binder in the electrolyte normally decreases the mechanical properties of the binder/solids

blend. Thus, a "good" binder/solids blend should maintain "good" mechanical properties after exposure to the liquid electrolyte.

(4) The binder should have a certain chemical activity. That is, the binder should be crosslinkable to inhibit viscous flow. In addition, coupling agents to enhance the interfacial adhesion between the binder and the electrode particles, including carbon black and active material particles, are needed.

(5) The binder and the chemical additives needed should not react with lithium. Otherwise, they will add extra irreversible capacity to the electrode.

(6) In order to find a "good" binder for eventual commercialization, we must also consider the commercial availability of the proposed chemicals.

In a solids-filled polymer composite, the interactions between the polymer chains themselves and between the polymer chains and the solid components are Van der Waals interactions and perhaps involve some hydrogen bonds. However, both of these are relatively weak interactions. Such solids-filled polymer composites have very poor elasticity and break at very small strain. The poor mechanical properties of such composites are insufficient to tolerate the huge volumetric changes of the solid fillers, such as the amorphous metallic negative electrode material in composite electrodes. The polymer system in such composites can degrade quickly under huge internal strain, which can be more than 200% during charge/discharge cycling.

If we can introduce some covalent bonds between the polymer molecules themselves and between polymer molecules and the solid components, we should be able to dramatically improve the mechanical properties of the composite. Figure 1.8

schematically depicts the chemical route we propose for solids-filled elastomeric composites. The solid line and the dashed line represent two different elastomer chains. The crosslinking agent is a bifunctional molecule, whose functional groups can chemically, covalently bond to the backbone of the polymer chain. Hence, it can significantly improve the interaction between the polymer chains. The coupling agent or adhesion promoter (AP), is another bifunctional molecule that can chemically bond to both the polymer chain and the solid components (the carbon black particle or the active material particle). The difference between the crosslinking agent and the coupling agent is that the coupling agent has two different functional groups, which can react with the polymer chain and the solid surface respectively.

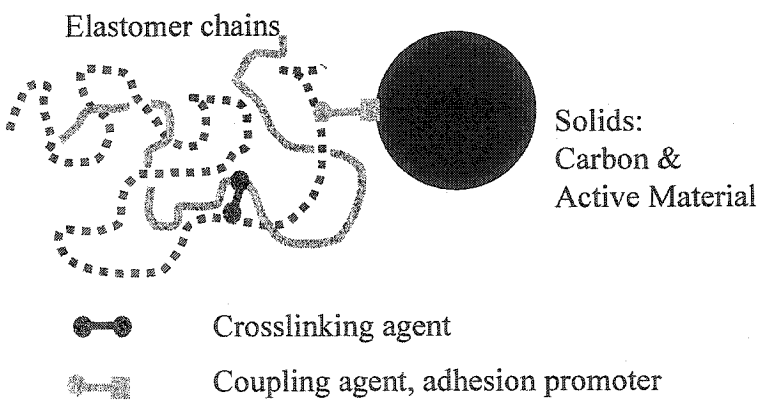

Figure 1.8 Schematic of the chemical route proposed to improve the mechanical properties of the solid-filled elastomeric composite (the elastomeric binder) Notice that the solid line and the dashed line represent different elastomer chains.

1.5 Scope of this thesis

It is our belief that the capacity fading of composite electrodes of amorphous metallic alloys results from the poor mechanical properties of the conventional binder system. It is the scope of this thesis to verify the critical importance of the binder system for high-volume-change alloys and to point toward practical solutions to improve the capacity retention of composite electrodes incorporating metallic negative electrode materials.

Chapter 2 gives a brief introduction to polymer mechanics. Some definitions that describe the mechanical properties of polymers and their solid-filled composites are summarized. Some chemical routes to improve the mechanical properties of polymers and solids-filled polymer composites are briefly summarized as well. Chapter 3 gives a simple description of the experimental details, which include the preparation of samples, the testing methods used, and the specifications of the materials studied.

The potential capability of poly(vinylidene fluoride-hexafluoropropylene) (PVDF-HFP) to improve the capacity retention of silver-coated amorphous $Si_{0.64}Sn_{0.36}$ (a-$Si_{0.64}Sn_{0.36}$/Ag, 10 wt% silver coating) will be examined in chapter 4. In chapter 5, the effect of molecular weight (MW) of PVDF-HFP on the mechanical and electrical properties of the binder system will be investigated as well as the effect of MW on the cycling behavior of a-$Si_{0.64}Sn_{0.36}$/Ag electrodes incorporating such PVDF-HFP-based elastomeric binder systems. Chapters 6 and 7 focus on another elastomeric binder system, poly(vinylidene fluoride-tetrafluoroethylene-propylene) (PVDF-TFE-P). The superiority of the elastomeric binder system over the conventional PVDF binder will be fully demonstrated in chapter 6. Chapter 7 presents electrochemical results from a

combinatorial experiment. Chapter 7 gives a detailed discussion of the effect of the active material loading, the lower cutoff voltage, the compression of the electrodes, the crystallization of the amorphous material, and the electrolyte type. Conclusions and suggestions for the future work are presented in chapter 8.

Chapter 2 Introduction to polymer mechanics

2.1 Mechanical properties of polymer samples

Hooke's force law is described in university physics textbooks, e.g. the one by Reese [38]. Hooke's law can be expressed by the following equation,

$$F = kx, \tag{2-1}$$

where k is the spring constant and has SI units of N/m, and F is the force needed to change the length of the spring by x. The spring constant can be doubled by placing two identical springs in parallel, and the spring constant can be reduced to 50% if two identical springs are placed in series. Figure 2.1 shows the relationship between F and x for: (a) a single spring; (b) two identical springs in parallel; and (c) two springs in series, respectively. The spring constant depends on the length and cross-sectional area of the sample (spring). So, the spring constant is not an effective way to describe the mechanical properties of a material.

Instead, if we normalize the force (F) by the cross-sectional area of the spring and normalize the deformation (x) by the original length of the spring, we obtain

$$\frac{F}{A} = \frac{k \times L_0}{A} \times \frac{x}{L_0}, \tag{2-2}$$

where A is the cross-sectional area of the sample (spring), and L_0 is the original length of the sample (spring). Figure 2.2 shows F/A as a function of x/L_0 for the three types of springs described in Figure 2.1. Now, all the springs show the same trend.

Materials scientists use the Young's modulus (E), the strain (ε), and the stress (σ), to describe the mechanical properties of materials.

$$E = \frac{k \times L_0}{A} \tag{2-3}$$

$$\sigma = \frac{F}{A} \tag{2-4}$$

$$\varepsilon = \frac{x}{L_0} \tag{2-5}$$

In some cases, another definition, the nominal stress (*f*), will also be used,

$$f = \frac{F}{A_0}, \tag{2-6}$$

where A_0 is the original cross-sectional area of the sample (spring). Generally, the Young's modulus (E), the nominal stress (*f*), and the stress (σ) have units of MPa while the strain (ε) is dimensionless. Now, equation 2-1 can be written as the following,

$$\sigma = E\varepsilon . \tag{2-7}$$

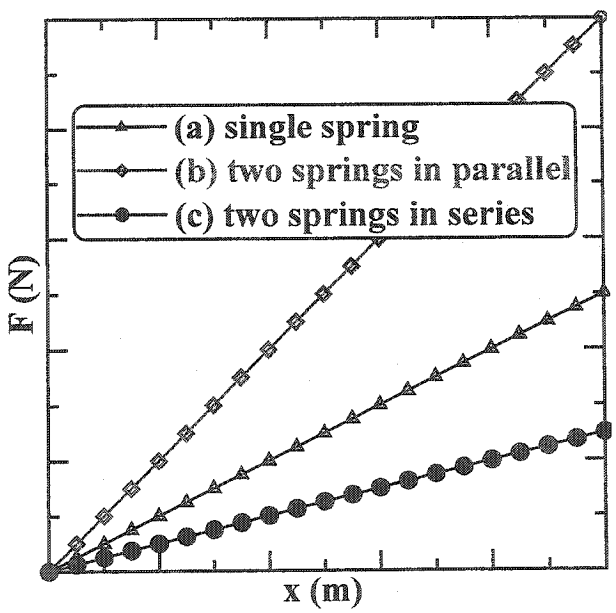

Figure 2.1 Force displacement curves showing the dependence of the spring constant on springs in series or parallel

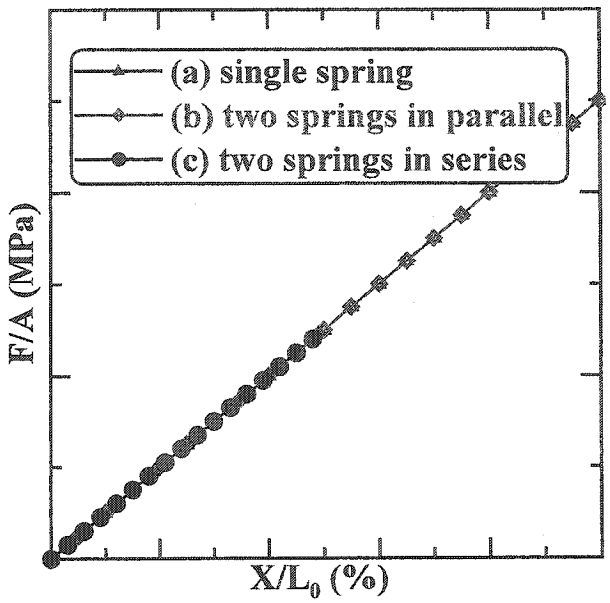

Figure 2.2 F/A vs. X/L_0 showing that the Young's modulus is independent of the size of the sample (spring).

2.2 Random walk model for elastomers

An elastomer is usually an amorphous material, which can be approximately described by the random walk model [39, 40]. If we randomly pick a monomer in a polymer chain, the probability to find the next bonded monomer is a spherically symmetric function in 3D space.

$$p(r) = \begin{cases} 1/4\pi & r = l \\ 0 & else \end{cases}, \tag{2-8}$$

where p(r) is the distribution function of the next bonded monomer at a distance r, and l is the bond length between the monomers. Based on the random walk model, we can develop a relation between the length of the polymer chain and its equilibrium end-to-end distance or the root mean square length (l_{rms}).

$$l_{rms} = \sqrt{< r^2 >} = \sqrt{n} l , \tag{2-9}$$

where n is the number of bonds between the two end monomers, which can be more than 1000 for high molecular weight polymers. Apparently, the polymer chain can be extended by $n^{1/2}$ times before changing the chemical bond configuration, or internal energy. However, the stretching process places the polymer chain in a position with a smaller number of equivalent configurations, which means a decrease in entropy. Therefore, the elasticity of the polymer is mostly dominated by the configuration, or entropy, change of the polymer, and the polymer system is also called an entropy spring.

In order to develop a relation between the stress and the strain of a polymer sample, a constant volume assumption will be used. The assumption assumes the volume of the polymer sample is constant during deformation and is valid for most polymer systems.

$$A_0 L_0 = AL = AL_0 \lambda = AL_0 (1 + \varepsilon) \tag{2-10}$$

In equation 2-10, λ is the deformation ratio of the polymer sample. Based on the random walk model and the constant volume assumption, the nominal stress can be expressed [41] as the following,

$$f = \nu k_B T(\lambda - \frac{1}{\lambda^2}), \tag{2-11}$$

where ν is the number of the polymer chains per unit volume, k_B is the Boltzmann's constant ($1.3806\times10^{-23} J\cdot K^{-1}$), and T is the temperature. Under a small deformation, i.e. small ε, equation 2-11 can be simplified to the following,

$$\sigma = f = 3\nu k_B T\varepsilon. \tag{2-12}$$

Equation 2-12 is valid only when the strain is small. Actually, it's not so useful in this thesis since we are interested in the maximum elongation of the binder film and equation 2-12 will not valid at such strain.

2.3 Mechanical models

The mechanical behavior of polymeric materials is usually discussed in terms of two particular types of ideal materials, an elastic solid and a viscous liquid. The viscoelasticity of the polymer system can be represented pictorially by models comprising massless Hookean springs (elastic solids) and Newtonian dashpots (viscous liquids). A spring behaves exactly like a metal spring, stretching instantly under stress and holding that stress indefinitely. A dashpot is considered to be an oil-filled cylinder with a loosely fitting piston. Under stress, the piston moves through the fluid at a rate proportional to the stress. On removing the stress, there is no recovery.

Springs and dashpots can be put together to develop mathematically amenable models of the viscoelastic behavior of the polymer system. Figures 2.3a and 2.3b show two simple arrangements, the Voigt model (or the Kelvin model, Figure 2.3a) and the Maxwell model (Figure 2.3b). The Maxwell model has been successfully used to simulate the stress relaxation of linear polymers, the time dependence of the stress under a constant strain. However, it cannot simulate the creep of the polymer, which is the elongation of the polymer film under a constant stress, and the stress relaxation of a crosslinked polymer. The Voigt model is useful for simulating the creep of polymers. In the Voigt model, the dashpot is placed in parallel to the spring, so an infinite force is needed to give an instantaneous strain. Hence, the Voigt model cannot simulate the stress relaxation of the polymer.

Combining the advantages of the Maxwell model and the Voigt model, four-element models are frequently used. Figure 2.3c also shows one arrangement of four elements that we adopt in this thesis. We call this the linear model.

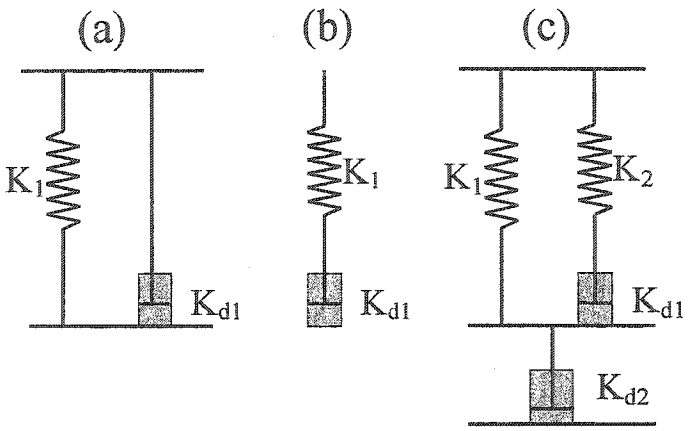

Figure 2.3 Schematic of (a) the Kelvin or Voigt model, (b) the Maxwell model, and (c) the four-element model (the linear model)

2.4 Chemical modification of polymers and their solids-filled composites

As chemists, we are interested in chemical routes to change the properties of polymers and their solids-filled composites to match our requirements. Several chemical routes have been widely reported in the literature to modify the properties of polymers and their composites. The chemicals used include crosslinking agents [42-46], coupling agents (or adhesion promoters) [47-52], and plasticizers [53-59].

2.4.1 Crosslinking agents

Crosslinking is a chemical technique used to improve the mechanical properties of polymers and their solids-filled composites. Figure 2.4 schematically shows a crosslinked polymer network. The solid lines represent two polymer chains, and X-R-X represents the crosslinking molecule, in which X represents the functional group. Viscoelastic flow is common in un-crosslinked linear polymers because of the weak interaction between polymer chains. Chemical bonds can be introduced between chains

with crosslinking agents so that the interaction between polymer chains is dramatically improved. In a typical linked polymer network, viscoelastic flow is significantly suppressed and the mechanical properties can be greatly improved. Crosslinking agents reported in the literature include diisocyanates [42], maleic anhydride [43], silanes [45], diamino-compounds [60-63], and bisphenols [60, 61]. Radiation and heating are also used to crosslink some unsaturated polymers, such as the ethylene propylene butadiene elastomer and styrene butadiene rubber (SBR) [46].

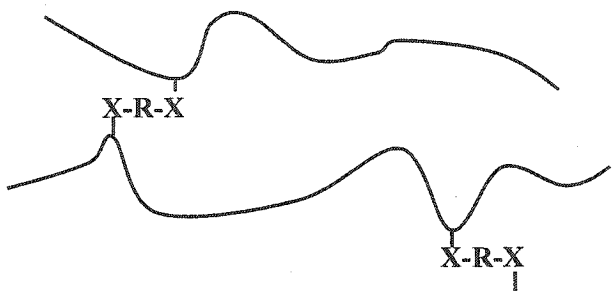

Figure 2.4 Schematic of a crosslinked polymer network

Worthy of mention is that the effective crosslinking degree is often quite unpredictable because of network defects present in the polymer network even when crosslinking agents and chemical additives are added. Figure 2.5 schematically illustrates two types of network defects: (a) "loose loops" , where a chain folds back on itself and (b) "loose ends", where a chain does not contribute to the network [39]. Normally, the introduction of the crosslinking can be quantitatively or qualitatively detected by the change of the glass transition temperature (T_g) [42, 43, 46, 64], the heat capacity (C_p) [65], the Young's modulus (E) [62], the maximum elongation at break [46], and the

swelling of crosslinked samples in solvents [61, 65, 66]. The linear model is also a useful tool to study the effective crosslinking degree [62].

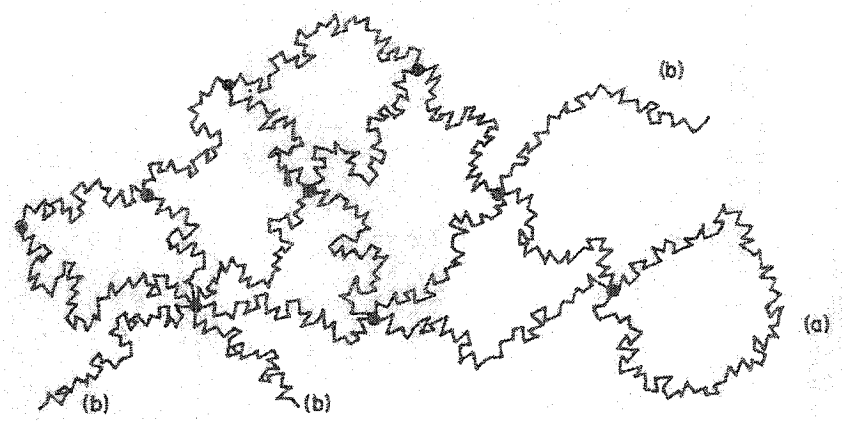

Figure 2.5 Types of network defects present in a crosslinked polymer system (a) loose loop; and (b) loose end (Extracted from reference [39])

2.4.2 Coupling agent

A coupling agent, or adhesion promoter, is a bifunctional molecule that can react with both the polymer and the surface of a solid to enhance the bonding between the polymer and the solid component. Typically, a coupling agent can be expressed as X-R-Y. X is the functional group that reacts with the polymer chain. Normally, X is similar to the active groups of the crosslinking agent and is matched to the chemical properties of the polymer. Y is the functional group that reacts with the solid surface and is normally determined by the functional groups on the solid surface. Generally, silanes are widely used as coupling agents since the –Si-OR group in silanes can easily react with acidic functional groups, such as –OH on non-metallic surfaces. Some commonly used silane coupling agents are listed in Table 2.1 [52].

A typical coupling reaction of a silane is shown in equation 2-13. The functional group X is used to react with the polymer chain. Depending on the group X, silane coupling agents are divided into 9 classes, which are shown in Table 2.1. Chemical structures of representative coupling agents for each class are shown in Figure 2.6. As shown in Table 2.1, each class of coupling agent can only react with certain polymers, which are divided into five groups and are listed in the last column of Table 2.1.

(2-13)

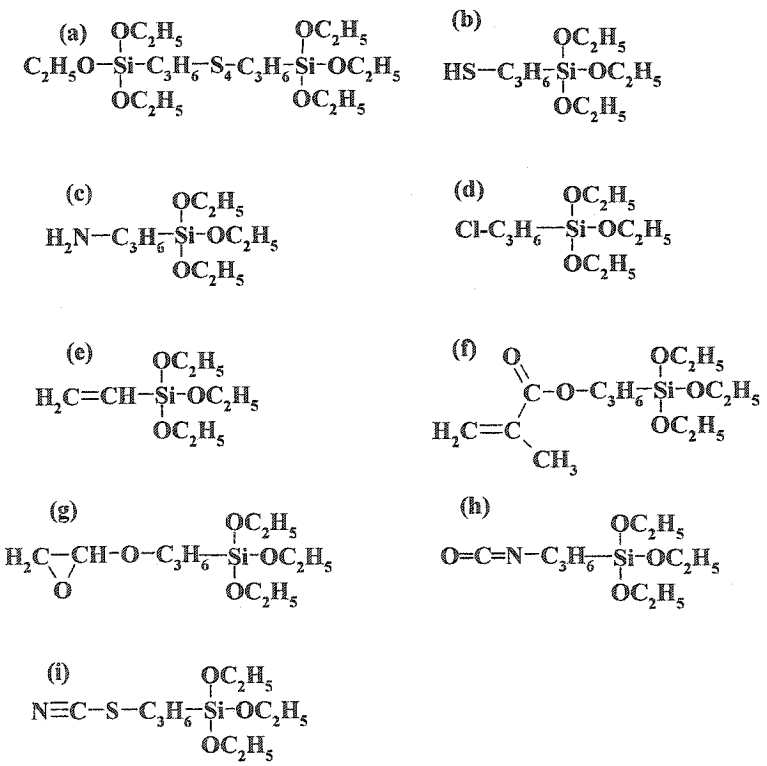

Figure 2.6 Some examples of commonly used silanes

(a) TESPT, (b) MPTES, (c) APTES, (d) CPTES, (e) VTES, (f) MOPTES, (g) GOPTES, (h) ICPTES, and (i) TCPTES (One example for each class)

Table 2.1 Nine classes of silane coupling agents

Class	Example molecule	Abbreviation (Commercial Name)	Chemical structure	Applied polymer
Polysulfide class	Bis-[3-(triethoxysilyl)propyl]-tetrasulfide	TESPT (Degussa Si-69)	Fig. 2.6a	Unsaturated polymers
Mercapto class	3-mercaptopropyltriethoxysilane	MPTES (UC A189)	Fig. 2.6b	Unsaturated polymers, and Halongenated polymers
Amino class	3-aminopropyltriethoxysilane	APTES (UC A1100)	Fig. 2.6c	Unsaturated polymers
Chloro class	3-chloropropyltriethoxysilane	CPTES (Degussa Si 230)	Fig. 2.6d	Halogenated polymers
Vinyl class	Vinyltriethoxysilane	VTES (UC A171)	Fig. 2.6e	Peroxide cured and unsaturated polymers (free radical-based reaction)
Methacrylate class	3-methacryloxypropyltriethoxysilane	MOPTES	Fig. 2.6f	
Epoxy class	3-glycidoxy-propyltriethoxysilane	GOPTES (UC A187)	Fig. 2.6g	Unsaturated polymers (free radical) and polyurethane
Isocyanato class	3-isocyanatopropyltriethoxysilane	ICPTES (UC A1310)	Fig. 2.6h	Polyurethane
Thiocyanato class	3-cyanatopropyltriethoxysilane	TCPTES (Degussa Si 264)	Fig. 2.6i	Unsaturated polymers

2.4.3 Plasticizer

In some strong polymer systems, such as highly crosslinked polymers [56], polyaniline (PAni) [59], and poly(vinyl chloride) (PVC) [54], local chain order arises from the presence of constraints, which restrict chain motion. Figure 2.7 schematically illustrates an example of local chain order in such a high-interaction polymer. The polymer chains in the ordered region are fully extended so that a change of internal energy will occur if the polymer is under strain. Generally, a polymer with local chain order has poor elasticity and high Young's modulus. In order to improve the elasticity of such high-strength polymers, some small molecules, called plasticizers, can be used to increase the number of configurations accessible to the polymer chains. Typically, the interaction between the plasticizer and the monomer is stronger than that between the unbonded monomers. As an example, dodecylbenzenesulfonic acid was used as the plasticizer of polyaniline [59].

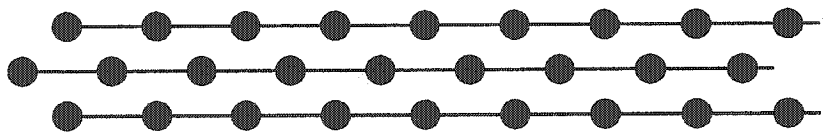

Figure 2.7 Schematic illustration of ordering arrangement of monomers

It is important to distinguish plasticizers from organic solvents. Both plasticizers and organic solvents can weaken the contribution from the interaction between polymer chains, but they are quite different. Normally, plasticizers are nonvolatile organic compounds, that can be well dispersed in the polymer matrix and that remain in the polymer matrix as long as possible. Although solvents have a similar influence on

polymer materials as plasticizers, they can't be called "plasticizers" because they are volatile. The composition and properties of the solvent-swelled polymer material change from time to time (out of control). The only way to maintain the plasticizer-like properties of the solvent swelled polymer is to immerse the polymer material in an excess of solvent. In this case, an equilibrium-swelled state is reached and the vaporization of a small amount of the solvent has little impact on the composition of the polymer material. Based on the interaction between a solvent and polymer molecules, the equilibrium swelled state of the polymer in the solvent can be: (a) complete dissolution, which results from the infinite swelling of a linear polymer in a good solvent; (b) a gel, which is from the swelling of a lightly crosslinked polymer in a good solvent; (c) a "brittle" material, in which a heavily crosslinked polymer is greatly swelled in a good solvent so that the polymer chains are in configurations close to their elongation limit; and (d) an improved elastic material with low amount of polymer swelling in an intermediate solvent.

Chapter 3 Experimental details

3.1 Polymers investigated in this thesis

The polymers investigated were poly(vinylidene fluoride) (PVDF, Solvay Co., Belgium), poly(vinylidene fluoride-hexafluoropropylene) (PVDF-HFP, Dyneon Corp.) with different molecular weights, and poly(vinylidene fluoride-tetrafluoroethylene-propylene) (PVDF-TFE-P, Dyneon Corp.). Some information about the polymers is listed in Table 3.1. The PVDF-HFP copolymers will be investigated to shed light on the impact of molecular weight, which controls the Mooney viscosity listed in Table 3.1. The molecular weight increases in the order of FC2211, FC2230, FC2261Q and FC2178.

Table 3.1 Specification of the polymers used

Commercial name	Chemical name	F% by weight	Mooney Viscosity	Solvent	Supplier
Solef 1008/1001	PVDF	59.4*	N/A	NMP	Solvay Co.
FC2211	PVDF-HFP	65.9	20	Ketone	Dyneon Co.
FC2230	PVDF-HFP	65.9	38	Ketone	Dyneon Co.
FC2261Q	PVDF-HFP	65.9	63	Ketone	Dyneon Co.
FC2178	PVDF-HFP	65.9	100	Ketone	Dyneon Co.
BRE-7131X	PVDF-TFE-P	N/A	N/A	Ketone	Dyneon Co.

*Calculated value based on its monomer ($C_2H_2F_2$).

The Mooney Viscosity is widely used in industry as an index of the molecular weight of polymers. Generally, the Mooney viscosity is measured by sandwiching the

melted polymer (i.e. at 121°C) between two parallel discs, and measuring the torque needed to rotate the discs at a certain angular velocity, i.e. 2 rotations per minute (rpm). Then, the Mooney viscosity of the polymer is ranked from 0 to 100 based on the torque measured. The detailed measuring standard is described in ASTM D 1646.

3.2 Preparation of polymer and polymer/SS films for mechanical and electrical measurements

The polymers (PVDF, FC2211, FC2230, FC2261Q, FC2178 and BRE-7131X) were dissolved in solvent (N-methyl pyrrollidinone (NMP, Aldrich) for PVDF, and methyl ethyl ketone (MEK, Aldrich) for the others) to obtain solutions containing 20 wt% polymer. Then, a measured amount of Super-S carbon black (SS, MMM Carbon, Belgium), the crosslinking agent, the coupling agent, and chemical additives were added to the polymer solution. The amount of the components added was described by part per hundred ratio of the mass of the polymer (pph). Notice that we always use the highest wt% component in the sample as the reference and set its content to 100 pph. After shaking for 15 minutes, the final mixture was then cast on a piece of TEFLON release film (3M Co.) using a notch bar spreader with a gap of 0.4 mm. After that, PVDF and PVDF/SS films were dried in an oven at 90°C overnight, while PVDF-HFP, PVDF-HFP/SS, PVDF-TFE-P, and PVDF-TFE-P/SS films were dried in air overnight before use. Then, the dry films were cut into narrow strips for mechanical and electrical measurements. The widths of PVDF-based films and elastomer-based films are about 1 mm and 5 mm respectively. The PVDF-based films are quite stiff. However, the homemade stress-strain tester was specially designed for elastomeric composites. Hence,

the PVDF-based films had to be carefully cut into very narrow strips to avoid breaking the load cell.

3.3 Preparation of samples for the peel test

The sliced PVDF-TFE-P terpolymer was dissolved in MEK to make a solution containing 20 wt% PVDF-TFE-P. Then 3 pph (part per hundred ratio of the mass of PVDF-TFE-P) 1,4-diazabicyclo[2.2.2]octane (DABCO, Aldrich), 4 pph CaO (Fisher Scientific), 25 pph SS, and measured amounts of triethylenetetramine (TETA, Aldrich) and 3-aminopropyltriethoxysilane (Adhesion promoter, APTES, Aldrich), if any, were added to the PVDF-TFE-P solution. After shaking for 15 minutes, the final mixture was then cast on a 50 mm by 25 mm piece of silicon wafer (Silicon Inc.) and dried in air for >24 hours. The silicon wafer was used to mimic the surface silicon atoms in a-$Si_{0.64}Sn_{0.36}$ or a-Si. A knife was then used to cut and remove the excess binder film on the wafer to obtain a binder strip (about 5 mm wide) on the silicon wafer surface as shown in Figure 3.1.

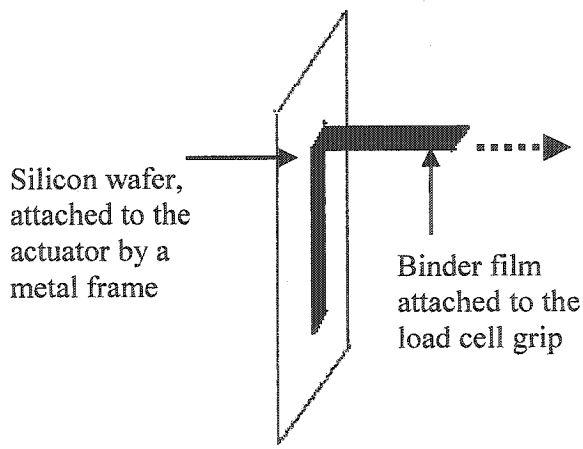

Figure 3.1 Schematic of a sample for the peel test

3.4 Preparation of electrodes

3.4.1 MCMB electrode using PVDF

PVDF was first dissolved in NMP to prepare a 10 wt% PVDF solution. 0.300 g mesocarbon microbeads (MCMB, heat-treated to about 2650°C, Osaka Gas, Japan) was mixed with 0.030 g SS, 0.300 g PVDF solution and 0.750 g NMP. After shaking in a small vial with several stainless steel beads for 15 minutes, the slurry was then cast on a piece of copper foil (ca. 10 μm thick) using a notch bar spreader with a gap of 0.4 mm. The electrode was dried in an oven at 90°C overnight before use.

3.4.2 a-$Si_{0.64}Sn_{0.36}$/Ag electrode using PVDF

0.300 g silver-coated amorphous $Si_{0.64}Sn_{0.36}$ (a-$Si_{0.64}Sn_{0.36}$/Ag, ca. 10 wt% silver coating, 3M Co.) was mixed with 0.060 g SS, 0.300 g 10 wt% PVDF solution (mentioned in 3.4.1) and 0.750 g NMP. After shaking in a small vial with several stainless steel beads for 15 minutes, the slurry was then cast on a piece of copper foil using a notch bar spreader with a gap of 0.4 mm. The electrode film was dried in an oven at 90°C overnight before use.

3.4.3 a-$Si_{0.64}Sn_{0.36}$/Ag electrodes using elastomers

0.300 g a-$Si_{0.64}Sn_{0.36}$/Ag was mixed with 0.060 g SS, 0.300 g 10 wt% elastomer solution (FC2211, FC2230, FC2261Q, FC2178, or BRE-7131X), measured amounts of TETA, APTES, CaO, DABCO, and 0.750-0.900 g MEK. The amount of MEK depends on the precise value of the room temperature. Normally, more MEK is used during the

summer months. After shaking in a small vial with several stainless steel beads for 15 minutes, the slurry was then cast on a piece of copper foil using a notch bar spreader. The electrode was dried in air overnight and then dried in an argon flow at 110°C for 24 hours before use.

3.4.4 Combinatorial electrode film using PVDF

9.036 g a-$Si_{0.64}Sn_{0.36}$/Ag, 1.809 g SS, and 5.028 g 20 wt% PVDF solution in NMP were added to a polypropylene bottle. Then 31.8 g NMP and 3 zirconia milling media were added and the bottle was closed with its lid and shaken for 30 minutes to mix the slurry. After shaking, the slurry was spread as a "bead" along a straight line on a piece of flattened copper foil (10 μm thick, 25 cm wide and ca. 30 cm long) supported on a glass plate (Steps 1 and 2 in Figure 3.2). Then the slurry bead was spread in the perpendicular direction using a tilted notch bar spreader (33 cm long) with a gap between the bottom of the spreader and the top of the copper foil ranging from 0 to 250 μm as shown by step 3 in Figure 3.2. The film was dried in an oven at 90°C overnight before use. An array of 6×4 electrodes were cut out of the film as illustrated in Figure 3.3. The compression step, if desired, was carried out before cell assembly.

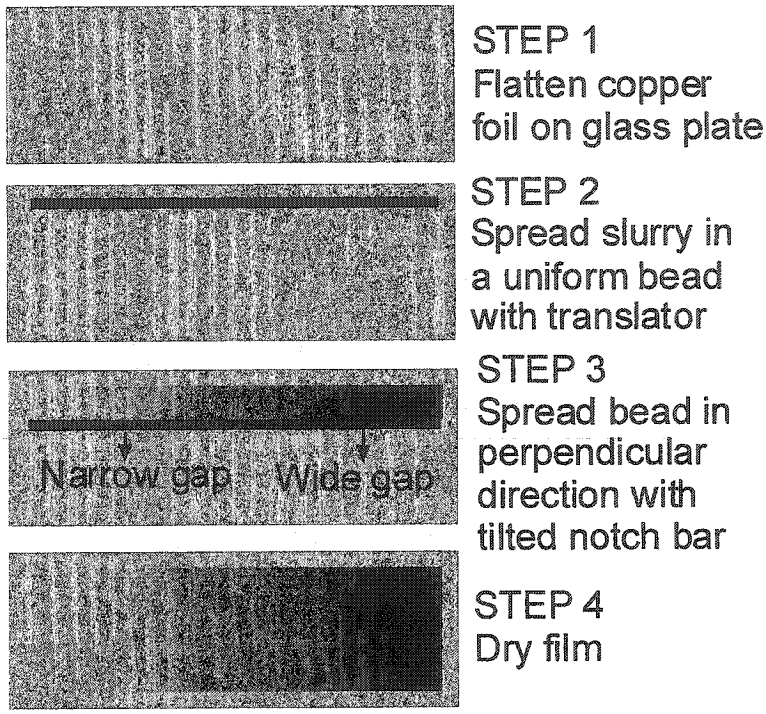

Figure 3.2 Schematic of the production of the electrode with the combinatorial thickness gradient.

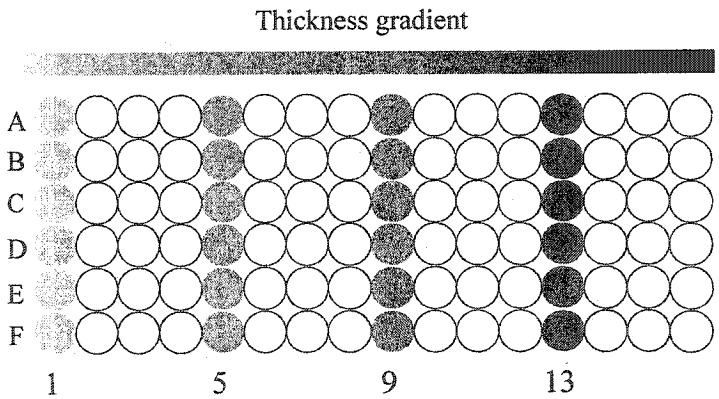

Figure3.3 The array of PVDF-based electrodes prepared. Rows A-C were used to study the effect of the lower cutoff voltage; Rows A, D-F were used to study the effect of compression

3.4.5 Combinatorial electrode film using PVDF-TFE-P

10.038 g a-$Si_{0.64}Sn_{0.36}$/Ag, 2.000 g SS, 5.028 g 20 wt% PVDF-TFE-P solution in MEK, 0.039 g CaO, 0.031 g DABCO, 0.042 g TETA, and 0.477 g APTES were added to a polypropylene bottle. Then 29.8 g MEK and 3 zirconia milling media were added and the bottle was closed with its lid and shaken for 30 minutes to mix the slurry. After shaking, a combinatorial electrode film was made as described in section 3.4.4. The film was dried in air overnight before use. An array of 9×16 electrodes were cut out of the film as illustrated in Figure 3.4. Then the electrodes were labeled and heated in an argon flow at 110°C for 24 hours. The compression step, if desired, was carried out after heating.

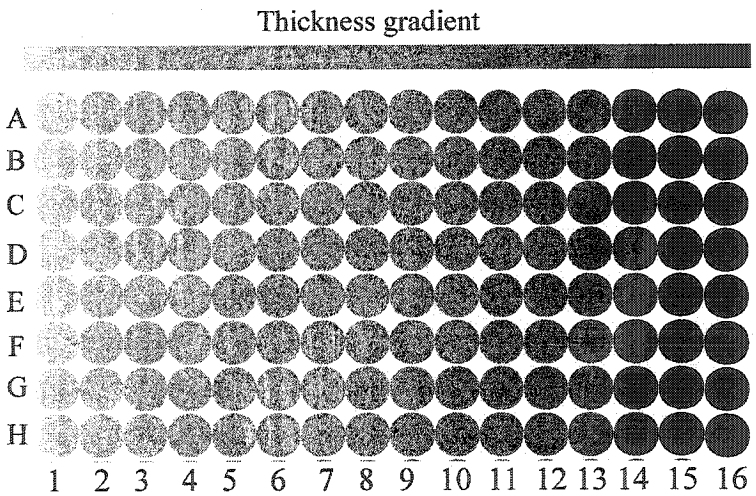

Figure 3.4 The array ofPVDF-TFE-P-based electrodes prepared. Rows A-C were used to study the effect of the lower cutoff voltage; Rows A, D-F were used to study the effect of compression; Rows A, G-H were used to study the effect of the electrolyte.

3.5 Mechanical and electrical characterization

During the charge/discharge of the electrode, the negative electrode material particles will contract or expand, which will cause relaxation, elongation or breaking of the binder. Hence, it is important to study the mechanical and electrical behavior of binder/solids films under the cyclic deformation. A stress-strain tester designed and built at Dalhousie was used for this purpose. Figure 3.5 shows a photograph of the dual-unit stress-strain tester. The instrument has two complete units as shown in Figure 3.5 and allows for simultaneous testing of two samples. A single stress-strain testing unit is schematically shown in Figure 3.6. A program, whose interface is shown in Figure 3.7, was written in Visual Basic to communicate with the motion controllers and the multimeter.

The two stress-strain testing units and two in-situ resistance testing units, which will be described in the following section, share one computer and the hardware interface, and the current program enables the computer to fully control the four different units simultaneously and independently. The computer controls the action of actuators through motion controllers.

Figure 3.6 shows a block diagram of a stress-strain tester. The actuator can cyclically stretch or release a binder film using programmed steps. The load cell is a force sensor, which transfers the force it experiences into a potential signal. There are two leads connected to the ends of the binder film via grips. These two leads are used to measure the resistance of the film during the experiment. The multimeter collects the signal from both load cells and resistance leads, and converts them into digital signals for the computer. With such a system, we are able to study the mechanical and electrical

properties of dry binder films and swelled binder films as well as the adhesion strength of binder films to a solid surface.

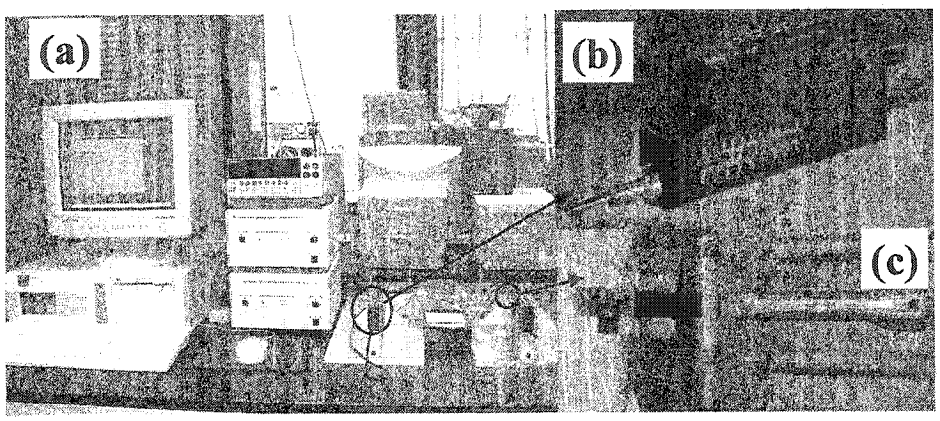

Figure 3.5 (a) View of the dual-unit stress-stress tester, (b) side view of the actuator, and (c) top view of the sample holder for dry samples.

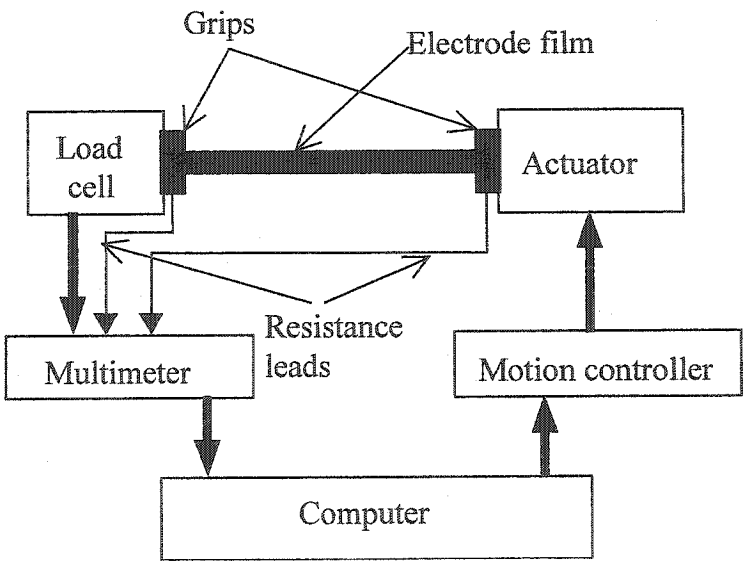

Figure 3.6 Schematic of a stress-strain tester

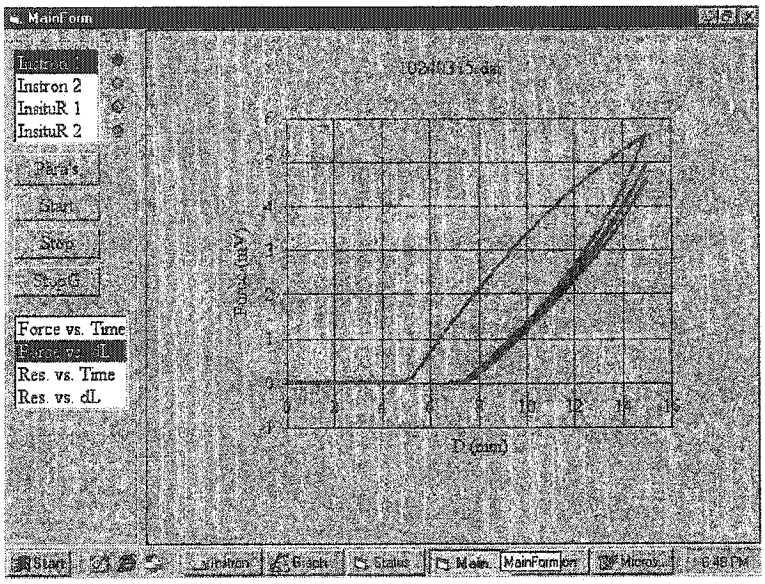

Figure 3.7 A snapshot of the software interface for stress-strain testers and in-situ resistance testing units

3.5.1 Investigation of dry binder films

Figure 3.8 shows typical data collected on a TETA-crosslinked PVDF-HFP/SS film. Figure 3.8a shows a typical experimental stress-strain curve measured until the sample broke. Three parameters are used to describe the stress-strain curve. The *Young's modulus, E,* is the slope of the stress-strain curve at small strain. The maximum strain that the film can be stretched before breaking is called the maximum elongation before break, or the breaking strain. The stress at the breaking point is defined as the breaking stress. Figure 3.8b shows a typical resistivity variation of the binder film during stretching. The nominal resistivity, ρ_n, is defined as

$$\rho_n = \frac{RA_0}{L_0} \tag{3-1}$$

where R is the measured resistance of the binder/solid film, and A_0 and L_o are the original cross-sectional area and length of the film, respectively.

Figure 3.9 shows stress-strain, and nominal resistivity-strain curves for a TETA-crosslinked PVDF-HFP/SS composite film under cyclic deformation. The maximum stress, σ_{max}, is the stress measured at maximum strain during a cyclic deformation or the relaxation test (Figures 3.9a and 3.10a). The rebound is the value of the strain where the stress-strain curve reaches zero stress at the end of the first deformation cycle.

Figure 3.10a shows the relaxation of applied stress at fixed strain as a function of time, and the change of the nominal resistivity is shown in Figure 3.10b. Two parameters, σ_{max} and σ_{end} are used to define the amount of relaxation that occurs in a specific time. We define the relaxation as,

$$Relaxation = \frac{\sigma_{\max} - \sigma_{end}}{\sigma_{\max}} \times 100\%. \qquad (3\text{-}2)$$

The amount of relaxation depends on the time of the experiment. Normally, we measure the amount of relaxation that occurs in 60 minutes.

All stress-strain curves reported here were measured using a strain rate of ±0.01 strain per minute. A slow rate was chosen to mimic the conditions within a lithium-ion battery where electrode expansion and contraction cycles take on the order of one hour.

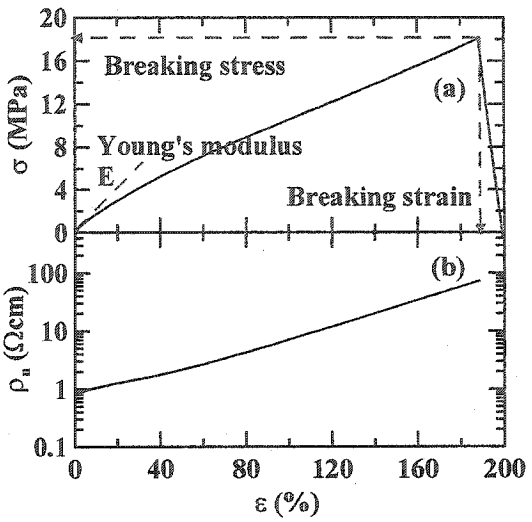

Figure 3.8 (a) stress vs. strain, and (b) nominal resistivity vs. strain of a TETA-crosslinked PVDF-HFP/SS composite film showing the definitions of breaking strain, breaking stress, and Young's modulus (E)

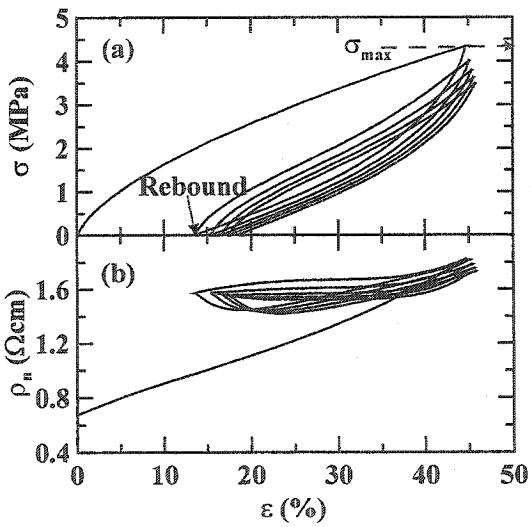

Figure 3.9 (a) stress vs. strain, and (b) nominal resistivity vs. strain of a TETA-crosslinked PVDF-HFP/SS composite film under cyclic deformation showing the definitions of the maximum stress (σ_{max}), and the rebound after stretching

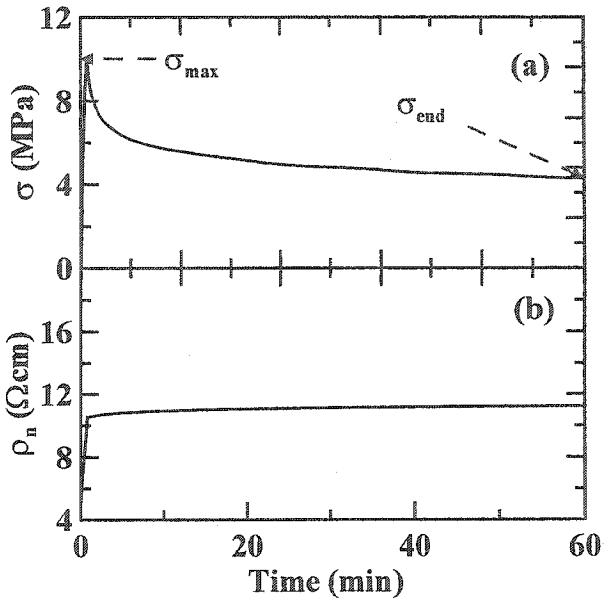

Figure 3.10 (a) stress vs. time, and (b) nominal resistivity vs. time of a PVDF-HFP/SS composite film during a relaxation test

3.5.2 Investigation of swelled binder films

In order to study the properties of binder films swelled in liquid solvent, special modification was made to the sample grips, as schematically shown in Figure 3.11. The solvent used was a mixture of ethylene carbonate (EC, Aldrich) and diethyl carbonate (DEC, Aldrich) with a ratio of 1:2 by volume. After the sample was successfully mounted in the grips, the container with the liquid solvent was lifted and the sample film was immersed in the solvent for 5 minutes before the measurement started. During this time the polymer swelled in the solvent. During the experiment, some electrochemical reactions, such as the electrochemical decomposition of the solvent, could occur if the potential difference between the Al grips reached over 4 V. Hence, the current used for the resistance measurement was set to a small value of 0.5 μA. Therefore, it is not

unusual to see some noise in the nominal resistivity versus strain results since small voltage measurements were usually recorded. The strain rate was set to ±0.05 strain per minute to decrease the effect of solvent (i.e. DEC) evaporation.

Figure 3.12 shows a typical resistivity variation of a binder film during swelling. From the data, we can see that the film reaches its equilibrium-swollen state in less than 1 minute. Figure 3.13 shows typical stress-strain data of a swelled binder film in EC/DEC (1:2, v/v). Notice that that resistivity of the film under large strain is so high that the decomposition of solvent occurs when the strain is larger than 80%.

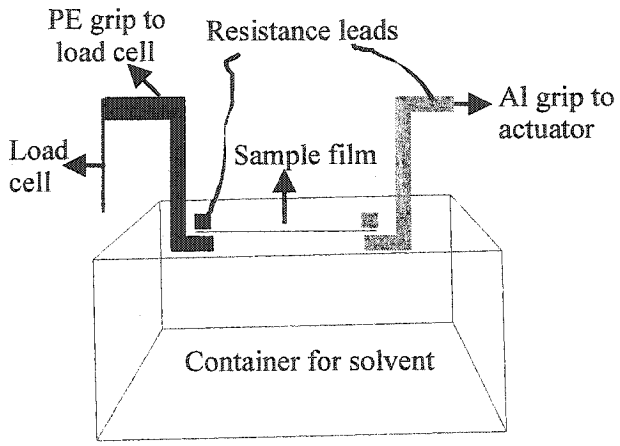

Figure 3.11 Schematic of the specially designed grips to study the mechanical and electrical properties of binder films swelled in the liquid solvent.

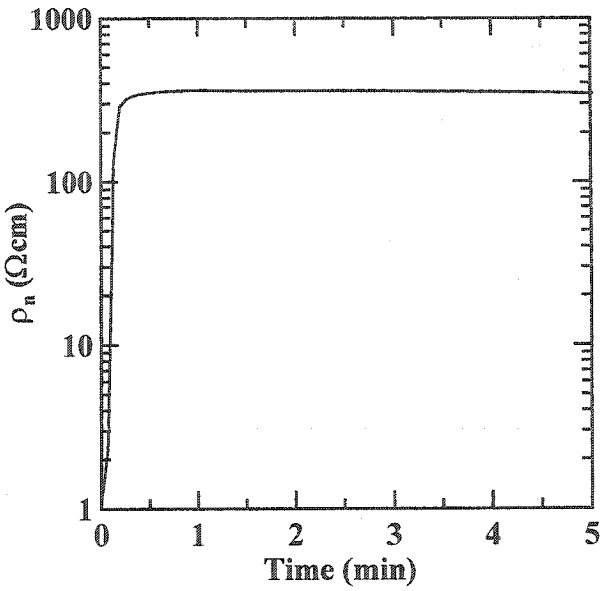

Figure 3.12 Typical resistance change of a TETA-crosslinked PVDF-HFP/SS film swelled in EC/DEC (1:2, v/v)

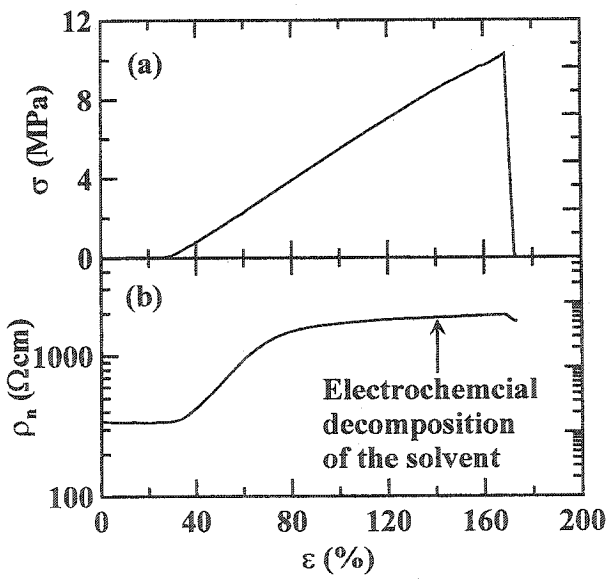

Figure 3.13 (a) stress vs. strain, and (b) nominal resistivity vs. strain of a TETA-crosslinked PVDF-HFP/SS composite film swelled in EC/DEC (1:2, v/v)

3.5.3 Peel test

A sample prepared for the peel test is schematically shown in Figure 3.1. A silicon wafer was used to mimic the surface (silicon atoms) of amorphous $Si_{0.64}Sn_{0.36}$. The free end of the binder film was attached to a load cell via a grip, and the silicon wafer was attached to an actuator via a metal frame. Then, the force applied to the load cell was recorded while the actuator pulled the silicon wafer. Figure 3.14 shows typical data for the peel test. At the beginning, the binder film was stretched and became taut. The force applied increases as the actuator moves backward. At a certain point the force applied is equal to the adhesion strength, and the binder film will peel up and the force will remain constant. Notice that the adhesion strength, or the adhesion energy, shown in Figure 3.14 is about 20 J/m^2. The adhesion energy was obtained by dividing the force measured with the width of the binder film.

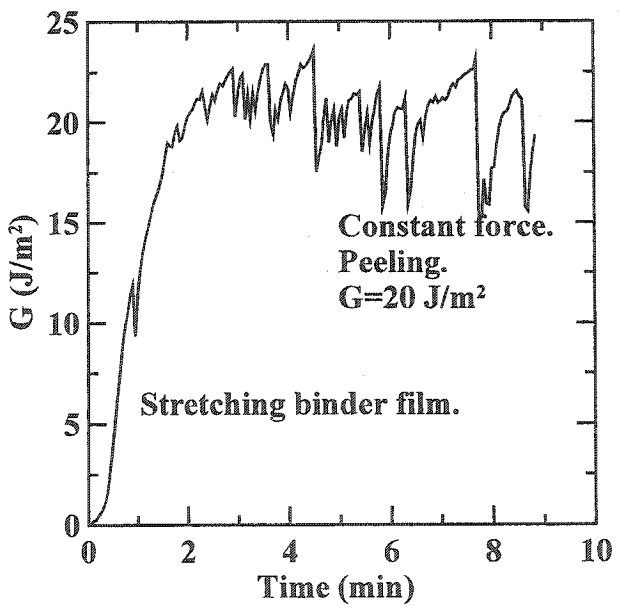

Figure 3.14 Typical data for a peel test to measure the adhesion strength between the binder film and the silicon wafer

3.6 Soaking Test

To evaluate the amount of swelling of the crosslinked polymer films, the films were immersed in the mixed solvent [EC/DEC (1:2 by volume)] for 24 hours. Then the film was dried quickly with a paper towel (in <1 minute) to eliminate the solvent drops on the surface. The mass of the film before and after soaking was measured to determine the % weight uptake of films, which is defined here to be the swelling ratio. The typical mass of samples used for the soaking test was about 0.2-1.0 g.

3.7 In-situ Resistance technique

The *in-situ* resistance cell, measurement method and measuring electronics are very similar to those described by Baudais et al. [67]. However, *in-situ* resistance results in reference [67] were made on pure evaporated films of micrometer thickness. Here the studies are being made on composite electrodes, containing negative electrode material, carbon black and binder, which are about 75 micrometers thick.

Figure 3.15 shows the current collector design used in our test cells to provide an appropriate current path through the negative electrode, with which to measure the resistance of the electrode across the gap. The current collector is a copper film, ca. 1 μm thick, deposited using a RF sputtering machine on a cleaned glass microscope slide. The glass slide, with the sputtered copper film is called the negative electrode plate here. A narrow gap, ca. 1.0 mm wide, was masked in the copper film. A well-mixed electrode slurry, which is described in section 3.4, was cast as a thin film across the gap using a notch bar spreader with a gap of 0.3 mm. Before assembling the cell, excess film on the

substrate was gently removed with a scalpel to leave a square electrode (about 1 cm × 1 cm) spanning the gap.

Figure 3.16 shows an exploded view of the in-situ resistance cell. The base plate is made of TEFLON and has a slot machined into the top surface to hold the negative electrode plate. Four screws are threaded through this base plate to secure the top plate of the cell. The cells used a polypropylene microporous separator, an electrolyte (1M $LiClO_4$ dissolved in EC/DEC (1:2, v/v), Mitsubishi Chemical), and a Li counter electrode. The lithium metal rests against the top plate, which has an O-ring groove. A Kalrez O-ring was used to seal the cell. The cells were assembled in an argon-filled glove box.

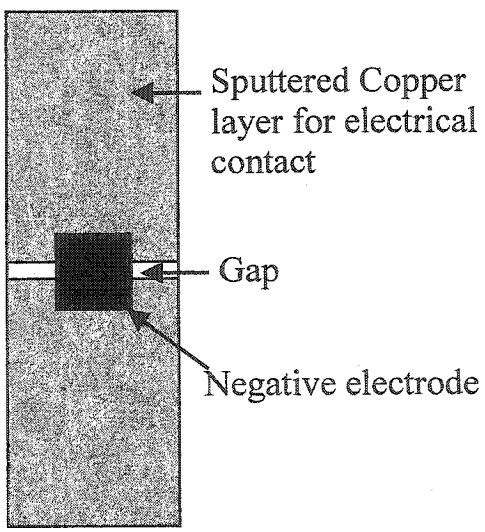

Figure 3.15 Schematic of the negative electrode on the negative electrode plate used for the in-situ resistance measurement

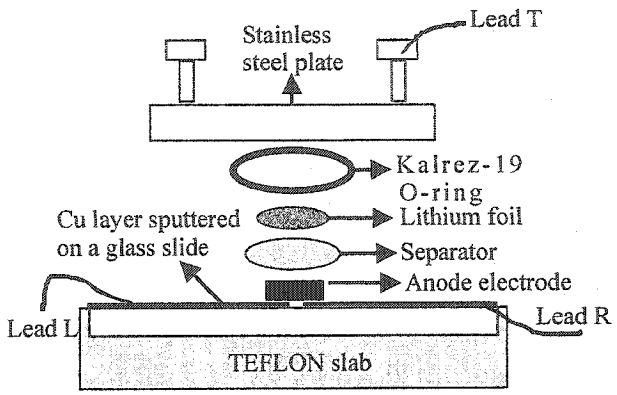

Figure 3.16 Exploded view of the in-situ resistance cell

Figure 3.17 shows a photograph of the dual-unit in-situ resistance testing system built at Dalhousie. During charge or discharge to a given state of charge, the two copper contacts were electrically connected together so that the entire negative electrode was at the same potential. Once the desired state of charge was reached, the cell was then placed in an open circuit condition and a current pulse was applied across the negative electrode using the leads L and R in Figure 3.16. The potential drop across the electrode was measured as a function of time during the current pulse. The voltage profile recorded was fitted to obtain the resistance of the electrode.

Figure 3.18 shows a typical voltage response of the electrode to the pulse current input during the resistance measurement. Apparently, the voltage response to the pulse current input is not a square wave as expected by Ohm's law. The curved voltage peaks are caused by the transport of lithium ions between the half-electrodes during the measurement [67]. When a current passes through the electrode film across the gap, a small potential difference is set up between the half-electrodes. Therefore, a small compositional difference (x in a-$Li_xSi_{0.64}Sn_{0.36}$/Ag) between the half-electrodes is needed

to match the potential difference. Thus, the lithium atoms have to be redistributed between the half-electrodes. Figure 3.19 schematically shows the ionic pathway that is able to transport charge during the resistance measurement. The charge transfer rate is controlled by the ionic resistance (R_i) between the half-electrodes, and the amount of charge that can be transferred by the ionic pathway is limited by the differential capacity (C) of the half-electrodes and the potential difference.

Figure 3.20 shows an equivalent circuit, that incorporates the electrical (R) and ionic (R_i, C) paths [67], which was used to fit the experiments. An example of the good fit to the experimental data is also shown in Figure 3.18. Normally, the current pulse used to measure the resistance was ±25μA for MCMB composite electrodes and ±1μA for a-$Si_{0.64}Sn_{0.36}$/Ag composite electrodes.

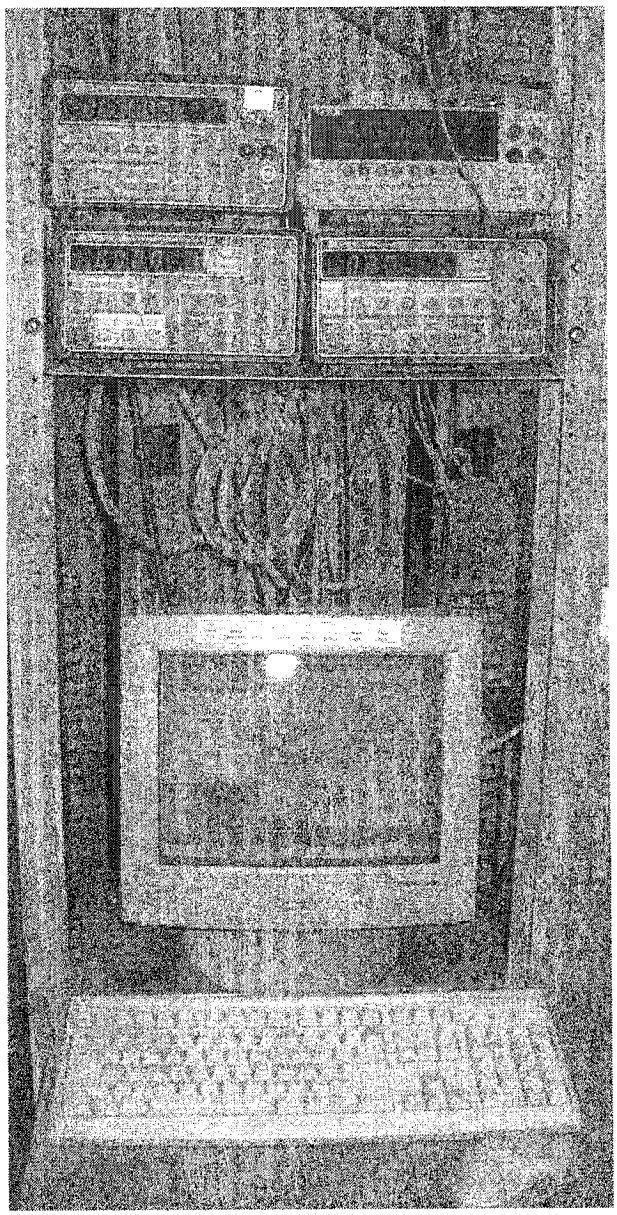

Figure 3.17 A photograph of the dual-unit in-situ resistance testing system

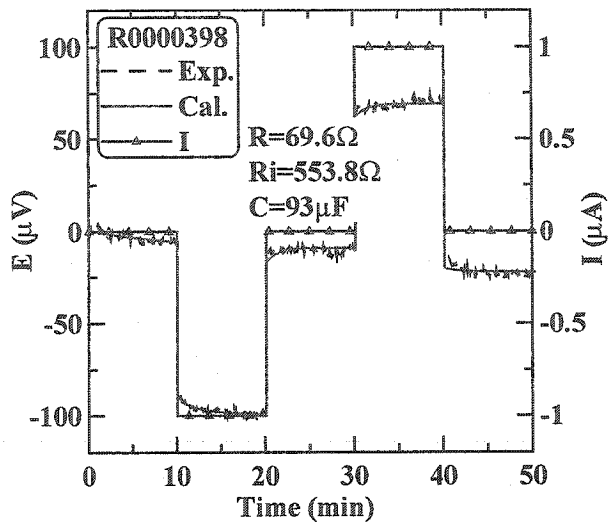

Figure 3.18 A typical voltage response of an a-$Si_{0.64}Sn_{0.36}$/Ag electrode to the pulse current sequence. A pulse current sequence of 0, -1, 0, 1, and 0 μA was applied to measure the resistance.

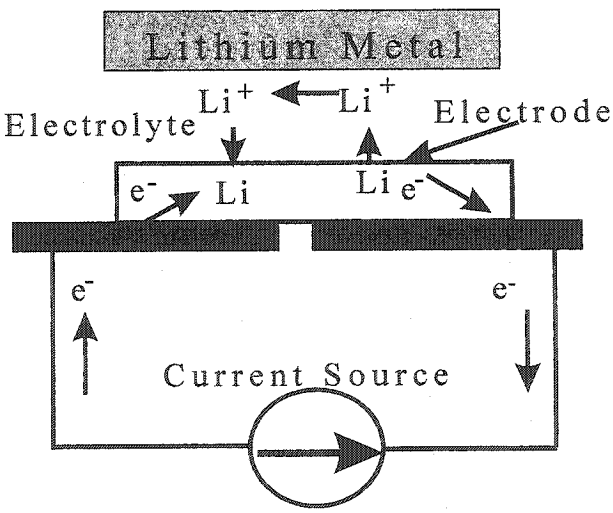

Figure 3.19 Current flow carried by the ionic path during resistance measurement

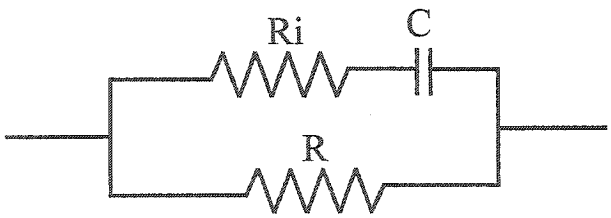

Figure 3.20 The equivalent circuit used to fit the experimental data of a-$Si_{0.64}Sn_{0.36}$/Ag electrodes.

3.8 Coin cell construction and testing

The electrochemical performance of negative electrodes was tested in 2325 (23 mm diameter, 2.5 mm thickness) coin cells. Figure 3.21 shows an exploded view of a lithium coin cell used for electrochemical characterization. The cell stack consists of a working electrode (negative electrode in this study), a microporous polypropylene (PP) separator (Celgard 2502), a counter electrode (lithium metal) and an appropriate amount of electrolyte. The electrolyte used was 1M $LiPF_6$ in a mixed solution of ethylene carbonate (EC) and diethyl carbonate (DEC) with a ratio of 1:2 by volume. The cell stack was held in place with a spacer and a spring. After the whole cell was assembled, it was crimp-sealed. All cells were assembled in an argon-filled glove box. In a few cases, 1M $LiBF_4$, 1M $LiClO_4$, 1M LiBETI, respectively, in EC/DEC (1:2, v/v) were used instead of $LiPF_6$-based electrolyte.

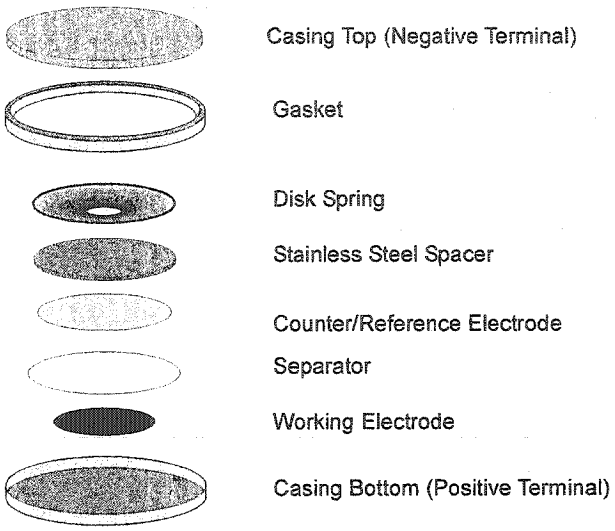

Figure 3.21 An exploded view of a coin type test cell

Computer controlled chargers made by E-One/Moli Energy and by Maccor were used to characterize the cells. Cells were discharged and charged between a lower cutoff potential and an upper cutoff potential with a computer-controlled constant-current charger system. Tests were made at a constant temperature of 30°C. During discharge, the potential of the cell drops. The discharge current is stopped when the cell potential reaches the lower cutoff potential. During charge, the potential of the cell increases and the current is stopped when the cell potential reaches the upper cutoff potential. The raw cycling data recorded by the charger system is the cell voltage versus time.

A program, "Datamangler", developed by D. A. Stevens was used to calculate the cell potential versus the specific capacity, differential capacity versus cell potential and the specific capacity versus the cycle number based on the raw data from the charger systems.

3.9 In-situ thickness measurement

The in-situ thickness cell is almost the same as the normal coin type test cell except that the spring is replaced with two spacers. The spring was removed so that the thickness change of the electrode can be measured by monitoring the thickness change of the whole cell. The three spacers fill the internal volume of the cell casing. An exploded view of the in-situ thickness cell is schematically shown in Figure 3.22.

Figure 3.23 shows a schematic of the in-situ thickness measurement. The cell was connected to the Moli charger system in the same way as a regular coin-type test cell, but with the casing bottom facing up. A linear voltage displacement transducer (LVDT, ATA 2001, Schaevitz) touched the casing bottom. Thickness changes of the cell moved the probe vertically and the displacement of the probe was detected by the LVDT. The output signal of the LVDT was recorded by the slave channel of the charger system. Using the master-slave technique provided by the Moli charger system, the potential of the electrode and the thickness changes of the cell can be monitored simultaneously. Then, the theoretical thickness changes of the lithium foil were accounted for to obtain the thickness change of the working electrode.

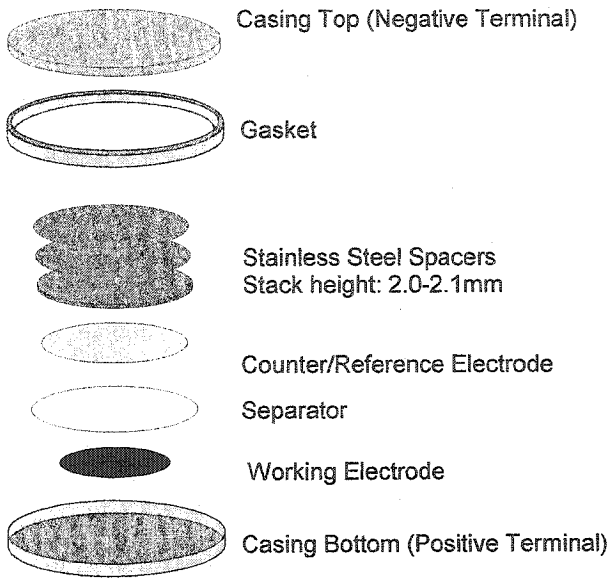

Figure 3.22 An exploded view of the in-situ thickness cell

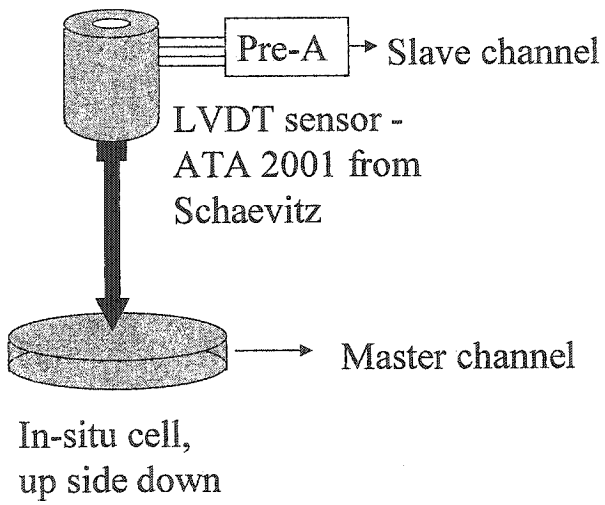

Figure 3.23 Schematic of the in-situ thickness measuring system

3.10 Other physical characterizations

Powder X-ray diffraction (XRD) was used to confirm the amorphous state of the negative electrode materials, a-$Si_{0.64}Sn_{0.36}$ and a-$Si_{0.64}Sn_{0.36}$/Ag. The diffractometer used

was a Siemens D500 diffractometer, which has a copper target X-ray tube and a diffracted beam monochromator. A flat stainless steel holder with a rectangular well in the center was used to hold the powder samples. The X-ray scattering angle range measured was between 10^{o} and 90^{o} with a step size of 0.05^{o}. The count time was 30 seconds per step.

Scanning electron microscopy was used to investigate the morphology and size of negative electrode materials used. Differential scanning calorimetry (DSC) was used to measure the crystallization temperature of the amorphous materials, a-$Si_{0.64}Sn_{0.36}$ and a-$Si_{0.64}Sn_{0.36}$/Ag.

3.11 Specifications of negative electrode materials used

The negative electrode materials discussed in this thesis are a-$Si_{0.64}Sn_{0.36}$, and a-$Si_{0.64}Sn_{0.36}$/Ag (with 10 wt% silver coating). Both of the materials were provided by 3M Company. The a-$Si_{0.64}Sn_{0.36}$ was prepared using a sputtering machine, which deposited the a-$Si_{0.64}Sn_{0.64}$ on a metal substrate in a thick layer. The material was removed from the substrate by a high-impact blow. The removed chunks were then ground into powder at 3M using automated grinding equipment. Figure 3.24a shows SEM images of some a-$Si_{0.64}Sn_{0.36}$ particles. The particle size is about 10-20 microns. The surface of the a-$Si_{0.64}Sn_{0.36}$ particles is quite smooth with some small humps (Figure 3.24b). Then, a layer of silver was deposited on the surface of the a-$Si_{0.64}Sn_{0.36}$ particles by electroless deposition to obtain a-$Si_{0.64}Sn_{0.36}$/Ag. Figure 3.24c shows the particle size of a silver-coated negative electrode material particle. Figure 3.24d clearly shows that the particle was evenly covered with a layer of silver particles, whose size is about 100 nm. Almost

no bare a-$Si_{0.64}Sn_{0.36}$ surfaces can be observed with SEM. The amorphous state of the materials was confirmed by X-ray diffraction patterns (Figure 3.25). The sharp peaks in the XRD patterns are associated with the XRD pattern of crystalline silver particles on the surface of a-$Si_{0.64}Sn_{0.36}$/Ag particles.

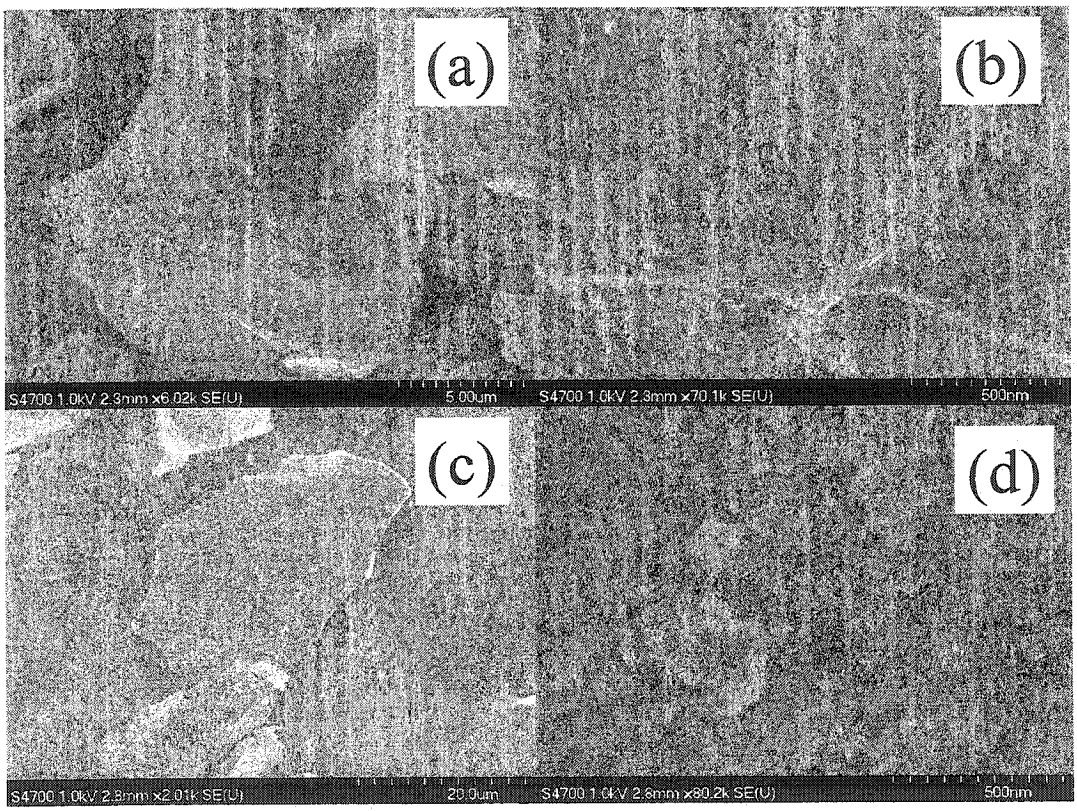

Figure 3.24 (a) SEM image of a-$Si_{0.64}Sn_{0.36}$ (low magnification), (b) SEM image of a-$Si_{0.64}Sn_{0.36}$ (high magnification), (c) SEM image of a-$Si_{0.64}Sn_{0.36}$/Ag (low magnification), and (d) SEM image of a-$Si_{0.64}Sn_{0.36}$/Ag (high magnification)

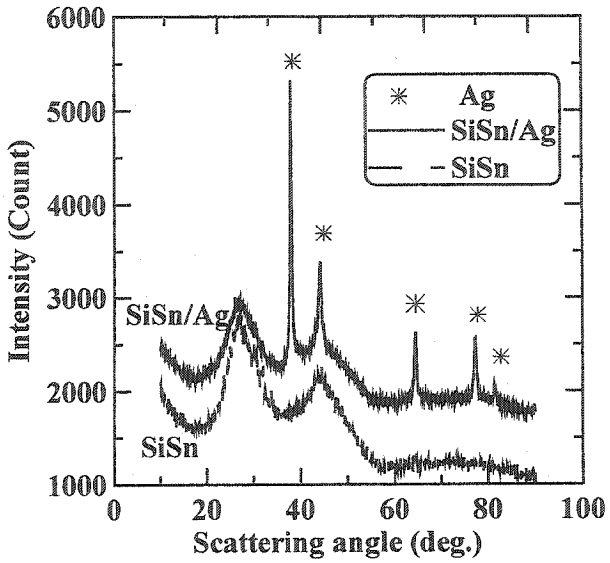

Figure 3.25 XRD patterns of a-$Si_{0.64}Sn_{0.36}$ and a-$Si_{0.64}Sn_{0.36}$/Ag

Chapter 4 PVDF-HFP-based elastomeric binder system

4.1 Introduction

Carbon-filled polymer composites, especially based on PVDF, have been widely used in lithium-ion batteries as an electrode binder to maintain physical integrity of the electrode and to help maintain an electrical pathway between active material particles and the current collector [16, 17, 19-26, 28, 29]. The mechanical and electrical properties of the carbon-filled polymeric binder may therefore impact the performance of lithium-ion and other batteries.

However, the mechanical and electrical properties of the binder system were widely ignored until recently. The first publication about the impact of the binder system on the cycling performance of metallic alloy composite electrodes appeared in 1999 [68]. The author used polyethylene (PE) as a flexible binder for ultrafine Sn and $SnSb_x$ composite electrodes. Compared to the electrodes using the PVDF-based binder, the ultrafine Sn and $SnSb_x$ electrodes using the PE-based binder had better capacity retention. However, only a minor improvement was obtained. One year later, Besenhard et. al. proposed the use of crosslinked binders to improve the capacity retention of Sn and SnSb composite electrodes [13]. However, no follow up publication about the importance of the binder system appeared until we published a series of research works to successfully address the critical importance of the binder system [60-63, 69, 70].

According to the tether model we propose, it is apparent that an elastomer with good mechanical properties is not enough to maximize the capacity retention of metallic alloy composite electrodes. Good adhesion strength between the polymer and solid

components of composite electrodes, carbon black particles and active material particles, is critical as well. A poly(vinylidene fluoride-hexafluoropropylene) (PVDF-HFP, FC2178) polymer was carefully investigated as a potential elastomeric binder system to improve the capacity retention of a-$Si_{0.64}Sn_{0.36}$/Ag composite electrodes.

4.2 Mechanical and electrical characterization of FC2178 and FC2178/SS samples

4.2.1 Mechanical models

It is our long-term goal to determine the link between the mechanical properties of the binder system and the electrochemical performance of the resulting electrode. As a first step, it is important to describe the mechanical properties of the binder system with a suitable mechanical model. Two mechanical models were used to describe the mechanical properties of the crosslinked polymer and polymer/carbon black blends, respectively.

4.2.1.1 The linear model

Springs and dashpots are the basic elements used to simulate the mechanical behavior of polymers [39]. Figure 4.1 shows a schematic of a four-element linear model. In the linear model, K_1 and K_2 are the Young's modulus of the springs used to represent the strength of the polymer, while K_{d1} and K_{d2} are constants of the dashpots used to model the viscosity of the polymer. This linear model was used to study the mechanical properties of the FC2178 polymer and the effect of crosslinking in the absence of carbon black.

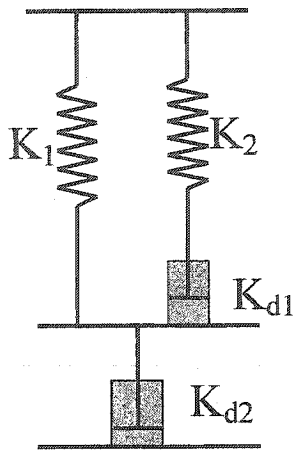

Figure 4.1 Schematic of the linear model used to describe the mechanical properties of polymer films. K_1 and K_2 are spring constants in the model and K_{d1} and K_{d2} are constants used to characterize the viscosity of the dashpots in the model.

4.2.1.2 The bilinear model

Normally, carbon black is used in polymers and binders as a conductive filler. When carbon black was added to the polymer, the mechanical properties changed dramatically and the linear model couldn't fit cyclic stress-strain experiments properly. A bilinear element was needed to describe the effect of the carbon black. Figure 4.2 shows a schematic of the bilinear model. Compared to the linear model, the bilinear model has a bilinear element placed in series with a third dashpot. The stress of the bilinear element, σ_n, is described by two parameters, k_{s1} and k_{s2} as shown in equation (4-1);

$$\sigma_n = \begin{cases} k_{s1}\varepsilon & \varepsilon \geq \varepsilon_{\max} \\ k_{s1}\varepsilon_{\max} - k_{s2}(\varepsilon_{\max} - \varepsilon) & \varepsilon_e < \varepsilon \leq \varepsilon_{\max} \\ 0 & \varepsilon \leq \varepsilon_e \end{cases} \tag{4-1}$$

where ε is the strain, ε_{max} is the largest strain applied in the deformation history and ε_e is the strain at which a new equilibrium length of the bilinear element is established.

Figure 4.3 shows a diagram of the stress-strain behavior of the bilinear element as described by equation (4-1) with $\varepsilon_e = 0.4$. Physically, the bilinear element is meant to represent a carbon black strand connected to viscoelastic polymer at each end. As the element is stretched the carbon black strand rotates to be parallel to the stretching direction, thus establishing a new, longer equilibrium length. When the stress is removed, the polymer contracts, but we assume the carbon black strand does not rotate fully back to the original position and the element goes "slack" at the point "f" in Figure 4.3. Although this bilinear element is empirically derived, we will show that it captures the main behavior of carbon black-filled polymer composites studied here.

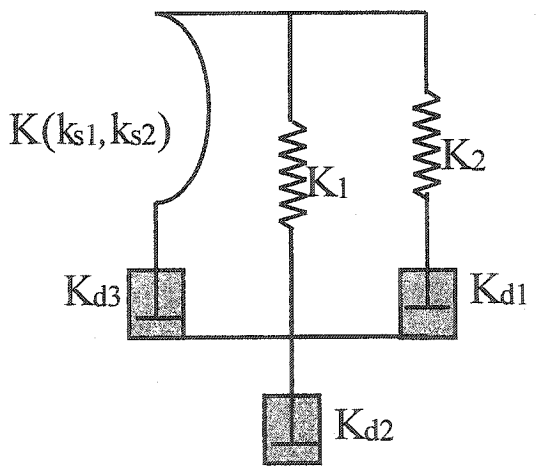

Figure 4.2 Schematic of the bilinear model used to describe the mechanical properties of polymer/carbon black films. K_1 and K_2 are spring constants in the model and K_{d1}, K_{d2} and K_{d3} are constants used to characterize the viscosity of the dashpots in the model. $K(K_{s1}, K_{s2})$ describes the stiffness of the bilinear element. Parameters K_{s1} and K_{s2} are described in equation (4-1).

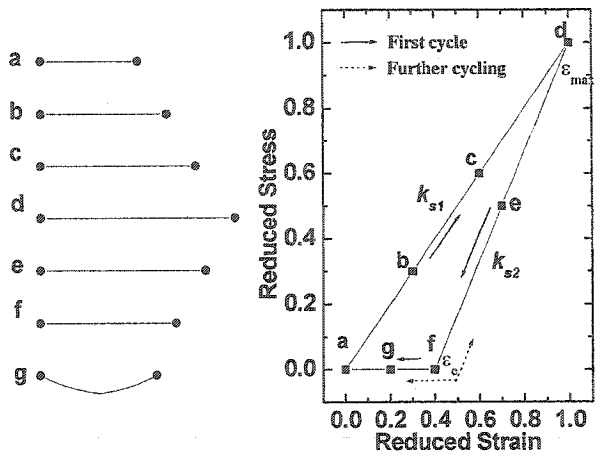

Figure 4.3 The stress-strain curve of the bilinear element proposed. (a) Initial state of the bilinear element, (a)-(d) a stretched bilinear element, which is taut, (d)-(f) a releasing, but taut, bilinear element, (f) a bilinear element with its new equilibrium length, and (g) a slack element if further released.

4.2.2 Poor mechanical properties of PVDF compared to FC2178

Figure 4.4 compares the mechanical and electrical properties of PVDF/SS and FC2178/SS films. Figure 4.4a shows the stress versus strain for PVDF/SS and FC2178/SS films stretched to the breaking point. Both PVDF/SS films with 10 pph and 25 pph SS, respectively, can only be stretched to about 4% before breaking. The extensibility is quite poor. Compared to PVDF/SS films, FC2178/SS films have much better elongation before breaking. The FC2178 film with 11 pph SS can be extended to about 50% strain without breaking. Even when 25 pph SS is added, the film can be stretched to about 20% before breaking. Figure 4.4b shows the nominal resistivity vs. strain of PVDF/SS films and FC2178/SS films. When the SS content increases from 10

pph to 25 pph, the nominal resistivity of both PVDF/SS films and FC2178/SS films decreases.

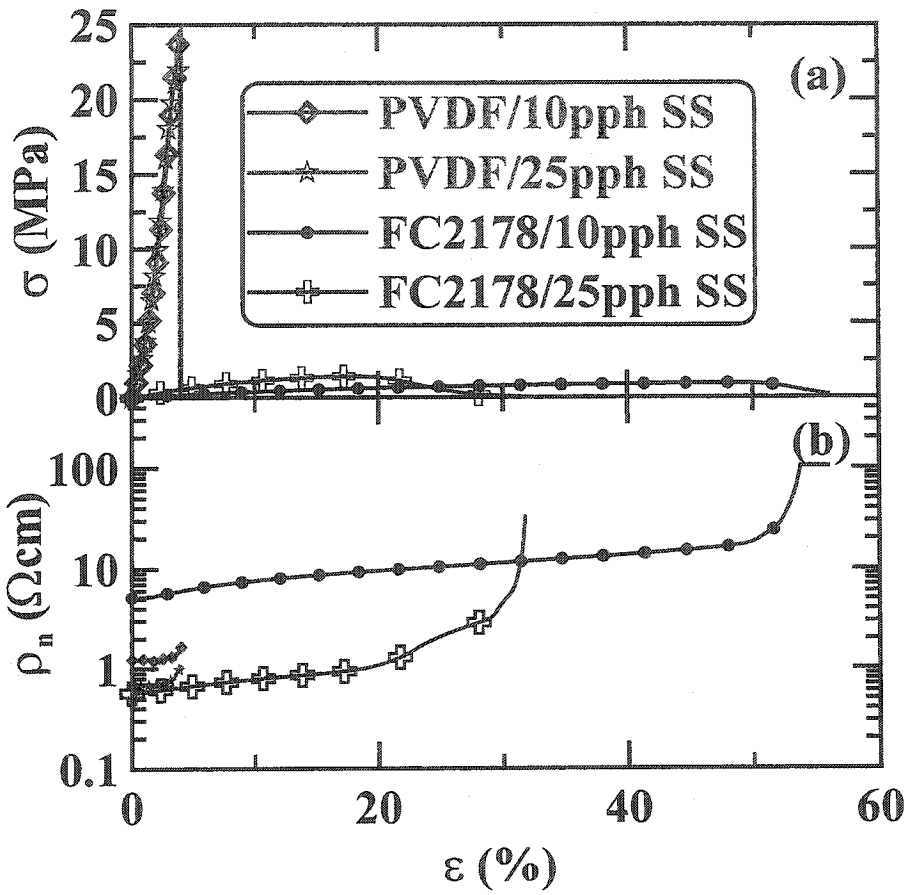

Figure 4.4(a) Stress vs. strain and (b) nominal resistivity vs. strain showing the elongation till break behavior of PVDF/SS and FC2178/SS films.

4.2.3 Effect of carbon black on the properties of FC2178

Figure 4.5a shows the effect of the SS content on the mechanical properties of FC2178/SS films. As the SS content increases, the Young's modulus of the FC2178/SS film increases and the maximum elongation before break decreases significantly. When 5.2 pph SS was used, the film could be elongated by 60% before breaking. However, the

film with 25 pph SS could only be stretched by 20%. Figure 4.5b shows the effect of the SS content on the nominal resistivity of FC2178/SS films. As the SS content increases, the resistivity decreases. The nominal resistivity increases exponentially with the strain applied.

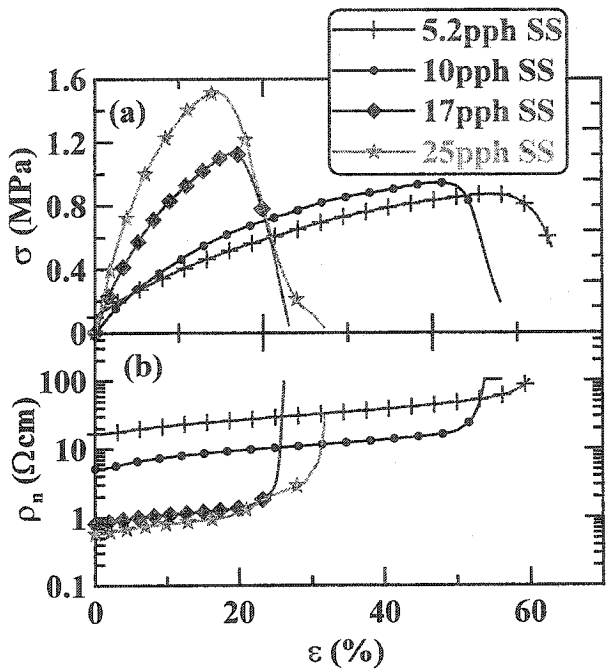

Figure 4.5 (a) Stress vs. strain and (b) nominal resistivity vs. strain showing the effect of the SS content on the breaking behavior of FC2178/SS films

4.2.4 Crosslinking of FC2178 with TETA

The active material is an essential component of electrodes for lithium-ion batteries. The addition of active materials (normally > 400 pph polymer) will dramatically degrade the mechanical properties of the binder film like additions of SS do. Hence, the mechanical properties of the FC2178/SS system may not be sufficient for applications

with large volumetric changes. Fortunately, the mechanical properties of FC2178/SS films can be significantly improved by crosslinking.

The VDF monomer in PVDF-HFP (FC2178) can react with a base to form an unsaturated carbon-carbon double bond as shown in equation 4-2. Carbon-carbon double bonds in the backbone of the polymer chains can act as the active sites for crosslinking and coupling reactions. For instance, $-NH_2$ in an organic molecule can be added to a carbon-carbon double bond. Equation 4-3 shows the reaction of the active site in the polymer backbone with a bifunctional molecule, triethylenetetramine (TETA), which will be used as the crosslinking agent for PVDF-HFP.

$$\text{-}CH_2\text{-}CF_2\text{-} + \text{base} \rightarrow \text{-}CH{=}CF\text{-} + HF\cdot\text{base} \tag{4-2}$$

$$\text{-}CH{=}CF\text{-} + NH_2\text{-}R\text{-}NH_2 \rightarrow \text{-}CH_2\text{-}CF(\text{-}NH\text{-}R\text{-}NH_2)\text{-} \tag{4-3}$$

A series of FC2178 films were prepared with different TETA contents, which ranged from 0 to 10 pph. The stress-strain curves collected are shown in Figure 4.6. All curves were fitted with the linear model, and the fitted results are also shown in Figure 4.6 for comparison. As the TETA content increases, the Young's modulus of the binder film increases and the rebound point decreases. When 10 pph TETA was used, the stress-strain curve is almost linear, and rebounds to a very small strain (about 3%). This sample behaves almost as a Hooke's-law spring.

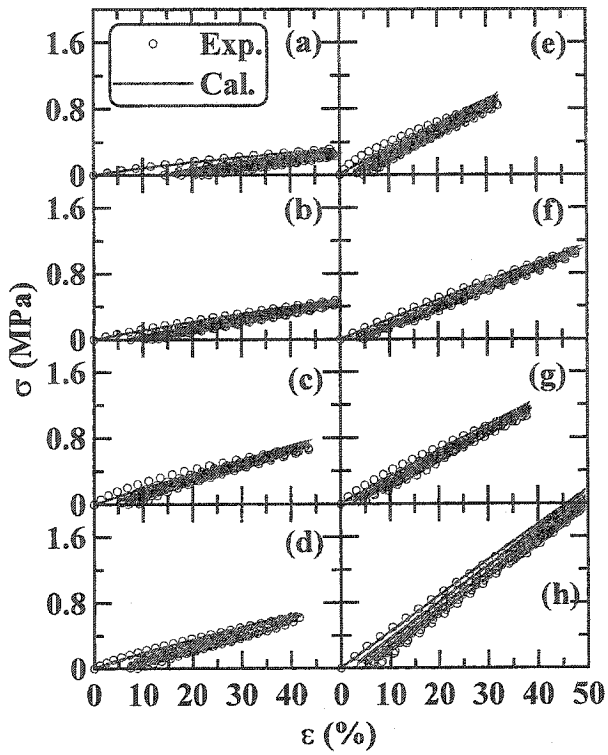

Figure 4.6 Stress vs. strain curves of TETA-crosslinked FC2178 films with (a) 0.0 pph TETA, (b) 0.3 pph TETA, (c) 0.9 pph TETA, (d) 1.2 pph TETA, (e) 2.0 pph TETA, (f) 2.9 pph TETA, (g) 5.0 pph TETA, and (h) 10.0 pph TETA

The parameters used to fit the linear model to the data in Figure 4.6 are listed in Table 4.1. Figure 4.7 shows the fitted parameters plotted as functions of the TETA content. The parameters, K_2 and K_{d1} do not show a clear trend with the TETA content. However, K_1 and K_{d2} show a strong dependence on TETA content. They increase linearly when the TETA content is less than 4 pph, and continue to increase more slowly when more than 4 pph TETA is used. These parameters increase because the films are getting stiffer (K_1) and more viscous (K_{d2}).

Table 4.1 Best-fit parameters of the linear model to crosslinked FC2178 films

TETA content (pph)	K_1 (MPa)	K_2 (MPa)	K_{d1} (10^2 MPa·S)	K_{d2} (10^5 MPa·S)
0.0	0.70	0.81	4.1	0.14
0.3	0.89	0.30	3.6	0.77
0.9	1.8	0.85	1.5	1.1
1.2	1.6	1.3	3.8	0.81
2.0	3.0	1.9	2.7	1.9
2.9	3.7	10	3.2	2.0
5.0	3.2	3.1	1.2	2.5
10.0	4.4	16	0.68	3.6

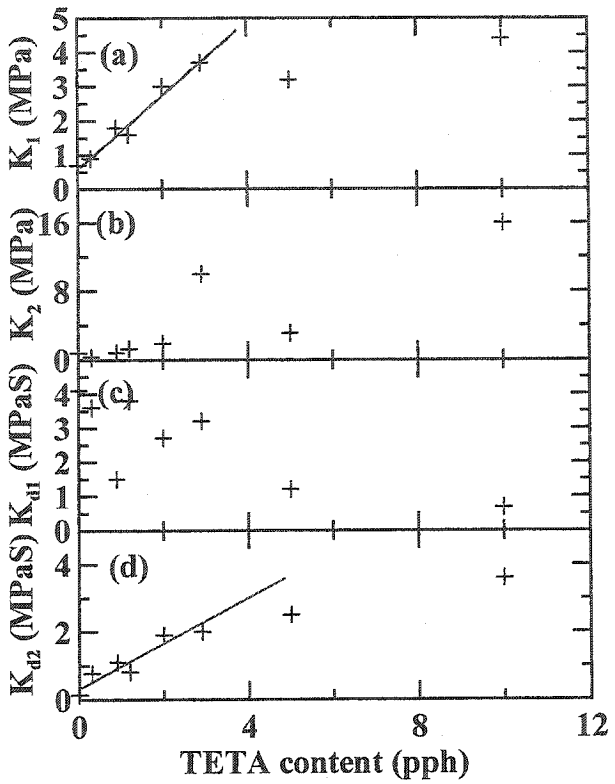

Figure 4.7 The effect of crosslinking on the parameters of the linear model for FC2178 films: (a)K_1 vs. TETA content, (b) K_2 vs. TETA content, (c) K_{d1} vs. TETA content, and (d) K_{d2} vs. TETA content.

Figure 4.8 shows the effect of the TETA content in FC2178 films on the maximum stress at a given strain, the rebound point from the same strain and the relaxation in stress of films held at fixed strain. The maximum stress at fixed strain increases with TETA content when less than 3 pph TETA is used (Figure 4.8a). The rebound point and the amount of relaxation decrease with the TETA content. When the TETA content is larger than 3 pph, the rebound point is less than 10% strain (Figure 4.8b) and the amount of stress relaxation is constant near 10% (Figure 4.8c). Crosslinking with TETA not only increases the strength of polymer films but also suppresses the viscoelastic flow of

polymer chains. However, the improvement of the mechanical properties slows down when the TETA content is above 3 pph.

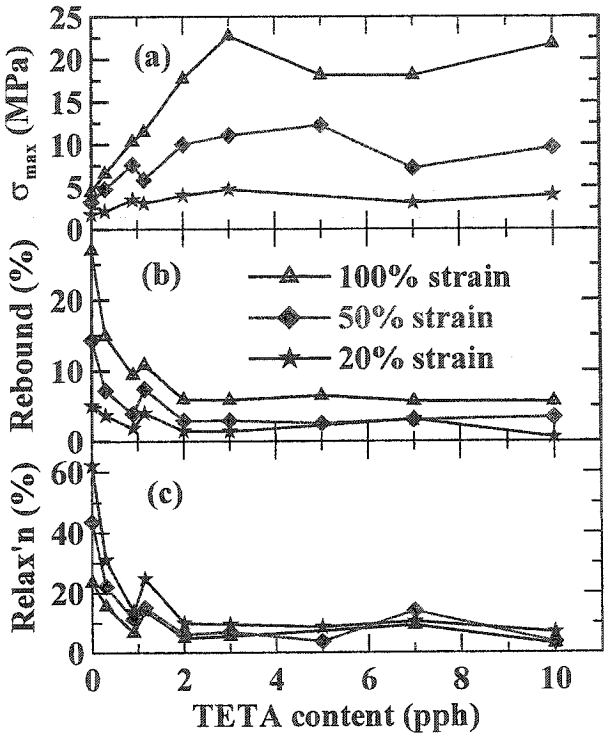

Figure 4.8 The effect of TETA on the mechanical properties of FC2178 films: (a) maximum stress vs. TETA content, (b) rebound vs. TETA content, and (c) percent stress relaxation vs. TETA content

4.2.5 Introducing the bilinear element in the mechanical model

Solids, for example the carbon black and the active material, are essential components of the electrode. We would like to be able to use the mechanical model to describe films that are similar to electrodes. However, the linear model doesn't describe experiment well when SS is added to the polymer. Figure 4.9 shows the poor agreement

between the experiment and the simulation, using the linear model, for a FC2178/TETA film containing 25 pph SS. The best-fit parameters for the linear model are listed in the first row of Table 4.2. After the first stretch, the experimental curve shows sharply rising regions when the strain is larger than 40%. This corresponds to an increase in the modulus of the binder film. However, calculated results do not show this behavior. Under the extreme condition that the dashpot viscosities are infinite, the linear model reduces to a spring with a constant modulus. There is no way to explain the upward curvature in the experiment. Thus, the linear model cannot simulate regions with an increasing modulus, and a bilinear element is needed to describe this behavior.

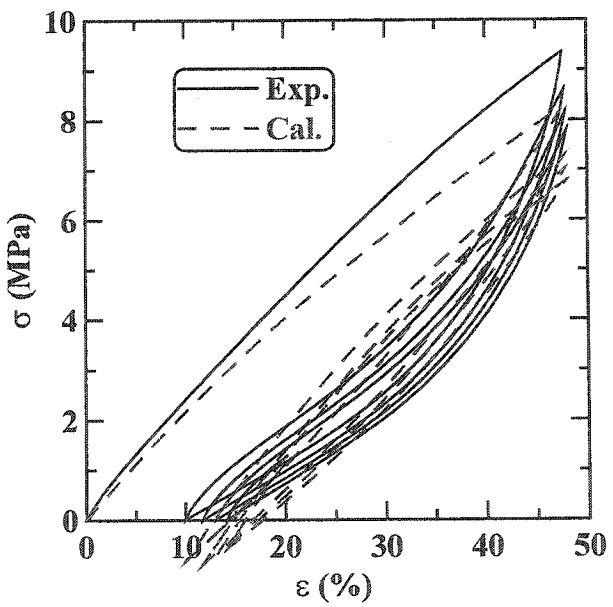

Figure 4.9 An attempt to describe the stress-strain curve of an FC2178 film incorporating 25 pph SS and 6.0 pph TETA using the linear model.

Table 4.2 Best-fit parameters of the bilinear model to experiments (Figure 4.9 and 4.11)

	K_1 (MPa)	K_2 (MPa)	K_{s1} (MPa)	K_{s2} (MPa)	K_{d1} (10^4 MPa S)	K_{d2} (10^5 MPa S)	K_{d3} (10^3MPa S)	Figure
a	12	12	N/A	N/A	2.1	1.3	N/A	4.9
a'	10	8.2	8.0	25	0.82	9.3	1.7	4.11a
b	12	7.9	6.6	24	0.64	4.4	4.0	4.11b
c	15	14	7.0	17	0.28	3.1	9.2	4.11c

Figure 4.10a shows a stress-strain curve for a cross-linked FC2178 sample containing 25 pph SS and 6.0 pph TETA, which was first strained to 45%, then released to zero stress and then strained beyond 45%. Notice that the sample has "memory" of its original behavior (same slope in the stress-strain curve) when it is strained beyond 45%. Figure 4.10b shows stress-strain curves for two identical films, which have been first strained to 40% and then cycled to 13% or to 30% strain repeatedly. The data cycled to 13% show no hint of a region of increasing modulus, while there is some increase in modulus when the film is stretched to 30%. A bilinear element is needed that can "memorize" the deformation history and that has little effect when the strain is small, after an initial high-strain extension.

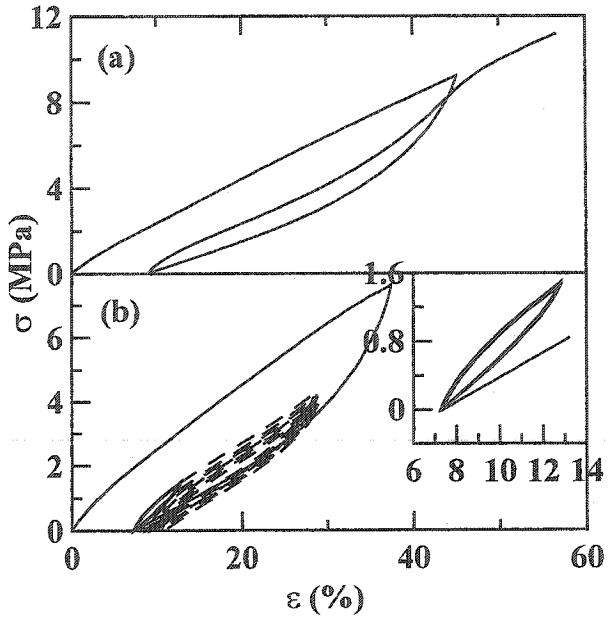

Figure 4.10 Features that cannot be explained by the linear model. (a) 'Memory' effect, and (b) linear and bilinear stress vs. strain of an FC2178 film with 25 pph SS and 6.0 pph TETA

We propose that the bilinear element resemble the behavior of a string. Carbon black is composed of chains of carbon nano-spheres that can attach one to the next. It is quite filamentary. When the polymer is stretched we believe carbon black filaments will first rotate to be parallel to the stretching direction. At this point, the "string" will be taut, and stretching of the polymer attached to the end of the carbon black will occur. If the stress is released, only a small contraction will occur before the stress reaches zero.

Figure 4.3 shows a schematic model of the bilinear element we propose. As the element is stretched (a→b→c→d) carbon black filaments rotate to be parallel to the stretching direction, thus establishing a new, longer equilibrium length. When the stress is removed, the polymer contracts (d→e→f), but we assume the carbon black strand does

not rotate fully back to the original position and the element goes "slack" at the point "f" in Figure 4.3. After that, the stress will be zero if the strain is further reduced (f→g→a). Further cycling follows the path g↔f↔e. If the element is stretched beyond the point e (the maximum strain in the history), a new ε_{max} is reached and the stress increases with strain with a slope of k_{s1} instead of K_{s2}. Based on the above discussion, a bilinear element was added to the mechanical model (see Figure 4.2). The stress within the bilinear element, σ_n, can be described by equation 4-1.

Figure 4.11 shows stress-strain curves calculated using the bilinear model compared to the data in Figures 4.9 and 4.10. The best-fit parameters are also listed in Table 4.2 (rows a', b and c respectively). Figure 4.11a shows the fitting to the cyclic stress-strain curve. The bilinear model fits the experimental curve very well. It also models the upturn of the stress at about 40% strain, which is beyond the capability of the linear model. The singular point at about 40% strain occurs at the point where the bilinear element establishes its new equilibrium length. When the strain is less than 40%, the contribution of the bilinear element to the stress is zero, while springs K_1 and K_2 shown in Figure 4.2 are still stretched and the stress varies with strain with a smaller slope as shown in Figure 4.11. The bilinear model can also model the "memory" effect of the polymer film with SS (Figure 4.11b) and the linear cycling behavior at small strain (Figure 4.11c). The parameters listed in Table 4.2 provide good fits to the data in Figure 4.11, but we do not feel they are unique. For example, each of the parameter sets a', b and c in Table 4.2 produce stress-strain curves that agree almost exactly during the initial extension. The parameter sets differ slightly in order to fit the subsequent behavior.

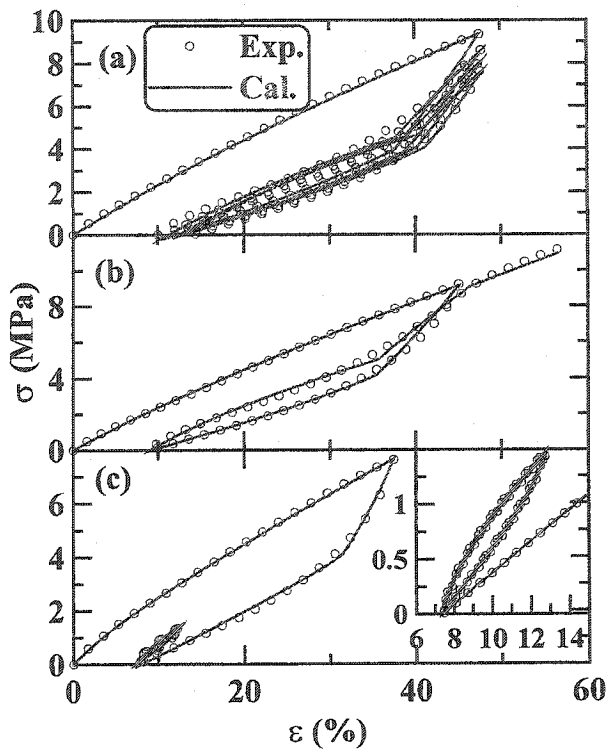

Figure 4.11 Testing the bilinear model's description of carbon-filled crosslinked FC2178. (a) The increase of modulus at large strain during cyclic deformation, (b) the "memory" effect for films cycled once and then strained further and (c) the linear behavior at small strain after a large initial strain history. Note: the sample used was FC2178 with 25 pph SS and 6.0 pph TETA

4.2.6 Effect of TETA on the properties of FC2178 films containing 25 pph SS

When no TETA was added, the FC2178 film with 25 pph SS easily broke at about 20% strain (see Figure 4.5a). The addition of TETA improves the mechanical properties, and all films can be cyclically stretched to 50% strain without breaking. Figure 4.12 shows stress-strain curves (open circles) during cyclic deformation for films with different TETA content. As the TETA content increases, the maximum stress of the

films increases from about 4 MPa (1 pph TETA) to about 9 MPa (6 pph TETA). Moreover, the rebound point in the stress-strain curves decreases from 15% to about 10%. Figure 4.12 also shows best-fittings (solid lines) to experiments using the bilinear model. Apparently, the bilinear model fits all experiments quite well. The best-fit parameters are listed in Table 4.3. The parameters K_1, K_{d1} and K_{d3} increase with the TETA content.

Figure 4.13 shows the effect of TETA on the nominal resistivity of FC2178 films with 25 pph SS. The nominal resistivity of all the samples ranges from 1.5 to 2.5 Ω·cm during cyclic deformation. The addition of TETA has no significant impact on the value of nominal resistivity. However, the results clearly demonstrate the effect of TETA on the reversibility. As the TETA content increases, the difference in nominal resistivity between loading and unloading cycles decreases after the first cycle. When 6.0 pph TETA was used, the nominal resistivity changes reversibly during cycling. This may be attributed to the crosslinking in the polymer matrix. As the degree of crosslinking increases, the modulus of the polymer matrix increases and the possibility of carbon black re-orientation decreases. Hence, the reversibility should increase with the TETA content.

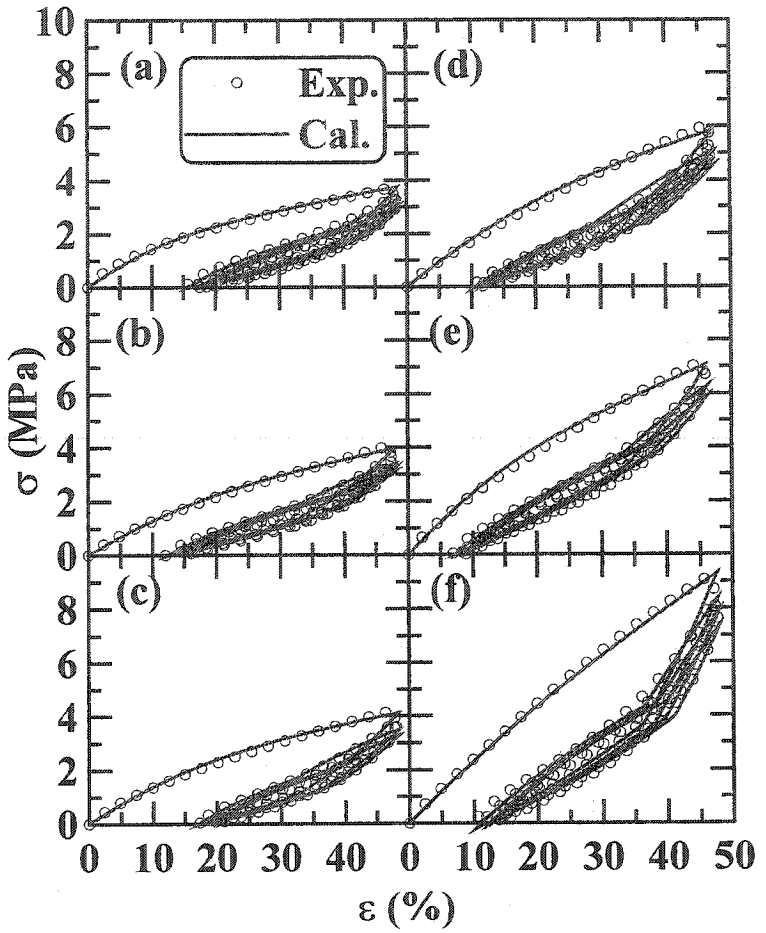

Figure 4.12 Stress vs. strain curves showing the effect of TETA on the mechanical properties of FC2178 films with 25 pph SS (a) 1.0 pph TETA, (b) 2.0 pph TETA, (c) 3.0 pph TETA, (d) 4.0 pph TETA, (e) 5.0 pph TETA and (f) 6.0 pph TETA. Best-fit calculations using the bilinear model are also shown.

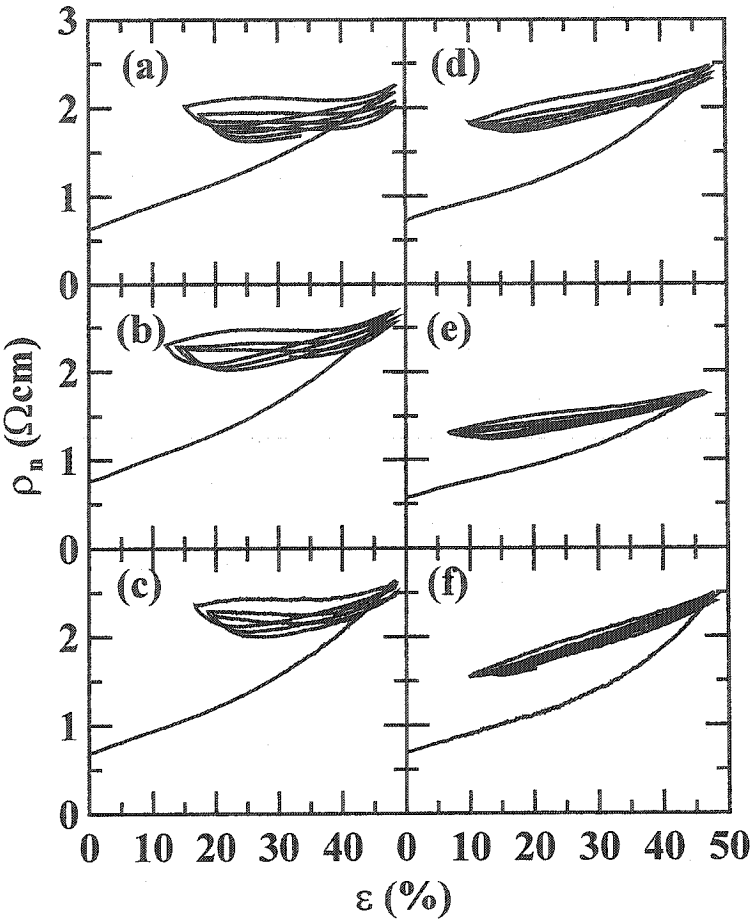

Figure 4.13 Nominal resistivity vs. strain curves showing the effect of TETA on the electrical properties of FC2178 films with 25 pph SS (a) 1.0 pph TETA, (b) 2.0 pph TETA, (c) 3.0 pph TETA, (d) 4.0 pph TETA, (e) 5.0 pph TETA and (f) 6.0 pph TETA.

Table 4.3 Best-fit parameters of the bilinear model to crosslinked FC2178 films containing SS

TETA content (pph)	K_1 (MPa)	K_2 (MPa)	K_{s1} (MPa)	K_{s2} (MPa)	K_{d1} (10^3 MPa·S)	K_{d2} (10^5 MPa·S)	K_{d3} (10^3 MPa·S)
1.0	4.4	5.8	4.5	7.4	4.0	6.8	0.69
2.0	4.6	4.6	5.0	5.4	4.2	1.5	1.5
3.0	4.8	6.4	4.5	5.2	6.2	4.9	1.5
4.0	5.7	5.2	4.8	6.2	8.4	3.2	3.6
5.0	6.6	4.9	4.3	13	7.8	4.4	4.1
6.0	11	8.4	7.0	15	12	1.6	8.7

4.3 Mechanical and electrical characterization of swelled FC2178 and FC2178/SS films

4.3.1 Swelling of TETA-crosslinked FC2178 in EC/DEC (1:2, v/v)

The crosslinked FC2178 polymer samples were immersed in the EC/DEC (1:2, v/v) mixed solvent for 1, 2, and 3 days, respectively. Then the change of weight, which was caused by the uptake of the solvent, was recorded. The ratio of the mass change to the original mass of the polymer sample is defined as the swelling ratio. Figure 4.14 shows the swelling ratio of TETA-crosslinked FC2178 polymer samples as a function of TETA content. The un-crosslinked polymer completely dissolved in the EC/DEC, while the samples with less than 0.5 pph TETA dramatically swelled in the solvent and a gel was formed. Three data sets are shown in Figure 4.14 for 1, 2, and 3 days respectively. Only a small difference was observed among the data sets. Clearly, the swelling ratio of the

samples decreases with the TETA content. Even when 10 pph TETA was added, the sample can still uptake more than 100 wt% solvent (EC/DEC, 1:2v/v).

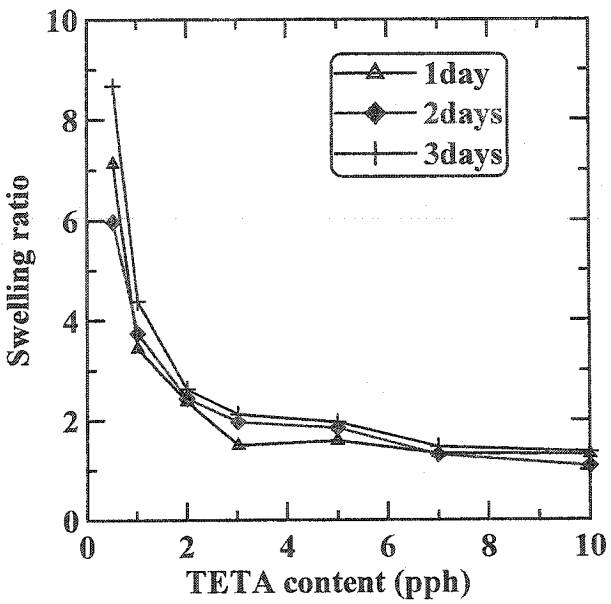

Figure 4.14 Swelling ratio vs. TETA content of TETA-crosslinked FC2178

4.3.2 Mechanical properties of swelled FC2178 samples

Figure 4.15 shows the stress-strain curves of TETA-crosslinked FC2178 films, which were swelled in EC/DEC (1:2, v/v) for 5 minutes before measurement. The stress-strain curves clearly indicate the dimensional change of polymer films during swelling. Even though films were mounted taut between grips, upon immersion in the solvent the resulting expansion (about 80% in length) caused the films to go slack. This is why the stress in Figure 4.15 does not begin to increase until the strain (measured from the dry length) reaches about 80% when the new equilibrium length of the swelled film is reached. It is not surprising to observe large dimensional changes since the samples with

4 and 5 pph TETA can uptake about 150 wt% organic solvent (Figure 3.14). After the new equilibrium point was reached, the stress increased almost linearly with the strain, and both samples broke at about 140% strain.

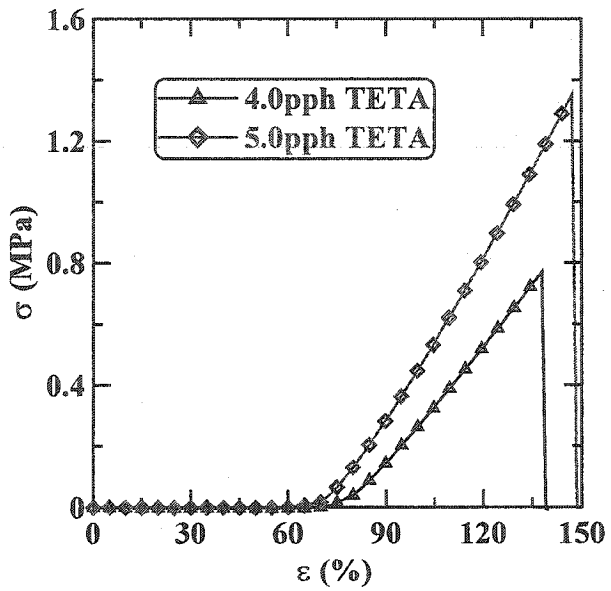

Figure 4.15 Stress vs. strain of TETA-crosslinked FC2178 films swelled in EC/DEC (1:2, v/v)

4.3.3 Mechanical and electrical properties of swelled FC2178/SS samples

In a practical electrode for lithium-ion batteries, Super-S carbon black (SS) can be used as the conductive filler. It is important to study the mechanical and electrical properties of carbon-filled composites during and after swelling in the organic solvent (EC/DEC, 1:2 v/v).

As illustrated in Figure 4.14, TETA-crosslinked polymers can uptake more than 100% liquid solvent and this leads to a large dimensional change in the polymer films.

When the polymer is loaded with conductive fillers, such as Super-S carbon black, the resistivity of composites changes during swelling and can be used as an indicator to study the swelling kinetics of composites in the liquid solvent. Figure 4.16 shows the nominal resistivity vs. swelling time of TETA-crosslinked FC2178 films filled with 25 pph SS. The nominal resistivity increases rapidly and reaches its maximum in 1 minute. The difference of the initial resistivity results from the poor control of the experiment. Generally, the binder film was first immersed in the organic solvent, then the program was started to collect data. The time between these two steps was not rigorously controlled, and is inconsistent among different samples. Hence, the initial resistivity shown in Figure 4.16 is the nominal resistivity immediately after swelling, and is different from sample to sample. After 1 minute, the nominal resistivity remains approximately constant. Therefore, the samples were believed to be completely swelled in the solvent in 5 minutes, and all the samples were pre-swelled in EC/DEC (1:2, v/v) for 5 minutes before the measurement.

Comparing samples with different TETA content, one observes that the TETA content has a dramatic impact on the resistivity of binder films after swelling. When the TETA content increases from 1 pph to 5 pph, the nominal resistivity after swelling decreases from about 300 Ω·cm to about 10 Ω·cm. Therefore, high TETA content is highly desired to maintain good electrical conductivity of binder films.

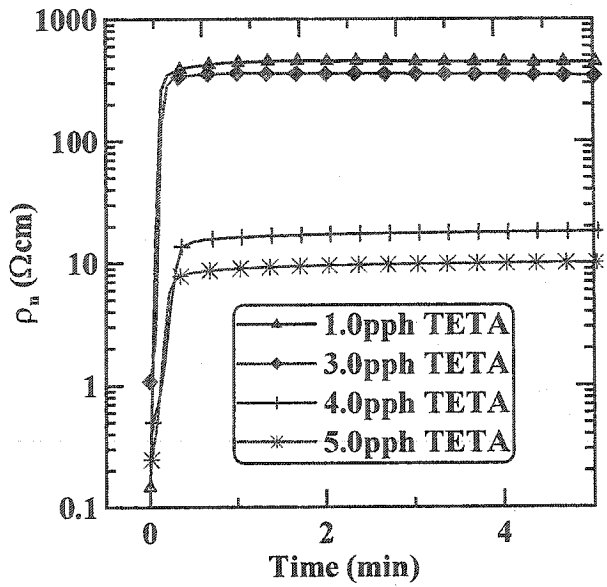

Figure 4.16 Nominal resistivity of TETA-crosslinked FC2178/SS films as a function of swelling time. 25 pph SS was added to the composites.

Figure 4.17a shows stress-strain curves of TETA-crosslinked FC2178 films filled with 25 pph SS. After swelling in EC/DEC, the films expanded by about 25% in the stretching direction. Once the film was taut, the stress increased linearly with the strain. The elastic modulus, or the slope of stress-strain curve, increases with the TETA content. The maximum elongation before break of the swelled films decreases with the TETA content. When 1 pph TETA was used, the film broke at about 200% strain. However, the films with 4 pph or 5 pph TETA could only be stretched to about 100%.

Figure 4.17b shows the nominal resistivity of composites after swelling and during strain. The nominal resistivity of swelled films increases exponentially once the films are taut. It should be pointed out that the plateaus in the nominal resistivity of samples with low TETA content are not real. Since the samples with low TETA content can uptake quite a lot of organic solvent, the resistance of the sample film was as high as 1 MΩ.

Even if a very low current, e.g. 0.5 μA, was used to measure the resistance, the voltage across the sample film can be as high as 5 V, which leads to the electrochemical decomposition of the organic solvent (EC/DEC) on the aluminum grips.

Figures 4.16 and 4.17b show that the nominal resistivity of binder films after swelling dramatically decreases with the TETA content. However, Figure 4.17a suggests that low TETA content is desired to maintain good mechanical properties. Therefore, the content of TETA should be carefully optimized to balance the mechanical and electrical properties.

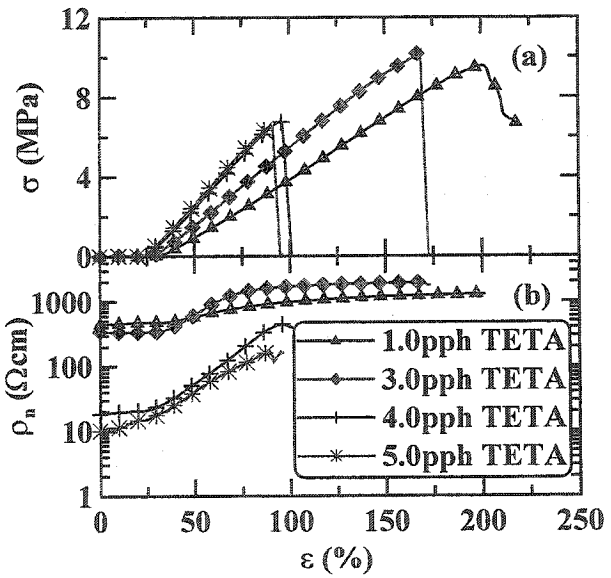

Figure 4.17 (a) Stress-strain and (b) Nominal resistivity-strain curves of TETA-crosslinked FC2178/SS swelled in EC/DEC (1:2 by volume). 25 pph SS was added to the samples.

4.4 Importance of the coupling agent

The poor mechanical behavior of binder/solids composites can also result from a poor interfacial bond between the polymer and the solids. A coupling agent is a bifunctional molecule to enhance the adhesion strength between the polymer and the solids. Silanes are widely used as coupling agents (adhesion promoters), whose –Si-OR groups can react with acidic groups, such as –OH, on the surface of nonmetallic solids. The $-NH_2$ group in TETA is the functional group that reacts with the carbon-carbon double bonds in the backbone of the polymer chain. Combining both ideas, 3-aminopropyltriethoxysilane (APTES) was used as a bifunctional surface coupling agent for FC2178/solids composites.

Figure 4.18 shows the stress-strain and resistivity-strain curves for samples containing 25 pph SS. When the content of APTES is less than 3.0 pph, the film breaks at about 50% strain. If 5.0 pph APTES is added, the film can be extended to 250% without breaking. The nominal resistivity of the binder film increases exponentially with the strain applied and the content of APTES has little or no impact on the resistivity of binder films (see Figure 4.18b).

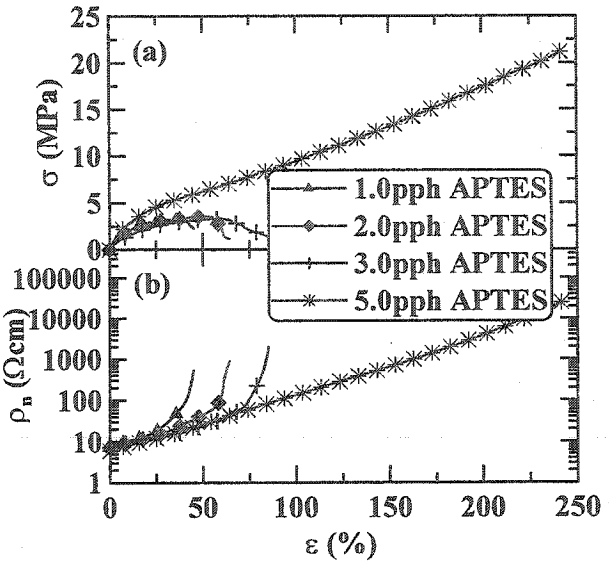

Figure 4.18 (a) Stress vs. strain and (b) nominal resistivity vs. strain of FC2178/SS composites using APTES as the coupling agent. 25 pph SS was added to the samples.

Figure 4.19 shows cyclic stress-strain and nominal resistivity-strain curves for the sample containing 25 pph SS and 5 pph APTES. The modulus of the film is more than 10 MPa, and it rebounds to about 15% strain, which is acceptable. Notice that no crosslinking agent, TETA, was added to this sample. It could probably rebound at a strain less than 15% if TETA was added to suppress the viscoelastic flow of polymer chains. The film also displays very good electrical conductivity with an average resistivity of less than 25 Ω·cm during the cyclic deformation.

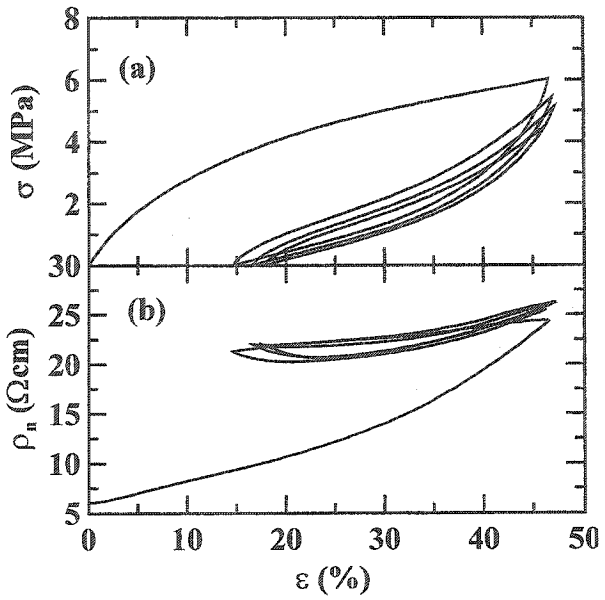

Figure 4.19 (a) Stress vs. strain and (b) nominal resistivity vs. strain of FC2178 composite incorporating 25 pph SS and 5.0 pph APTES

In order to suppress the viscoelastic flow of polymer chains, 5.0 pph TETA was added to the FC2178/SS composite as well as 5.0 pph APTES. Because the polymer matrix was heavily crosslinked, the maximum elongation before break of such a binder film is about 60% (Figure 4.20). Compared to the FC2178/SS sample with 5.0 pph APTES only (Figure 4.19), the sample containing 5.0 pph TETA and 5.0 pph APTES (Figure 4.20) has smaller nominal resistivity. When only 5.0 pph APTES was added, the nominal resistivity of the binder film was about 25 Ω·cm at 45% strain (Figure 4.19). However, if 5.0 pph TETA was added as well, the nominal resistivity was about 10 Ω·cm at 60% strain (Figure 4.20). The improvement of the electrical conductivity is probably associated with the suppression of viscoelastic flow of polymer chains and the suppression of the mechanical degradation of the polymer matrix during deformation. With the addition of 5.0 pph TETA and 5.0 pph APTES, the binder film could be

cyclically deformed to 45% with a small rebound of about 8% (Figure 4.21), which is much smaller than the rebound of the sample without TETA (Figure 4.19). After the first stretching, both stress and nominal resistivity have very good reversibility upon cyclic deformation.

Figure 4.22 shows stress-strain and nominal resistivity-strain curves of a FC2178/SS/TETA/APTES film after swelling in EC/DEC (1:2, v/s) for 5 minutes. Notice that 5.0 pph TETA and 5.0 pph APTES were added. The film expanded about 25% in the stretching direction after swelling. The maximum elongation before break of the binder film is about 100%, which is larger than that of the dry film with the same recipe. This can be explained by the plasticizer-like behavior of the solvent. The composite film was heavily crosslinked and the chain motion was restricted by the bonding introduced. During swelling, the organic solvent interacts with the polymer chains and increases the number of chain configurations that are accessible to the polymer chains. Hence, the swelled composite film had better elasticity than the dry film (Figure 4.20 vs. Figure 4.22).

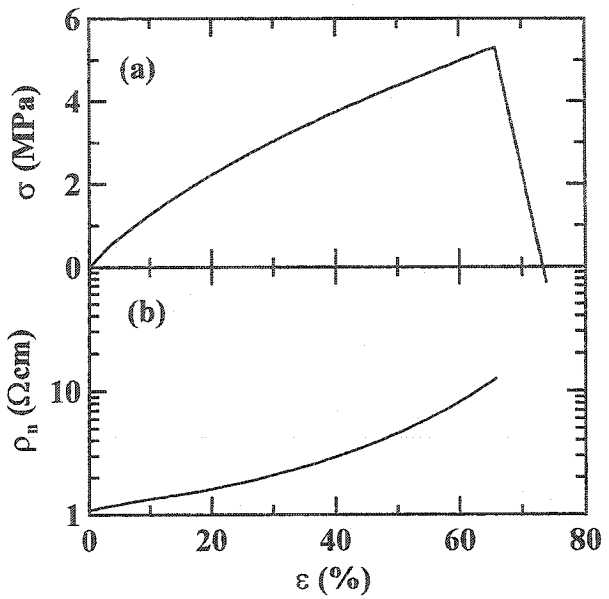

Figure 4.20 (a) Stress vs. strain and (b) nominal resistivity vs. strain of FC2178 composite incorporating 25 pph SS, 5.0 pph APTES, and 5.0 pph TETA

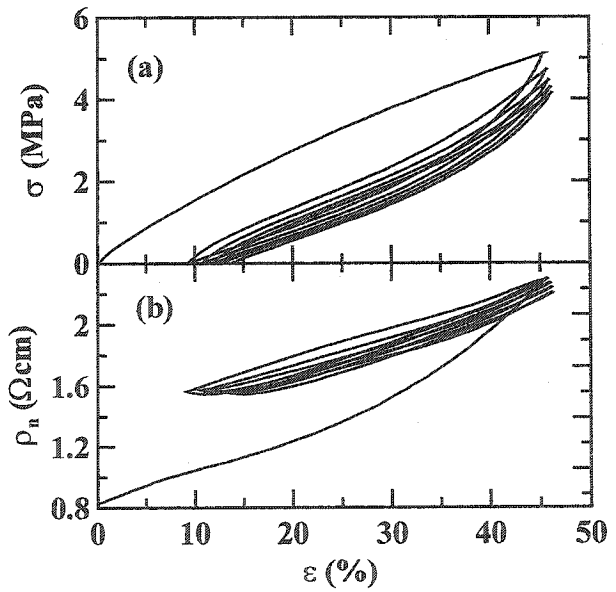

Figure 4.21 (a) Cyclic stress vs. strain and (b) nominal resistivity vs. strain of the FC2178 composite incorporating 25 pph SS, 5.0 pph APTES, and 5.0 pph TETA

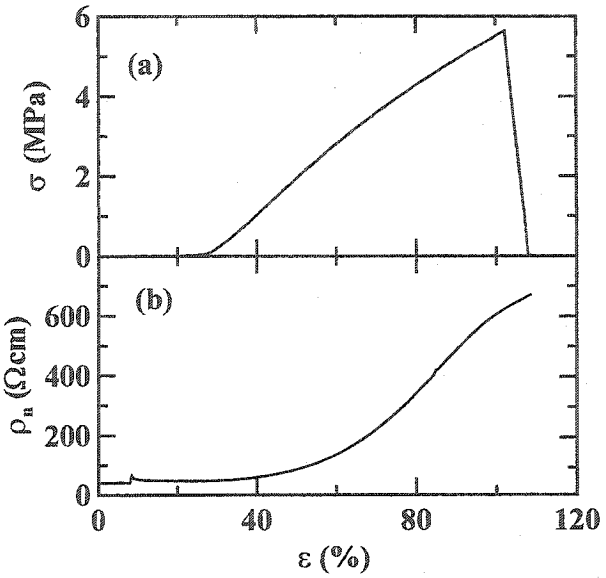

Figure 4.22 (a) Stress vs. strain and (b) nominal resistivity vs. strain of swelled FC2178 composite incorporating 25 pph SS, 5.0 pph APTES, and 5.0 pph TETA

The sample was first swelled in EC/DEC (1:2, v/v) for 5 minutes before measuring in EC/DEC.

4.5 Electrochemical characterization of a-$Si_{0.64}Sn_{0.36}$/Ag electrodes

In the previous sections, the mechanical and electrical properties of binder films without any active material, a-$Si_{0.64}Sn_{0.36}$/Ag, were discussed. However, if the active material is introduced, the working recipe has to be optimized again.

Figure 4.23 shows the capacity vs. cycle number of a-$Si_{0.64}Sn_{0.36}$/Ag electrodes incorporating 2.0 pph (part per hundred ratio of the mass of a-$Si_{0.64}Sn_{0.36}$/Ag) TETA as a function of the APTES content. The cells were made after the electrodes dried in air overnight (no heating). The capacity of the cells decreases quickly with the cycling number. Almost 60% capacity was lost after 100 cycles. However, no big difference was observed among the cells incorporating different amounts of APTES. Figure 4.24

shows that, if the electrodes were heated in an argon flow at 110°C for 24 hours, the capacity retention was greatly improved. This is because the heating step helps to remove the moisture in electrodes and to increase the crosslinking and coupling efficiency at a higher temperature.

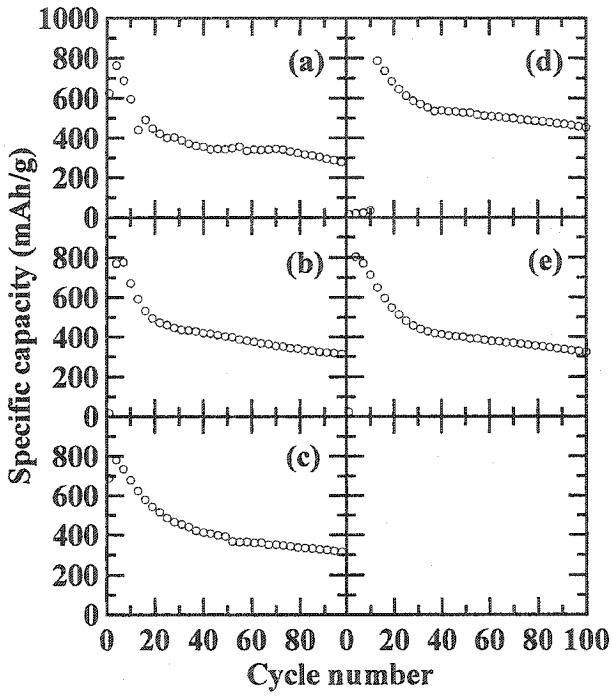

Figure 4.23 Capacity vs. cycle number of a-$Si_{0.64}Sn_{0.36}$/Ag electrodes incorporating 2.0 pph TETA and different amounts of APTES, (a) 1.0 pph, (b) 2.0 pph, (c) 3.0 pph, (d) 4.0 pph, and (e) 5.0 pph.

The cells were made directly after the electrodes dried in air overnight.

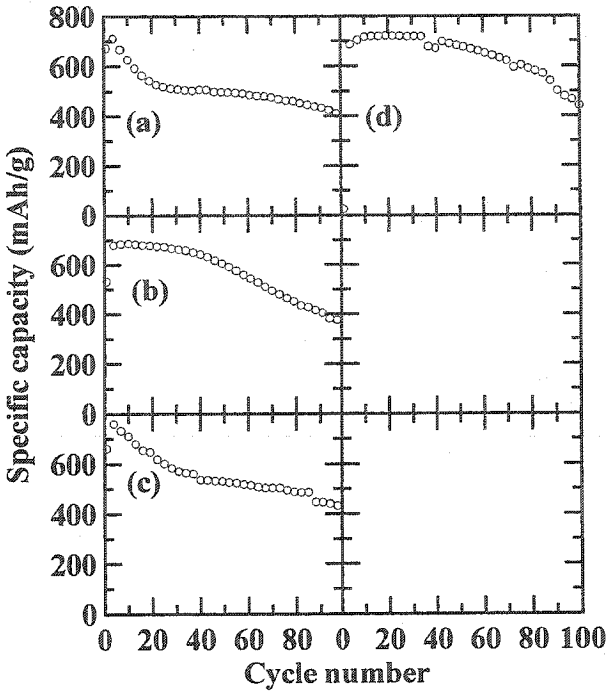

Figure 4.24 Capacity vs. cycle number of thermally treated a-$Si_{0.64}Sn_{0.36}$/Ag electrodes incorporating 2.0 pph TETA and different amounts of APTES, (a) 1.0 pph, (b) 2.0 pph, (c) 3.0 pph, and (d) 4.0 pph.

The electrodes were heated in an argon flow at 110°C for 24 hours before use.

Figure 4.25 shows the capacity vs. cycle number of a-$Si_{0.64}Sn_{0.36}$/Ag electrodes incorporating 4.0 pph APTES as a function of the TETA content. All electrodes were heated in an argon flow at 110°C for 24 hours. The TETA content has a small impact on the capacity retention of electrodes. No consistent trend was obtained. For instance, compared to the cell with 2.0 pph TETA, the cell with 1.0 pph TETA has a smaller capacity for some reason while it has a better capacity retention. In general, the electrode incorporating 2.0 pph TETA and 4.0 pph APTES (see Figure 4.25e) is better than the others since it has a relatively high capacity (about 700 mAh/g) and about 56% of the maximum capacity was maintained after 100 cycles.

An a-$Si_{0.64}Sn_{0.36}$/Ag electrode incorporating PVDF binder was characterized as the control experiment and is shown in Figure 4.26. The maximum capacity of the electrode incorporating PVDF binder was about 790 mAh/g. As shown in Figure 4.25, the cell with 2.0 pph TETA is not the best cell in terms of the capacity retention. However, it is the cell with a capacity (about 730 mAh/g) closest to the control cell (PVDF-based). Hence, the cell incorporating 4.0 pph APTES and 2.0 pph TETA was selected to compare to the PVDF-based cell showing the effect of the binder system. Notice that both cells shown in Figure 4.26 have similar areal density. The capacity retention of a-$Si_{0.64}Sn_{0.36}$/Ag composite electrodes was improved by replacing PVDF with a PVDF-HFP-based binder.

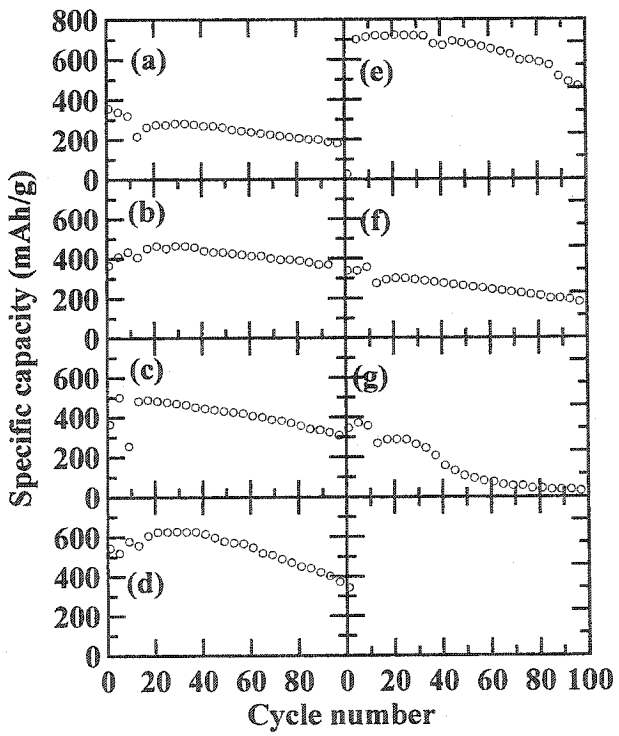

Figure 4.25 Capacity vs. cycle number of a-$Si_{0.64}Sn_{0.36}$/Ag electrodes incorporating 4 pph APTES and different amounts of TETA: (a) 0 pph, (b) 0.5 pph, (c) 1.0 pph, (d) 1.5 pph, (e) 2.0 pph, (f) 2.5 pph, and (g) 3.0 pph

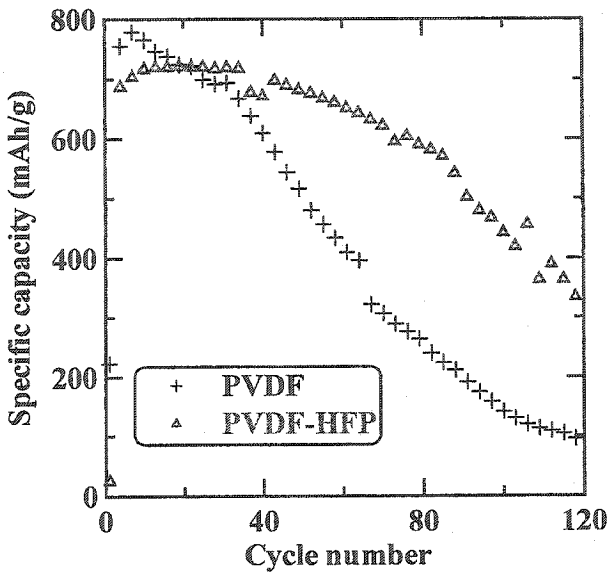

Figure 4.26 Capacity retention of a-$Si_{0.64}Sn_{0.36}$/Ag electrodes incorporating PVDF and PVDF-HFP-based elastomeric binder showing the effect of the binder

4.6 Summary

In order to verify the tether model proposed to understand the capacity fading of amorphous metallic alloy composite electrodes (section 1.4), the mechanical and electrical properties of PVDF-HFP (FC2178)-based binder films were investigated in detail. A crosslinking agent, triethylenetetramine (TETA), was used to suppress the viscoelastic flow of polymer chains and to improve the mechanical properties of the binder, while the coupling agent, 3-aminopropyltriethoxysilane (APTES), was added to improve the adhesion strength between the binder matrix and solid components of composite electrodes. The capacity retention of a-$Si_{0.64}Sn_{0.36}$/Ag composite electrode was improved by replacing PVDF with a PVDF-HFP-based elastomeric binder.

Even when the polymer (FC2178) was highly crosslinked, it still uptook more than 100 wt% organic solvent (EC/DEC, 1:2, v/v) and became brittle after swelling. The high

swelling ratio leads to a large dimensional change of the binder films and a high resistivity after swelling. Hence, a high crosslinking degree is required to minimize the swelling ratio of binders in EC/DEC and to decrease the resistivity of binders after swelling. However, high crosslinking degree decreases the elasticity of binder films.

According to results shown in this chapter, an elastomer that can only uptake a controlled amount of the organic solvent is desired. However, the selection of the next elastomer should also be subject to the requirement of an acceptable ionic conductivity in the presence of the organic solvent.

Chapter 5 Effect of the Molecular Weight of PVDF-HFP

5.1 Introduction

In chapter 4, we demonstrated that the capacity retention of a-$Si_{0.64}Sn_{0.36}$/Ag composite electrodes was slightly improved by replacing PVDF-based binder with a PVDF-HFP-based elastomeric binder system. We currently have four different PVDF-HFP copolymers (FC2211, FC2230, FC2261Q, and FC2178) with different molecular weights, which can be used to study the impact of polymer molecular weight on the electrochemical behavior of a-$Si_{0.64}Sn_{0.36}$/Ag composite electrodes. Their chemical compositions are identical, but their molecular weights increase in the same order (from FC2211 to FC2178).

5.2 Comparison of dry binder films

Figure 5.1 shows stress-strain curves of TETA-crosslinked PVDF-HFP films with 4.0 pph TETA. All the films can be extended to 250% strain before breaking. The molecular weight of the polymer affects the strength of the TETA-crosslinked PVDF-HFP films. The Young's modulus of the films increases with the molecular weight of the polymer.

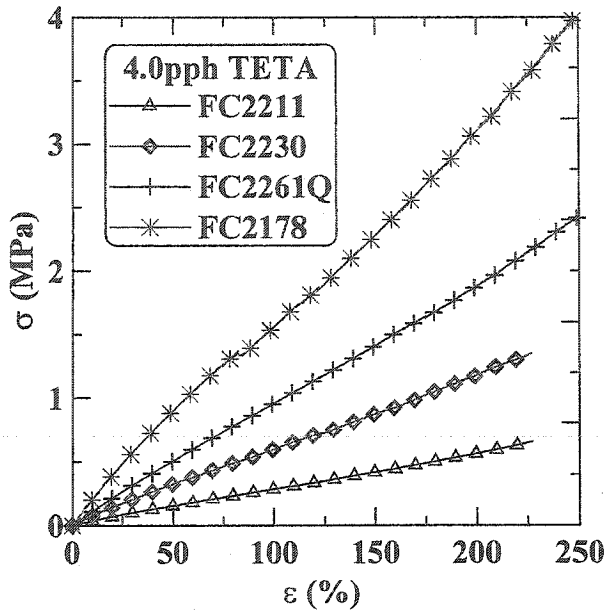

Figure 5.1 Stress vs. strain curves of TETA-crosslinked PVDF-HFP films of different molecular weights

Figure 5.2 shows cyclic stress-strain curves of TETA-crosslinked PVDF-HFP films deformed up to 50% strain showing the impact of the molecular weight. The experimental data were also fitted with the linear model (see Figure 3.19). A summary of the mechanical properties of the polymer films and best-fit parameters are listed in Table 5.1. Apparently, the Young's modulus, the maximum stress at 50% strain, the spring constants (K_1 in the linear model), and the viscosity of the dashpot (K_{d2} in the linear model) increase with the molecular weight of the polymer, while the rebound point decreases with the molecular weight. These differences can be attributed to the difference in the length of the polymer chains. Although the chemical compositions of the four polymers (FC2211, FC2230, FC2261Q, and FC2178) are the same, a long polymer chain in a high molecular weight polymer (i.e. FC2178) has a greater likelihood to be physically entangled with other polymer chains. Hence, the number of network

defects, loose loops or free ends, in the crosslinked polymer system decreases as the length of the polymer chains increases. Therefore, we expect more effective crosslinks in a higher molecular weight polymer, presuming the same amount of TETA was used.

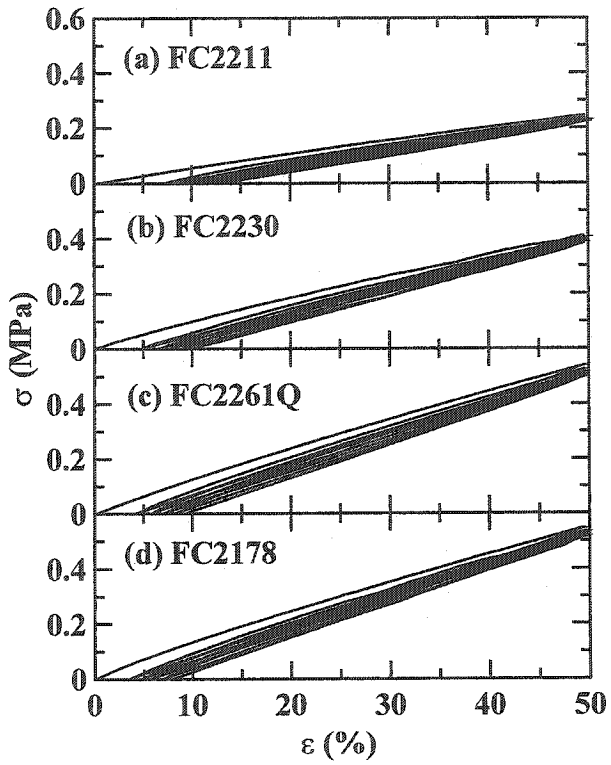

Figure 5.2 Stress-strain curves of (a) FC2211, (b) FC2230, (c) FC2261Q, and (d) FC2178 crosslinked with 4 pph TETA

Figure 5.3a shows stress-strain curves of PVDF-HFP composites containing 25 pph SS and 4.0 pph TETA. The sample prepared from FC2178 broke at about 200% strain, while the others could be extended to 250% without breaking. Figure 5.3b shows nominal resistivity-strain curves of the composites. These curves approximately overlap each other. The molecular weight of the polymer has no or little impact on the resistivity of the composites.

Table 5.1 A comparison of PVDF-HFP samples crosslinked with 4 pph TETA

Polymer	Mechanical properties			Best-fit parameters of the linear model			
	E (MPa)	σ_{max} (MPa)	Rebound (%)	K_1 (MPa)	K_2 (MPa)	K_{d1} (10^4Mpa S)	K_{d2} (10^6MPa S)
FC2211	0.54	0.25	7.2	0.45	0.15	1.6	3.9
FC2230	0.98	0.41	4.7	0.79	0.17	2.0	9.5
FC2261Q	1.33	0.54	4.2	1.03	0.18	3.4	15.6
FC2178	1.34	0.55	3.4	1.08	0.16	1.9	18.2

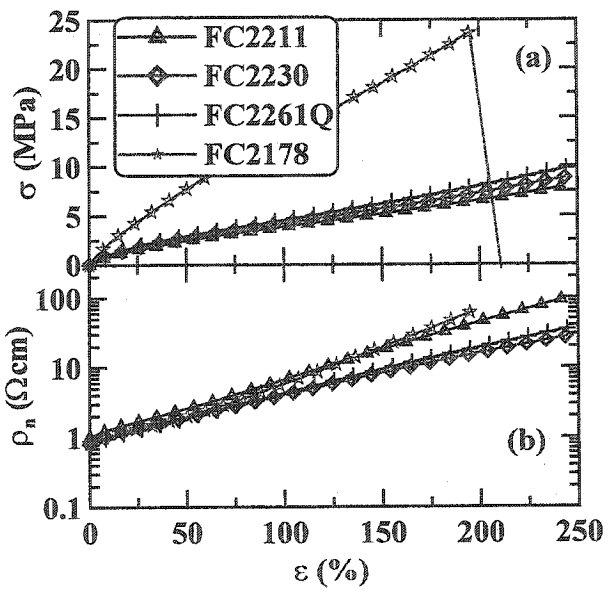

Figure 5.3 (a) Stress vs. strain, and (b) nominal resistivity vs. strain of TETA-crosslinked PVDF-HFP/SS films containing 4.0 pph TETA and 25 pph SS

Figure 5.4 shows cyclic stress-strain and nominal resistivity-strain curves of PVDF-HFP/SS composites containing 25 pph SS and 4.0 pph TETA. The cyclic stress-strain curves of the binder films show the impact of polymer molecular weight. The binder film prepared from FC2211 (low molecular weight) doesn't show clear bilinear behavior,

which was discussed in section 4.2.5 of this thesis, in its stress-strain curve (Figure 5.4a). However, bilinear behavior is clearly observed in the stress-strain curve of the FC2178-based binder film (Figure 5.4d). A nice transition from the linear behavior (FC2211) to bilinear behavior (FC2178) can be seen in Figure 5.4. Moreover, the rebound point also decreases with the molecular weight of the polymers. The FC2178-based binder film rebounded to 10% strain when the stress was removed.

The different behavior of the samples using different polymers can be explained by the decreasing number of network defects with increasing polymer molecular weight, which means that the FC2211-based sample had more network defects and less effective crosslinks. Therefore, the FC2211-based film (see Figure 5.4a) was weaker than the FC2178-based film (see Figure 5.4d). If the FC2211-based film was deformed beyond 50% strain, a larger stress would result and induce the rotation of SS strands (the bilinear behavior). In order to verify this point, an FC2211-based film was cyclically deformed to 100% strain. The stress-strain and nominal resistivity-strain curves of this film are shown in Figure 5.5. When the film was extended to 100% strain, the stress was about 4.3 MPa, which is equivalent to the maximum stress of the sample shown in Figure 5.4d. This suggests that a force is needed to rotate an SS strand in a viscous matrix (crosslinked polymer), and the rotation of the SS strands is negligible when the stress is small. The bilinear behavior clearly appears when the stress is large enough, for instance, 4.0 MPa. Therefore, it is reasonable to see linear behavior when the strain is small or when the film is weak.

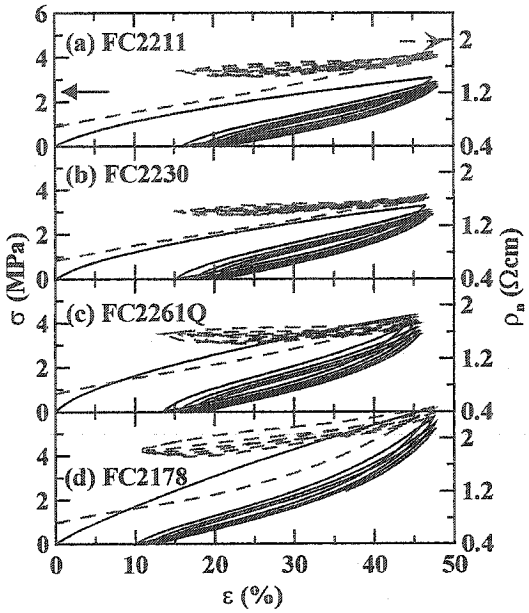

Figure 5.4 Stress vs. strain and nominal resistivity vs. strain curves of TETA-crosslinked PVDF-HFP/SS films under cyclic deformation. 4.0 pph TETA and 25 pph SS were added to each sample.

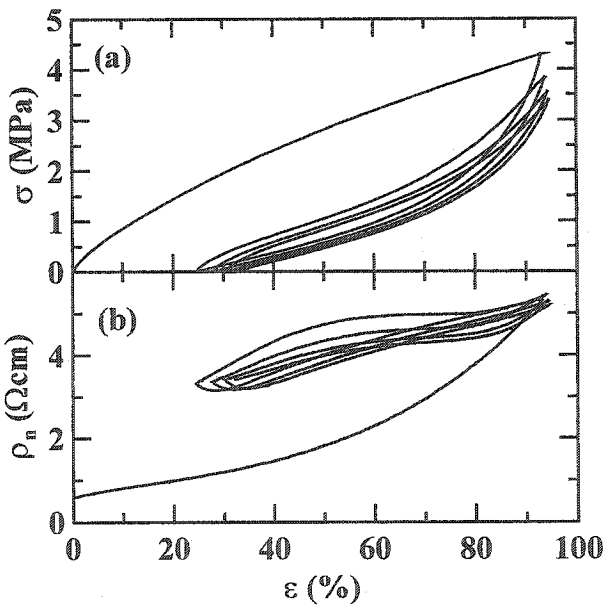

Figure 5.5 (a) Stress-strain and (b) nominal resistivity-strain curves of FC2211/SS film cyclically deformed to 100% strain. 4.0 pph TETA and 25 pph SS were added

5.3 Comparison of swelled binder films

Figure 5.6 shows the swelling ratios (by mass) of TETA-crosslinked PVDF-HFP samples in EC/DEC (1:2, v/v). The swelling ratio decreases with increasing TETA content. Generally, the swelling ratio of a high molecular weight polymer is smaller than that of a low molecular weight polymer with the same TETA content. FC2211 samples crosslinked with less than 3 pph TETA dissolved in EC/DEC (1:2, v/v). Even when the FC2211-based sample was heavily crosslinked with 10 pph TETA, the sample uptook more than 150 wt% EC/DEC (1:2, v/v). The swelling ratios of FC2230, FC2261Q, and FC2178 were almost the same when more than 5 pph TETA was added.

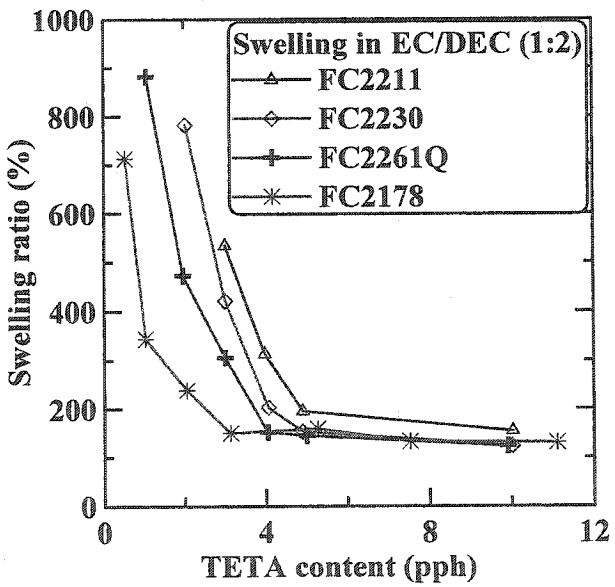

Figure 5.6 Swelling ratios of TETA-crosslinked PVDF-HFP samples

Swelling experiments of TETA-crosslinked FC2178/SS composites, which contained 25 pph SS, were also carried out to study the impact of incorporated SS. When less than 3 pph TETA was added, the composites dissolved in EC/DEC (1:2, v/v),

presumably because the incorporated SS decreased the number of effective crosslinks and hence weakened the interaction between polymer chains. The swelling ratios of samples with 3 pph, 4 pph, and 5 pph TETA were 144.5%, 91.1%, and 85.0%, respectively. On the other hand, the samples without SS can uptake more than 100% EC/DEC (1:2, v/v) (see Figure 5.6).

Figure 5.7 shows stress-strain curves of TETA-crosslinked PVDF-HFP films (4.0 pph TETA) swelled in EC/DEC (1:2, v/v) for 5 minutes before measurements were taken. As shown in Figure 5.5, the polymer crosslinked with 4.0 pph TETA can uptake more than 100 wt% EC/DEC (1:2, v/v). It is not surprising to see that all the samples have a very large expansion in the stretching direction. The FC2211-based sample expanded by 100% in the stretching direction while the others expanded by about 80%. The FC2261Q film crosslinked with 4.0 pph TETA has the largest breaking strain (~220%). This is surprising to us, but repeatable. Molecular weight distribution data might be useful to understand this surprising result.

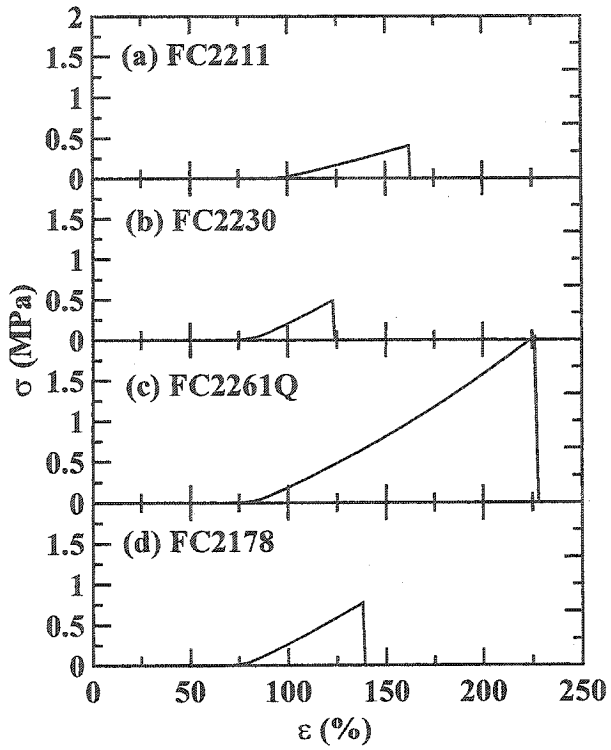

Figure 5.7 Stress-strain curves of swelled PVDF-HFP films. All samples were crosslinked with 4.0 pph TETA.

Figure 5.8a shows stress-strain curves of PVDF-HFP/SS composite films containing 25 pph SS and 4.0 pph TETA after swelling in EC/DEC (1:2, v/v). All the films broke at about 100% strain, and only small differences were observed between the samples. After swelling in EC/DEC (1:2, v/v), the FC2178/SS film expanded by 25% in the stretching direction, while the other films expanded by about 30%. Meanwhile, the samples without SS expanded by more than 80% after swelling (see Figure 5.6). This can be associated with the interaction between SS particles and polymer chains since SS is a high structure material. Compared to the polymer matrix, SS is a stiff material and will not expand after swelling in EC/DEC (1:2, v/v). Therefore, the interaction between SS and the polymer

matrix can suppress the volumetric expansion during swelling. Less solvent can be uptaken after complete swelling just as was discussed in the swelling experiment.

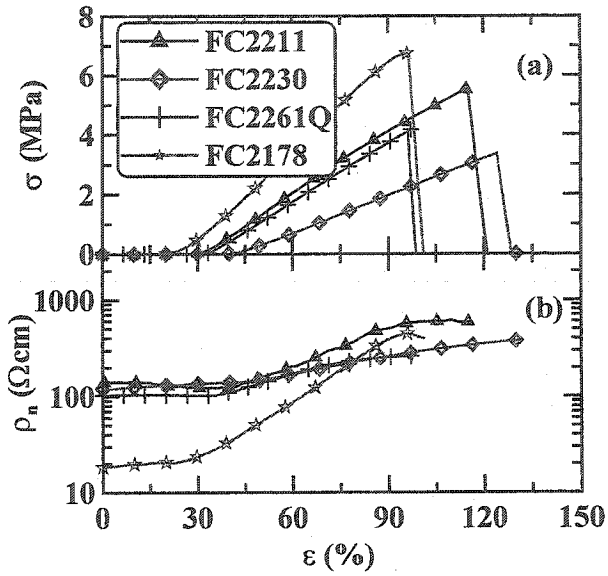

Figure 5.8 (a) Stress vs. strain, and (b) nominal resistivity vs. strain of swelled PVDF-HFP/SS films containing 4.0 pph TETA and 25 pph SS

Figure 5.8b shows nominal resistivity-strain curves of the composite films after swelling in EC/DEC (1:2, v/v). The FC2178/SS film differed from the others. After complete swelling in EC/DEC (1:2, v/v), the resistivity of FC2178/SS film started from a small value (~20 Ω·cm), and increased exponentially during stretching. Generally, the nominal resistivity of FC2178/SS film is about 1/5 of the nominal resistivity of other films under the same condition (the SS content, the TETA content, and the strain). This result suggests that the FC2178-based binder system might be more promising than the others to improve the capacity retention of high-volume-change metallic alloy composite electrodes.

5.4 Electrochemical characterization

Figure 5.9 shows the cell potential versus specific capacity curves of a-$Si_{0.64}Sn_{0.36}$/Ag electrodes incorporating the different PVDF-HFP binder systems. The cell incorporating the FC2178-based binder (shown in Figure 5.9d) was first discharged to 0.22 V and then cycled between 0.2 V and 1.0 V with a constant current of 160 mA/g. Because of the high impedance surface layer on the lithium foil counter electrode, two activation cycles were needed before the cell can cycle properly as expected. In order to minimize the impact of the initial cell impedance, the other cells (shown in Figures 5.9a, 5.9b, and 5.9c) were first discharged for 3.5 hours and then cycled between 0.2 V and 1.0 V with a constant current of 160 mA/g.

Figure 5.10 shows the specific capacity versus cycle number for the cells, whose potential-capacity curves were shown in Figure 5.9. For some reason(s), the cells using FC2230 and FC2261Q have a smaller capacity, which means a smaller particle expansion ratio. Meanwhile, the cells using FC2211 and FC2178 have a relatively large capacity (~750 mAh/g), which means a large particle expansion ratio. A more reliable way is to compare cells with the same maximum capacity to minimize the impact of particle expansion ratio. Figure 5.10 suggests that FC2178 might be better than the other polymers. However, more reliable data needs to be collected to show the impact of the polymer molecular weight.

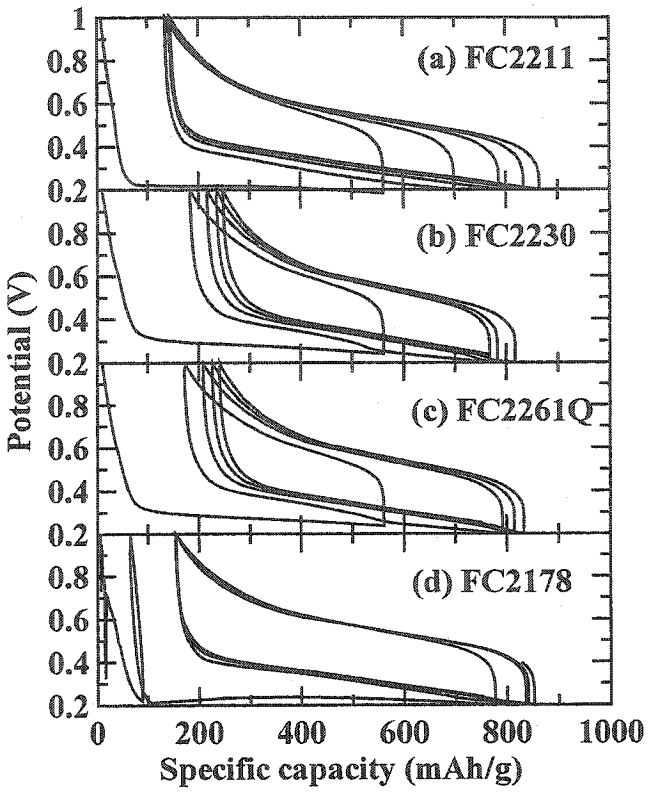

Figure 5.9 Voltage curves of a-$Si_{0.64}Sn_{0.36}$/Ag electrodes using different polymers

Recipe: 100 pph a-$Si_{0.64}Sn_{0.36}$/Ag + 20 pph SS + 10 pph PVDF-HFP + 2 pph TETA + 4 pph APTES

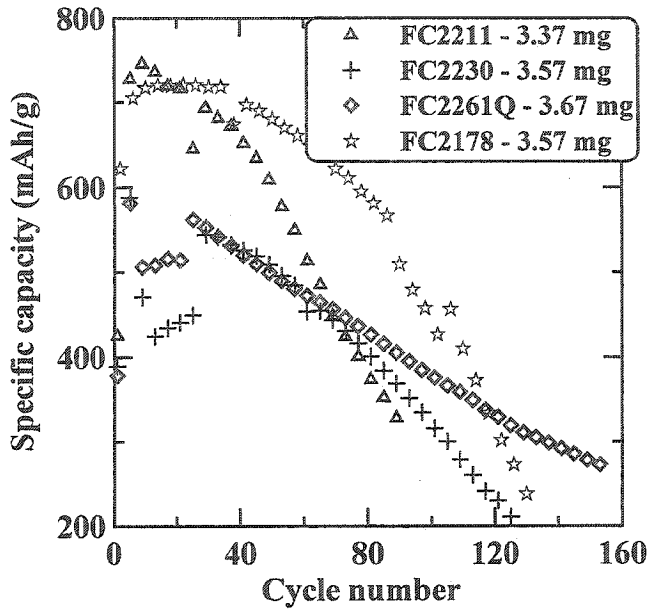

Figure 5.10 Specific capacity vs. cycle number of a-$Si_{0.64}Sn_{0.36}$/Ag electrodes using PVDF-HFP-based binders. The mass of a-$Si_{0.64}Sn_{0.36}$/Ag in each electrode is indicated in the legend. The voltage curves are shown in Figure 5.9.

5.5 Summary

In order to understand the impact of the polymer molecular weight on the cycling performance of high-volume-change metallic alloy composite electrodes, a series of PVDF-HFP copolymers with different molecular weight were studied. The polymers studied were FC2211, FC2230, FC2261Q, and FC2178. The molecular weight increases from FC2211 to FC2178.

It was demonstrated that the polymer molecular weight had an impact on the mechanical and electrical properties, and swelling behavior of crosslinked PVDF-HFP and its SS-filled composites. The mechanical and electrical characterization suggests that the number network defects of crosslinked polymer network decrease with increasing

polymer chain length. The unexpected large breaking strain of TETA-crosslinked FC2261Q after swelling implies that the molecular weight distribution range might be also important as well.

The electrochemical characterization of a-$Si_{0.64}Sn_{0.36}$/Ag composite electrodes showed that all the polymers could function as binders. However, the cycling data of the cells using different polymers (different molecular weight) are far from being conclusive. More reliable data needs to be collected for all the systems and this should be the focus of future work.

Chapter 6 PVDF-TFE-P-based Elastomeric Binder System

6.1 Introduction

Chapters 4 and 5 discussed the potential application of the PVDF-HFP-based elastomeric binder system to improve the capacity retention of a-$Si_{0.64}Sn_{0.36}$/Ag composite electrodes. However, fluorinated polymers, including poly(vinylidene fluoride-hexafluoropropylene) (PVDF-HFP), can sometimes be readily swollen, gelled or dissolved by non-aqueous liquid electrolytes used in lithium-ion batteries [71-73]. Swelling or dissolution can cause deterioration in the adhesion of electrode materials to the current collector. Although the swelling of PVDF-HFP in non-aqueous solvents (e.g. EC/DEC, 1:2, v/v) can be controlled to some degree by introducing crosslinking, more than 100 wt% organic solvent can still be absorbed by highly crosslinked PVDF-HFP samples (up to 10 pph TETA). However, over-crosslinking greatly deteriorates the elasticity of PVDF-HFP films, and the maximum elongation of the film decreases with the TETA content (if overcrosslinked). Hence, a compromise between the swelling and the elasticity of PVDF-HFP-based binder systems is needed to maximum the performance in lithium-ion batteries incorporating amorphous metallic alloys.

Fluorinated polymers can absorb a relatively large amount of non-aqueous electrolyte because of highly polar bonds (C-F). On the other hand, polypropylene absorbs none because both C-H bonds and C-C bonds are non-polar or slightly polar and the solvents are polar. Additions of propylene to the fluoroelastomer should reduce swelling during exposure to non-aqueous electrolytes. Therefore, a commercially

available terpolymer, poly(vinylidene fluoride-tetrafluoroethylene-propylene) (PVDF-TFE-P, BRE-7131X) was chosen for careful evaluation.

6.2 Mechanical and electrical study of PVDF-TFE-P and PVDF-TFE-P/SS films

6.2.1 Effect of chemical additives

The polymer studied, PVDF-TFE-P, contained some bisphenol as supplied. Bisphenol is a crosslinker for fluorinated elastomers. As recommended by the supplier, the polymer can be crosslinked by heating with additions of CaO and MgO. The reaction mechanisms can be summarized as follows. A base such as MgO or CaO dehydrofluorinates the fluoroelastomer backbone as shown by equations 6-1 and 6-2. The VDF unit reacts with the base to form an active site, unsaturated -CH=CF-. After that, a bifunctional molecule, such as bisphenol, is added to the backbone to provide crosslinking (equation 6-3).

$$-CH_2-CF_2- + \tfrac{1}{2}\,MgO \rightarrow -CH=CF- + \tfrac{1}{2}MgF_2 + \tfrac{1}{2}\,H_2O \qquad (6\text{-}1)$$

$$-CH_2-CF_2- + \tfrac{1}{2}\,CaO \rightarrow -CH=CF- + \tfrac{1}{2}CaF_2 + \tfrac{1}{2}\,H_2O \qquad (6\text{-}2)$$

$$-CH=CF- + HO-C_6H_4-R-C_6H_4-OH \rightarrow -CH_2-CF(-O-C_6H_4-R-C_6H_4-OH)- \qquad (6\text{-}3)$$

Figure 6.1 shows the stress-strain curves of bisphenol-crosslinked PVDF-TFE-P films that were prepared with different contents of MgO and CaO. These films were all heat-treated at 110°C for 24 hours. The experimental curves were also fitted with the linear model. The best fit parameters for the spring constants K_1 and K_2 and the dashpot viscosities, K_{d1} and K_{d2} are listed in Table 6.1. Only small differences between the

samples heated with only MgO, only CaO and with both can be seen from both Figure 6.1 and the fitted parameters in Table 6.1.

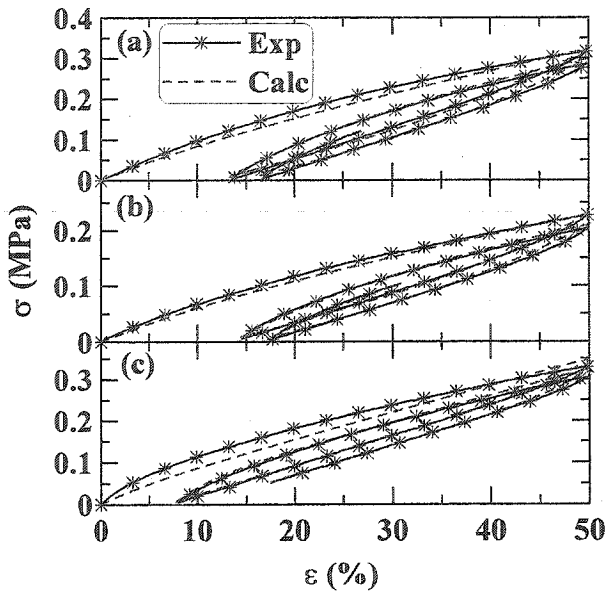

Figure 6.1 Stress-strain curves of cured PVDF-TFE-P (110°C for 24 hours) showing the effect of the additives MgO and CaO (a) 6 pph MgO and 2 pph CaO; (b) 8 pph MgO; (c) 8 pph CaO. The data are the symbols and the solid lines are calculated stress-strain behavior using the linear model and the parameters in Table 6.1.

The sample with 8 pph CaO (Figure 6.1c) has slightly better mechanical properties than the other samples. It has the largest spring constant, K_1, the largest dashpot viscosity, K_{d2} and rebounds closest to its original length when the stress is removed. Hence, CaO was chosen as the inorganic base for the new crosslinking recipe with TETA. However, the degree of crosslinking needs to be improved because the values of K_1 and K_{d2} are still quite small. Although the sample with the manufacturer's recommended ratio of 2 pph CaO and 6 pph MgO was not the best one, films made using

the recommended recipe were used for comparison to the TETA-crosslinked films hereafter.

Table 6.1 Best-fit parameters of the linear model to the data shown in Figures 6.1 and 6.2

		K_1 (MPa)	K_2 (MPa)	$K_{d1}(10^2$MPa S)	$K_{d2}(10^4$MPa S)
Heating (Figure 6.1)	(a)	0.59	0.39	2.9	2.1
	(b)	0.42	0.28	2.2	1.3
	(c)	0.69	0.51	1.2	2.6
TETA (Figure 6.2)	(a)	1.23	0.28	2.4	9.8
	(b)	0.33	0.36	3.1	1.0
	(c)	0.54	0.28	2.6	3.4

The amount of crosslinking can be increased by two methods. Both MgO and CaO have dual roles in the reactions, they both act as a base to dehydrofluorinate the backbone and as a reagent to consume the byproduct, HF. Since an organic solvent, MEK, was used to dissolve the polymer, a strong organic base, such as DABCO, will enhance the basic environment and produce more unsaturated active sites in the backbone of polymer chains. In addition, the content of the crosslinker, bisphenol, is set by the amount added by the manufacturer to the initial as-received polymer. Another crosslinking agent, TETA, can be added to increase the density of crosslinks. The crosslinking reaction involving TETA is given by equation 6-4, where the group R is $-C_2H_4-NH-C_2H_4-NH-C_2H_4-$.

$$-CH=CF- + NH_2-R-NH_2 \rightarrow -CH_2-CF(-NH-R-NH_2)- \qquad (6\text{-}4)$$

Figure 6.2 shows the cyclic stress-strain curves of TETA (5 pph) crosslinked PVDF-TFE-P with different additives. Figure 6.2a shows results for a film cast with TETA, DABCO and CaO. Figures 6.2b and 6.2c show the results for a film cast with TETA and DABCO (Figure 6.2b) and for a film cast with TETA and CaO (Figure 6.2c). The results in Figure 6.2 show that the film is much stiffer, but still very elastic, when both DABCO and CaO are used. Both a strong organic base, like DABCO, and an inorganic compound, i.e. CaO, to consume the HF produced, must be included to achieve good mechanical properties.

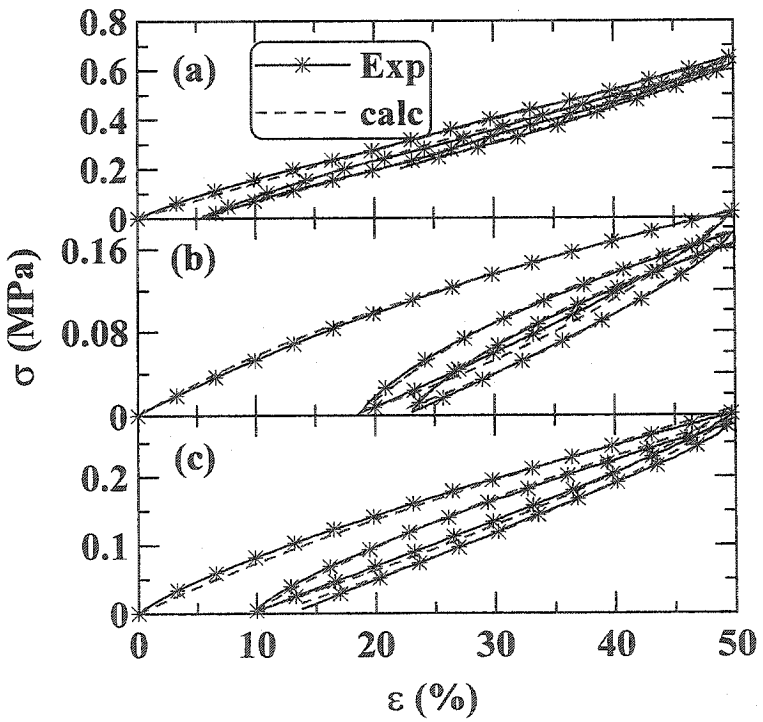

Figure 6.2 Stress-strain curves of TETA-crosslinked PVDF-TFE-P showing the effect of DABCO and CaO (a) 5 pph TETA + 3 pph DABCO + 4 pph CaO; (b) 5 pph TETA + 5 pph DABCO; (c) 5 pph TETA + 5 pph CaO. The data are the symbols and the solid lines are calculated stress-strain behavior using the linear model and the parameters in Table 6.1.

The linear model was used to fit the stress-strain curves in Figure 6.2, and the best-fit parameters are listed in table 6.1. Compared to films crosslinked by the heating recipe (shown in Figure 6.1 and Table 6.1), both K_1 and K_{d2} increased significantly for the film crosslinked with TETA, DABCO and CaO (Figure 6.2a). K_1 increased from 0.59 MPa to 1.23 MPa, and K_{d2} increased from 2.1 MPa·S to 9.8 MPa·S. The sample described by Figure 6.2a rebounds to 1.06 times its original length when the stress is removed, significantly better than the samples prepared by the heating recipe.

6.2.2 Mechanical properties of crosslinked PVDF-TFE-P films

Figure 6.3 shows stress-strain curves for the bisphenol-crosslinked PVDF-TFE-P films as a function of heat treatment conditions. The strength of the polymer film increases with the heating time at 110°C, presumably due to an increased density of crosslinks. As expected, the crosslinking reaction is faster at higher temperature (180°C). The sample cured at 110°C for 24 hours has almost the same mechanical properties as the sample cured at 180°C for 3 hours. In order to avoid possible crystallization of the active material, a-$Si_{0.64}Sn_{0.36}$, a lower temperature (110°C) was adopted for the heating recipe in experiments to be described below.

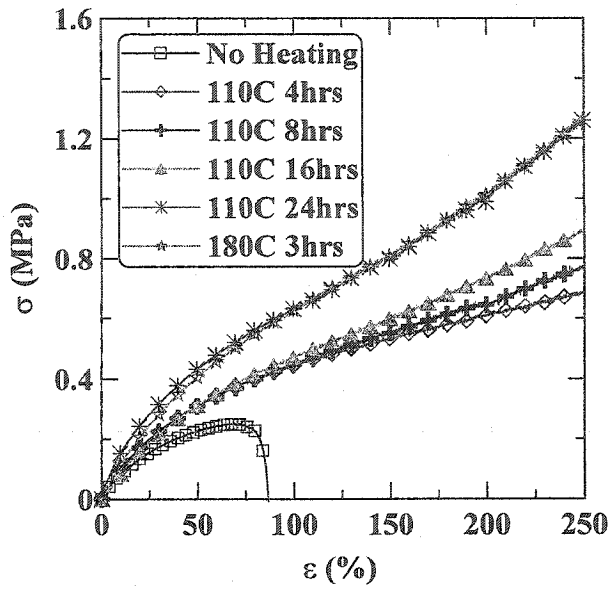

Figure 6.3 Stress-strain curves of cured PVDF-TFE-P (curing conditions listed in the inset) with strains up to 250%

In Figure 6.3 the slope of stress-strain curves of bisphenol-crosslinked samples decreases as the strain nears 50% strain. The decrease of the slope is caused by the viscoelastic flow of polymer chains in the un-crosslinked or lightly crosslinked samples. For the un-crosslinked sample, the viscoelastic flow is so significant that eventually the film breaks at about 80% strain. In the high strain region, the slope of the stress-strain curve increases with strain. This phenomenon is called non-Gaussian behavior, which can be described by the theory of James and Guth [41]. However, this theory does not fit the data in Figure 6.3 because of the obvious viscous flow.

Figure 6.4 shows the stress-strain curves of TETA-crosslinked PVDF-TFE-P films. Both viscoelastic flow and non-Gaussian behavior can be seen in the curves. By simply comparing the scale of the vertical axis in Figures 6.3 and 6.4, one can easily see that the samples prepared using the TETA recipe are more crosslinked than the samples prepared

by the heating recipe. When 4 pph or 5 pph TETA was added, the viscoelastic flow was almost eliminated by the crosslinks. Hence, these two samples can be fitted with equations 6-5 and 6-6 derived by Guth and James [41] and discussed by Ward (equation 3.27 in ref. [39]);

$$f = \frac{NkT}{3} n^{1/2} \left(L^{-1}\left(\frac{\lambda}{n^{1/2}}\right) - \lambda^{-3/2} L^{-1}\left(\frac{1}{\lambda^{1/2} n^{1/2}}\right) \right) \tag{6-5}$$

$$\sigma = f * \lambda \tag{6-6}$$

where f is the nominal stress, σ is the true stress, N is the number of freely jointed chains per unit volume, n is the number of chain links between successive cross-links, λ is the elongation ratio and $L^{-1}()$ is the inverse Langevin function.

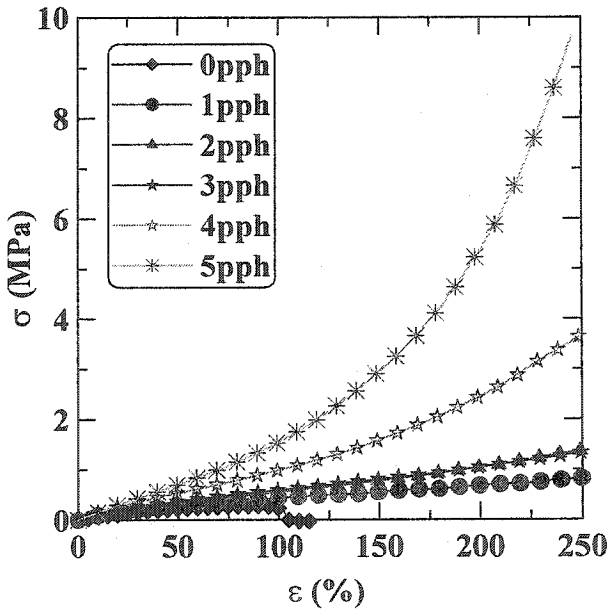

Figure 6.4 Stress-strain curves of TETA-crosslinked PVDF-TFE-P with strains up to 250%. The amount of TETA added to each sample is indicated in the legend.

Figure 6.5 shows that equations 6-5 and 6-6 can fit the experiments well for a suitable choice of parameters, listed in Table 6.2. The fitted parameters clearly indicate

the impact of TETA on the degree of crosslinking. That is, N increases and n decreases with TETA content, as expected.

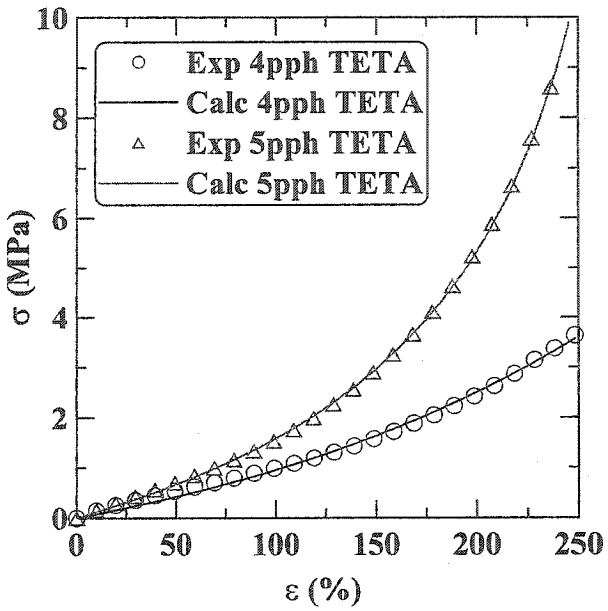

Figure 6.5 Fitting stress-strain curves of TETA-crosslinked PVDF-TFE-P. The solid lines are calculations using equations 6-5 and 6-6 with the parameters listed in Table 6.2.

Table 6.2 Best-fit parameters of equations 6-5 and 6-6 to the data in Figure 6.5 for the highly crosslinked PVDF-TFE-P films.

TETA content (pph)	νkT (MPa)	n	χ^2
4	0.086	57	3.77
5	0.126	18	1.11

Figures 6.6 and 6.7 show the stress-strain curves of bisphenol and TETA-crosslinked PVDF-TFE-P films, respectively, under cyclic deformation to 50% strain. Both figures

show that the mechanical properties are improved by increasing the degree of crosslinking. The stiffness of the polymer film increases as the crosslinking increases. As the degree of crosslinking increases, the film rebounds closer to its original length when the stress is removed. However, the TETA-crosslinked films have much better mechanical properties than the films crosslinked with the heating recipe. When 5 pph TETA was added, the stress at 50% strain was 0.66 MPa, and the film rebounded to 5% strain when the stress was removed. For the bisphenol-crosslinked sample (heated for 24 hours at 110°C), the stress at 50% strain was only about 0.32 MPa and the film rebounded to 12% strain.

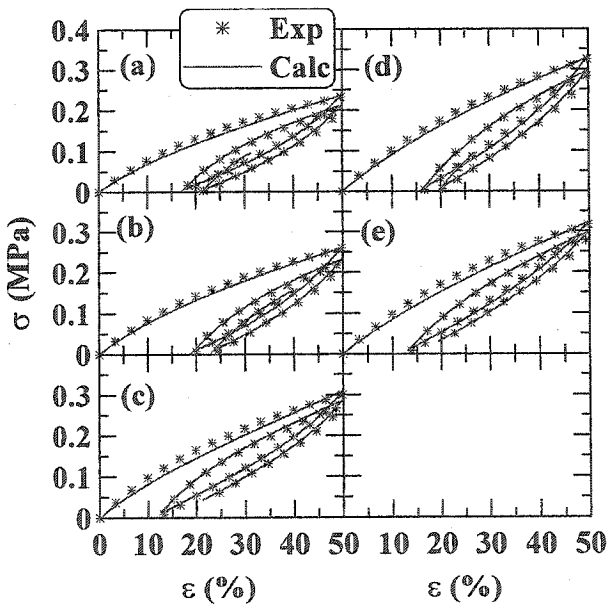

Figure 6.6 Cyclic stress-strain curves of bisphenol-crosslinked PVDF-TFE-P films at 110°C for (a) 0hrs; (b) 4hrs; (c) 8hrs; (d) 16hrs; and (e) 24hrs. The data are the symbols and the solid lines are calculated stress-strain behavior using the linear model and the parameters in Table 6.3.

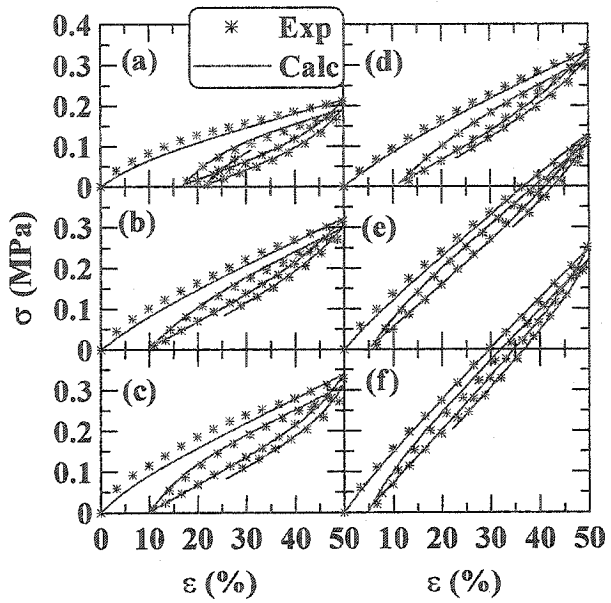

Figure 6.7 Cyclic stress-strain curves of TETA-crosslinked PVDF-TFE-P films with different TETA contents: (a) 0 pph; (b) 1 pph; (c) 2 pph; (d) 3 pph; (e) 4 pph; and (f) 5 pph. The data are the symbols and the solid lines are calculated stress-strain behavior using the linear model and the parameters in Table 6.4.

Table 6.3 Best-fit parameters of the linear model to the stress-strain curves of bisphenol-crosslinked PVDF-TFE-P films (Figure 6.6)

Time (hrs)	K_1 (MPa)	K_2 (MPa)	K_{d1} (10^2MPa S)	K_{d2} (10^4MPa S)
0	0.44	0.42	2.6	0.89
4	0.46	0.46	3.6	0.98
8	0.58	0.47	3.0	1.8
16	0.58	0.41	2.2	1.9
24	0.59	0.39	2.9	2.1

Table 6.4 Best-fit parameters of the linear model to the stress-strain curves of TETA-crosslinked PVDF-TFE-P (Figure 6.7)

TETA (pph)	K1 (MPa)	K2 (MPa)	Kd1 (10^2MPa S)	Kd2 (10^4MPa S)
0	0.41	0.46	2.1	0.74
1	0.62	0.32	1.9	2.1
2	0.66	0.57	2.0	1.9
3	0.71	0.34	2.8	2.8
4	1.0	0.34	1.5	6.8
5	1.3	0.44	1.5	7.9

In order to determine the effect of crosslinking, the cyclic deformation curves were fitted with the linear model. The calculated curves are also shown in Figures 6.6 and 6.7. Tables 6.3 and 6.4 list the best-fit parameters of the linear model and Figure 6.8 shows how the parameters K_1 and K_{d2} vary with heating time (for the bisphenol crosslinking method) and with TETA content. Crosslinking with TETA at levels of 4 or 5 pph causes a rapid increase in the film stiffness and viscosity, leading to improved mechanical properties.

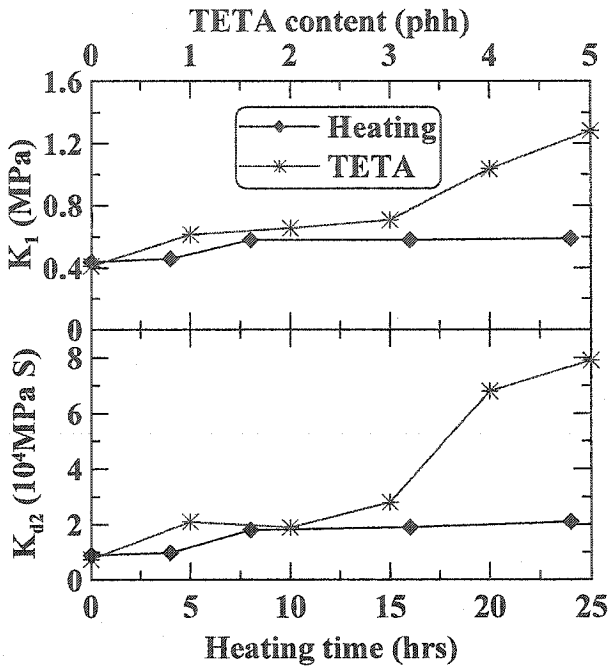

Figure 6.8 Comparison of the best-fit parameters of the linear model to the data in Figures 6.6 and 6.7. (♦) heating recipe; and (*) TETA-based recipe.

6.2.3 Mechanical and electrical properties of crosslinked PVDF-TFE-P/carbon black composites

It is our opinion that the mechanical and electrical properties of electrode films, which contain active solids, carbon black and polymer binder, under large-strain cyclic deformation must be stable. The mechanical and electrical properties must not degrade with increasing number of deformations in order for the electrodes to display good capacity retention with charge-discharge cycle number. In order to gain some appreciation of the effect of solids loading on the mechanical and electrical properties of crosslinked PVDF-TFE-P films, we decided to load the polymer films to the level of 25 pph SS. It is well known that the addition of carbon black will decrease the elasticity of

the polymers while improving the electrical conductivity. In this section, SS-filled PVDF-TFE-P films with different amounts of crosslinking and different crosslinking recipes are compared in terms of mechanical and electrical properties.

Figures 6.9a and 6.10a show the stress-strain curves of SS-filled PVDF-TFE-P films as a function of the relative amount of crosslinking for films crosslinked by the heating method and the TETA method, respectively. The breaking point of the composite films has been severely degraded by the addition of SS. The film crosslinked with bisphenol (110°C for 24 hours) can only be strained to 60% before breaking, and the film crosslinked with 4 pph TETA can be extended by 100%. The maximum elongation of the film with 5 pph TETA is about 160%. In both figures, the improvement of mechanical properties with crosslinking is clear. The maximum elongation before break increases with the amount of crosslinking, and the TETA crosslinking method apparently gives a higher degree of crosslinking than the bisphenol crosslinking method.

Figures 6.9b and 6.10b show the nominal resistivity-strain curves of SS-filled films as a function of the relative amount of crosslinking. The nominal resistivity (ρ_n) increases with the strain for samples prepared by both crosslinking methods. However, the nominal resistivity-strain curves for polymer/SS films with different amounts of crosslinking degree almost overlap. No significant impact of crosslinking on the resistivity was found.

Figure 6.11 shows the cyclic stress-strain curves of SS-filled polymer films crosslinked with TETA. Only samples containing more than 3 pph TETA can be stretched to 50% strain without breaking and only results for these samples are shown. As the TETA content increases, the maximum stress increases and the film rebounds

closer to its original length when the stress is removed. However, no striking improvement of strength with TETA content can be seen. Figure 6.12 shows the nominal resistivity-strain curves measured for the same films during the deformations shown in Figure 6.11. No obvious difference can be seen in the resistivity-strain behavior as a function of the TETA content. The nominal resistivity rises from ~1 Ω·cm and is stable at about 2.5 Ω·cm during the cyclic deformation. The addition of TETA improves the maximum elongation of the PVDF-TFE-P/SS composites while the electrical properties are basically unaffected by the addition of the crosslinks.

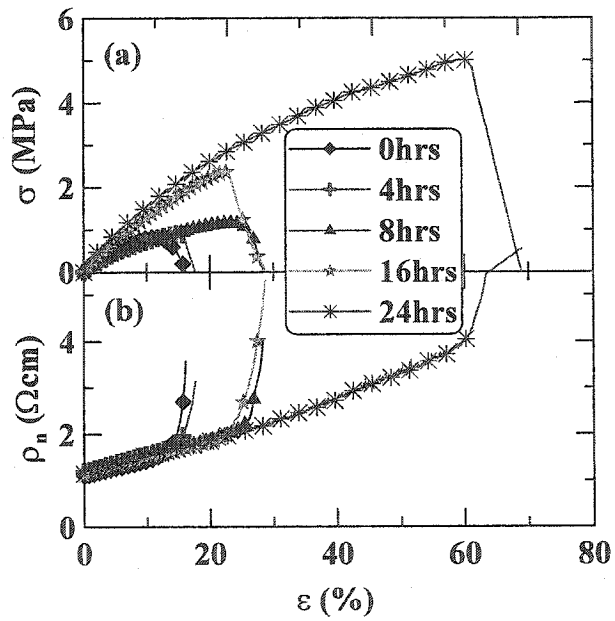

Figure 6.9 (a) Stress-strain and (b) nominal resistivity-strain curves of the bisphenol-crosslinked (110°C, 24 hours) SS-filled PVDF-TFE-P composites (25 pph SS)

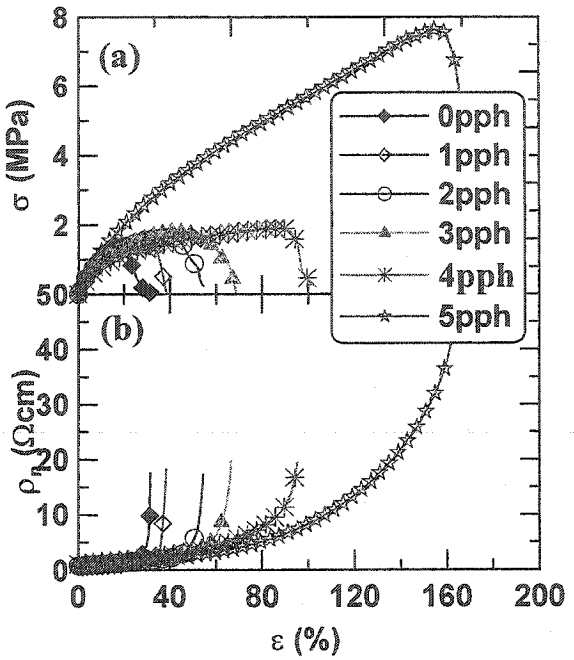

Figure 6.10 (a) Stress-strain and (b) nominal resistivity-strain curves of the TETA-crosslinked SS-filled PVDF-TFE-P composites (25 pph SS)

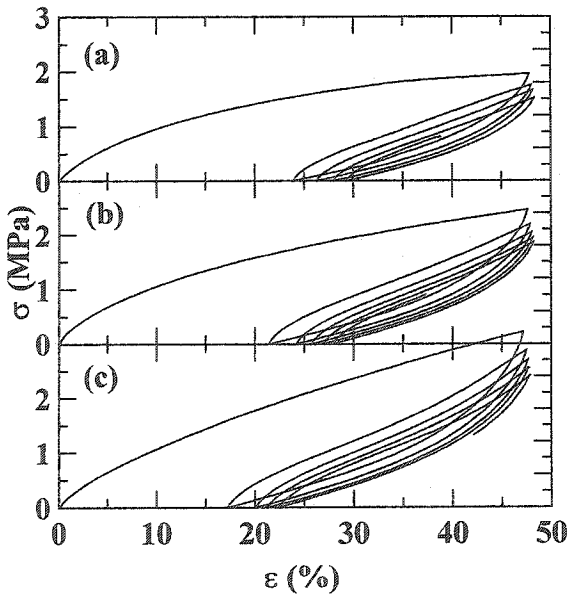

Figure 6.11 Cyclic stress-strain curves of the TETA-crosslinked SS-filled PVDF-TFE-P composites: (a) 3 pph TETA; (b) 4 pph TETA; and (c) 5 pph TETA

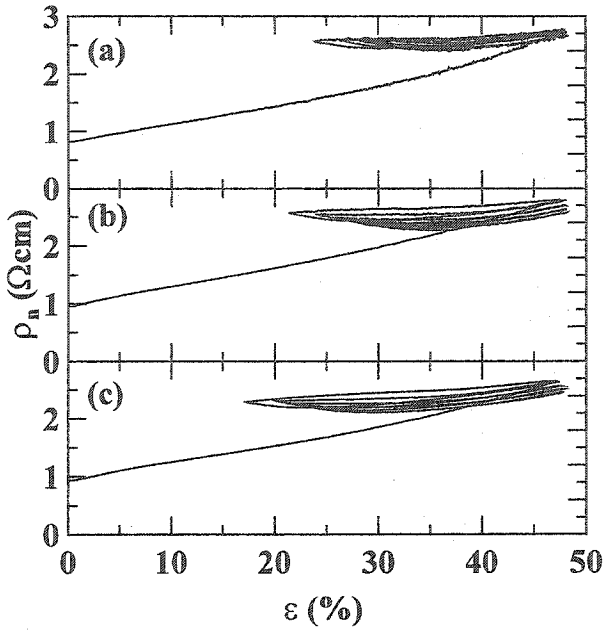

Figure 6.12 Cyclic nominal resistivity-strain curves of TETA-crosslinked SS-filled PVDF-TFE-P composites: (a) 3 pph TETA; (b) 4 pph TETA; and (c) 5 pph TETA

6.3 Mechanical and electrical study of swelled PVDF-TFE-P and PVDF-TFE-P/SS samples

6.3.1 Swelling of crosslinked PVDF-TFE-P and carbon-filled PVDF-TFE-P composites

The crosslinked polymer samples were immersed in the EC/DEC (1:2, v/v) mixed solvent for 24 hours, and then the change of weight, which was caused by the uptake of the solvent, was recorded. Figure 6.13 shows the swelling ratios of the crosslinked PVDF-TFE-P films as a function of the amount of crosslinking. For both sets of polymers, the amount of solvent absorbed decreases with increased crosslinking. The uncrosslinked film absorbs 140 wt% solvent by weight while the film crosslinked with 5

pph TETA absorbs 47 wt% solvent by weight. The equilibrium-swelling ratio of the polymer can be controlled by the amount of crosslinking.

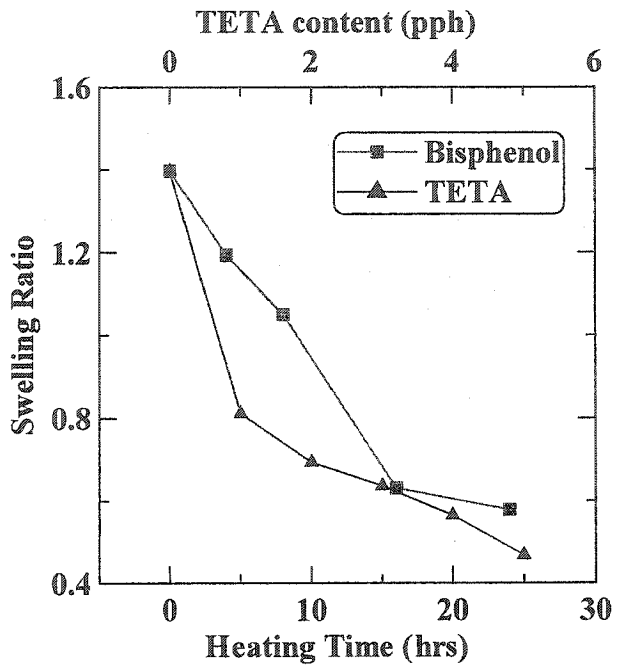

Figure 6.13 The swelling ratios of crosslinked PVDF-TFE-P in EC/DEC(1:2, v/v) (■) bisphenol crosslinking recipe and (▲) TETA crosslinking recipe

As mentioned above, the polymer can uptake more than 40 wt% liquid solvent and this causes the volumetric expansion of the polymer. For bisphenol-crosslinked PVDF-TFE-P/SS samples, the nominal resistivity increases rapidly and reaches its maximum in about 1 minute. However, it takes about 2 minutes for the TETA-crosslinked samples to reach their equilibrium-swelled states. All samples were believed to be completely swelled in the solvent in 5 minutes, and all the samples in the following sections were pre-swelled in EC/DEC (1:2, v/v) for 5 minutes before mechanical and electrical measurements.

6.3.2 Mechanical properties of bisphenol-crosslinked PVDF-TFE-P swelled in EC/DEC

Figure 6.14 shows the stress-strain curves of bisphenol-crosslinked PVDF-TFE-P films, which were swelled in EC/DEC (1:2, v/v) for 5 minutes before measurement. The stress-strain curves clearly indicate the dimensional change of the polymer films after swelling. Even though the films were mounted taut between the grips, upon immersion in the solvent the resulting expansion (about 20% in length) caused the films to go slack. This is why the stress in Figure 6.14 does not begin to increase until the strain (measured from the dry length) reaches about 20% when the new equilibrium length of the swelled film is reached. After that point, the stress increases almost linearly with the strain. When the polymer film was not heated, assuming that no or negligible crosslinking was introduced, the film swelled significantly in the solvent and the stress during stretching was small and the film broke at a small strain. When the dry films, before measurement, were heated in argon at 110°C to introduce crosslinking, the elastic modulus (the slope of the curves in Figure 6.14) increased with the heating time. This is believed to be the effect of the crosslinking introduced. When the film was heated at 110°C for less than 16 hours, the film could be stretched to 250% strain without breaking. However, if the film was heated longer to introduce more crosslinks, the film broke at a smaller strain. For example, a relatively high degree of crosslinking can be achieved by heating for 72 hours, but the film breaks at about 140% strain.

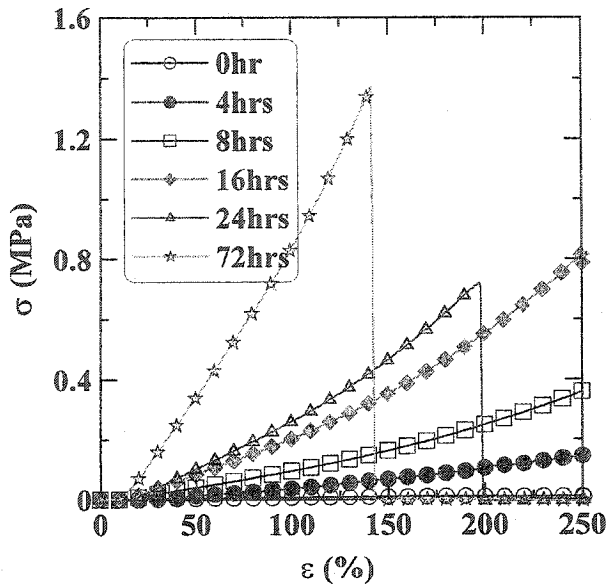

Figure 6.14 Stress-strain curves of bisphenol-crosslinked PVDF-TFE-P heated at 110°C. The samples were immersed in EC/DEC (1:2, v/v) during the measurement.

Figure 6.15 shows the cyclic stress-strain curves of bisphenol-crosslinked PVDF-TFE-P in EC/DEC (1:2, v/v). Since a large breaking strain is our desired objective, only the data for samples heated at 110°C for 4 (Figure 6.5a), 8 (b),16 (c) and 24 (d) hours are shown in Figure 6.15. All the four samples studied could be cyclically deformed to 100% strain without breaking. The samples have almost the same reversibility during cyclic deformation, and may be acceptable for our application.

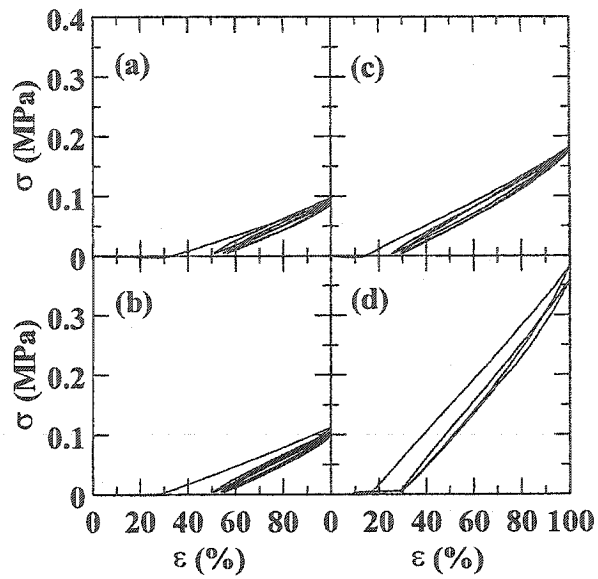

Figure 6.15 Cyclic stress-strain curves of bisphenol-crosslinked PVDF-TFE-P heated at 110°C for (a) 4 hours, (b) 8 hours, (c) 16 hours, and (d) 24 hours. The samples were immersed in EC/DEC (1:2, v/v) during the measurement.

6.3.3 Mechanical properties of TETA-crosslinked PVDF-TFE-P swelled in EC/DEC

Figure 6.16 shows the stress-strain curves of TETA-crosslinked PVDF-TFE-P films swelled in EC/DEC (1:2, v/v). The elastic modulus of the films increases with the TETA content. When the content of TETA is less than 3 pph, the film can be stretched to 250% strain without breaking. When 4 or 5 pph TETA was added, the film broke at about 120% strain. Comparing the sample without TETA (TETA-crosslinking recipe in Figure 6.16) to the sample without heating (bisphenol-crosslinking recipe in Figure 6.14), one can see that the sample without TETA (Figure 6.16) has a visible elastic modulus and a larger breaking strain (>250%). This suggests that a small amount of crosslinking was introduced even when no TETA was added under the preparation conditions. A possible explanation is that the highly basic conditions of the TETA-crosslinking recipe assists

bisphenol, which was already incorporated in the polymer by the manufacturer, to introduce a small number of crosslinks at room temperature, even though a higher temperature is suggested with the recommended recipe.

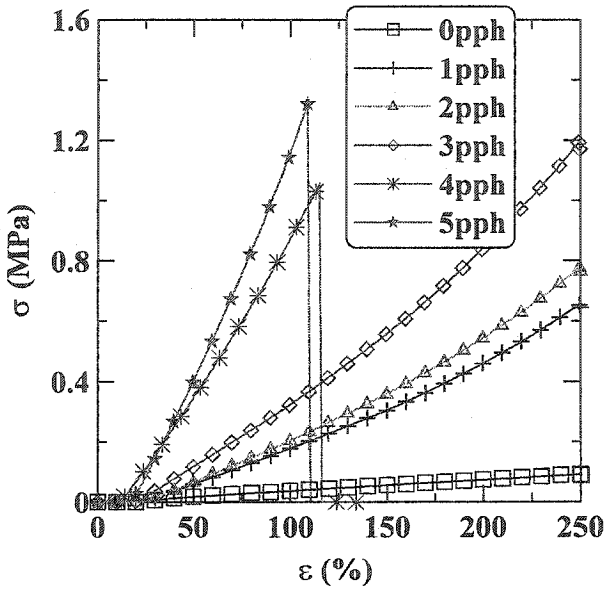

Figure 6.16 Stress-strain curves of TETA-crosslinked PVDF-TFE-P. The samples were immersed in EC/DEC (1:2, v/v) during the measurement.

Figure 6.17 shows the cyclic stress-strain curves of TETA-crosslinked PVDF-TFE-P in EC/DEC with the TETA content ranging from 0 to 4 pph. Since the breaking strain of the sample crosslinked with 5 pph TETA was slightly larger than 100%, it could be stretched to 100% strain but broke during the second cycle. Hence, Figure 6.17 doesn't include the data for the sample with 5 pph TETA. Compared to samples crosslinked with bisphenol (Figure 6.15), the TETA-crosslinked samples show almost no hysteresis during cyclic deformation. The films establish their new equilibrium length at about 20% strain regardless of the amount of TETA added. After that, the stress increases linearly with the strain up to 100%. The most interesting point is that the stress-strain curve completely

overlaps after the first stretching, and almost no hysteresis was observed. We believe that such behavior can be attributed to the swelling of the crosslinked polymer. When the polymer was immersed in the solvent, the solvent interacted with polymer chains and decreased the physical interaction between polymer chains. Most of the uncrosslinked ends lose the physical entanglement with other polymer chains and became free ends, reducing the viscoelastic properties of the polymer [39]. Hence, the highly crosslinked polymer network responds like a true spring after swelling as shown in Figure 6.17.

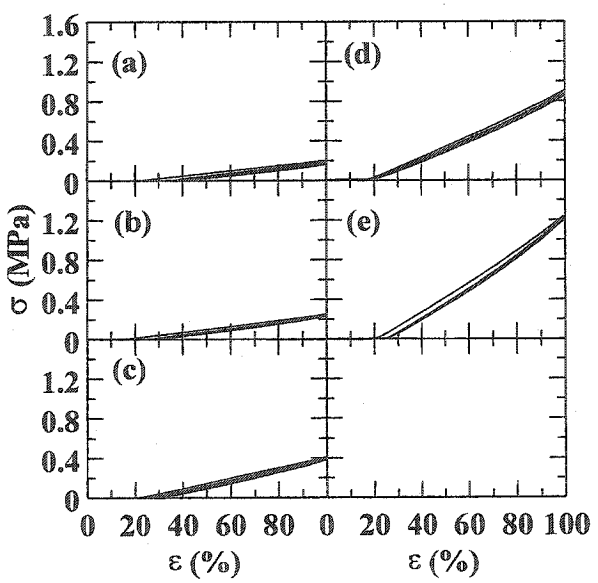

Figure 6.17 Cyclic stress-strain curves of TETA-crosslinked PVDF-TFE-P with (a) 0 pph, (b) 1 pph, (c) 2 pph, (d) 3 pph, and (e) 4 pph TETA. The samples were immersed in EC/DEC (1:2, v/v) during the measurement.

6.3.4 Mechanical and electrical properties of bisphenol-crosslinked PVDF-TFE-P/SS swelled in EC/DEC

Figure 6.18a shows the stress-strain curves of bisphenol-crosslinked PVDF-TFE-P filled with 25 pph SS. After swelling in EC/DEC (1:2, v/v), the films expanded by about 10% in the stretching direction. When the film is taut, the stress increases linearly with the strain. The elastic modulus, or the slope of the stress-strain curve, increases with the heating time for crosslinking. Even when the sample was heated for 24 hours, the film broke at about 50% strain. Figure 6.18b shows the nominal resistivity of the composites after swelling and during strain. The nominal resistivity ranges from 6 Ω·cm to about 12 Ω·cm during stretching. Since no sample can be stretched up to 100% strain, no data will be presented for the cyclic deformation of the bisphenol-crosslinked composites.

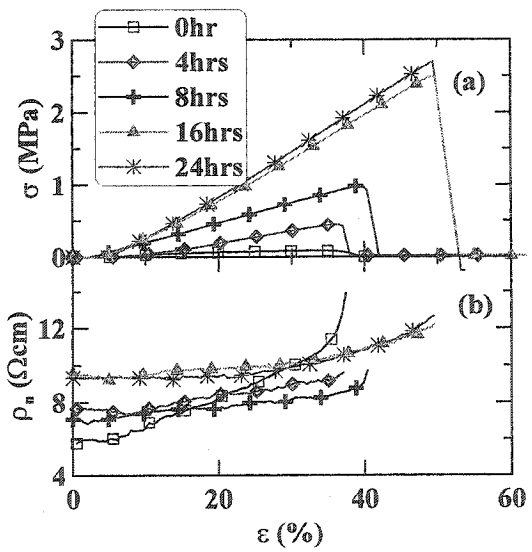

Figure 6.18 (a) Stress-strain and (b) Nominal resistivity-strain curves of bisphenol-crosslinked PVDF-TFE-P/SS immersed in EC/DEC (1:2, v/v). Samples with 25 pph SS were heated at 110^{O}C in an argon flow for the times indicated in the legend.

6.3.5 Mechanical and electrical properties of TETA-crosslinked PVDF-TFE-P/SS swelled in EC/DEC

Figure 6.19a shows the stress-strain curves of TETA-crosslinked PVDF-TFE-P/SS composites after swelling in EC/DEC (1:2, v/v). When the TETA content was less than 4 pph, the breaking strain of the swelled composites increased with the amount of TETA added. When 4 pph TETA was added, the composite film could be stretched to 170% strain before breaking. However, further addition of TETA to the composite decreased the breaking strain. When 5 pph TETA was added, the breaking strain decreased to about 125% strain. Figure 6.19b shows the nominal resistivity-strain curves of the swelled composites. All the curves approximately overlap each other. Apparently, the crosslinking introduced by TETA has little impact on the resistivity of the swelled composites.

Figure 6.20 shows the cyclic deformation of TETA-crosslinked PVDF-TFE-P/SS composites after swelling in EC/DEC (1:2, v/v). The samples with 3, 4 and 5 pph TETA have almost the same stress-strain profiles, except for the scales of the stress axes in Figure 6.20. The sample with 3 pph TETA could be cyclically deformed to 100% strain and broke during the third cycle. Samples with 4 and 5 pph TETA could be cyclically stretched to 100% strain and released without breaking. By comparison, the maximum elongation of the swelled PVDF/SS film containing 25 pph SS was less than 10%. The nominal resistivity of TETA-crosslinked composites has very good reversibility after the first stretching and varies within the range of 20-30 Ω·cm.

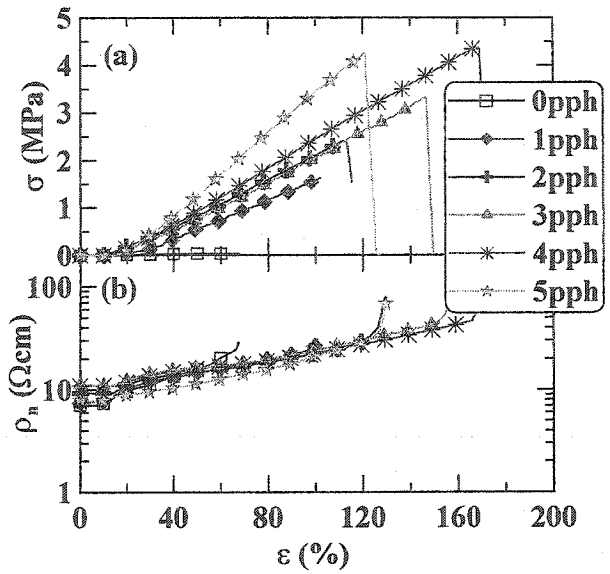

Figure 6.19 (a) Stress-strain and (b) Nominal resistivity-strain curves of TETA-crosslinked PVDF-TFE-P/SS immersed in EC/DEC (1:2, v/v). 25 pph SS was added to the samples. The amount of TETA added to each sample is indicated in the legend

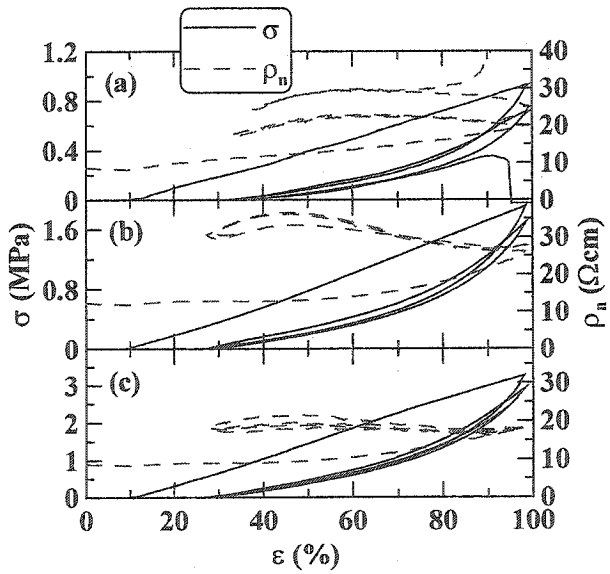

Figure 6.20 Stress versus strain and nominal resistivity versus strain during cyclic deformation of TETA-crosslinked PVDF-TFE-P/SS composites immersed in EC/DEC (1:2, v/v). The samples had (a) 3 pph, (b) 4 pph and (c) 5 pph TETA added. 25 pph SS was added to the samples.

6.4 Effect of the coupling agent

6.4.1 Coupling between PVDF-TFE-P and SS

A series of PVDF-TFE-P/SS composites containing 25 pph SS and different amount of APTES were prepared to study the effect of the coupling agent. Figure 6.21 shows stress-strain and nominal resistivity-strain curves of the PVDF-TFE-P/SS composites after drying in air overnight. All the samples broke at about 30% strain. No clear trend about the impact of APTES was observed. However, when the samples were investigated again after storing for more than 24 hours, a clear trend was observed. The addition of APTES greatly improved the mechanical properties of PVDF-TFE-P/SS composites (Figure 6.22a). Comparing Figure 6.21 and Figure 6.22, one observes that the reaction time is important for APTES to be functionalized. It suggests that the reaction of the coupling agent is a slow reaction, and that it needs more time to complete the coupling reaction between the polymer matrix and SS particles.

The maximum elongation before break of the composite without APTES is about 10%. The breaking strain of the composites increases with the content of APTES. When 5.1 pph APTES was added and stored for more than 24 hours, the composite film could be extended to 130% before breaking. Figure 6.23a shows the stress at 10% strain as a function of the APTES content. The stress at 10% strain increases with the APTES content. The improvement of the mechanical properties can be associated with the chemical bonds between the SS and polymer chains introduced by APTES. Since an SS particle can have many functional groups, -OH, on the surface, more than one APTES molecule can bond to a single SS particle. Therefore, SS particles with multiple APTES ($-NH_2$) can act as bulk crosslinking agents. Figure 6.22b shows the nominal resistivity of

PVDF-TFE-P/SS composites as a function of both the strain and the APTES content. The nominal resistivity of the composites at 10% strain is summarized in Figure 6.23b. Apparently, the resistivity increases exponentially with the strain and the addition of APTES has no or little impact on the resistivity.

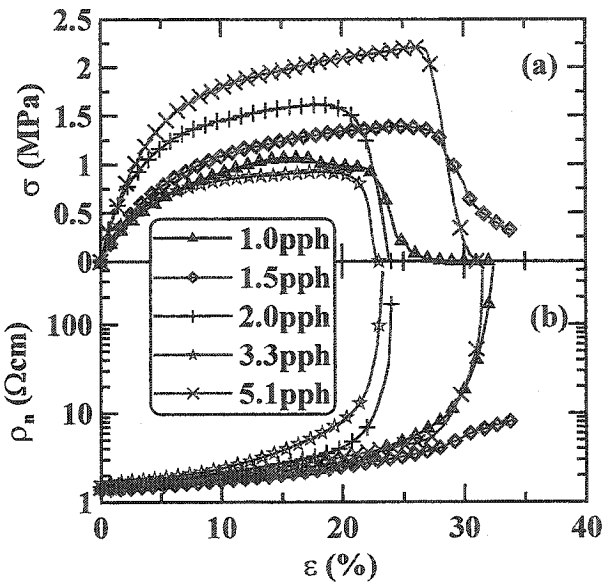

Figure 6.21 (a) Stress vs. strain, and (b) nominal resistivity vs. strain of PVDF-TFE-P/SS composites showing the effect of APTES. Notice that 25 pph SS was added to each sample, and that the samples were evaluated after drying in air overnight.

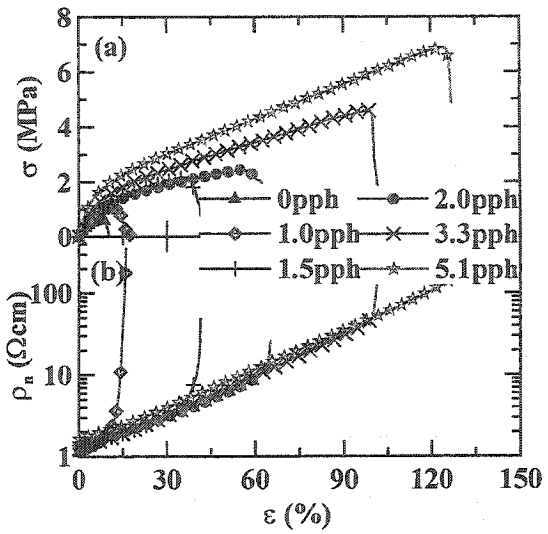

Figure 6.22 (a) Stress vs. strain, and (b) nominal resistivity vs. strain of PVDF-TFE-P/SS composites showing the effect of APTES. Notice that 25 pph SS was added to each sample, and that the samples were stored for more than 24 hours before measurement.

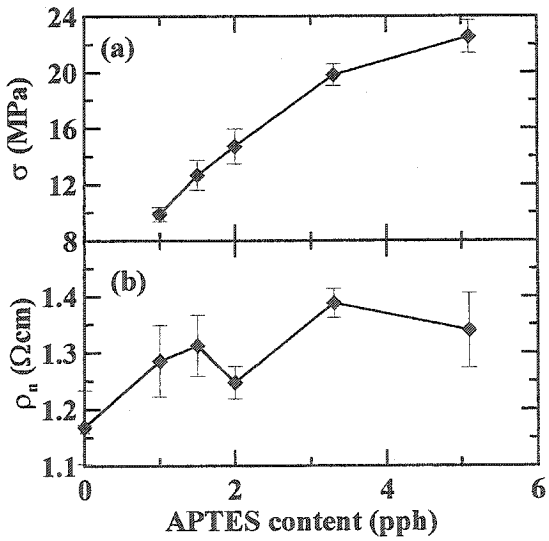

Figure 6.23 (a) The stress and (b) the nominal resistivity at 10% strain of PVDF-TFE-P/SS composites showing the impact of added APTES. Notice that 25 pph SS was added to each sample, and that the samples were stored for more than 24 hours.

Figure 6.24a shows the cyclic stress-strain curve of a PVDF-TFE-P/SS sample containing 25 pph SS and 5.1 pph APTES. The film rebounded at 25% strain when the stress was removed, and the stress at 50% strain decreases quickly with cycle number. The poor cycling behavior results from the viscoelastic flow of polymer chains because of the limited crosslinking provided by added APTES. In fact, TETA will be added to provide sufficient crosslinking and to suppress the viscoelastic flow of polymer chains. Figure 6.24b shows the nominal resistivity of the PVDF-TFE-P/SS film during the cyclic deformation. The nominal resistivity rises from 1.5 Ω·cm initially to about 16 Ω·cm at 50% strain. By comparison of Figure 6.20, the high resistivity in Figure 6.24b apparently result from the viscoelastic flow of the polymer chains. After the first stretching, the nominal resistivity was stable at about 16 Ω·cm.

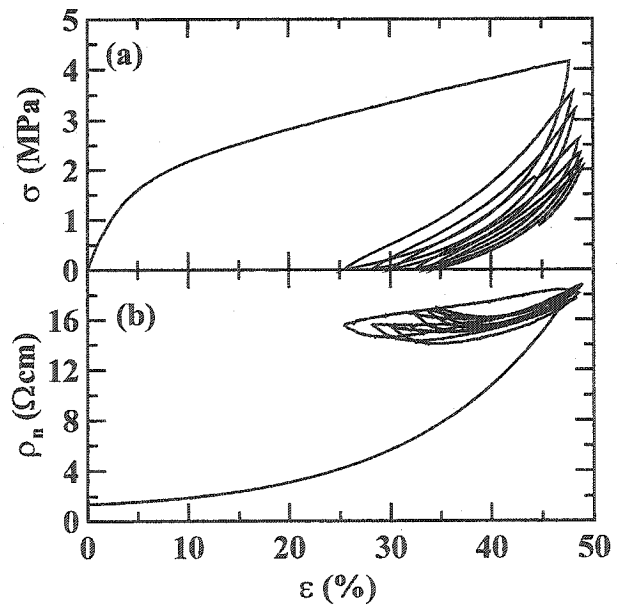

Figure 6.24 (a) Cyclic stress-strain and (b) nominal resistivity-strain curves of a PVDF-TFE-P/SS composite containing 25 pph SS and 5.1 pph APTES

In order to suppress the viscoelastic flow of polymer chains, a sample containing 5.0 pph TETA and 3.6 pph APTES was prepared and evaluated. Figure 6.25 shows the stress-strain and nominal resistivity-strain curves of the binder film. With the addition of TETA, the film can be extended to 200% before breaking. The nominal resistivity rises from 1.8 Ω·cm to about 400 Ω·cm at the breaking strain (200%). Figure 6.26a shows the stress-strain curve of the binder film under cyclic deformation. Compared to the sample with APTES only (Figure 6.24a), the mechanical properties of the film containing both TETA and APTES were greatly improved. The sample film rebounded at about 12% strain when the stress was removed, and the stress at 50% strain was stable at about 3.5 MPa upon cycling. The nominal resistivity rises from 1.7 Ω·cm to 4.5 Ω·cm at 50% strain (Figure 6.26b), which is much smaller than that of sample containing 5.1 pph APTES only (Figure 6.24b). Moreover, the nominal resistivity changed reversibly after the initial stretching.

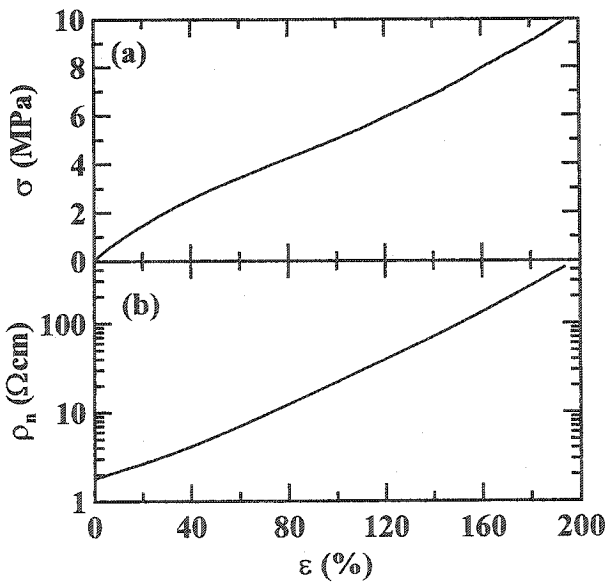

Figure 6.25 (a) Stress-strain and (b) nominal resistivity-strain curves of a PVDF-TFE-P/SS composite containing 25 pph SS, 5.0 pph TETA, and 3.6 pph APTES

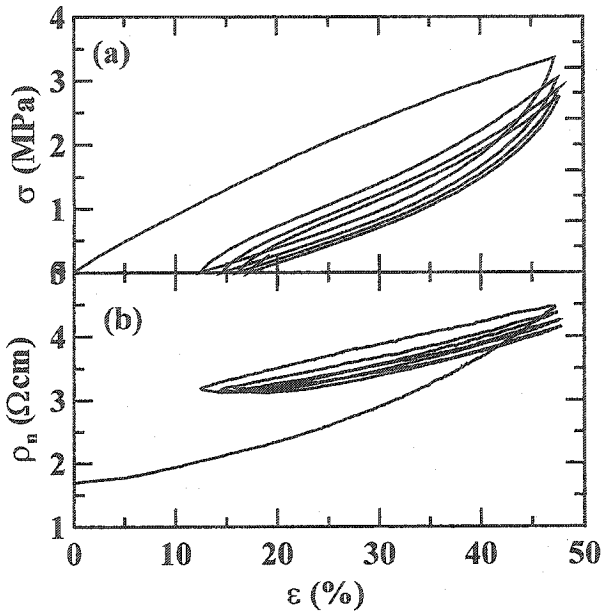

Figure 6.26 (a) Cyclic stress-strain and (b) nominal resistivity-strain curves of a PVDF-TFE-P/SS composite containing 25 pph SS, 5.0 pph TETA, and 3.6 pph APTES

6.4.2 Coupling between PVDF-TFE-P and the silicon surface

It is also very important to study the coupling capability of APTES between PVDF-TFE-P and the active material particle, a-Si or a-SiSn. A silicon wafer was used to mimic the surface of a-Si and a-$Si_{0.64}Sn_{0.36}$. Then, the peel test was carried out to measure the adhesion strength of the binder film to the surface of the silicon wafer.

Figure 6.27 shows the results of peel tests on the binder films with and without the coupling agent, APTES. No TETA was added, and 25 pph SS was added as the filler to enhance the binder strength. When no coupling agent was added, the adhesion energy is about 12 J/m^2. However, when 0.9 pph APTES was added, the binder film broke instead of peeling from the silicon wafer. The result implies that the adhesion energy is higher than 120 J/m^2, more than an order of magnitude larger than when no adhesion promoter is

added. Hence, we can expect to suppress the failure between the polymer-solid interface by adding APTES.

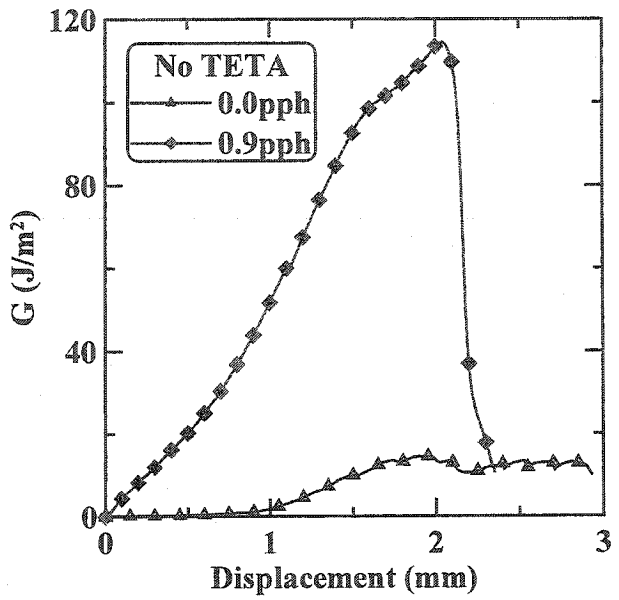

Figure 6.27 Peel tests of binder films without TETA on silicon wafers showing the significant impact of APTES

In the real application, TETA is added as the crosslinking agent to suppress the viscoelastic flow of polymer chains as suggested in Figure 6.26. Figure 6.28 shows the results of peel tests on the binder films with 5.0 pph TETA and 25 pph SS. With the addition of 5.0 pph TETA, the binder film can be easily peeled up from the silicon wafer even when 1.8 pph APTES was added. Compared to Figure 6.27, the addition of TETA greatly deteriorates the adhesion strength between the binder films and silicon wafers. For the films without APTES, the adhesion strength decreases from 12 J/m^2 to about 3.5 J/m^2. The adhesion strength between the film containing 5.0 pph TETA and 1.8 pph APTES and the silicon wafer is only about 20 J/m^2.

It is not surprising to see the counter effect of TETA because both TETA and APTES use $-NH_2$ as the active group to react with the carbon-carbon double bond in the backbone of the polymer chain, the amount of which is limited by the chemical composition of the polymer and the reaction condition. The added TETA will compete with APTES to bond to the active sites in polymer chains. If too much TETA is added, the coupling efficiency of APTES will be greatly deteriorated. Therefore, it is very important to carefully balance the contents of TETA and APTES to ensure good mechanical properties and good adhesion strength.

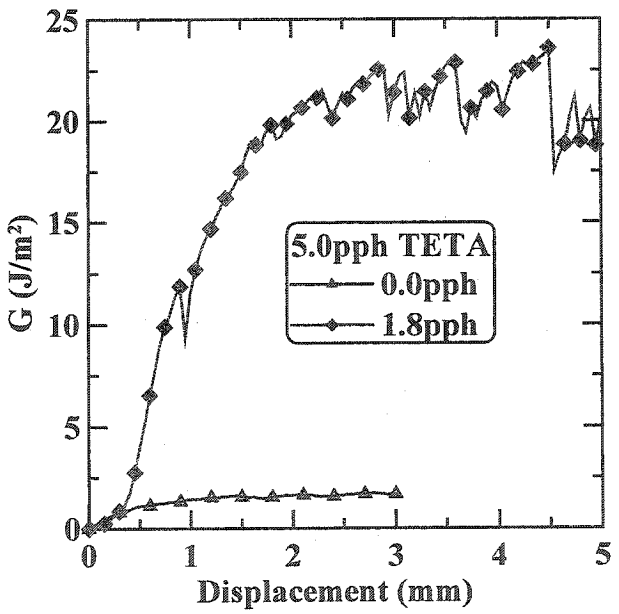

Figure 6.28 Peel tests of binder films with TETA on silicon wafers showing the counter effect of TETA on the adhesion strength

6.5 Effect of heating

It was shown in section 6.4 that the coupling reaction of APTES is a slow reaction and needs more than 24 hours to complete. By heating the samples at a low temperature, i.e. 110°C, the reaction can be accelerated and more APTES will be active. In fact, it is also shown in the following section that the heating step at 110°C is desired to maximize the capacity retention of a-$Si_{0.64}Sn_{0.36}$/Ag composite electrodes incorporating the PVDF-TFE-P-based elastomeric binder. Therefore, it is important to study the effect of the heating step on the mechanical and electrical properties of the binder. In order to achieve this, a series of PVDF-TFE-P-based samples prepared and heated in an argon flow at 110°C for 24 hours were characterized to show the impact of the heating step.

6.5.1 Effect of heating on TETA-crosslinked PVDF-TFE-P films

Figure 6.29 shows stress-strain curves of TETA-crosslinked PVDF-TFE-P films after heating. When only less than 2.0 pph TETA was added, the film could be extended to 250% without breaking. However, when more than 2.0 pph TETA was added, the film broke at a smaller strain. The maximum elongation before break decreases with the TETA content used. The film with 4.0 pph TETA broke at 175%, and its breaking stress was about 7.5 MPa.

Comparing Figures 6.4 and 6.29, one observes that the heating at 110°C greatly increases the strength of TETA-crosslinked PVDF-TFE-P films and decreases the maximum elongation of the films. A possible reason is that heating at 110°C pushes along the dehydrofluorination reaction of PVDF-TFE-P (see equation 6-2) to give more active sites and increases the efficiency of the crosslinking reaction (see equation 6-4).

Therefore, more active crosslinks can be expected after heating at 110°C. The small value of the maximum elongation after heating results from the overcrosslinking of PVDF-TFE-P films.

Figure 6.30 shows cyclic stress-strain curves of TETA-crosslinked PVDF-TFE-P films after heating. The films could be cycled reversibly after the initial stretching, and the strength of the films increases with the TETA content. Compared to Figure 6.7, the heated films were stronger than the un-heated ones with the same TETA content.

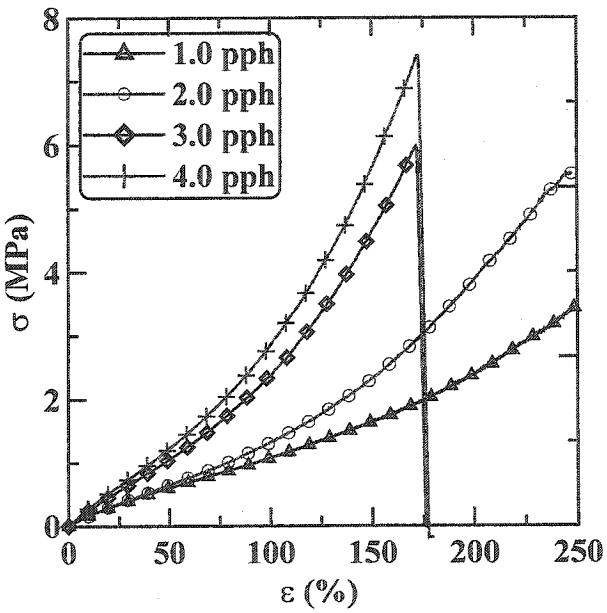

Figure 6.29 Stress vs. strain of TETA-crosslinked PVDF-TFE-P films after heating in an argon flow at 110°C for 24 hours

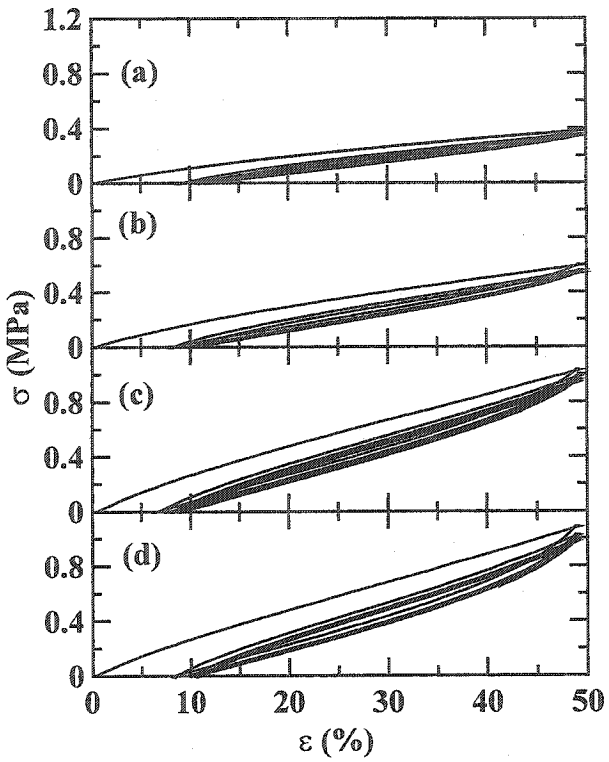

Figure 6.30 Cyclic stress-strain curves of heated PVDF-TFE-P films with different amount of TETA: (a) 1.0 pph, (b) 2.0 pph, (c) 3.0 pph, and (d) 4.0 pph.

Figure 6.31 shows the stress-strain curves of heated and TETA-crosslinked PVDF-TFE-P films after swelling in EC/DEC (1:2, v/v) for 5 minutes. The films expanded by about 20% in the stretching direction after swelling in EC/DEC (1:2, v/v). After the films were taut, the stress increased almost linearly with the strain applied. The modulus of the films after swelling increases with the TETA content, while the maximum elongation before break decreases. Compared to the un-heated samples (see Figure 6.16), the heated samples had a larger modulus and a smaller maximum elongation before break.

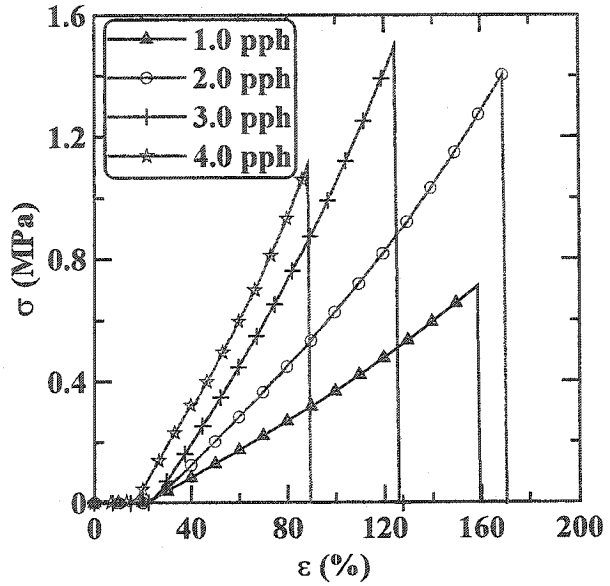

Figure 6.31 Stress vs. strain curves of heated and TETA-crosslinked PVDF-TFE-P films after swelling in EC/DEC (1:2, v/v)

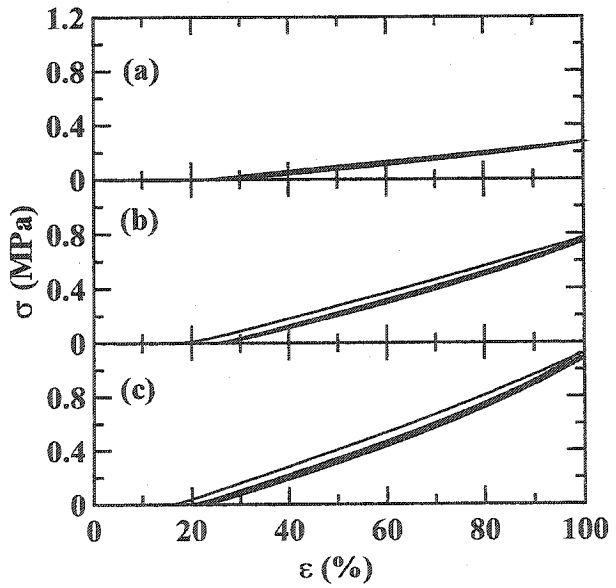

Figure 6.32 Cyclic stress-strain curves of heated and TETA-crosslinked PVDF-TFE-P films after swelling in EC/DEC (1:2, v/v) incorporating (a) 1.0 pph, (b) 2.0 pph, and (c) 3.0 pph TETA.

Figure 6.32 shows cyclic stress-strain curves of heated and TETA-crosslinked PVDF-TFE-P films after swelling in EC/DEC (1:2, v/v) for 5 minutes. The film containing 4.0 pph TETA could only be stretched to 90% before breaking. Hence, the sample containing 4.0 pph TETA was not included in Figure 6.32. It is clear that the strength of the films increases with the TETA content. The films were cycled with almost no hysteresis after the initial stretching.

6.5.2 Effect of heating on TETA-crosslinked PVDF-TFE-P/SS films

Figure 6.33a shows stress-strain curves of heated PVDF-TFE-P/SS containing 25 pph SS. All the films broke at around 70% strain. When more than 3.0 pph TETA was added, the stress-strain curves were almost the same, presumably since the same crosslinking degree was achieved with excess TETA. When 5.0 pph APTES was used instead of TETA, the stress-strain curve almost overlapped with that of the sample containing 3.0 or 5.0 pph TETA. This is probably due to the crosslinking effect of APTES as explained in section 6.4.

The mechanical properties of un-heated composites were already shown in Figure 6.10a. The strength and the maximum elongation of PVDF-TFE-P/SS films increases with the increasing TETA content. No saturation was found up to 5.0 pph TETA. However, Figure 6.33a shows that a saturated crosslinking was achieved when more than 3.0 pph TETA was used and the films were heat-treated. The only explanation is that the heating step increases the crosslinking efficiency of TETA.

Figure 6.22a also shows that the un-heated sample containing 5.1 pph APTES could be stretched to 130% with a breaking stress of 7.9 MPa. When the sample containing 5.0

pph APTES was heated (see Figure 6.33), the film broke at about 60%, and the breaking stress was also about 8.0 MPa. The modulus of the heated sample was almost twice that of the unheated sample. This also results from the improved coupling efficiency caused by heating.

Figure 6.33b shows nominal resistivity-strain curves of the PVDF-TFE-P/SS composites. Apparently, the resistivity is independent of the content of TETA and APTES used.

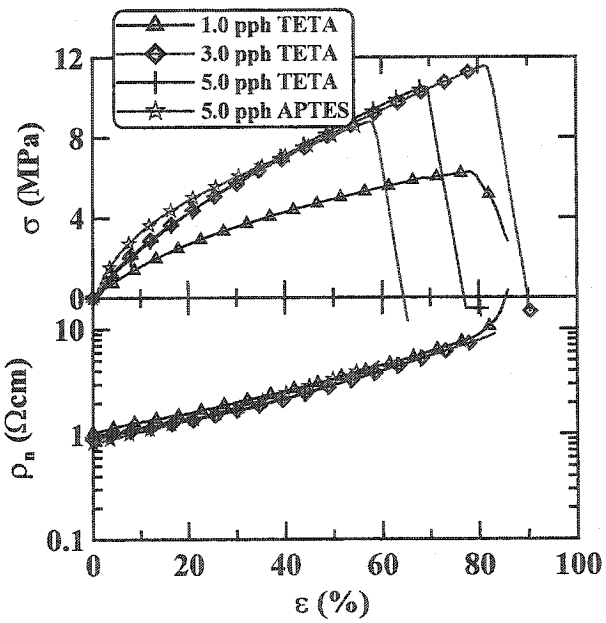

Figure 6.33 (a) Stress vs. strain, and (b) nominal resistivity vs. strain of heated PVDF-TFE-P/SS composites incorporating 25 pph SS and different amounts of TETA and APTES

Figure 6.34a shows stress-strain curves of the heated samples after swelling in EC/DEC (1:2, v/v) for 5 minutes. 25 pph SS was added to each sample. All the films broke at about 60% strain regardless of the TETA and APTES content. Figure 6.34b

shows nominal resistivity-strain curves of the binder films. After swelling in EC/DEC (1:2, v/v) for 5 minutes, the initial resistivity of the binder film decreased with the TETA content (<3.0 pph). When more than 3.0 pph TETA was added, the resistivity of the binder film was almost the same, presumably because a saturated crosslinking has been achieved. During stretching, the nominal resistivity of the binder films increased while the difference among the samples was maintained.

The sample containing 5.0 pph APTES had the smallest initial resistivity. This is probably due to the combined crosslinking and coupling effects of APTES, while TETA lacks the coupling effect. The sample containing 5.0 pph APTES is expected to have more constraints involving SS particles and polymer chains than the TETA-crosslinked samples. Hence, the swelling of the binder film in EC/DEC (1:2, v/v) was further limited by the coupling effect of APTES and the film had the smallest initial resistivity. During stretching, the nominal resistivity of the binder films increased with the strain. Comparing the nominal resistivity of TETA-crosslinked samples (3.0 pph or 5.0 pph) and the sample containing 5.0 pph APTES, one observes that the difference in nominal resistivity decreased during stretching. This is probably because APTES is not a good crosslinking agent as TETA, and more mechanical degradation of the composite occurred during stretching.

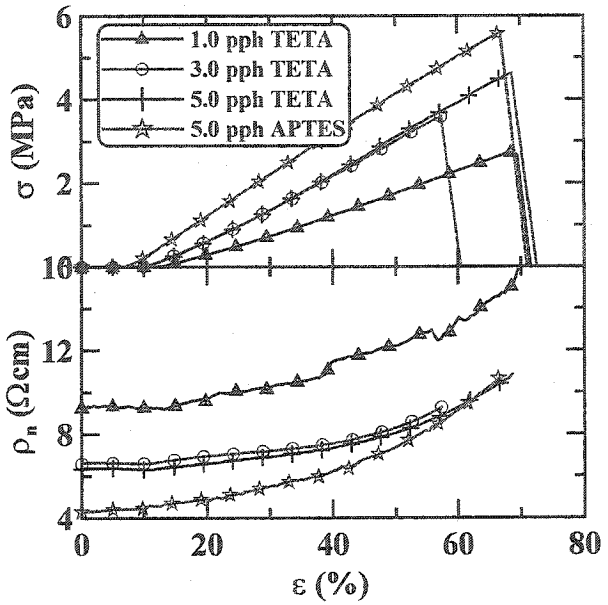

Figure 6.34 (a) Stress vs. strain, and (b) nominal resistivity vs. strain of heated and TETA-crosslinked PVDF-TFE-P/SS films after swelling in EC/DEC (1:2, v/v). 25 pph SS was added to each sample.

6.6 Electrochemical characterization

6.6.1 Effect of SS loading

Substantial experimental evidence has been shown that the resistivity of the binder film increases exponentially with the strain applied during the initial stretching and that the resistivity remains high after the initial stretching. In the real composite electrode, the binder system will be subject to a high strain as well when lithium atoms insert into the metallic alloy particles. Therefore, it is important to incorporate a suitable amount of SS in the composite electrode to ensure an acceptable electrical conductivity under strain when the negative material particles expand greatly.

In order to study the impact of the content of SS in composite electrodes, a series of electrodes were prepared with different SS content. In order to describe the recipe for the electrode conveniently, the content of active material is set to 100 pph (part per hundred ratio of the mass of the active material).

Figures 6.35 shows the voltage curves of a-$Si_{0.64}Sn_{0.36}$ electrodes during charge/discharge cycling, while Figure 6.36 shows the voltage curves of a-$Si_{0.64}Sn_{0.36}$/Ag electrodes during charge/discharge cycling. The electrodes incorporated 100 pph active material, 10 pph PVDF-TFE-P, 0.3 pph TETA, 1.0 pph APTES, 0.4 pph CaO, 0.3 pph DABCO, and different amounts of SS. All the electrodes were heated in an argon flow at 110°C for 24 hours before use. All the cells were first discharged to 0.22 V and then cycled between 1.0 V and 0.2 V with a constant current of 60 mA/g. The areal density of the electrodes is about 5 mg/cm^2 (active material).

Figures 6.37 and 6.38 show that a high SS content is required for good cycling performance of a-$Si_{0.64}Sn_{0.36}$ and a-$Si_{0.64}Sn_{0.36}$/Ag composite electrodes. When the content of SS is low, such as 5 pph, the cells had high resistance during discharge, and low capacity was accessed during the first discharge. When more SS was added, the electrodes had a lower resistance and discharged to the expected capacity. In addition, the electrodes with higher SS content had better capacity retention. Therefore, high SS content is desired for low resistance and better capacity retention.

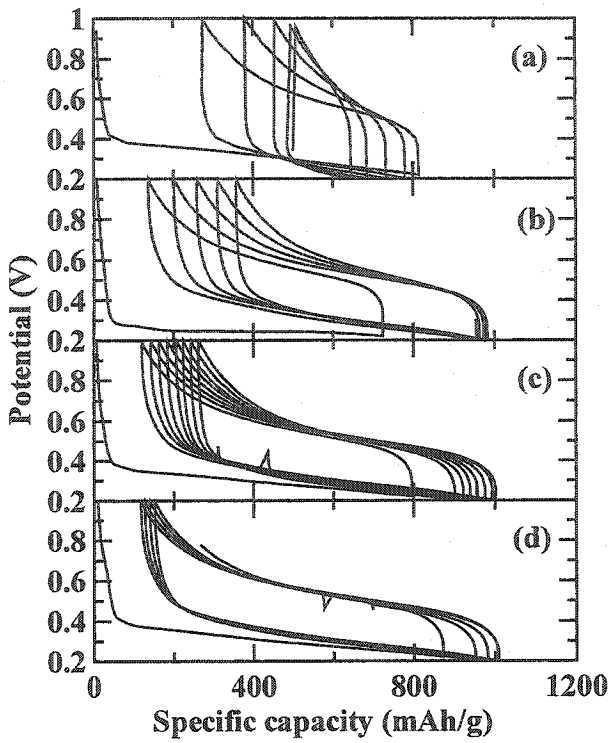

Figure 6.35 Voltage profile of Li/a-$Si_{0.64}Sn_{0.36}$ cells incorporating different amounts of SS: (a) 5 pph, (b) 12 pph, (c) 16 pph, and (d) 20 pph

Recipe – a-$Si_{0.64}Sn_{0.36}$: PVDF-TFE-P : TETA : APTES: CaO : DABCO = 100 : 10 : 0.3 : 1.0 : 0.4 : 0.3

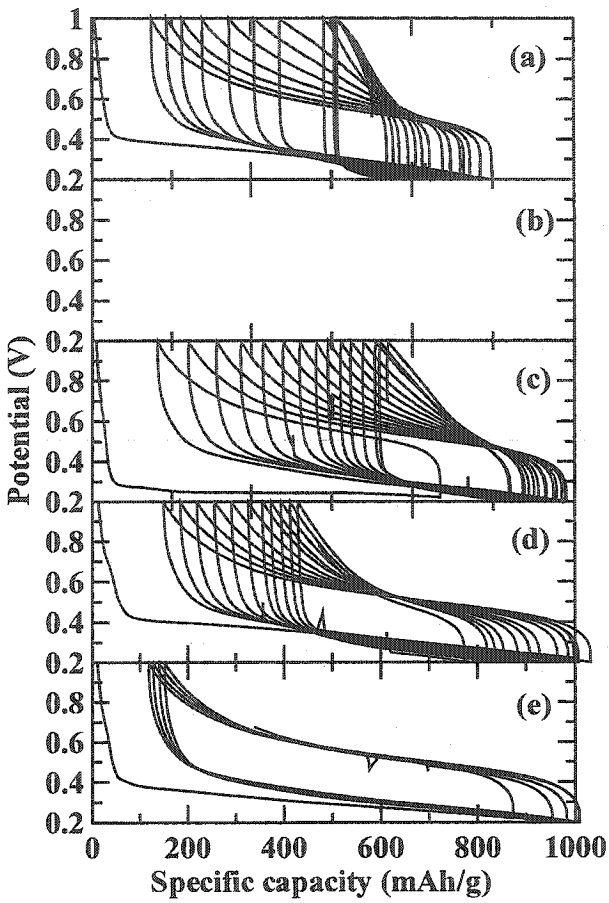

Figure 6.36 Voltage profile of Li/a-$Si_{0.64}Sn_{0.36}$/Ag cells incorporating different amount of SS: (a) 5 pph, (b) 8 pph, (c) 12 pph, (d) 16 pph, and (e) 20 pph

Recipe – a-$Si_{0.64}Sn_{0.36}$/Ag:PVDF-TFE-P:TETA:APTES:CaO:DABCO = 100:10:0.3:1.0:0.4:0.3

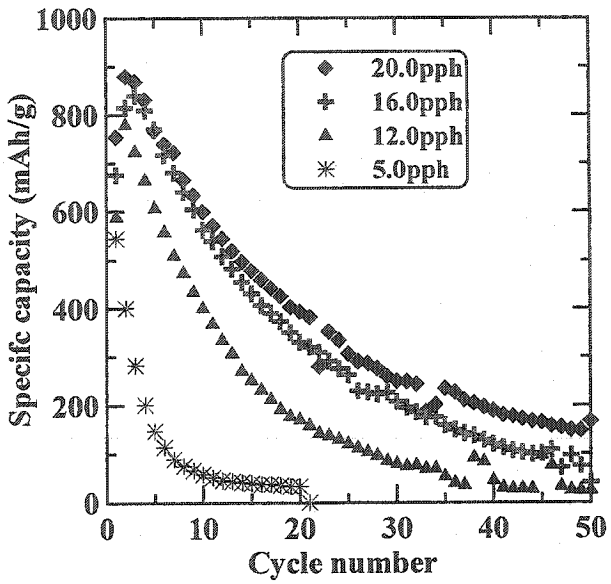

Figure 6.37 Capacity retention of a-$Si_{0.64}Sn_{0.36}$ electrodes showing the impact of the SS content. First discharged to 0.22 V, and then cycled between 0.2 V and 1.0 V with a constant current of 60 mA/g.

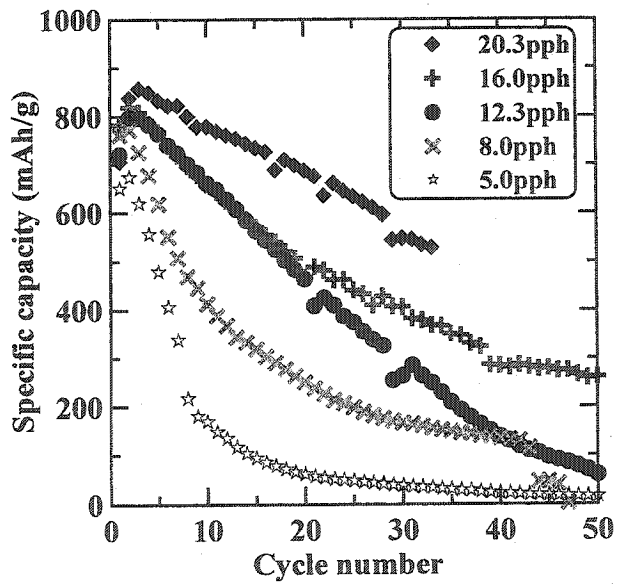

Figure 6.38 Capacity retention of a-$Si_{0.64}Sn_{0.36}$/Ag electrodes showing the impact of the SS content. First discharged to 0.22 V, and then cycled between 0.2 V and 1.0 V with a constant current of 60 mA/g.

Figures 6.37 and 6.38 show the capacity versus cycle number of a-$Si_{0.64}Sn_{0.36}$ and a-$Si_{0.64}Sn_{0.36}$/Ag electrodes respectively. Both data sets clearly illustrate that the SS content strongly affects the capacity retention of the electrodes and that a high SS content is desired. However, electrodes with more than 20 pph SS were not investigated. Figures 6.35d and Figure 6.36e show that the cells incorporating 20 pph SS can be cycled quite well, and suggest that further improvements using even larger SS contents might be possible. However, electrodes with such large SS content would not be acceptable formulation for practical cells. In addition, increasing the SS content will also increase the irreversible capacity loss due to the formation of SEI on the surface of SS. Therefore, 20 pph SS will be used in all the electrodes mentioned hereafter.

Figures 6.37 and 6.38 show that a-$Si_{0.64}Sn_{0.36}$/Ag electrodes have much better capacity retention than a-$Si_{0.64}Sn_{0.36}$ electrodes with the same recipe (SS content). The capacity retention of the a-$Si_{0.64}Sn_{0.36}$/Ag electrode incorporating 20 pph SS is quite reasonable. The same trend also appears in the following experiments although only the results for a-$Si_{0.64}Sn_{0.36}$/Ag electrodes will be shown hereafter. It has been reported that a silver coating also improved the cycling behavior of Si composite electrodes [74]. However, the mechanism is not well understood at this point.

6.6.2 Superiority of the elastomeric binder

Figure 6.39 shows the specific capacity vs. cycle number for five representative cells to demonstrate the effect of the binder system on the cycling performance of Li/(a-$Si_{0.64}Sn_{0.36}$/Ag) cells cycled between 0.2 and 1.0 V. The recipes of the electrodes are shown in Table 6.5. Many cells were constructed and tested to verify the trends shown in

Figure 6.39. All cells were first discharged to 0.22 V and then cycled between 0.2 and 1.0 V with a constant current of 60 mA/g. Data sets A-D show the cycling results for a-$Si_{0.64}Sn_{0.36}$/Ag in PVDF-TFE-P-based elastomeric binder systems prepared with different recipes. As a comparison, the result of the control cell, a-$Si_{0.64}Sn_{0.36}$/Ag incorporating PVDF binder, is shown in Figure 6.39 as data set e. Electrodes a-c were heated in an argon flow at 110°C for 24 hours before use.

Table 6.5 Preparation recipes of electrodes A-E to study the effect of the binder system

Electrode	Polymer	TETA (pph[1])	APTES (pph)	Post thermal treatment [2]	Areal density[3] (mg/cm^2)
A	PVDF-TFE-P	0.4	4.7	Yes	5.55
B	PVDF-TFE-P	0	4.7	Yes	6.17
C	PVDF-TFE-P	0	0	Yes	7.13
D	PVDF-TFE-P	0.4	4.7	No	6.84
E (control)	PVDF	0	0	No	5.67

[1] part per hundred ratio to the mass of a-$Si_{0.64}Sn_{0.36}$/Ag

[2] Heated at 110°C in an argon flow for 24 hours

[3] The mass of a-$Si_{0.64}Sn_{0.36}$/Ag per unit area of the electrode.

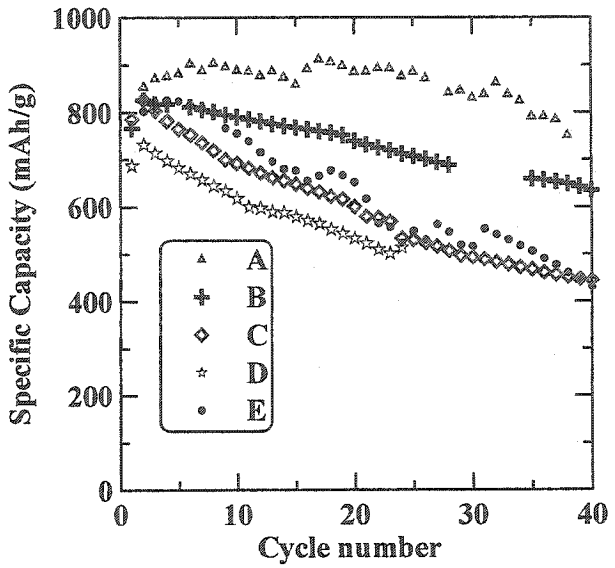

Figure 6.39 Specific capacity vs. cycle number for electrodes A-E (Table 6.5) showing the effect of the binder system on the cycling performance of a-$Si_{0.64}Sn_{0.36}$/Ag composite electrodes

When PVDF was used as the binder for the a-$Si_{0.64}Sn_{0.36}$/Ag electrode, the capacity faded quickly with increasing cycling number. The initial specific capacity is 810 mAh/g, and only about 60% of the capacity was maintained after 30 cycles (data set e in Figure 6.39).

Data sets B and C in Figure 6.39 show the results of cells with and without the coupling agent (APTES), respectively. If no APTES was added, the cell was as poor as the control cell (data set e in Figure 6.39). With the addition of 4.7 pph APTES (with respect to the mass of a-$Si_{0.64}Sn_{0.36}$/Ag), the cycling performance of a-$Si_{0.64}Sn_{0.36}$/Ag was greatly improved as shown by data set B in Figure 6.39. If 0.4 pph TETA was added as well as 4.7 pph APTES, a further improvement to the capacity retention of a-$Si_{0.64}Sn_{0.36}$/Ag was obtained as shown by data set A in Figure 6.39. A stable specific

capacity of about 800 mAh/g was maintained for about 40 cycles. If the electrode containing TETA and APTES was not thermally treated, the cycling result (data set d in Figure 6.39) is as bad as the control cell. Apparently, the adhesion promoter, crosslinking agent and the post thermal treatment are critical to improve the cycling performance of a-$Si_{0.64}Sn_{0.36}$/Ag composite electrodes.

Although the crosslinking and coupling reactions can proceed at room temperature, more active sites, >C=C<, for the crosslinking agent and the adhesion promoter can be obtained with a thermal treatment at 110°C in an argon flow. The heating at 110°C might also help to remove the moisture from the electrodes. A low temperature of 110°C was selected to avoid the crystallization of a-$Si_{0.64}Sn_{0.36}$/Ag.

6.6.3 Effect of the electrode thickness and the electrolyte

The capacity of electrode A shown in Figure 6.39 faded quickly after 40 cycles. In order to collect more data to investigate the capacity retention of a-$Si_{0.64}Sn_{0.36}$/Ag composite electrodes under extensive cycling, thin electrodes (about 3.0 mg/cm^2 active material) with the best recipe (electrode A in Table 6.5) were prepared and the cells were cycled at a higher current, 160 mA/g. Figure 6.40 shows the capacity versus cycle number for Li/(a-$Si_{0.64}Sn_{0.36}$/Ag) cells using the thin electrodes described above. The cells used different electrolyte salts. Some cells, such as the one using LiBETI electrolyte, had a small capacity at the beginning. After several activation cycles, the cells recovered completely and cycled well (see Figure 6.41). It is believed that there was a high resistance surface layer, i.e. LiOH and Li_2CO_3, on the surface of the Li foil counter electrode. The initial impedance was quite high and the cell was unable to provide its

expected capacity at the high current density (0.48 mA/cm^2) applied. However, after several activation cycles, fresh lithium surface was exposed and the cell impedance dropped. After that, the cell could be cycled as expected.

The capacity versus cycle number for a Li/(a-$Si_{0.64}Sn_{0.36}$/Ag) cell using $LiPF_6$ electrolyte is shown as the open triangles in Figure 6.40. The cell was cycled for 160 cycles while maintaining more than 55% of its maximum capacity, which is much better than the results shown in Figure 6.39. The only difference between these two cells is the thickness of the electrodes. It seems that a thinner electrode is preferred for extensive cycling.

Figure 6.40 also shows a comparison between different electrolytes. The $LiBF_4$ electrolyte is very poor since that cell lost about 90% of its capacity in 10 cycles. Generally, cells using $LiN(SO_2CF_2CF_3)_2$ (LiBETI) electrolyte had the best performance. The significant impact of the salts might be associated with the chemical stability of the salts and the SEI formed. LiBETI has a high chemical stability, and HF will not form as the SEI forms [75]. HF could damage the chemical bonding between the binder and the a-$Si_{0.64}Sn_{0.36}$/Ag particles. The SEI formed in $LiBF_4$ electrolyte has a high concentration of LiF according to the literature [76, 77]. The poor cycling performance of the cells using $LiBF_4$ electrolyte might result from the poor elasticity of the SEI (LiF).

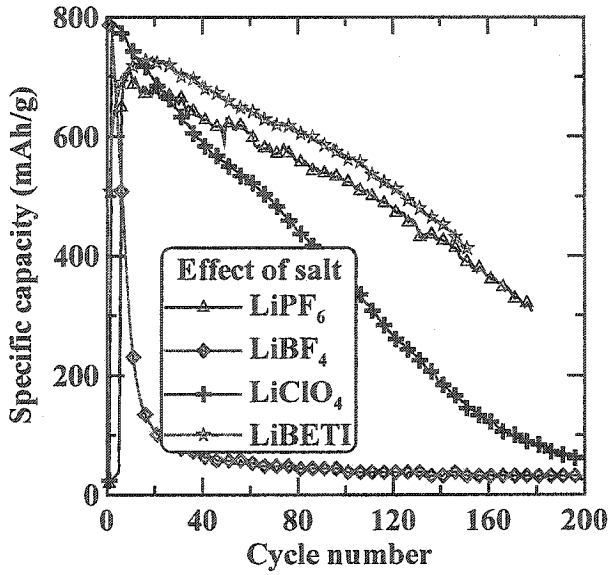

Figure 6.40 Specific capacity vs. cycle number for thin electrodes showing the effect of the electrolyte. Notice the electrolytes used are 1M salt in EC/DEC (1:2, v/v)

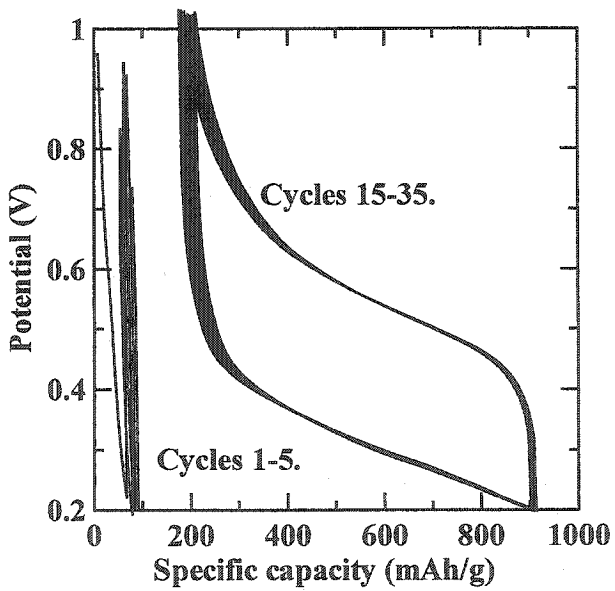

Figure 6.41 Voltage versus specific capacity of a Li/(a-$Si_{0.64}Sn_{0.36}$/Ag) cell using the LiBETI-based electrolyte

6.7 Mechanical degradation of binder

Although the tether model has been described in detail in chapter 1, this model is briefly repeated here to show the motivation for the in-situ resistance experiment. Figure 6.42a schematically shows the initial state of the composite electrode. Figure 6.42b shows a compact electrode during discharge after lithium atoms have been inserted into active material particles and the particles expand. Figure 6.42c shows changes in the electrode that can occur when a compact electrode (shown in Figure 6.42b) is further discharged. These changes include; (a) "shuffling" of the active material particles, (b) highly stretched tethers, (c) broken tethers, and (d) electrically isolated particles. The mechanical degradation of the binder system will lead to electrical resistance growth of the electrode.

If a gap is incorporated into the middle of the current collector, we can study the mechanical degradation of the binder system (tethers) during charge/discharge cycling by monitoring the resistance of the electrode film across the gap (Figure 6.42d). The two half-current-collectors are electrically connected during charge/discharge cycling. When measuring the electrode resistance, the cell is placed in an open circuit state, and the half-current-collectors are disconnected and used to measure the resistance of the electrode film across the gap.

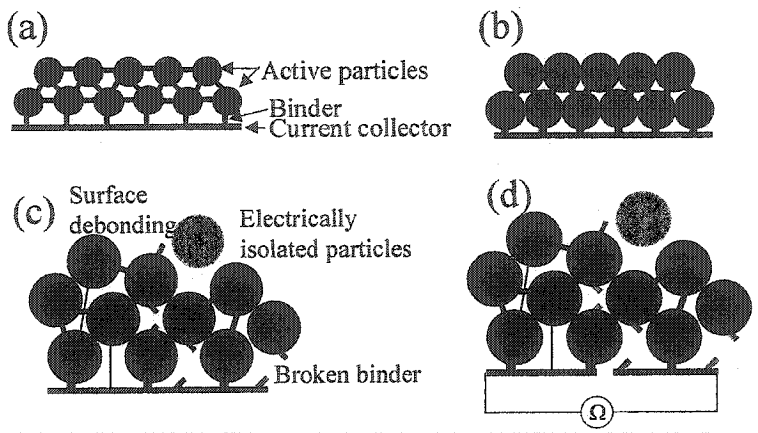

Figure 6.42 Schematic of the tether model showing the motivation for the in-situ resistance experiment

6.7.1 In-situ resistance of MCMB electrodes

MCMB has excellent cycling performance and its electrochemical properties have already been well characterized [78-80]. The electrical conductivity of graphite with different lithium contents has also been reported in the literature [78]. Therefore, graphitized MCMB is a good control material to verify the experiment and the interpretation of the data.

An in-situ cell incorporating a MCMB electrode was first discharged or charged to a certain state of charge using a specific current of 30 mA/g with the leads L and R (shown in Figure 3.16) connected together. The potential range of the in-situ cell during the experiment was 0.0-1.0 V. After each charge/discharge operation, the current was set to 0 with the leads L and R connected for 10 minutes. This helps to eliminate concentration gradients of Li^+ ions and Li atoms in the in-situ cell. Then a sequence of I = 0, -25, 0, 25, 0 μA was then applied through the leads L and R. Each segment in the current sequence was 10.0 minutes long.

Figure 6.43 shows typical voltage-time data for the MCMB electrode in response to the applied current. The voltage response to the square input current is almost a square wave, except that there are small curvatures at the very beginning of each segment. This means that the time constant of the RC response is quite small (< 2 min) and that it is safe to consider the resistance of the electrode as a simple ohmic system. Figure 6.43 also schematically shows a simple calculation of the resistance of the MCMB electrode.

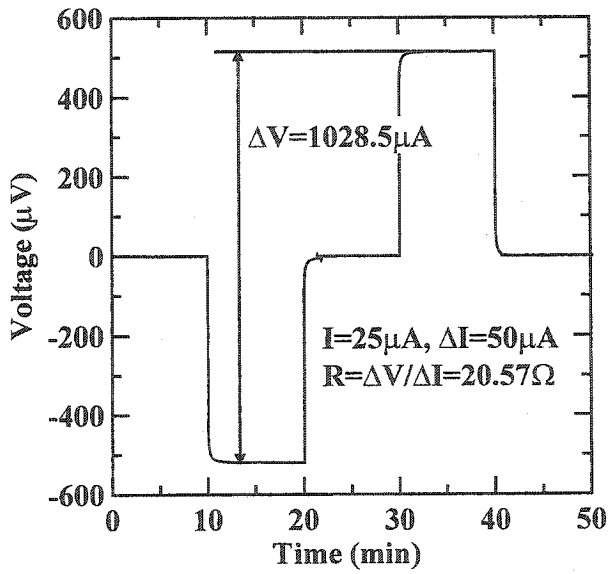

Figure 6.43 A typical voltage response of the MCMB electrode to the pulse current sequence. A sample calculation of the electrode resistance is included in the Figure.

Figure 6.44a shows the electrical resistance of the MCMB electrode as a function of the cumulative capacity. The cell potential vs. Li is also shown in Figure 6.44b. The resistance of the MCMB electrode follows an obvious trend. The resistance of the electrode increased slightly at the beginning of the initial discharge. This probably resulted from the formation of SEI on the MCMB surface. After that, the resistance

decreased when the lithium was inserted into MCMB and increased when the lithium was removed from MCMB. Based on results in the literature [78] we expect Li_xC_6 to become more metallic during the insertion of lithium and hence the resistance of the electrode decreases as lithium is added.

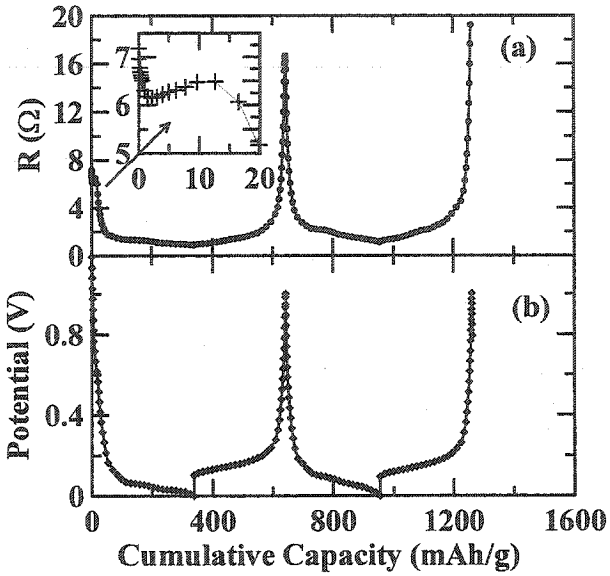

Figure 6.44 (a) The resistance of the MCMB electrode and (b) the cell potential vs. the cumulative capacity of the MCMB electrode. A pulse current sequence of 0, -25, 0, 25, and 0 μA was applied to measure the resistance.

6.7.2 In-situ resistance of an a-$Si_{0.64}Sn_{0.36}$/Ag electrode incorporating PVDF binder

Compared to MCMB, a-$Si_{0.64}Sn_{0.36}$/Ag has much larger volume changes during charge/discharge cycling, which leads to the shuffling of a-$Si_{0.64}Sn_{0.36}$/Ag particles and to the mechanical degradation of the binder system as explained earlier in this thesis and in reference [70]. Since the cells incorporating 20 pph SS showed reasonable cycling performance, 20 pph SS was also added to the electrode for in-situ resistance

experiments. The cell was charged/discharged with a constant specific current of 60 mA/g between 0.2 and 1.0 V. A small current pulse amplitude of 1 μA was applied when measuring the resistance of the electrode across the gap to avoid a large potential difference between the two half-electrodes.

Figure 6.45 shows a typical voltage response of an a-$Si_{0.64}Sn_{0.36}$/Ag electrode to the square current input. Even at the beginning when no current was applied (i.e. time < 10 min), the baseline starts from a potential different from 0 and decays approximately exponentially. Therefore, a first order exponential decay function (Equation 6-7) was adopted to model the baseline of the voltage response.

$$Baseline = A + B \times \exp(-kt) \tag{6-7}$$

A typical fit to the experimental data using the equivalent circuit (see Figure 3.20) is also shown in Figure 6.45. The data collected during the first two current sequences (0 and 1 μA, i.e. 0-20 minutes) was fitted to obtain R, R_i and C for most of the data collected.

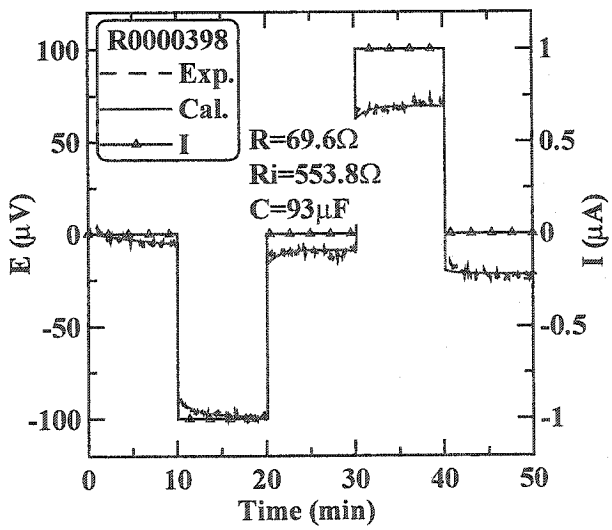

Figure 6.45 A typical voltage response of an a-$Si_{0.64}Sn_{0.36}$/Ag electrode to the pulse current sequence

Figure 6.46a shows the voltage profile of the a-$Si_{0.64}Sn_{0.36}$/Ag electrode during the first two cycles. The values of R, R_i and C obtained from the *in-situ* resistance experiment are also shown as functions of the cumulative capacity in Figures 6.48b, c and d, respectively. Several significant features can be noticed in Figure 6.46. The RC response of the electrode to the pulsed current input is obvious, and can be obtained by fitting the voltage response with the equivalent circuit (Figure 3.20). The initial resistance of the a-$Si_{0.64}Sn_{0.36}$/Ag electrode is about 80 Ω and a small peak (about 100 Ω) occurs at the beginning of the first discharge. After that, the resistance decreases during discharge. However, when the discharge capacity is larger than about 150 mAh/g (the volume expansion is greater than about 20%), the resistance remains roughly constant at about 50 Ω during the remainder of the first discharge.

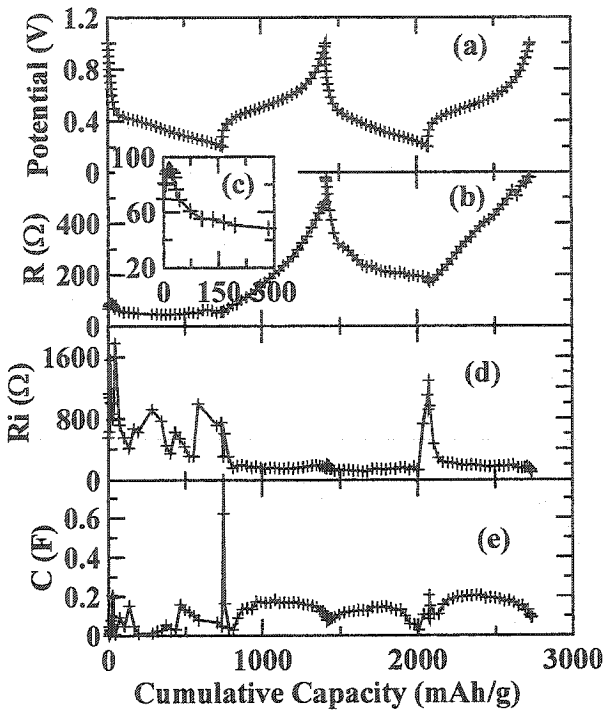

Figure 6.46 (a) Cell potential, (b) electrical resistance, (c) expanded view of the electrical resistance at the start of the experiment, (d) ionic resistance and (e) capacitance of the a-$Si_{0.64}Sn_{0.36}$/Ag electrode incorporating PVDF binder and 20 pph Super-S carbon black. A pulse current sequence of 0, -1, 0, 1, and 0 μA was applied to measure the resistance.

Figure 6.46d shows that the ionic resistance (R_i) of the a-$Si_{0.64}Sn_{0.36}$/Ag electrode during the first discharge is quite high compared to R_i during the following steps. Moreover, R_i always peaks at the bottom of the discharge. Figure 6.46e shows that the capacitance of the equivalent circuit is roughly constant, except when R_i is large and when R is small. This behavior is very repeatable and was observed from all the a-$Si_{0.64}Sn_{0.36}$/Ag electrodes we tested incorporating different binder systems. The fitted values of R_i and C also show large fluctuations during the first discharge, which can be

explained by considering the equivalent circuit model (Figure 3.20). When R is small, the contribution of the parallel R_iC path to the circuit impedance is insignificant. However, the fitting program will still find a set of fitting parameters for R_i and C that give the best fit between the experiment and the calculation, but the confidence in these fitted parameters will be low. The large fluctuations in both R_i and C are believed to be caused by the insensitivity of the calculated curves to the values of R_i and C when R is small.

We now discuss the interpretation of the results from the a-$Si_{0.64}Sn_{0.36}$/Ag experiments shown in Figure 6.46. At the start of the experiment, the a-$Si_{0.64}Sn_{0.36}$/Ag particles are "loosely" embedded in the binder system, or "tether" network [70]. The pores of the electrode are filled with the liquid electrolyte to provide necessary ionic paths. When the cell is initially discharged, the particles expand, and the electrode becomes more tightly packed. Hence, it is reasonable for R to decrease. After a certain discharge level, the a-$Li_xSi_{0.64}Sn_{0.36}$/Ag particles touch each other, the porosity cannot be reduced further, and the electrical conductivity of the touching a-$Li_xSi_{0.64}Sn_{0.36}$/Ag particles will dominate the conductivity of the electrode. Hence, the resistance of the electrode will remain at a relatively low level although the shuffling of particles and breaking of "tethers" is occurring during this step. When the cell is charged (removing lithium), the a-$Li_xSi_{0.64}Sn_{0.36}$/Ag particles shrink and the electrode becomes less tightly packed. The a-$Si_{0.64}Sn_{0.36}$/Ag particles will lose direct contact with one another, and the effect of the broken binder "tethers" will appear in the electrical resistance. Thus, the electrical resistance will increase significantly as the a-$Li_xSi_{0.64}Sn_{0.36}$/Ag particles shrink, as is observed in Figure 6.46b. The high electrical resistance at the top of charge results

from the breaking of the binder "tethers". It is our goal to find an elastomeric binder to reduce the amount of broken "tethers" and hence allow good cycling performance of electrodes with high-volume-change materials, such as a-$Si_{0.64}Sn_{0.36}$/Ag.

Figures 6.47a and 6.47b show the voltage response of the electrode to the current pulse sequence at 0.2 V of the 1st and 2nd cycle respectively. It is very easy to observe the growth of the resistance of the electrode from the change of the amplitude of the voltage response. The curves fitted to the experiments are also shown in Figure 6.47. Figures 6.48a-d show the response of the electrode to the current pulse sequence at 1.0 V, 0.6 V (discharging), 0.2 V, and 0.6 V (charging), respectively, during the second cycle. Figure 6.48 demonstrates that both the electrical resistance and the time constant of the RC response are modulated by the potential of the in-situ cell.

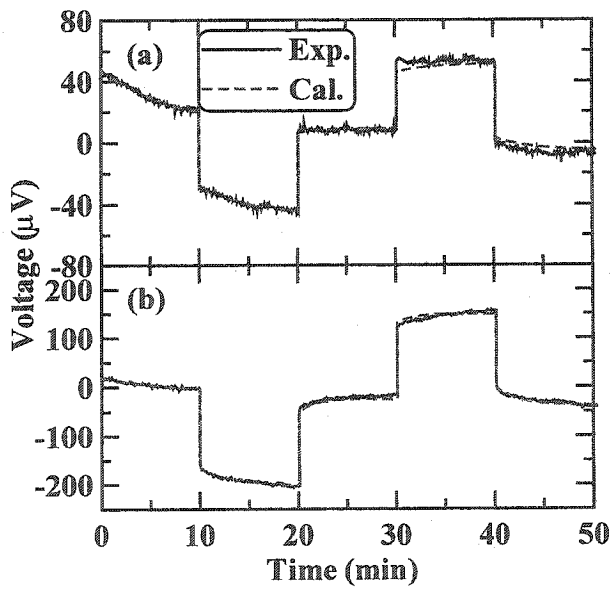

Figure 6.47 Voltage response of the a-$Si_{0.64}Sn_{0.36}$/Ag electrode incorporating PVDF binder to the pulse current sequence at 0.2 V for the (a) 1st and (b) 2nd cycle. The experimental data are the solid curves and the calculated results are the dashed curves.

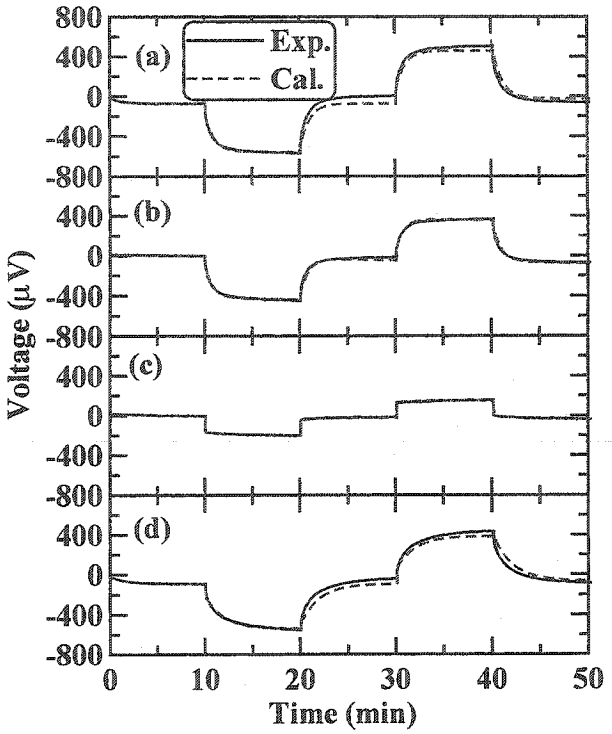

Figure 6.48 Voltage response of the a-$Si_{0.64}Sn_{0.36}$/Ag electrode incorporating PVDF to the pulse current sequence at (a) 1.0 V, (b) 0.6 V during discharge, (c) 0.2 V, and (d) 0.6 V during charge. The results were collected during the 2nd cycle of the cell. The experimental data are the solid curves and the calculated results are the dashed curves.

6.7.3 In-situ resistance of an a-$Si_{0.64}Sn_{0.36}$/Ag electrode incorporating PVDF-TFE-P binder

In section 6.6, we discussed an elastomeric binder system, which significantly improved the cycling performance of a-$Si_{0.64}Sn_{0.36}$/Ag composite electrodes. It is therefore of great interest to study the resistance changes of an a-$Si_{0.64}Sn_{0.36}$/Ag electrode incorporating the proposed PVDF-TFE-P-based elastomeric binder system. An in-situ resistance cell was assembled with the proposed composite electrode recipe. The cell was discharged and charged using a constant specific current of 60 mA/g between 0.2 V

and 1.0 V. The current pulse sequence applied to measure the resistance was 0, -1, 0, 1 and 0 μA.

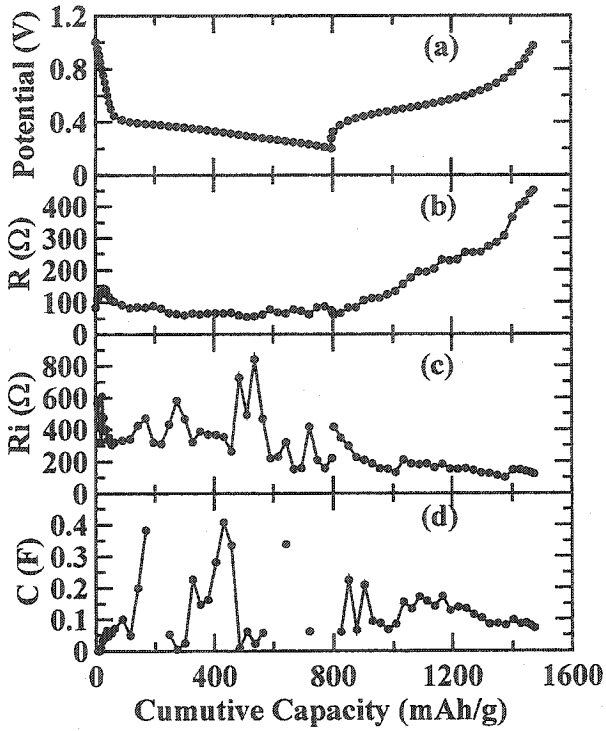

Figure 6.49(a) cell potential, (b) electrical resistance, (c) ionic resistance and (d) capacitance of the a-$Si_{0.64}Sn_{0.36}$/Ag electrode incorporating a PVDF-TFE-P-based elastomeric binder. A pulse current sequence of 0, -1, 0, 1, and 0 μA was applied to measure the resistance.

Figure 6.49 shows the results of the in-situ experiment on the a-$Si_{0.64}Sn_{0.36}$/Ag electrode incorporating the PVDF-TFE-P-based elastomeric binder. Similar to the results for the PVDF electrode shown in Figure 6.46, the electrical resistance of the electrode is almost constant during the first discharging step. The resistance during the first charge also increases quickly just as it did in Figure 6.46. The behavior of the PVDF and

PVDF-TFE-P binders during the first cycle are very similar. However, the capacity retention of a-$Si_{0.64}Sn_{0.36}$/Ag electrodes using PVDF-TFE-P binder is better than electrodes using PVDF binder, so it is important to monitor the resistance changes of these electrodes over many discharge-charge cycles.

It took 1~1.5 hours to measure a single data point in Figure 6.49. It took about 4 days to measure a complete cycle. Therefore, a faster experiment was needed to investigate the resistance changes as a function of cycle number. Another two in-situ cells were made with the proposed PDVF-TFE-P recipe and were investigated with a faster experiment. In the fast experiment, the specific current was set to 100 mA/g, and the resistance was only measured at 1.0 V, 0.6 V (discharging), 0.2 V and 0.6 V (charging). Also, a longer period of 30 minutes was allocated after each charge/discharge operation for the cell to relax and eliminate the Li^+ ion and Li atom concentration gradients in the cell. The current pulse sequence applied to measure the resistance was set to 0, -1, 0, 1 and 0 μA. Each segment lasted for 20 minutes.

Figure 6.50 shows the electrode resistance for two in-situ cells incorporating electrodes of a-$Si_{0.64}Sn_{0.36}$/Ag in PVDF-TFE-P as a function of both the cell potential and the cycle number. The solid symbols represent the results for an in-situ cell for up to ten cycles, and the hollow symbols represent the results for another in-situ cell, which completed only four cycles before the experiment was terminated. The results for both cells are in good agreement. The resistance reaches its maximum at the top of the charging step and reaches its minimum at the bottom of the discharging step, as in Figures 6.46 and 6.49. There is a big jump in resistance between the first cycle and the second cycle. This jump may be attributed to the breaking of tethers during the first

discharge step. After the first cycle, the resistance increases slowly with the cycle number. This is believed to be caused by the fatigue of the binder system under cyclic deformation.

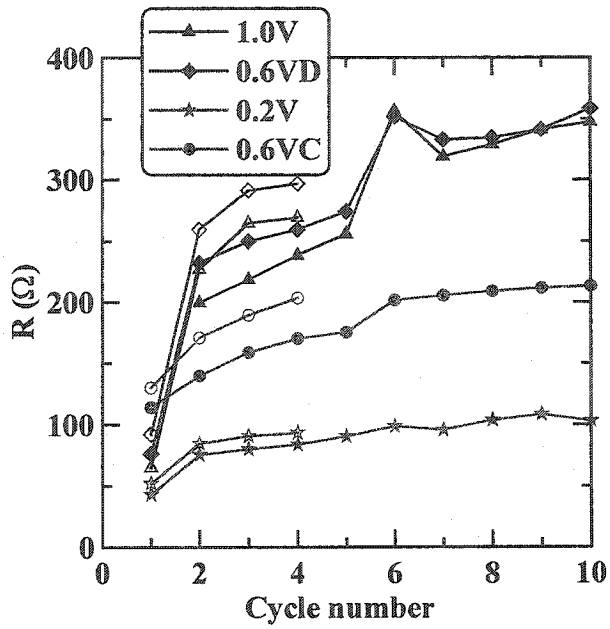

Figure 6.50 Electrical resistance of the a-$Si_{0.64}Sn_{0.36}$/Ag electrode incorporating the PVDF-TFE-P-based elastomeric binder vs. cycle number at different cell potentials. The data was collected with the fast experiment and a pulse current sequence of 0, -1, 0, 1, and 0 μA was applied to measure the resistance. The open symbols represent data for the second cell.

Figure 6.51 shows the resistance changes for an a-$Si_{0.64}Sn_{0.36}$/Ag electrode using PVDF as the binder for comparison. The experiment described by Figure 6.51 was performed under identical conditions to the experiment described by Figure 6.50. Compared to the results shown in Figure 6.48, the resistance of the electrode during the first cycle is quite large. This can result from a different gap width in the middle of the

current collectors since the narrow gap (about 1 mm wide) was not well controlled during sputtering. A comparison of Figures 6.50 and 6.51 shows that the electrode resistance increases more rapidly with cycle number for the PVDF binder than for the elastomeric PVDF-TFE-P binder. Apparently, the increase of the electrode resistance with cycle number is significantly suppressed by using an elastomeric binder with APTES.

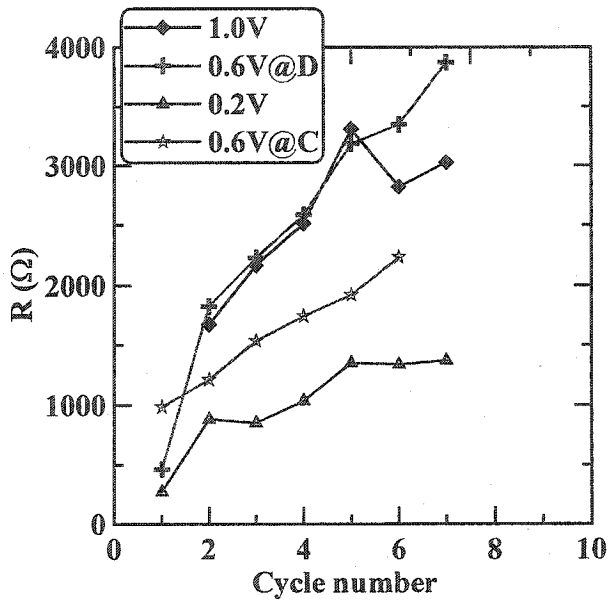

Figure 6.51 Electrical resistance of the a-$Si_{0.64}Sn_{0.36}$/Ag electrode using PVDF as the binder vs. cycle number at different cell potentials. The data was collected with the fast experiment and a pulse current sequence of 0, -1, 0, 1, and 0 μA was applied to measure the resistance.

Figure 6.52 shows the ionic resistance of the electrode using the PVDF-TFE-P-based elastomeric binder as functions of both the cell potential and the cycle number. The ionic resistance of the electrodes is stable in the 100-200 Ω range, except that it hikes at the

bottom of each discharging step. Figure 6.53 shows the voltage response of the same electrode to the pulse current sequence input at 0.2 V illustrating the dependence of the resistance on the cycle number. The resistance of the electrode was initially small (Figure 6.53a), and jumped up to about 100 Ω at the second cycle (Figure 6.53b). Only small resistance growth can be seen from the second cycle to the 10^{th} cycle (Figure 6.53d). Figure 6.54 shows the voltage response of the electrode to the pulse current sequence input during the 10^{th} cycle demonstrating both the modulation of the resistance of the electrode and the time constant of the RC response on the cell potential.

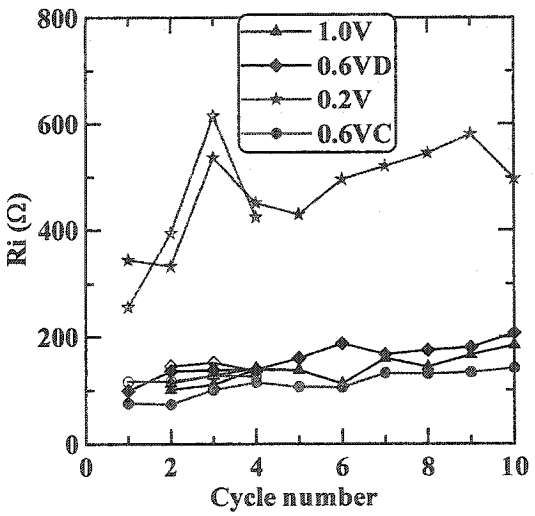

Figure 6.52 Ionic resistance change of the a-$Si_{0.64}Sn_{0.36}$/Ag electrode incorporating the PVDF-TFE-P-based elastomeric binder vs. cycle number at different cell potentials. The data was collected with the fast experiment and a pulse current sequence of 0, -1, 0, 1, and 0 μA was applied to measure the resistance.

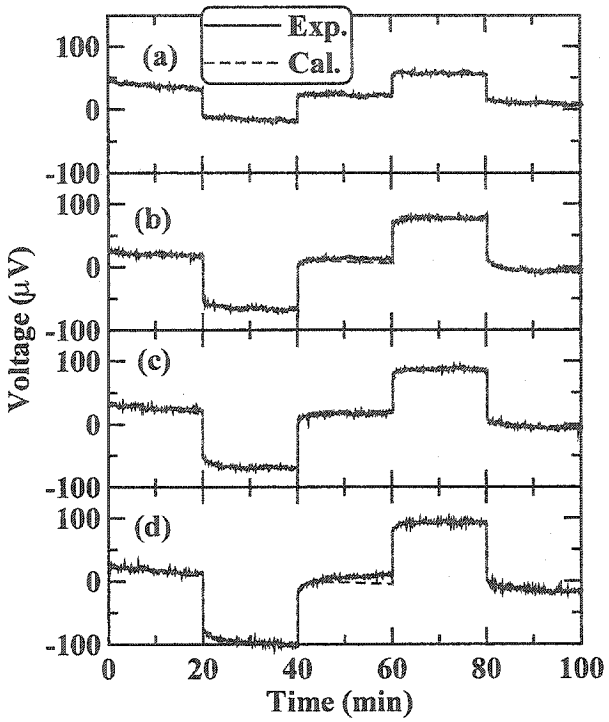

Figure 6.53 Voltage response of the a-$Si_{0.64}Sn_{0.36}$/Ag electrode incorporating the PVDF-TFE-P-based elastomeric binder to a pulse current sequence input at 0.2 V of the (a) 1st, (b) 2nd, (c) 5th, and (d) 10th cycle. . The experimental data are the solid curves and the calculated results are the dashed curves.

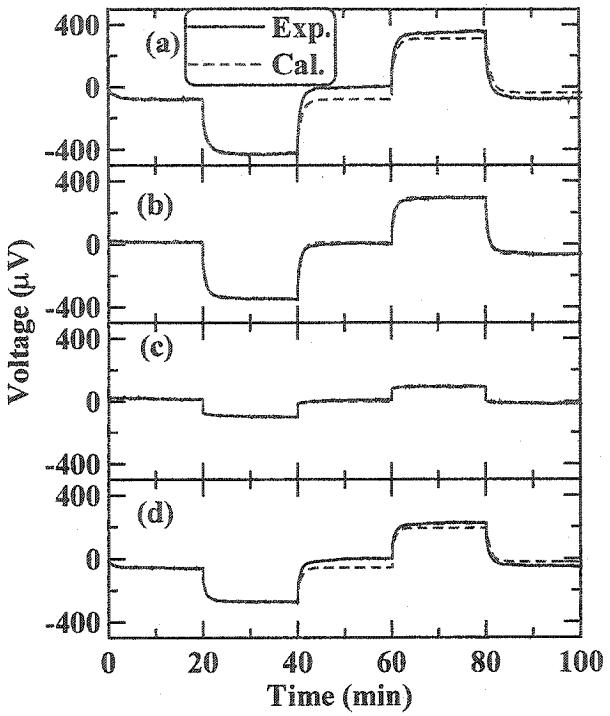

Figure 6.54 Voltage response of the a-$Si_{0.64}Sn_{0.36}$/Ag electrode incorporating the PVDF-TFE-P-based elastomeric binder to the pulse current sequence at (a) 1.0V, (b) 0.6V during discharge, (c) 0.2V, and (d) 0.6V during charge for the 10^{th} cycle. The experimental data are the solid curves and the calculated results are the dashed curves

6.8 Summary

The mechanical and electrical properties of poly(vinylidene fluoride-tetrafluoroethylene-propylene) (PVDF-TFE-P)-based binders were investigated carefully. A TETA-based crosslinking recipe was proposed to improve the mechanical properties of the PVDF-TFE-P-based binder so that it can tolerate the large volumetric change of a-$Si_{0.64}Sn_{0.36}$/Ag particles during charge/discharge cycling.

The addition of the coupling agent, APTES, greatly improves the adhesion strength between the PVDF-TFE-P matrix and the SS particles and active material particles in the

composite electrodes. However, APTES cannot suppress the viscoelastic flow of polymer chains efficiently. The crosslinking agent, TETA, is used to enhance the interaction between polymer chains and to improve the mechanical properties of the polymer matrix. The results of peel tests show that the addition of TETA competes with APTES to react with the active sites in the polymer backbone of chains. It is apparently important to balance the amount of TETA and APTES to maximize the performance of the binder system. In the optimized recipe, the ratio of TETA to APTES is very small (0.4 : 4.7), which suggests that APTES is more important than TETA.

The capacity retention of a-$Si_{0.64}Sn_{0.36}$/Ag composite electrode was significantly improved by simply replacing PVDF binder with the proposed PVDF-TFE-P-based elastomeric binder. The critical importance of the elastomeric binder system was also supported by the results of in-situ resistance experiments.

It was also shown that the thickness of the electrodes and the choice of the electrolyte salt had a big impact on the capacity retention of a-$Si_{0.64}Sn_{0.36}$/Ag. More detailed experiments on the impact of the thickness of the electrodes and the electrolyte type will be presented in the next chapter.

Chapter 7 Combinatorial and In-situ Experiments

7.1 Introduction

Chapter 6 has successfully demonstrated the importance of elastomeric binders for high-volume-change amorphous alloy composite electrodes. The capacity retention of a-$Si_{0.64}Sn_{0.36}$/Ag composite electrodes was significantly improved by replacing the PVDF-based binder with a PVDF-TFE-P-based elastomeric binder. However, even with the use of an optimized elastomeric binder, it is still nontrivial to maximize the cycling performance of high-volume-change amorphous alloys, as we will illustrate in this chapter. Unlike electrodes of graphitized carbons, commonly used in Li-ion batteries today, the capacity retention of a-$Si_{0.64}Sn_{0.36}$/Ag electrodes is dramatically affected by the areal loading of the active material, the lower cutoff potential, and the electrode compression as well as the mechanical properties of the binder system. Variations in electrode design parameters that would have little or no effect on graphite-based electrodes have a strong effect on high-volume-change electrodes. The experimental evidence we will present here strongly suggests that a good understanding of the binder problem is crucial for the optimization, development, and commercialization of metallic alloy anode materials. We urge the community to get involved in investigating and understanding the binder problem.

7.2 Characterization of the thickness gradient

The combinatorial electrodes were prepared as described in sections 3.4.4 and 3.4.5. Figure 7.1a shows the loading of the active material, a-$Si_{0.64}Sn_{0.36}$/Ag on an electrode disc

(Φ = 12.8 mm, A=1.29 cm^2) as a function of position along the thickness gradient direction. The electrode film was prepared with the PVDF-TFE-P-based recipe described in section 3.4.5. There are 8 data sets shown in Figure 7.1a for each of the rows a-h shown in Figure 3.4. Apparently, the electrode film is uniform in the spreading direction because all the data sets agree well with each other. Furthermore, the loading of the active material, a-$Si_{0.64}Sn_{0.36}$/Ag, increases linearly with the position of the electrodes along the film.

Figure 7.1b shows the thickness of the electrodes as a function of the electrode position. The thickness of the electrode starts from 20 μm, which is probably determined by the particle size of the active material. The 8 data sets corresponding to the 8 rows of electrodes show the same thickness gradient. In order to study the effect of the electrode compression on the cycling performance of the electrodes, three sets of electrodes (D, E, and F) were compressed at 9800, 19600 and 29400 PSI (pounds per square inch), respectively. The thickness of the electrodes after compression is also shown in Figure 7.1b. Compression greatly reduces the thickness of the electrodes, and the thickness decreases with applied pressure. The thickness of the electrodes was reduced by about 50% after full compression. Electrode compression enables cell manufacturers to maximize the active material loading in cells of fixed volume and is therefore a crucial variable to study.

Figure 7.2 shows the active material loading gradient and the thickness gradient of a-$Si_{0.64}Sn_{0.36}$/Ag electrodes using PVDF as the binder. Because these electrodes were used as the control samples, a small electrode matrix was prepared. Only 6 electrode sets with

4 electrodes in each set were prepared as shown in Figure 3.3. A reliable gradient is also shown in the PVDF-based electrode matrix.

The details of the characterization of each electrode set are listed in Tables 7.1 (PVDF-TFE-P-based electrodes) and 7.2 (PVDF-based electrodes).

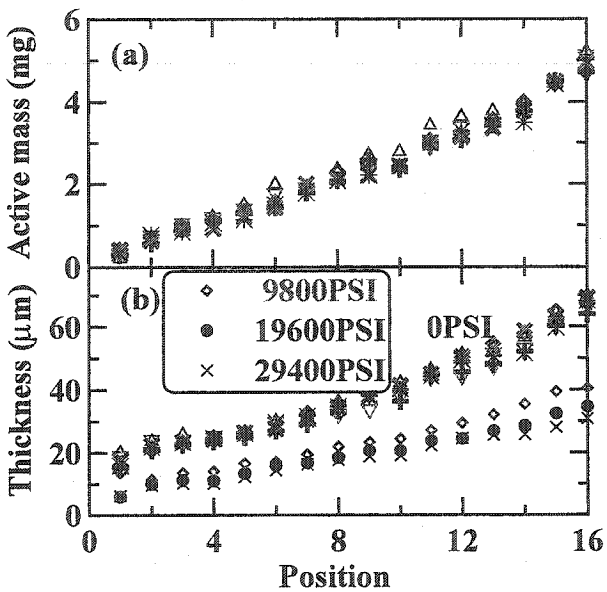

Figure 7.1 (a) The mass of active material per electrode and (b) the thickness of PVDF-TFE-P-based electrodes as functions of electrode position. Note that the thickness of electrodes D(9800 PSI), E(19600 PSI), and F (29400 PSI) after compression is also shown in the same graph.

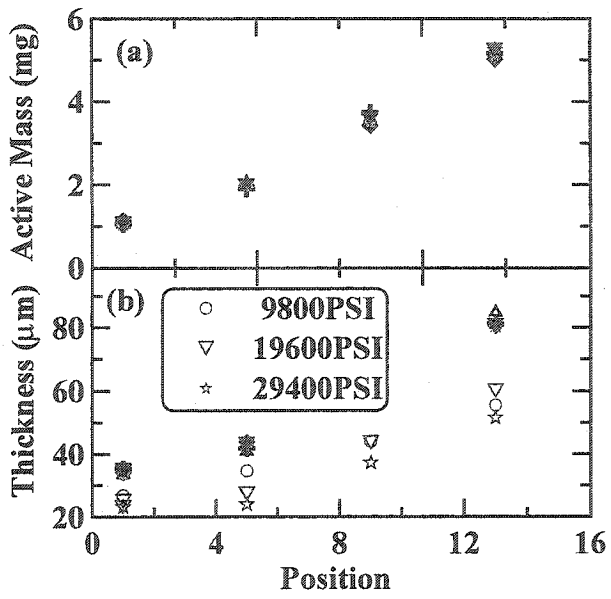

Figure 7.2 (a) The mass of active material per electrode and (b) the thickness of PVDF-based electrodes as functions of electrode position. Note that the thickness of electrodes D(9800 PSI), E(19600 PSI), and F (29400 PSI) after compression are also shown in the same graph.

Table 7.1 Experimental details of the PVDF-TFE-P-based electrodes used in the cycling tests

Row in Fig. 3.4	Cutoff potentials (V)	Specific Current (mA/g)	Compression (PSI)	Electrolyte
A	0.2-1.0	160	NA	1M $LiPF_6$ in EC/DEC (1:2)
B	0.1-1.0	160	NA	1M $LiPF_6$ in EC/DEC (1:2)
C	0.06-1.0	160	NA	1M $LiPF_6$ in EC/DEC (1:2)
D	0.2-1.0	160	9800	1M $LiPF_6$ in EC/DEC (1:2)
E	0.2-1.0	160	19600	1M $LiPF_6$ in EC/DEC (1:2)
F	0.2-1.0	160	29400	1M $LiPF_6$ in EC/DEC (1:2)
G	0.2-1.0	160	NA	1M $LiClO_4$ in EC/DEC (1:2)
H	0.2-1.0	160	NA	1M LiBETI in EC/DEC (1:2)

Table 7.2 Experimental details of the PVDF-based electrodes used in the cycling tests

Row in Fig. 3.3	Cutoff potentials (V)	Specific Current (mA/g)	Compression (PSI)	Electrolyte
A	0.2-1.0	160	NA	1M $LiPF_6$ in EC/DEC (1:2)
B	0.1-1.0	160	NA	1M $LiPF_6$ in EC/DEC (1:2)
C	0.06-1.0	160	NA	1M $LiPF_6$ in EC/DEC (1:2)
D	0.2-1.0	160	9800	1M $LiPF_6$ in EC/DEC (1:2)
E	0.2-1.0	160	19600	1M $LiPF_6$ in EC/DEC (1:2)
F	0.2-1.0	160	29400	1M $LiPF_6$ in EC/DEC (1:2)

7.3 Effect of the active material loading of electrodes

Figure 7.3 shows the cell potential versus specific capacity of the 16 PVDF-TFE-P-based electrodes in set C, which were not compressed, and were cycled between 0.06 and 1.0V using a $LiPF_6$-based electrolyte. The column number of each electrode (refer to Figure 3.4) is labeled on each small panel. The loading of the active material increases with the electrode column number. The cells cycled with a high Coulometric efficiency since the voltage profiles do not shift substantially to the right or left with the cycle number. Figure 7.3 shows that the cycling performance of the electrodes apparently depends on the active material loading. Electrodes 5-9 seem more promising than the others do. Detailed comparisons of specific capacity versus cycle number for these electrodes will be made later.

Figure 7.4 shows the specific capacity of a-$Si_{0.64}Sn_{0.36}$/Ag electrodes using the proposed PVDF-TFE-P-based elastomeric binder as functions of both the cycling number and the active material loading. The lower cutoff potential was set to 0.2 V. Cells 6 and 8 seem promising and have a good capacity retention. Almost 90% of the maximum capacity was retained after 100 cycles. Most of the cells had small capacity at the beginning because of the high impedance layer, i.e. LiOH and Li_2CO3, on the lithium foil counter electrode. After several activation cycles, the fresh lithium surface was exposed and the cells could be cycled as expected. It is not surprising to see that the capacity fades more quickly when the electrodes get thicker (from cell 8 to cell 16). As mentioned in previous chapters and in a previous publication [70] the capacity fading of a-$Si_{0.64}Sn_{0.36}$/Ag electrodes has been mainly attributed by us to interparticle motion and collisions, that we call "shuffling", during charge/discharge cycling, which leads to the

breaking of the binder tethers. The amount of shuffling that occurs in the top layers of electrode particles is amplified by the shuffling of particles closer to the current collector. Therefore, we expect the cycling performance to decrease as the thickness of the electrode increases.

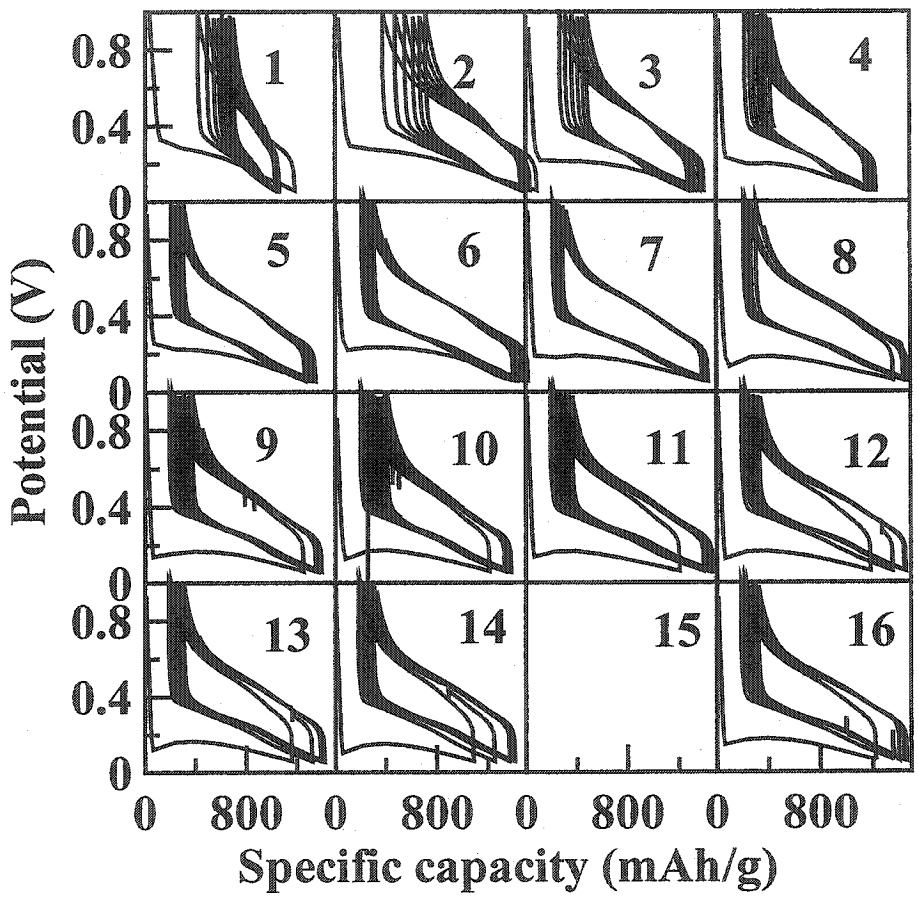

Figure 7.3 Voltage versus specific capacity of Li/(a-$Si_{0.64}Sn_{0.36}$/Ag) cells using the proposed PVDF-TFE-P-based elastomeric binder cycled between 0.06-1.0 V with a specific current of 160 mA/g. The electrodes were not compressed and the electrolyte used was 1M $LiPF_6$ in EC/DEC (1:2, v/v).

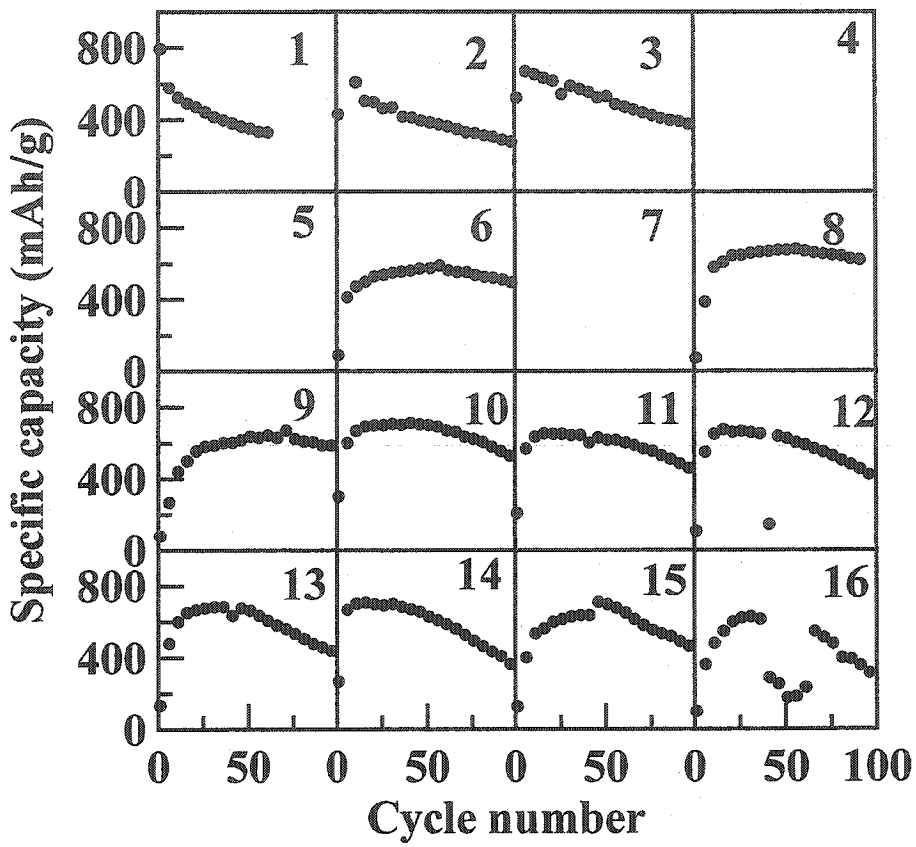

Figure 7.4 The specific capacity vs. cycle number showing the effect of electrode loading (thickness) on the capacity retention of a-$Si_{0.64}Sn_{0.36}$/Ag electrodes using the proposed PVDF-TFE-P-based elastomeric binder. The electrodes were not compressed. The cells were cycled between 0.2-1.0 V using a specific current of 160 mA/g. The electrolyte used was 1M $LiPF_6$ in EC/DEC (1:2, v/v).

The thinnest electrodes of those prepared (columns 1, 2, 3 in figure 3.4) did not even have enough material to evenly cover the surface of the current collector (copper foil). One can observe isolated particles and islands of a few particles by the naked eye. Because of the lack of electrical connection between islands, tether breaking can have a severe impact on the resistance growth of the electrode, since each island only has a "direct" current path down to the collector, as opposed to paths through other islands that

can occur in thicker, continuous, electrodes. Hence, the cells with very low active material loading (cells 1,2,3) apparently have worse capacity retention than cells 6 and 8.

As a comparison, Figure 7.5 shows the specific capacity of a-$Si_{0.64}Sn_{0.36}$/Ag electrodes using the PVDF binder as functions of both the cycling number and the active material loading. The capacity retention of the cells shown in Figure 7.5 is very poor. Almost all the capacity was lost in 100 cycles. Moreover, it seems that the active material loading has no impact on the capacity retention of the electrodes, which is quite different from the results shown in Figure 7.4. A possible explanation is that the poor performance of the PVDF binder overwhelmed the impact of the active material loading. The mechanical properties of the PVDF binder are so poor that the binder system was heavily damaged when discharged to 0.2V regardless of the active material loading.

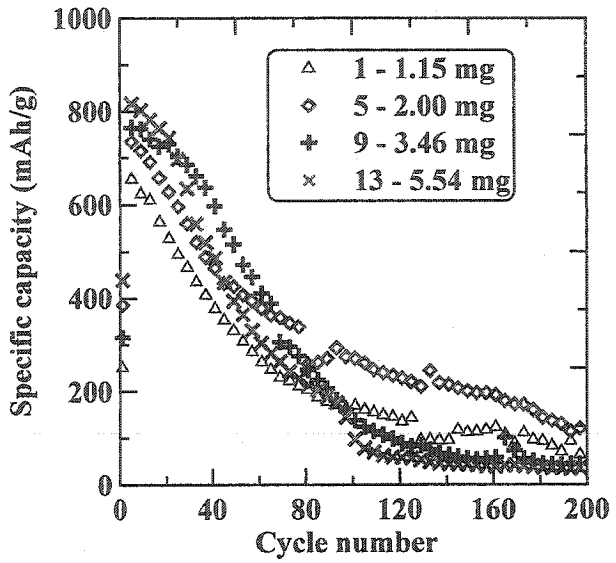

Figure 7.5 The specific capacity vs. cycle number showing the effect of electrode loading (thickness) on the capacity retention of a-$Si_{0.64}Sn_{0.36}$/Ag electrodes using the PVDF-based binder. The electrodes were not compressed. The cells were cycled between 0.2-1.0 V using a specific current of 160 mA/g. The electrolyte used was 1M $LiPF_6$ in EC/DEC (1:2, v/v).

7.4 Effect of the lower cutoff potential

In order to investigate the effect of the discharge level, and hence the volume change, on the cycling performance of the a-$Si_{0.64}Sn_{0.36}$/Ag electrodes, three sets of cells (A, B, and C) were cycled with a constant specific current of 160 mA/g between 0.2-1.0 V, 0.1-1.0 V, and 0.06-1.0 V, respectively. The potential ranges correspond approximately to volume changes of 125%, 160% and 200%, respectively [10]. The electrolyte used was 1M $LiPF_6$ in EC/DEC (1:2, v/v).

Figure 7.6 shows the specific capacity vs. cycle number of a-$Si_{0.64}Sn_{0.36}$/Ag electrodes showing the effect of the lower cutoff potential. The binder incorporated in

these cells was the PVDF-TFE-P-based elastomeric binder. As demonstrated in Figures 7.3 and 7.4, the electrodes in positions 6-9 are more promising than others are. Only cells in positions 6-9 were compared in Figure 7.6. The position of the cells is indicated on each small panel. The comparison of cells in each position shows a consistent trend. More capacity of a-$Si_{0.64}Sn_{0.36}$/Ag electrodes can be harnessed by lowering the cutoff potential. For instance, the cells can provide more than 1200 mAh/g capacity in the early cycles if cycled down to 0.06 V. However, the counter effect of a low cutoff potential is apparent. The large volumetric changes of the negative electrode material resulting from a lower cutoff potential accelerate the mechanical degradation of composite electrodes and hence increase the capacity fading of the electrodes. If the cells were cycled between 0.06 V and 1.0 V, more than 80% maximum capacity was lost in 100 cycles. If the lower cutoff potential was limited to 0.2 V, the capacity retention of the cells was quite good. Almost 90% maximum capacity remained after 100 cycles.

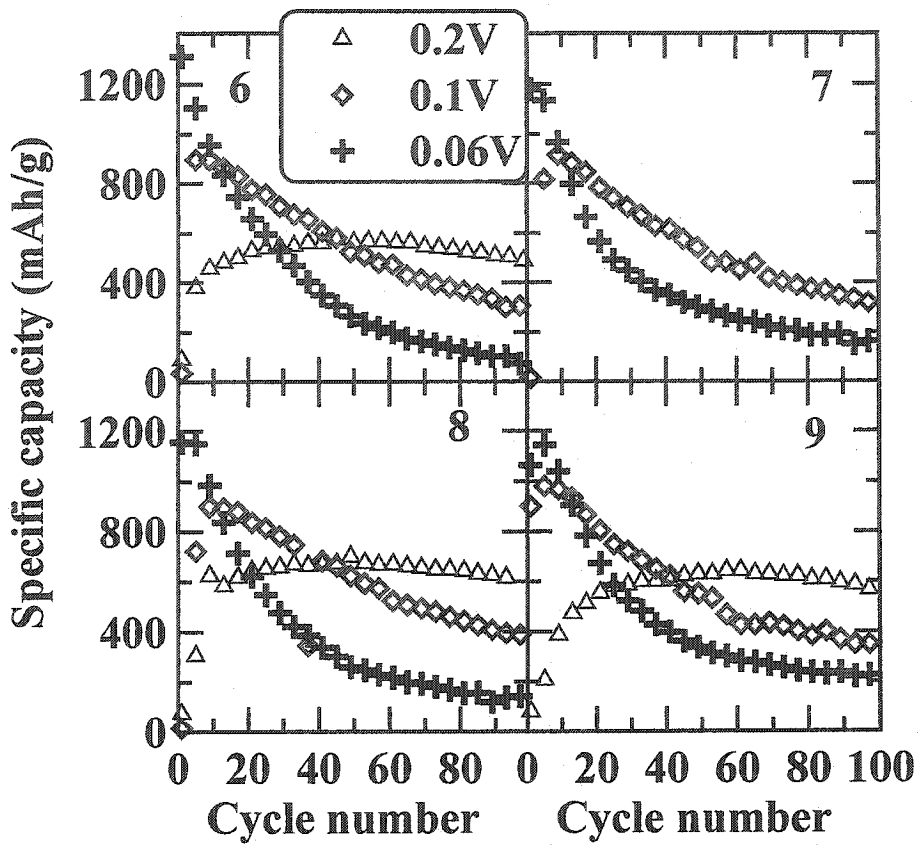

Figure 7.6 The specific capacity vs. cycle number showing the effect of the lower cutoff potential on the capacity retention of a-$Si_{0.64}Sn_{0.36}$/Ag electrodes using the proposed PVDF-TFE-P-based elastomeric binder. The electrodes were not compressed. The cells were cycled between 0.2-1.0 V using a specific current of 160 mA/g. The electrolyte used was 1M $LiPF_6$ in EC/DEC (1:2, v/v).

Figure 7.7 shows a comparison between the PVDF binder and the PVDF-TFE-P-based elastomeric binder. If the cells were cycled between 0.2 V and 1.0 V as suggested by Figure 7.6, significant differences can be observed between the PVDF binder and the PVDF-TFE-P-based elastomeric binder. The capacity retention of cells using the PVDF-TFE-P-based elastomeric binder is much better than that of the cells using PVDF binder. However, if the cells were cycled to a lower cutoff potential, the particle expansion ratio

apparently exceeds the tolerance limit of the PVDF-TFE-P-based elastomeric binder as well as the PVDF binder, a severe mechanical degradation of the binder systems in both cases resulted in poor capacity retention of the electrodes, and apparently overwhelmed the impact of the binder system. Hence, no significant difference was observed when the cells were discharged to 0.1 V and 0.06 V.

7.5 Effect of the compression of electrodes

In industry, electrode films are heavily compressed to maximize the active material loading in lithium-ion batteries. Typically, the thickness of electrodes can be reduced to about 50% after compression, substantial particle shuffling already occurs during the compression step. It is important to investigate the impact of electrode compression on the cycling performance of a-$Si_{0.64}Sn_{0.36}$/Ag composite electrodes.

Figure 7.8 shows the specific capacity vs. cycle number of a-$Si_{0.64}Sn_{0.36}$/Ag electrodes under different compression conditions. The binder used was the PVDF-TFE-P-based elastomeric binder. The comparison displays a very consistent trend. That is, the compression step significantly impaired the capacity retention of a-$Si_{0.64}Sn_{0.36}$/Ag electrodes. A comparison between the PVDF binder and the PVDF-TFE-P-based elastomeric binder also shows that no obvious difference was observed between the binders after the compression. This is because both electrode sets were in a very poor condition (broken tethers) after the compression. Another possible reason is that huge shuffling occurs in compressed electrodes even at 0.2 V since the porosity of the electrodes decreased after compression.

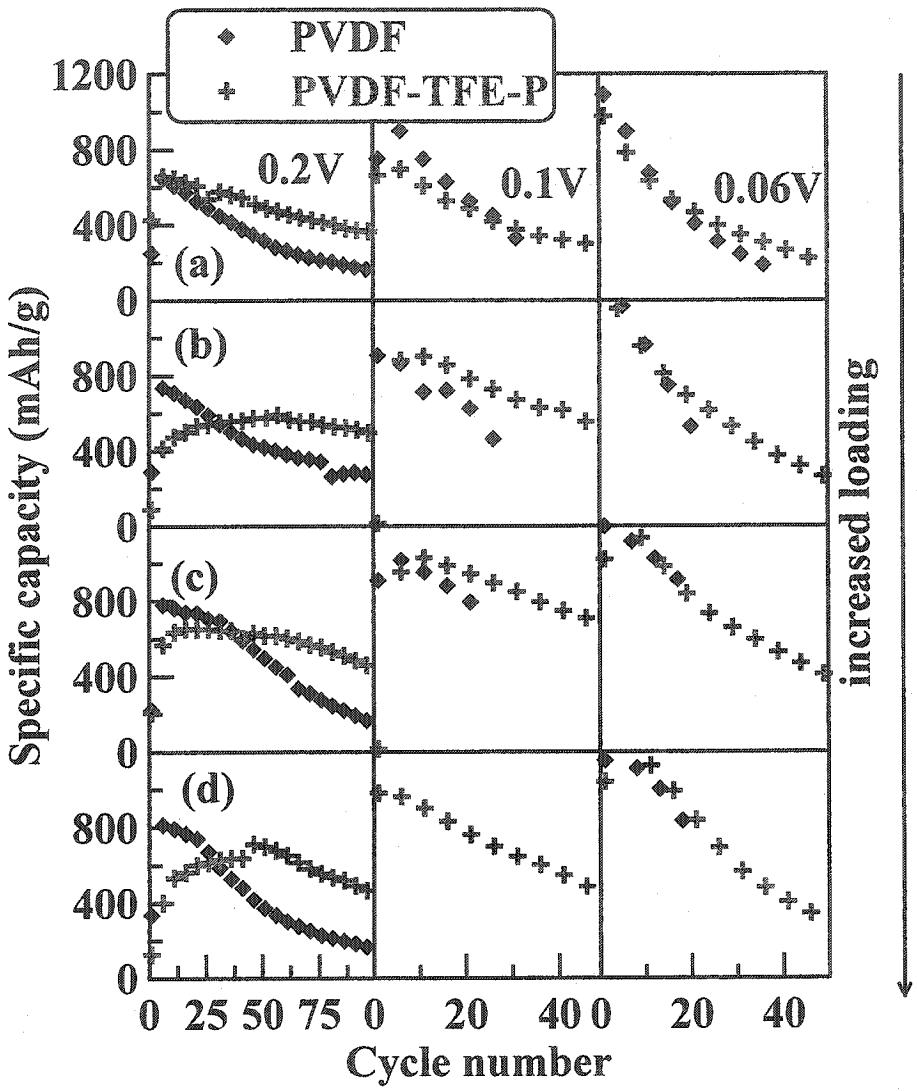

Figure 7.7 Specific capacities vs. cycle number of a-$Si_{0.64}Sn_{0.36}$/Ag electrodes showing the impact of the binder and the lower cutoff potential. The cells were cycled in the ranges of 0.2 –1.0 V (the first column), 0.1 – 1.0 V (the second column), and 0.06 – 1.0 V (the third column). The position of the PVDF-based electrodes and PVDF-TFE-P-based electrodes are 1/1 (row a), 5/6 (row b), 9/11 (row c), and 13/15 (row d). The pairs were selected based on a similar areal density of active material.

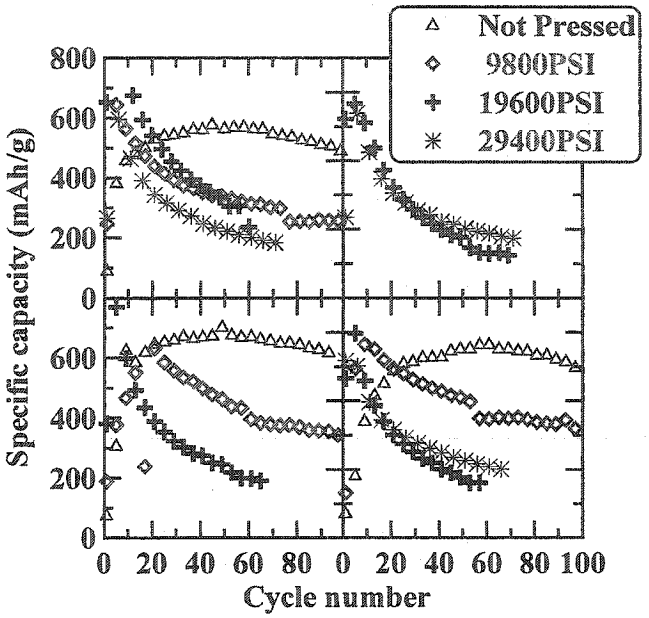

Figure 7.8 Specific capacity vs. cycle number of a-$Si_{0.64}Sn_{0.36}$/Ag electrodes using PVDF-TFE-P-based elastomeric binder showing the effect of compression. The cells were first discharged to 0.22 V and then cycled between 0.2 V and 1.0 V with a constant current of 160 mA/g.

7.6 Effect of the electrolyte type

Figure 7.9 shows the cycling performance of the Li/(a-$Si_{0.64}Sn_{0.36}$/Ag) cells using different electrolytes. Overall, the data for cells in the second row have the best capacity retention regardless of the electrolyte used. Generally, an areal density of about 2.0 mg/cm^2 is preferred. Comparing the capacity retention of the cells in each single panel, a consistent trend can be observed. That is, the cell using $LiClO_4$-based electrolyte has more rapid capacity fading, especially for the cells with thick electrodes. The advantage of LiBETI salt is obvious. The capacity retention of cells 5 to 8 using LiBETI is very good. Cells 13 and 14 have an areal density of about 3.0 mg/cm^2. Cells 13 and 14 using

$LiPF_6$-based electrolyte had relatively poor capacity retention: about 50% capacity remained after 100 cycles. On the other hand, the cells using LiBETI-based electrolyte were quite good and very small capacity fading was observed. Therefore, using LiBETI-based electrolyte can give us a wider operation window in terms of the active material loading.

7.7 Summary of the combinatorial experiment

In order to quantitatively investigate the capacity retention of all the cells, the cycle number, to which the capacity decreases to 80% of maximum capacity, was used as the indicator of the cycling performance. Figure 7.10a shows the effect of the lower cutoff potential on the cycling performance of a-$Si_{0.64}Sn_{0.36}$ electrodes. The cells cycled down to 0.06 V have very poor capacity retention. Less than 20 cycles were obtained before the capacity dropped below 80% of maximum. The cells cycled between 0.2 V and 1.0 V gave the best capacity retention. The cells having a loading range between 1.5 and 2.0 mg/cm^2 still maintained more than 80% capacity after 100 cycles.

Figure 7.10b shows the effect of electrode compression on the cycling performance of a-$Si_{64}Sn_{0.36}$ electrodes. Clearly, the cycling performance of the electrodes was severely impaired by compression. The negative impact of electrode compression has also been reported for Li-Sn alloy anodes [81]. The optimum active material loading remains between 1.5 and 2.0 mg/cm^2.

Figure 7.10c shows a comparison between different salts, $LiPF_6$, $LiClO_4$, and LiBETI. Generally, the cells using $LiClO_4$-based electrolyte gave the worst cycling performance and the cells using LiBETI-based electrolyte had the best cycling

performance. Moreover, the cells using LiBETI-based electrolyte tolerate a wider range in the active material loading. The difference between the salts might be caused by differences in chemical stability and in swelling behaviour of the binder in different electrolyte.

Most importantly, one must note that each of the 128 electrodes tested here would have shown at least 90% capacity retention had the active material been graphitized carbon instead of a-$Si_{0.64}Sn_{0.36}$. An analog of Figure 7.10 for graphitized electrodes would have shown little variation in % capacity retention for the first 100 cycles with the parameters that we varied in these experiments.

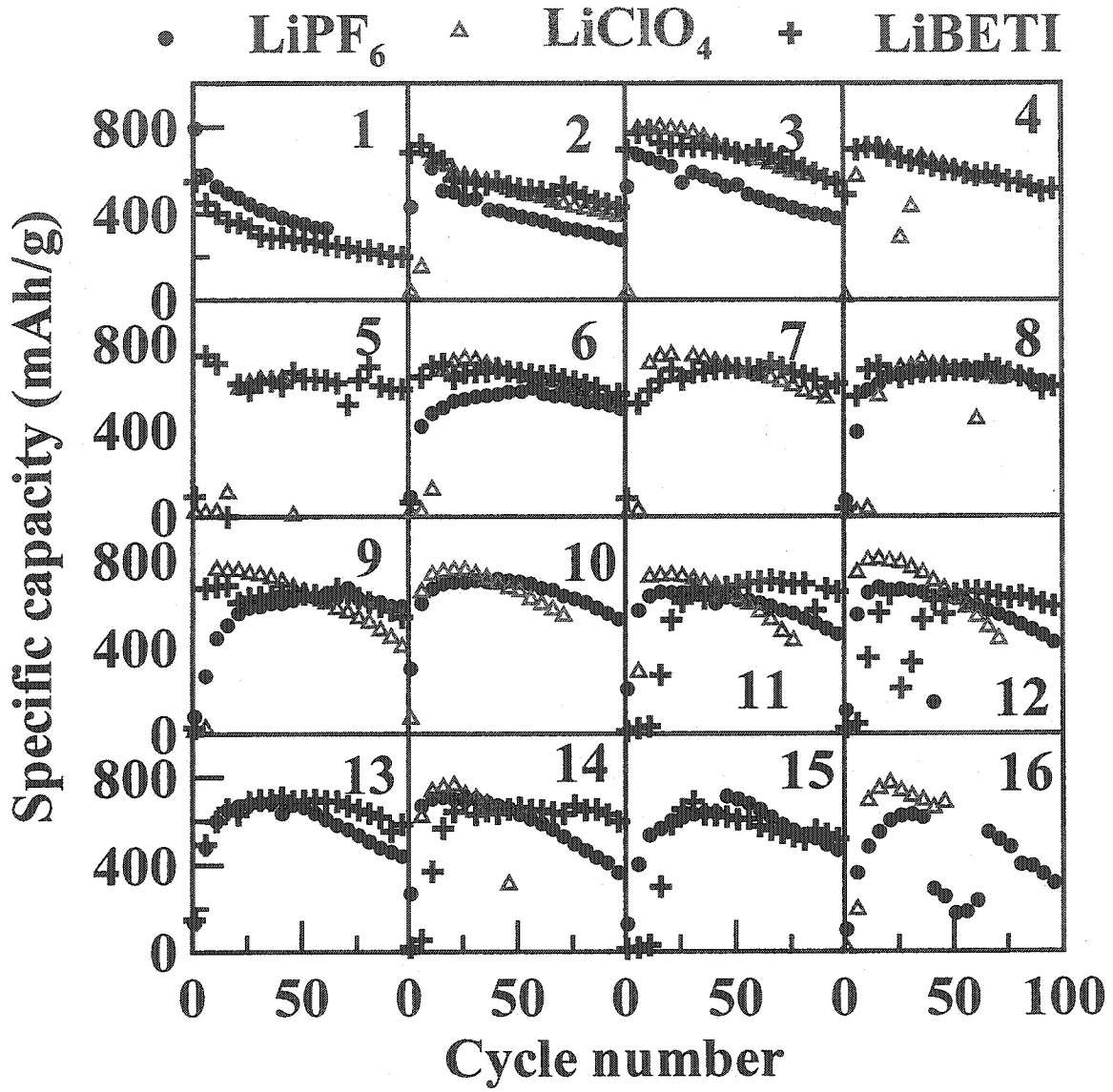

Figure 7.9 The specific capacity vs. cycle number of a-$Si_{0.64}Sn_{0.36}$/Ag electrodes using the proposed PVDF-TFE-P-based elastomeric binder showing the effect of the electrolyte type. The cells were cycled between 0.2-1.0 V using a specific current of 160 mA/g. The electrolytes used were 1M $LiPF_6$, 1M $LiClO_4$, and 1M LiBETI in EC/DEC (1:2, v/v).

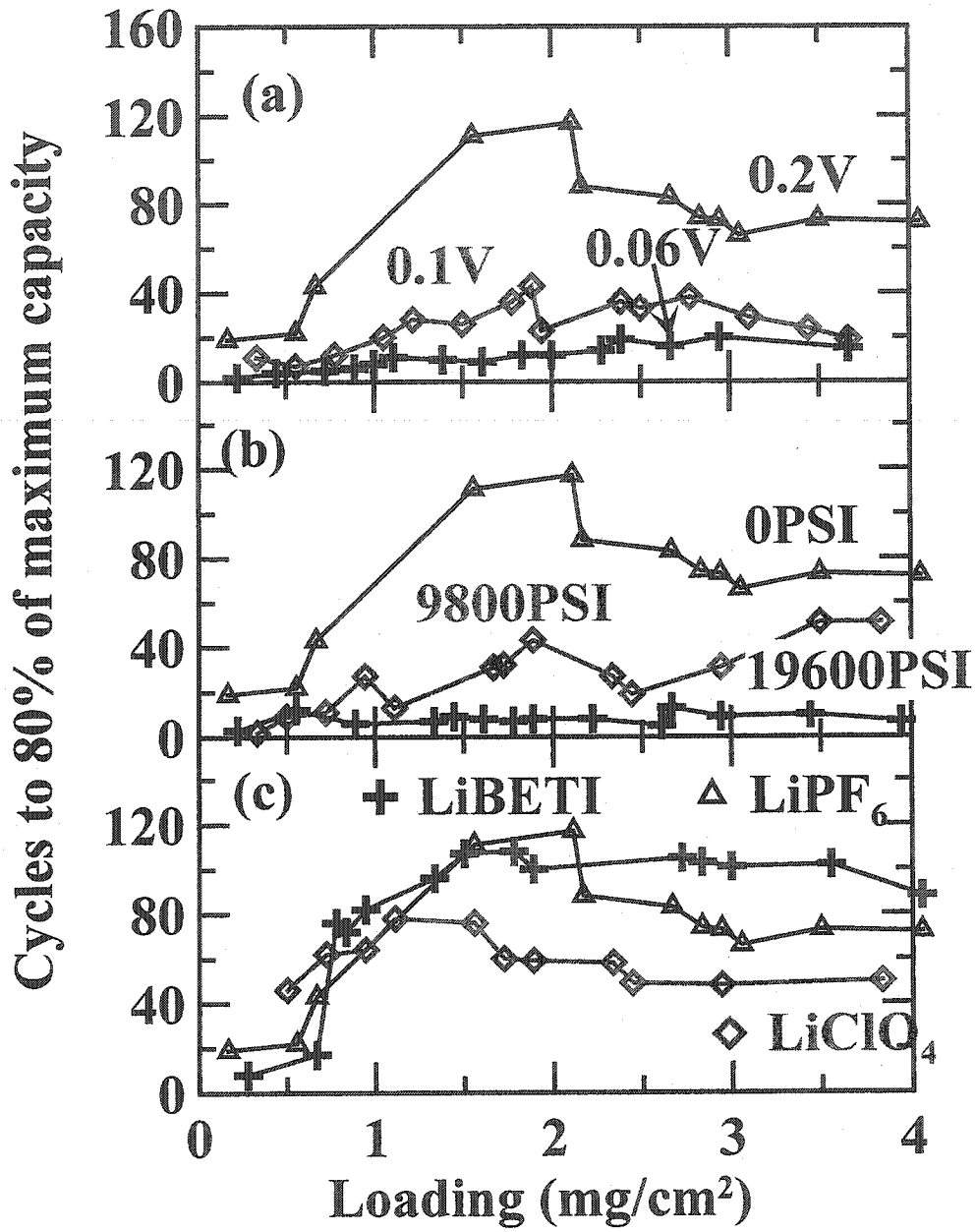

Figure 7.10 The charge-discharge cycle number at which 80% of the maximum cell capacity was reached vs. the loading of active material showing (a) the effect of lower cutoff potential, (b) the effect of compression, and (c) the effect of the electrolyte salt. The ordinate of these graphs could be defined as the "cycle life" in these experiments.

7.8 Observation of different cell behaviors with in-situ experiments

In the previous sections, it has been demonstrated that if the cell was discharged to a cutoff potential lower than 0.2 V, a particle expansion ratio of >125% apparently exceeded the tolerance limit of the proposed PVDF-TFE-P-based elastomeric binder system. Hence, it led a severe mechanical degradation of the binder during the charge/discharge cycling and a fast capacity fading of the electrode. In-situ resistance and in-situ thickness experiments were carried out to distinguish the behavior of a normal cell (cycled properly) from a dying cell.

7.8.1 In-situ resistance

In order to collect more data from a single cell, the fast in-situ resistance experiment was carried out. The cell was charged/discharged at a constant current of 100 mA/g during the charge/discharge periods.

Figure 7.11 shows the specific capacity of an in-situ resistance cell incorporating a-$Si_{0.64}Sn_{0.36}$/Ag composite electrode using the proposed PVDF-TFE-P-based binder. The cell was first cycled between 0.2 V and 1.0 V for 3 cycles. Figure 7.11 shows that the capacity of these cycles is approximately constant (about 840 mAh/g). The cell was then cycled between 0.1 V and 1.0 V for another 5 cycles, was then cycled between 0.06 V and 1.0 V. Naturally, the maximum capacity of the electrode increased a little when the lower cutoff potential decreased from 0.2 V to 0.1 V. However, the capacity decreased quickly with increasing cycle number. After 5 cycles, a small capacity of about 600 mAh/g was obtained. At this stage, a large fraction of the active material particles were probably electrically isolated (based on the tether model). Therefore, when the cell was

discharged to 0.06 V, only a small capacity increase was observed, and the capacity continues to decrease with increasing cycle number.

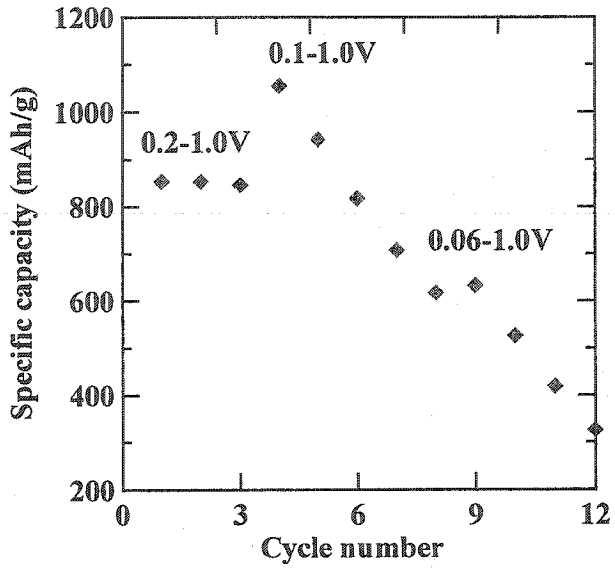

Figure 7.11 Specific capacity of the in-situ resistance cell showing the effect of the lower cutoff potential.

Figure 7.12 shows the resistance variation of the electrode film during discharging as a function of both the discharge level and the cycle number. During the first 3 cycles when the cell was cycled between 0.2 V and 1.0 V, the resistance at 0.2 V was small and showed small variation. The resistance at 0.6 V shows a big jump from the first cycle to the second cycle because of the broken tethers resulting from the first discharge as explained in the section 6.7. When the cell was discharged to 0.1 V during cycling, the resistance increased quickly with the cycling number.

Even when the cell was discharged to 0.1 V, the resistance at 0.1 V grew quickly just as the resistance at 0.2 and 0.6 V did. As explained in the previous section, when the

electrode was discharged to 0.1 V or less, the particle expansion ratio apparently exceeded the tolerance limit of the proposed binder, and hence severe mechanical degradation occurred. The sharp increase of the resistance at 0.1 V can be explained by the increasing the number of electrically isolated a-$Si_{0.64}Sn_{0.36}$/Ag particles resulting from the mechanical degradation of the binder, which decreased the number of electrical paths in the compact electrode (at 0.1 V). This agrees well with the capacity variation of the electrode.

When the cell was further discharged to 0.06 V, only a small capacity change was observed (see Figure 7.11). Hence, only a small resistance change can expected between the 7^{th} cycle (0.1 – 1.0 V) and the 8^{th} cycle (0.06 – 1.0V). In particular, the resistance of the electrode film was approximately unchanged during cycling between 0.06 V and 1.0 V. The low capacity of the degraded electrode (see Figure 7.11) means a low particle shuffling level, which alleviates the mechanical degradation of the binder. Therefore, a small variation of the resistance at 0.6 V and 0.2 V was observed. In a "loose" electrode (at 0.6 V and 0.2 V), the electrically connected a-$Si_{0.64}Sn_{0.36}$/Ag particles lose direct contact with each other and the conductivity of the electrode is dominated by the conductivity of the tether system. However, the electrically connected a-$Si_{0.64}Sn_{0.36}$/Ag particles in a compact electrode (at 0.06 V) form the electrical paths. The decrease of the amount of electrically connected a-$Si_{0.64}Sn_{0.36}$/Ag particles contributes to the resistance growth at 0.06 V.

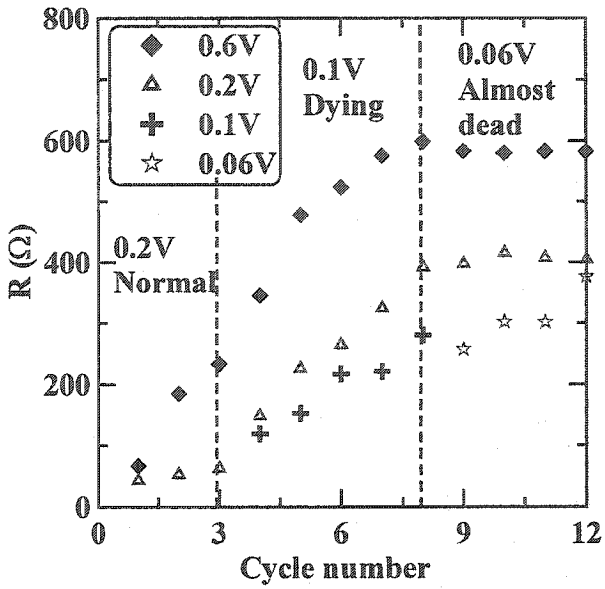

Figure 7.12 The resistance variation vs. cycle number of the electrode film during discharge

7.8.2 In-situ thickness experiment

Figure 7.13 shows the specific capacity of an in-situ thickness cell incorporating a-$Si_{0.64}Sn_{0.36}$/Ag composite electrode using the proposed PVDF-TFE-P-based binder. The thickness of the electrode was 88.1 μm, and the areal density was 6.52 mg/cm^2 of a-$Si_{0.64}Sn_{0.36}$/Ag. The cell was cycled to different lower cutoff potentials (0.2 V, 0.1 V, and 0.06 V) with a constant current of 80 mA/g. A thick electrode was used to provide an acceptable signal for the LVDT sensor although its capacity retention was not the best. The cycling sequence of the lower cutoff potential is 0.2-1.0 V (6 cycles) followed by 0.1-1.0 V (10 cycles) and 0.06-1.0 V (10 cycles). The results shown in Figure 7.13 are almost the same as those shown in Figure 7.11. The capacity retention is good when the

cell was cycled between 0.2 V and 1.0 V. However, the cell had a higher capacity and a faster capacity fading when it was discharged to a lower potential.

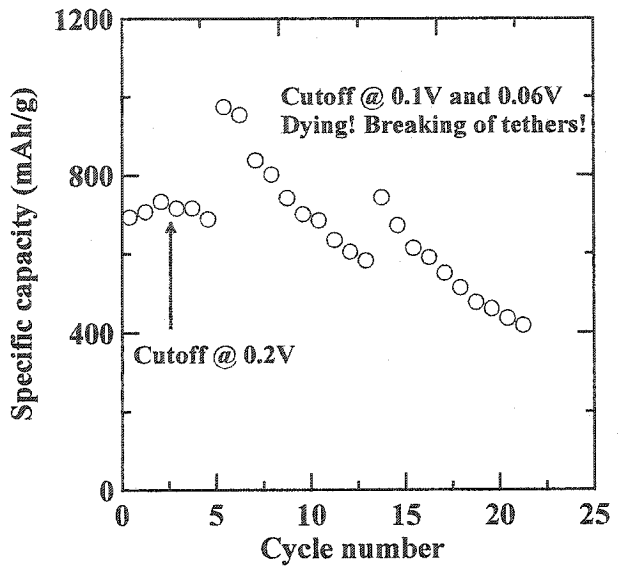

Figure 7.13 Specific capacity of the in-situ thickness cell showing the effect of the lower cutoff potential.

Figure 7.14a shows the cell potential vs. the cumulative capacity of the in-situ thickness cell during the first 3 cycles (0.2-1.0 V). Figure 7.14b shows the variation of the LVDT potential during the experiment. The LVDT signal is proportional to the thickness of the in-situ cell. Figure 7.14b clearly indicates that the thickness of the cell increases linearly with the amount of lithium atoms inserted in the negative electrode during the initial discharge. At the bottom of the initial discharge (0.2 V), the thickness increase of the cell was about 20 μm, which was calibrated with the amplification of the LVDT system. After the initial discharge to 0.2 V, the LVDT potential showed a very small variation during charge/discharge cycling between 0.2 V and 1.0 V. It means that

the thickness of the cell was almost constant. This result agrees well with the results reported by Miller et. al. [81]. Figure 7.14c shows the variation of the thickness of the negative electrode, which was obtained by subtracting the thickness variation of the lithium foil, calculated from its theoretical capacity and density, from the thickness variation of the cell.

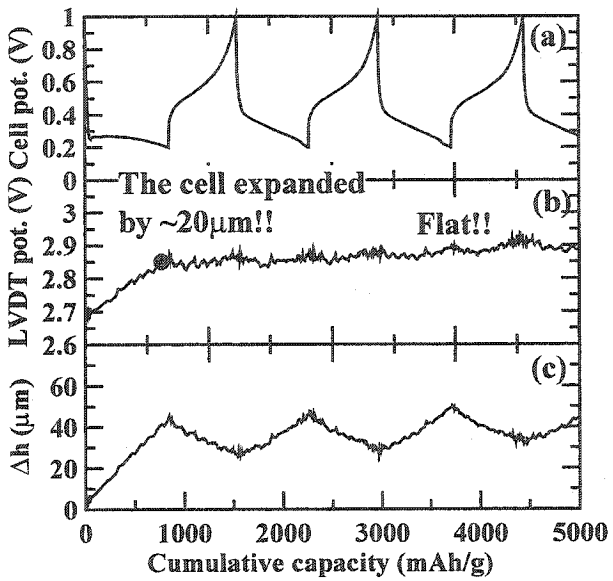

Figure 7.14 (a) cell potential, (b) LVDT potential, and (c) thickness variation of the negative electrode of the in-situ thickness cell during cycling (cycles 1-3)

Figure 7.15 shows the data of the whole experiment (up to 26 cycles). Instead of focusing on the thickness variation during charge/discharge cycling (Figure 7.14), Figure 7.15 gives a whole picture of the cell behavior based on the cycle number and the lower cutoff potential. Figure 7.15b shows the variation of the LVDT potential (thickness change of the cell). Figure 7.13 shows that the cell had a small capacity increase at the third cycle for some reason(s), probably due to temperature fluctuation. Figure 7.15b

also shows a small hump during the third cycle. Once the capacity decreased a little bit, the thickness of the cell decreased correspondingly. This means the thickness change of the cell, or the negative electrode, was reversible if the cell was cycled properly (0.2-1.0 V). When the cell was cycled between 0.1 V and 1.0 V, the thickness of the cell, or the negative electrode increased irreversibly. This could be assigned to the behavior of a dying cell (Figure 7.13). There is a small drop of LVDT potential at the 8th cycle. This is probably caused by a sliding of LVDT probe on the casing bottom, which slightly lowered the LVDT probe. When the cell was discharged to 0.06 V and most of the a-$Si_{0.64}Sn_{0.36}$/Ag particles were electrically isolated, the thickness of the cell had a very small variation with cycle number. The same trend can also be seen in the pattern of the electrode thickness variation.

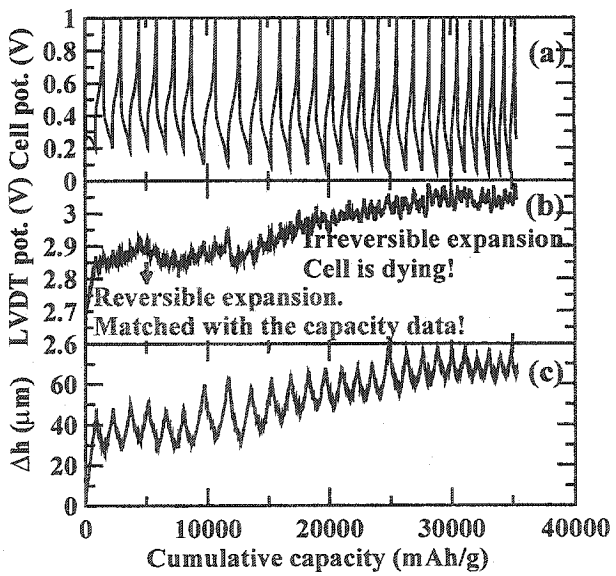

Figure 7.15 (a) cell potential, (b) LVDT potential, and (c) thickness variation of the negative electrode of the in-situ thickness cell during cycling. Cycling sequence: 0.2-1.0 V (6 cycles), 0.1-1.0 V (10 cycles), and 0.06-1.0 V (10 cycles)

7.9 Summary

The difficulty of evaluating the cycling performance of high-volume-change metallic alloys was fully demonstrated with a matrix of 8×16 cells, which were made from a single electrode film with a thickness gradient. The parameters examined included the mass loading, the lower cutoff potential, the compression pressure, and the salt in the electrolyte. All of the electrodes had the same elastomeric binder system, which, in itself, has numerous parameters to optimize, including, weight percent of binder, polymer chosen, polymer molecular weight, type of crosslinker, crosslinking method, type of adhesion promoter, amount of carbon black used, etc as we have discussed in chapter 6. The number of parameters is so large that combinatorial methods of electrode production and evaluation need to be adopted, in our opinion. These might be based on the procedures recently published by Meredith et al. [82].

The results presented strongly suggest that composite electrodes of high-volume-change metallic alloys need to be evaluated with an effective binder. Much of the experimental data in the literature has employed non-elastomeric binders under a single set of electrode conditions, so it is hard to believe that the electrodes were optimized, given the complexity of the problem. The experimental evidence strongly suggests that a good understanding of the binder system is critical for the research, development, and commercialization of alloy negative electrode materials. We urge the community to get involved in investigating and understanding the binder problem.

The different behavior of a normal cell, a dying cell, and a dead cell were observed with in-situ resistance and in-situ thickness experiments. Typically, a normal electrode has a small resistance, a low resistance growth rate, and a reversible

expansion/contraction of the electrode after initial discharge. The resistance and the thickness of a dying electrode increase quickly and irreversibly. When the cell is almost dead, the variation of resistance and thickness is small because of the small capacity delivered, but the value of the resistance and thickness still increase irreversibly.

Chapter 8 Conclusions and future work

8.1 Conclusions

In this thesis, the critical importance of elastomeric binder systems for large-volume-change electrode materials for lithium-ion batteries has been demonstrated experimentally.

A tether model was proposed to qualitatively understand the rapid capacity fading of large-volume-change electrodes for lithium-ion batteries. Experimental efforts were made to specially design an elastomeric binder system according to the requirements of the tether model. A poly(vinylidene fluoride-tetrafluoroethylene-propylene) (PVDF-TFE-P)-based elastomeric binder system was designed and optimized to significantly improve the capacity retention of composite electrodes containing a-$Si_{0.64}Sn_{0.36}$/Ag (10 wt% silver coating), which was used as the model of high-volume-change materials.

The difficulty of evaluating the cycling performance of high-volume-change metallic alloys was fully demonstrated with a combinatorial experiment on electrodes that have a thickness gradient. The parameters examined included the mass loading, the lower cutoff voltage, the compression pressure, and the electrolyte salt. All of the electrodes had the same elastomeric binder system, which, in itself, has numerous parameters to optimize, including the weight percentage of the binder, the polymer chosen, the polymer molecular weight, the type of crosslinker, the crosslinking method, the type of adhesion promoter, the amount of carbon black used, etc. The results presented strongly suggest that composite electrodes of high-volume-change metallic alloys need to be fairly evaluated with an effective binder.

The best recipe we have found is an electrode composed of 100 pph a-$Si_{0.64}Sn_{0.36}$/Ag, 10 pph SS, 10 pph PVDF-TFE-P, 0.4 pph CaO, 0.3 pph DABCO, 0.4 pph TETA, and 4.7 pph APTES. The electrodes were heated at 110°C in an argon flow for 24 hours before use. The preferred active material loading is about 3.0 mg/cm^2. The best cycling condition is to cycle the cells using uncompressed electrodes between 0.2 V and 1.0 V and using LiBETI-EC/DEC based electrolyte.

8.2 Future work

The experimental results shown in this thesis strongly suggests that a good understanding of the binder system is critical for the research, development, and commercialization of alloy negative electrode materials. We urge the community to get involved in investigating and understanding the binder problem.

8.2.1 Basic science of materials

In most literature work on composite electrodes of high-volume-change alloys, a polymer binder with poor elastomeric properties, such as poly(vinylidene fluoride) (PVDF) [16, 17, 19-26, 28, 29], was used to evaluate the charge-discharge cycling performance of the alloys. There is no reason for us to believe that such poor binders can tolerate the large volumetric changes (~250%) of negative electrode material particles. Therefore, it is very dangerous to evaluate high-volume-change electrodes using such a poor binder system. As an example, it has been clearly demonstrated in chapter 6 that the capacity retention of a-$Si_{0.64}Sn_{0.36}$/Ag was significantly improved by replacing the PVDF-

based binder with a PVDF-TFE-P-based elastomeric binder system. The experimental evidence presented here strongly suggests that many newly developed metallic anodes deserve to be evaluated a second time using a good binder system.

It was found that the capacity retention of a-$Si_{0.64}Sn_{0.36}$/Ag composite electrodes was much better than a-$Si_{0.64}Sn_{0.36}$ electrodes. It has been reported that the silver coating also improved the cycling behavior of Si composite electrodes [74]. Wu et. al. proposed that the coated silver enhances the formation of the solid electrolyte interphase (SEI) on Si particles, which help to maintain the electrical contact between the pulverized Si particles [74]. However, this explanation is far from being satisfactory. The interaction between the SEI and the particle is weak (Van der Waals bond), and the SEI is already greatly swelled or gelled in the organic solvent. It is hard to believe that such a layer can maintain the electrical contact between pulverized particles. In addition, the pulverization is not problematic for a-$Si_{0.64}Sn_{0.36}$ [10, 11], but the silver coating still improves the capacity retention of composite electrodes. In my opinion, the mechanism of the silver coating is not understood well yet.

We also noticed that the resistivity of a-$Si_{0.64}Sn_{0.36}$/Ag electrodes was much higher than that of MCMB electrodes with the same binder recipe, while the two types of electrodes had almost the same resistivity after heavy compression. This is a scientific mystery for us. The understanding of this mystery might give large-volume-change electrodes another boost in capacity retention.

The formulation of the binder system and optimization of electrode parameters have been discussed in detail in this thesis. However, the surface chemistry of the negative electrode material during charge/discharge cycling still remains untouched. The binder

system discussed in this thesis heavily relies on Si-O-Si junctions, which link the electrode components into a networked system. We showed that the presence of the Si-O-Si bonds greatly affected the capacity retention of high-volume-change electrodes. However, the Si-O bonds might be attacked by Li atoms during discharge. It is important to prove that such junctions for the coupling agent survive after charge-discharge cycles. If the coupling agent is damaged by lithium, then alternative chemistries need to be found.

8.2.2 Battery technology

The tether model has been experimentally verified, and can be used as an empirical theory to guide future research. There are still lots of work to do to maximize the capacity retention of large-volume-change electrodes.

The superiority of the PVDF-TFE-P-based elastomeric binder over the PVDF-based binder has been demonstrated in this thesis. However, PVDF-TFE-P cannot possibly be the best elastomer. There must be some better candidates in the current or near-future market. It is important to search for better binder systems to maximize the performance of large-volume-change electrodes. The tether model can be extremely useful to help distinguish the promising ones from the bad ones. Table 2.1 is a useful guide to help design a polymer/carbon black/crosslinking agent/coupling agent binder for each potential candidate. This is a huge project, but is very important for commercialization of metallic alloys and characterization of new materials.

Mechanical aging of polymeric materials under cyclic loading is common, and can lead to the deterioration of the mechanical and electrical properties of polymeric materials. The a-$Si_{0.64}Sn_{0.36}$/Ag electrodes containing the proposed elastomeric binder

also showed slow resistance growth with increasing cycle number presumably due to the aging of the binder during cyclic deformation (see section 6.7). The aging behavior of the binder system also needs to be investigated to maximize the capacity retention of large-volume-change electrodes.

8.2.3 Methodology

The difficulty of evaluating the cycling performance of high-volume-change metallic alloys has been fully demonstrated in chapters 6 and 7. We might also need to design new experiments to collect new information on the binder system. The number of parameters is so large that combinatorial methods of electrode production and evaluation need to be adopted, in our opinion. Methods to prepare thickness gradients, compositional gradients, and temperature gradients in polymer science have been established already. What we need to do is to modify them to match our application. These might be based on the procedures recently published by Meredith et al. [82]. A useful reference for combinatorial electrochemical characterization of electrode arrays was recently published by Fleischauer et. al. [83].

References

[1] D. Sperling, *Scientific American*, 275(**1996**), 54-59.

[2] C. W. Garrett, *Prog. Energ. Combust. Sci.*, 18(**1992**), 369-407.

[3] J. M. Tarascon; and M. Armand, *Nature*, 414(**2001**), 359-367.

[4] R. Fong, U. von Sacken; and J. R. Dahn, *J. Electrochem. Soc.*, 137(**1990**), 2009-2013.

[5] D. Aurbach, B. Markovsky, A. Shechter, Y. EinEli; and H. Cohen, *J. Electrochem. Soc.*, 143(**1996**), 3809-3820.

[6] K. Sayamasa, H. Yagi, Y. Kato, S. Matsuta, H. Tarui; and S. Fujitani, *Abs. # 52 at 11th International Meeting of Lithium Batteries*, IMBL11, Monterey, CA, **2002**.

[7] J. Graetz, C. Ahn, R. Yazami; and B. Fultz, *Abs. #317 at 204th ECS Meeting*, ECS204, Orlando, FL, **2003**.

[8] R. L. Turner, Amorphous metallic alloys, US Patent 20020162606 (**2002**).

[9] L. Y. Beaulieu, S. D. Beattie, T. D. Hatchard; and J. R. Dahn, *J. Electrochem. Soc.*, 150(**2003**), A419-A424.

[10] L. Y. Beaulieu, T. D. Hatchard, A. Bonakdarpour, M. D. Fleischauer; and J. R. Dahn, *J. Electrochem. Soc.*, 150(**2003**), A1457-A1464.

[11] L. Y. Beaulieu, K. W. Eberman, R. L. Turner, L. J. Krause; and J. R. Dahn, *Electrochem. Solid State Lett.*, 4(**2001**), A137-A140.

[12] L. Y. Beaulieu, K. C. Hewitt, R. L. Turner, A. Bonakdarpour, A. A. Abdo, L. Christensen, K. W. Eberman, J. L. Krause; and J. R. Dahn, *J. Electrochem. Soc.*, 150(**2003**), A149-A156.

[13] M. R. Wagner, M. Wachtler, M. Schmied, P. Preishuber-Pflugl, F. Stelzer, J. O. Besenhard; and M. Winter, *Abs. #73 at 10th International Meeting of Lithium Batteries*, IMLB10, Como, Italy, **2000**.

[14] L. H. Shi, H. Li, Z. X. Wang, X. J. Huang; and L. Q. Chen, *J. Mater. Chem.*, 11(**2001**), 1502-1505.

[15] J. Yang, Y. Takeda, N. Imanishi; and O. Yamamoto, *J. Electrochem. Soc.*, 146(**1999**), 4009-4013.

[16] J. Yang, M. Wachtler, M. Winter; and J. O. Besenhard, *Electrochem. Solid State Lett.*, 2(**1999**), 161-163.

[17] J. Yang, B. F. Wang, K. Wang, Y. Liu, J. Y. Xie; and Z. S. Wen, *Electrochem. Solid State Lett.*, 6(**2003**), A154-A156.

[18] K. D. Kepler, J. T. Vaughey; and M. M. Thackeray, *Electrochem. Solid State Lett.*, 2(**1999**), 307-309.

[19] I. Kim, G. E. Blomgren; and P. N. Kumta, *Electrochem. Solid State Lett.*, 6(**2003**), A157-A161.

[20] L. Fang; and B. V. R. Chowdari, *J. Power Sources*, 97-8(**2001**), 181-184.

[21] H. Y. Lee, S. W. Jang, S. M. Lee, S. J. Lee; and H. K. Baik, *J. Power Sources*, 112(**2002**), 8-12.

[22] H. Y. Lee; and S. M. Lee, *J. Power Sources*, 112(**2002**), 649-654.

[23] G. A. Roberts, E. J. Cairns; and J. A. Reimer, *J. Electrochem. Soc.*, 150(**2003**), A912-A916.

[24] H. Kim, J. Choi, H. J. Sohn; and T. Kang, *J. Electrochem. Soc.*, 146(**1999**), 4401-4405.

[25] A. Hayashi, M. Nakai, M. Tatsumisago, T. Minami; and M. Katadab, *J. Electrochem. Soc.*, 150(**2003**), A582-A587.

[26] J. T. Yin, M. Wada, S. Yoshida, K. Ishihara, S. Tanase; and T. Sakai, *J. Electrochem. Soc.*, 150(**2003**), A1129-A1135.

[27] X. W. Zhang, C. S. Wang, A. J. Appleby; and F. E. Little, *J. Power Sources*, 109(**2002**), 136-141.

[28] H. Li, X. J. Huang, L. Q. Chen, Z. G. Wu; and Y. Liang, *Electrochem. Solid State Lett.*, 2(**1999**), 547-549.

[29] L. M. L. Fransson, J. T. Vaughey, K. Edstrom; and M. M. Thackeray, *J. Electrochem. Soc.*, 150(**2003**), A86-A91.

[30] P. Villars; and L. D. Calvert, *Pearson's Handbook of Crystallographic Data for Intermetallic Phases*, ASM International, **1996**.

[31] J. Schoonman, *Solid State Ionics*, 135(**2000**), 5-19.

[32] O. Mao, R. L. Turner, I. A. Courtney, B. D. Fredericksen, M. I. Buckett, L. J. Krause; and J. R. Dahn, *Electrochem. Solid State Lett.*, 2(**1999**), 3-5.

[33] O. Mao, R. A. Dunlap; and J. R. Dahn, *J. Electrochem. Soc.*, 146(**1999**), 405-413.

[34] O. Mao; and J. R. Dahn, *J. Electrochem. Soc.*, 146(**1999**), 414-422.

[35] O. Mao; and J. R. Dahn, *J. Electrochem. Soc.*, 146(**1999**), 423-427.

[36] K. D. Kepler, J. T. Vaughey; and M. M. Thackeray, *J. Power Sources*, 82(**1999**), 383-387.

[37] H. J. Jung, M. Park, Y. G. Yoon, G. B. Kim; and S. K. Joo, *J. Power Sources*, 115(**2003**), 346-351.

[38] R. L. Reese, *Hooke's Force Law and Simple Harmonic Oscillation*, Brooks/Cole Publishing Company, New York, **1998**, 281-318.

[39] I. M. Ward; and D. W. Hadley, *An Introduction to the Mechanical Properties of Solid Polymers*, John wiley & Sons, New York, **1998**.

[40] D. A. McQuarrie, *Statistical Thermodynamics*, University Science Books, California, **1973**.

[41] H. M. James; and E. Guth, *J. Chem. Phys.*, 11(**1943**), 455-481.

[42] B. S. Chiou; and P. E. Schoen, *J. Appl. Polym. Sci.*, 83(**2002**), 212-223.

[43] B. C. Chun, S. H. Cha, Y. C. Chung; and J. W. Cho, *J. Appl. Polym. Sci.*, 83(**2002**), 27-37.

[44] E. Punkka, J. Laakso, H. Stubb; and P. Kuivalainen, *Phys. Rev.: B*, 41(**1990**), 5914-5918.

[45] K. P. Pramoda, Y. H. Lin, W. Y. Chen; and T. S. Chung, *Polym. Bull.* ,47(**2001**), 55-63.

[46] D. H. Yin, Y. Zhang, Y. X. Zhang, Z. L. Peng, Y. Z. Fan; and K. Sun, *J. Appl. Polym. Sci.*, 85(**2002**), 2667-2676.

[47] M. Baiardo, G. Frisoni, M. Scandola; and A. Licciardello, *J. Appl. Polym. Sci.*, 83(**2002**), 38-45.

[48] F. Severini, L. Formaro, M. Pegoraro; and L. Posca, *Carbon*, 40(**2002**), 735-741.

[49] T. Funasaka, T. Ashihara, S. Maekawa, S. Ohno, M. Meguro, T. Nishino; and K. Nakamae, *Intern. J. Adhesion Adhesives*, 19(**1999**), 367-371.

[50] S. Ganguly, S. Chakraborty, A. N. Banerjee; and P. Bhattacharya, *J. Appl. Polym. Sci.*, 85(**2002**), 2025-2033.

[51] D. Pantea, H. Darmstadt, S. Kaliaguine, L. Summchen; and C. Roy, *Carbon*, 39(**2001**), 1147-1158.

[52] S. S. Weng, S. S. Mun, S. Y. Cheong, S. Y. Leong; and L. A. Kwong, *Silane coupling agent*, http://www.sinrubtech.com.my/short%20notes/Short%20Notes%205.1.htm.

[53] M. Baiardo, G. Frisoni, M. Scandola, M. Rimelen, D. Lips, K. Ruffieux; and E. Wintermantel, *J. Appl. Polym. Sci.*, 90(**2003**), 1731-1738.

[54] B. L. Shah; and V. V. Shertukde, *J. Appl. Polym. Sci.*, 90(**2003**), 3278-3284.

[55] J. S. Choi; and W. T. Park, *Macromolecular Symposia*, 197(**2003**), 65-76.

[56] C. Forte; and S. Pizzanelli, *Macromolecules*, 36(**2003**), 4004-4009.

[57] H. Djidjelli, M. Kaci, A. Boukerrou, D. Benachour; and J. J. Martinez-Vega, *J. Appl. Polym. Sci.*, 89(**2003**), 3447-3457.

[58] D. Feldman, D. Banu, R. S. J. Manley; and H. Zhu, *J. Appl. Polym. Sci.*, 89(**2003**), 2000-2010.

[59] R. Faez; and M. D. Paoli, *J. Appl. Polym. Sci.*, 82(**2001**), 1768-1775.

[60] Z. H. Chen, L. Christensen; and J. R. Dahn, *J. Appl. Polym. Sci.*, (**2003**), in press.

[61] Z. H. Chen, L. Christensen; and J. R. Dahn, *J. Appl. Polym. Sci.*, (**2003**), in press.

[62] Z. H. Chen, L. Christensen; and J. R. Dahn, *J. Appl. Polym. Sci.*, 90(**2003**), 1891-1899.

[63] Z. H. Chen, L. Christensen; and J. R. Dahn, *J. Electrochem. Soc.*, 150(**2003**), A1073-A1078.

[64] L. Q. Yang, Z. M. Xie; and Z. M. Li, *J. Appl. Polym. Sci.*, 74(**1999**), 91-96.

[65] R. Veragraziano, F. Hernandezsanchez; and J. V. Cauichrodriguez, *J. Appl. Polym. Sci.*, 55(**1995**), 1317-1327.

[66] M. Baba, J. L. Gardette; and J. Lacoste, *Polymer Degradation and Stability*, 63(**1999**), 121-126.

[67] M. E. F. Baudais; and J. R. Dahn, *Solid State Ionics*, 66(**1993**), 175-181.

[68] J. Yang, Y. Takeda, N. Imanishi, T. Ichikawa; and O. Yamamoto, *J. Power Sources*, 79(**1999**), 220-224.

[69] Z. H. Chen, M. D. Fleischauer, L. Christensen; and J. R. Dahn, *submitted to J. Electrochem. Soc.*, (**2003**).

[70] Z. H. Chen, L. Christensen; and J. R. Dahn, *Electrochem. Comm.*, 5(**2003**), 919-923.

[71] A. Magistris, P. Mustarelli, F. Parazzoli, E. Quartarone, P. Piaggio; and A. Bottino, *J. Power Sources*, 97-8(**2001**), 657-660.

[72] P. Periasamy, K. Tatsumi, M. Shikano, T. Fujieda, Y. Saito, T. Sakai, M. Mizuhata, A. Kajinami; and S. Deki, *J. Power Sources*, 88(**2000**), 269-273.

[73] P. Periasamy, K. Tatsumi, M. Shikano, T. Fujieda, T. Sakai, Y. Saito, M. Mizuhata, A. Kajinami; and S. Deki, *Solid State Ionics*, 126(**1999**), 285-292.

[74] X. D. Wu, Z. X. Wang, L. Q. Chen; and X. J. Huang, *Electrochem. Comm.*, 5(**2003**), 935-939.

[75] D. D. MacNeil; and J. R. Dahn, *J. Electrochem. Soc.*, 150(**2003**), A21-A28.

[76] A. M. Andersson, M. Herstedt, A. G. Bishop; and K. Edstrom, *Electrochimica Acta*, 47(**2002**), 1885-1898.

[77] A. M. Andersson; and K. Edstrom, *J. Electrochem. Soc.*, 148(**2001**), A1100-A1109.

[78] D. Billaud, E. McRae; and A. Herold, *Mat. Res. Bull.*, 14(**1979**), 857.

[79] Q. Wang, H. Li, X. J. Huang; and L. Q. Chen, *J. Electrochem. Soc.*, 148(**2001**), A737-A741.

[80] A. Mabuchi, H. Fujimoto, K. Tokumitsu; and T. Kasuh, *J. Electrochem. Soc.*, 142(**1995**), 3049-3051.

[81] M. Heath, C. Silkowski, P. Sholtes, C. McIntyre; and J. Miller, *Abs. # 325 presented at the 204 ECS meeting*, 204 ECS meeting, Orlando, FL, **2003**.

[82] J. C. Meredith, A. Karim; and E. J. Amis, *Macromolecules*, 33(**2000**), 5760-5762.

[83] M. D. Fleischauer, T. D. Hatchard, G. P. Rockwell, J. M. Topple, S. Trussler, S. K. Jericho, M. H. Jericho; and J. R. Dahn, *J. Electrochem. Soc.*, 150(**2003**), A1465-A1469.